Universitat Autònoma de Barcelona

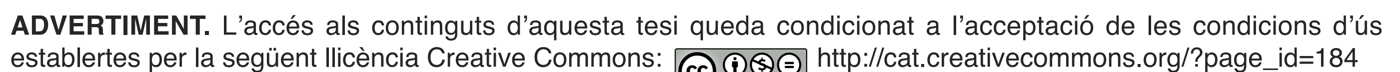

ADVERTIMENT. L'accés als continguts d'aquesta tesi queda condicionat a l'acceptació de les condicions d'ús establertes per la següent llicència Creative Commons: http://cat.creativecommons.org/?page_id=184

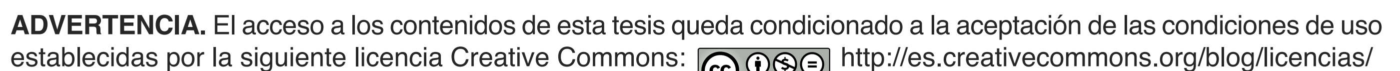

ADVERTENCIA. El acceso a los contenidos de esta tesis queda condicionado a la aceptación de las condiciones de uso establecidas por la siguiente licencia Creative Commons: http://es.creativecommons.org/blog/licencias/

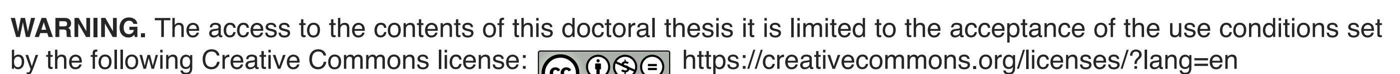

WARNING. The access to the contents of this doctoral thesis it is limited to the acceptance of the use conditions set by the following Creative Commons license: https://creativecommons.org/licenses/?lang=en

Microstructural Control of Epitaxial α-Quartz Films

Qianzhe ZHANG

Doctoral Thesis

Doctoral Studies in Material Science

Supervised by Dr. Martí Gich Garcia and Dr. Adrián Carretero-Genevrier

Tutor: Prof. Lluís Casas Duocastella

Departament de Física de la Universitat Autònoma de Barcelona

Facultat de Ciències

2019

Dr. Martí Gich Garcia, tenured scientist at the Institut de Ciència de Materials de Barcelona - Consejo Superior de Investigaciones Científicas; Dr. Adrián Carretero-Genevrier, permanent researcher at the Institut d'Électronique et des Systèmes (IES) – Université de Montpellier; and Prof. Lluís Casas Duocastella, professor at Departament de Geologia of Universitat Autònoma de Barcelona.

CERTIFY

that Qianzhe Zhang carried out under their direction the research work entitled "Controlling the Microstructure of Epitaxial α-Quartz Films". This work has been developed within a PhD program in Materials Science at the department of physics of Universitat Autònoma de Barcelona.

For that record they sign the certificate.

Dr. Martí Gich Garcia Dr. Adrián Carretero-Genevrier

Prof. Lluís Casas Duocastella

Bellaterra, July 2019

Acknowledgment

On 27th of September 2015, I arrived at Universitat Autònoma de Barcelona to begin my PhD research with the funding from Chinese Scholarship Council (CSC). Now, after four years working under the supervision of Martí Gich Garcia and Adrián Carretero-Genevrier, I have had a wonderful research experience and achieved many successful results which could give me an excellent PhD period. In addition, which may be more important to myself, I can feel that I have grown up after my PhD period with improving my research capabilities, and I'm sure this is the most precious thing to my further career. Recalling the whole time of my PhD study, I want to express my gratitude to everyone helped me, worked with me and supported me.

Firstly, I want to thank the Chinese Scholarship Council (CSC). Its scholarship gives me the opportunity to have a stable abroad study, which can let me focus all my energy on my PhD work and allow me to have a nice oversea life.

Secondly, I will say thanks to my parents. My parents are very supporting my decision of abroad study. During my 4-year abroad life, they never disturb me, never feel sad for my absence in their life, never say any dissatisfied thing to me. Instead, they always encourage me, support me, let me get down to finish my PhD study here.

Thirdly, I want to thank my two supervisors for accepting me as their PhD student. They have a deep knowledge about my PhD topic so that I can understand all the conceptions and techniques used in my research (such as dip-coating, sol-gel, lithography and piezoelectricity) better and faster. Simultaneously, they are very experienced and can always give me some useful suggestions and plans for improving my PhD experiment. Moreover, both of them have a high capability as scientists including high English level, professional writing skill for a scientific paper and perfect organization on activities such as conference, presentation, cooperation and so on. All these can prompt me closer to a real scientist.

Then, I want to thank my group members. We have a small but cosy research family named as "Nanoparticles and Nanocomposites". We have an excellent group leader Prof. Anna Roig. She is kind and manages all the daily things of the group well. She also helped me for many times and shared interesting stories with us. we are an international group due to my fellows come from different part of Earth (Spanish, Chinese, Indian, Polish and Egyptian). In the work time, we just help each other. And in the daily time, we often spend time together to share interesting news. Such a tiny family let me feel free and happy, which also is an important precondition for me to have a happy and propitious PhD research.

Well, besides my group, I also want to thank all the technicians in ICMAB for the analyses and measurements of my samples. In particular: Maite Simón, Andrés Gómez, Anna Crespi, Javier Campos, Joan Esquius, Judith Oró and Neus Romà. Thanks for teaching me how to use these specific techniques, helping me to analyse data in patience. Honestly, I cannot obtain all the successful results without your participations. Also thanks to technicians from other research facilities at UAB campus, namely Emma Rossinyol from the electron microscopy service and Guillaume Sauthier, responsible for XPS analysis at ICN2. Also special thanks to Jaume Gàzquez for his advanced TEM studies on epitaxial quartz films and to Andrés Gómez for Direct Piezoelectric Force Microscopy analysis.

In the meantime, I also want to say thanks to my "Nanochemlab" fellows in Montpellier. This is the other thing to thank Dr. Adrián Carretero-Genevrier. He opened a door to let me study at IES in University of Montpellier, where I met my new friends including David Sánchez, José Vila-Fungueiriño and Claire Jolly. They helped me a lot both for work and life. I had a wonderful time with all my Montpellier's friends.

At last, I want to thank all my CSC colleagues and my flatmates that work and live with me in Barcelona. I can get funny things with you every day and also your help. I knew many information and suggestions from you which can protect me from a freshman living in abroad.

Abstract

Epitaxial films of piezoelectric α-quartz could enable the fabrication of sensors with unprecedented sensitivity for prospective applications in electronics, biology and medicine. However, a prerequisite is harnessing the crystallization of epitaxial α-quartz, tailoring suitable film microstructures for nanostructuration. In my PhD work, we bring new insights into the crystallization of epitaxial α-quartz films on Silicon(100) from the thermal devitrification of nanoporous silica and the control the film microstructures: We show that by increasing the quantity of devitrifying agent (Sr) it is possible to switch from an α-quartz microstructure consisting of porous flat film to one dominated by larger and fully dense α-quartz crystals. The mechanism of Sr-assisted devitrification was also investigated simultaneously.

Then, we found that film thickness, annealing temperature, relative humidity and the nature of surfactant also play an important role in the control of the microstructure and homogeneity of the films. By increasing its, thickness it is possible to switch from a partly crystalline and porous film to fully a crystalline and dominated by dense crystals one. Annealing temperature can impact the crystallization process very deeply for it can change the dynamics and reactivity of Sr within the silica film. High relative humidity cooperates with a suitable surfactant to create perforations on the films via a water-induced phase separation phenomenon. This perforation can also influence the film crystallinity by altering the distribution of Sr inside film. All these studies on the one hand give us a better understanding of the mechanism of Sr-assisted devitrification and on the other hand can show us a versatile microstructural control of the epitaxial α-quartz film.

Besides, via a multilayer deposition method, we have extended the maximum thickness of the α-quartz films from a few hundreds of nm into the µm range. Moreover, in my thesis, we report unprecedented large-scale fabrications of ordered arrays of piezoelectric epitaxial α-quartz nanostructures on silicon(100) substrates by the combination of three cost-effective lithographic techniques: (i) laser transfer lithography, (ii) soft nanoimprint lithography on Sr-doped SiO_2 sol-gel thin films and (iii) self-assembled $SrCO_3$ nanoparticles reactive nanomasks. Epitaxial α-quartz nanopillars with different diameters (down to 50 nm) and heights (up to 2000 nm) were obtained for the first time. This part of my PhD work demonstrates the control over the shape, micro- and nano-patterning of α-quartz thin films while preserving its crystallinity, texture and piezoelectricity, which opens the opportunity to fabricate new high frequency resonators and high sensitivity sensors relevant in different fields of application.

Table of Contents

Acknowledgment

Abstract

Table of Contents

Chapter 1. Introduction 1

1.1. Quartz materials 2

1.1.1. SiO_2 polymorphs 2

1.1.2. Quartz structure 3

1.2. State-of-the-art about α-quartz materials 4

1.2.1. Traditional applications of α-quartz 4

1.2.2. Piezoelectric applications of α-quartz 6

1.2.3. Optical properties of α-quartz 6

1.2.4. Fabrication of α-quartz materials 7

1.2.5. Crystallization of α-quartz nanomaterials from amorphous SiO_2 9

1.3. Evaporation-induced self-assembly method 10

1.3.1. The preparation of initial solution 10

1.3.2. The evaporation-induced deposition 11

1.3.3. Sol-gel method 12

1.4. Sr-assisted sol-gel method to grow epitaxial α-quartz films 13

1.4.1. Our previous studies on the Sr-assisted synthesis of α-quartz films 13

1.4.2. Aims of my PhD work 15

1.4. Chapter references 15

Chapter 2. Motivation & Objectives 21

2.1. Motivation 22

2.2. Objectives 23

2.3. Chapter references 23

Chapter 3. Experimental Procedures 25

3.1. General synthetic process 26

3.2. Experimental section **26**

3.2.1. Silica sol preparation 26

3.2.2. Formation of gel film via dip-coating 29

3.2.3. thermal annealing 31

3.3. Characterization techniques **32**

3.3.1. Surface characterizations 33

3.3.2. Structural characterizations 35

3.3.3. Physical characterizations 37

3.4. Chapter references **38**

Chapter 4. Controlling α-Quartz Film Microstructures via Strontium-assisted Devitrification **39**

4.1. Different film microstructures controlled by R_{Sr} **40**

4.1.1. Partly crystalline films 41

4.1.2. Porous α-quartz films 44

4.1.3. Dense α-quartz films 49

4.1.4. Analysis of Sr compounds present in the films 57

4.2. Influence of R_{Sr} on film crystallinity **60**

4.2.1. Dynamic study of crystallization 60

4.2.2. R_{Sr} dependent crystallization 64

4.3. Microstructural characteristics and properties of films controlled by R_{Sr} 65

4.3.1. Densification & roughness 65

4.3.2. Crystallinity & epitaxy 67

4.3.3. DPFM test of piezoelectricity 69

4.4. Chapter conclusion **71**

4.5. Chapter references **72**

Chapter 5. Microstructural Control of Film During Synthesis **74**

5.1. Thickness of gel films **75**

5.1.1. The relationship between T_{gel} and U_w 75

5.1.2. The influence of T_{gel} in mixed regime 78

5.1.3. The influence of T_{gel} in draining regime 81

5.1.4. Limitation of the T_{gel} study 88

5.2. Investigating the influence of annealing temperature on the

microstructures of epitaxial α-quartz films..90

5.2.1. The influence of ***AT*** in porous α-quartz films 91

5.2.2. The influence of ***AT*** on the crystallization of dense films $\boldsymbol{R}_{\mathrm{Sr}}$ region 95

5.2.3. Investigation of crystallization at extra ***AT*** conditions..98

5.3. Perforations caused by water-induced phase separation.........................100

5.3.1. Water-induced phase separation...100

5.3.2. Perforation of porous film..102

5.3.3. Perforation of dense films 104

5.3.4. The role of surfactant on the perforation of films 106

5.4. Chapter conclusion..108

5.5. Chapter references 109

***Chapter 6. Nanostructure Engineering of Piezoelectric α-Quartz Films*............... 111**

6.1. Integration of epitaxial α-quartz thick films via multilayer deposition ...112

6.1.1. Multilayer deposition of films with dense microstructure 112

6.1.2. Multilayer deposition of films with porous microstructure.......................................115

6.1.3. Disadvantages of multilayer deposition method 117

6.2. Nanostructure engineering of epitaxial α-quartz thick films on silicon ...118

6.2.1. The lithographic techniques used in my work...119

6.2.2. Direct patterning of multilayer films by laser interference lithography.....................120

6.2.3. Soft nanoimprint lithography of multilayer films 123

6.2.4. Self-assembled $SrCO_3$ nanomask lithography of dense films 127

6.3. Chapter conclusion..129

6.4. Chapter references 129

***Chapter 7. General Conclusion & Future Expectations*.......................................131**

7.1. General conclusions... - 132 -

7.1.1. Investigation on the Sr-assisted devitrification mechanism of α-quartz films ....- 132 -

7.1.2. Versatile control of α-quartz films..- 133 -

7.2. Future work.. - 134 -

***Scientific Activities during My PhD Period*...137**

Chapter 1. Introduction

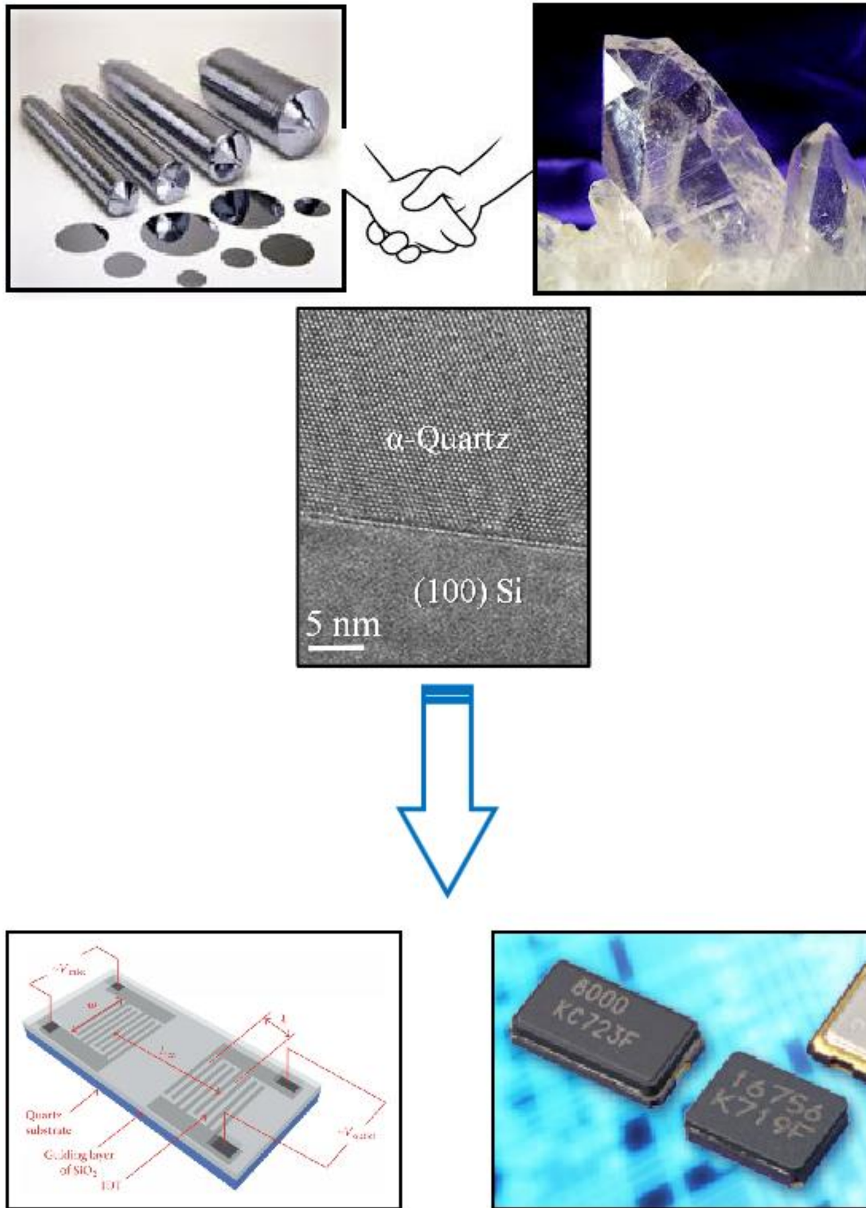

Chapter 1

In this chapter, the motivation of this PhD work is presented by describing the interest of α-quartz materials and the state-of-the-art and limitations of the methods to fabricate them. In addition, a brief description of sol-gel chemistry, dip-coating technique and alkaline metal-assisted crystallization is included. This will illustrate how α-quartz films could be obtained via a Strontium-assisted devitrification of silica films deposited by dip-coating, which is the main topic of this Thesis. Finally, the lithographic techniques used to enable the piezoelectric applications of our films are also introduced.

1.1. Quartz materials

Silicon and oxygen are the most abundant elements in the Earth's crust. Accordingly, silica (SiO_2), in the form of [SiO_4] tetrahedral networks, is a basic building block of most minerals. For centuries, those minerals have been massively exploited to produce building materials such as glass and concrete [1]. More recently, silicates have found a wide range of high-end applications from the use of zeolites in catalysis to the incorporation of Lutetium silicates in scintillators [2]. α-Quartz single crystals are a remarkable example of such high technology applications of minerals.

1.1.1. SiO_2 polymorphs

Silica (SiO_2), which is one of the key materials in many modern technological applications including microelectronics [3, 4], catalysis [5, 6], and photonics [7], presents relatively simple crystal structures but a large polymorph family [8] (11 crystalline and 2 non-crystalline polymorphs). A phase diagram displaying the pressure and temperature stability fields of the main silica polymorphs is presented in **Figure 1.1** [9].

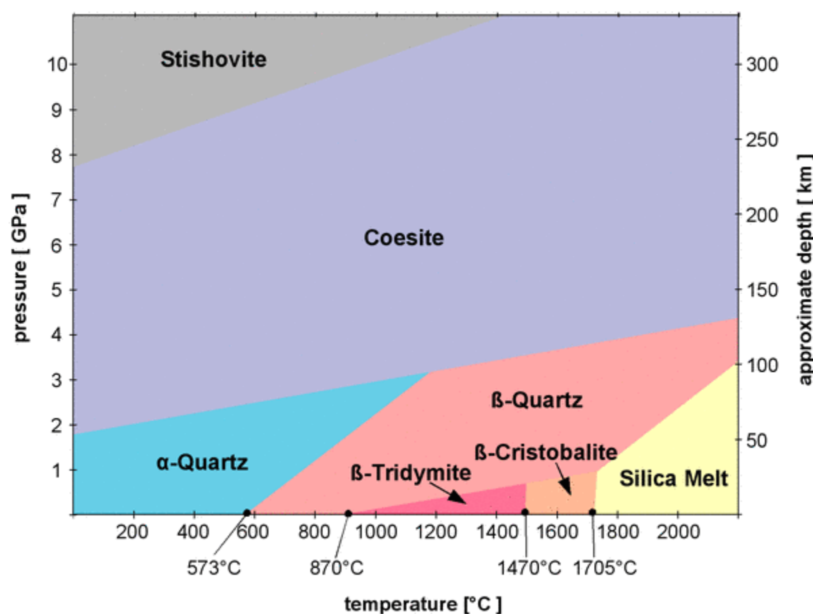

Figure 1.1. [9] Phase diagram of silica polymorphs.

This polymorphic richness is due to the relative flexibility of the O-Si-O angle which can accommodate different crystalline symmetries and enhances the ability of [SiO_4] tetrahedral to form many different lattice structures [10]. In the phase diagram, one can see that most phase transitions occur when the pressure is low (≤ 2 GPa). Under atmospheric pressure, the equilibrium sequence of phase transitions upon increasing temperatures below the melting point (~ 1705 ºC), includes transformations from α-quartz to β-quartz, then β-quartz to tridymite which is finally transformed into β-cristobalite. All crystalline phases consist of infinite frameworks of corner-sharing [SiO_4] tetrahedra. For example, β-tridymite and β-cristobalite consist of identical sheets of corner-sharing [SiO_4] joined in hexagonal close packed and face centered cubic arrangements, respectively.

1.1.2. Quartz structure

Quartz is the best-known crystalline silica polymorph for its abundance in nature and its wide use in industry since long time ago [11]. It is stable at atmospheric pressure, but it is found in two different structures depending on the temperature (see **Figure 1.2**).

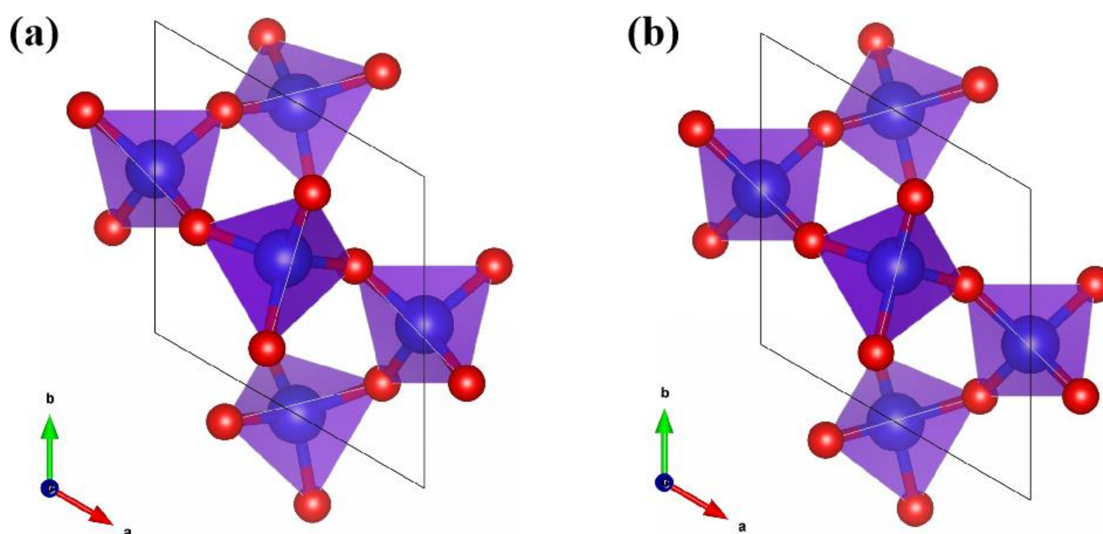

Figure 1.2. The lattice structures of two types of quartz: **(a)** α-quartz. **(b)** β-quartz.

Below 573ºC, α-quartz or low-temperature quartz, presents a structure as the one displayed in **Figure 1.2a**. α-quartz presents a trigonal symmetry with lattice parameters **a** = 4.91 Å, **b** = **c** = 5.41 Å; Si-O spacing is 1.61 Å, O-O spacing is 2.65 Å, Si-Si spacing is 3.04 Å; Si-O-Si angle is 144º; lattice energy is from 12967 to 15043 kJ/mol; Mohs hardness is 7 and density is 2.65 g/cm^3. Above 573ºC, α-quartz transforms reversibly into a hexagonal lattice structure named as β-quartz or high-temperature quartz, which is shown as **Figure 1.2b**. In this phase, **a** = 5.00 Å, **b** = **c** =

5.46 Å; Si-O spacing is 1.60 Å, O-O spacing is 2.65 Å, Si-Si spacing is 3.03 Å; Si-O-Si angle is 153º; lattice energy is 13596 kJ/mol; Mohs hardness is 7 and density is 2.51 g/cm^3. [1, 12]

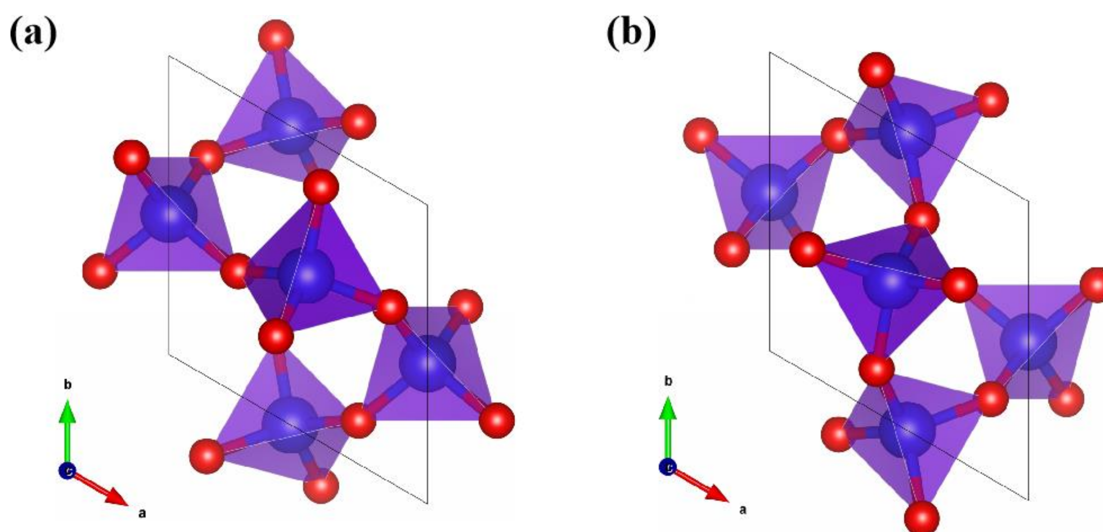

Figure 1.3. Two chiral lattice structures of α-quartz: **(a)** $P3_121$ (left handed); **(b)** $P3_221$ (right handed).

The structure of α-quartz is chiral [1, 13, 14] (*i.e.* it does not have a center of symmetry or mirror plane) and thus it exists in the lithosphere in two enantiomorphic structures, one being the mirror image of the other. **Figure 1.3** shows these two structures: One is a laevorotatory enantiomorph (or left handed enantiomorph, space group $P3_121$) containing left handed helices of $[SiO_4]$ tetrahedra running along the optical **c** axis; and the other is dextrorotatory enantiomorph (or right handed enantiomorph, space group $P3_221$) displaying right handed helices of $[SiO_4]$ tetrahedra [13]. In nature, the occurrence of both enantiomorphs is equally probable [14].

1.2. State-of-the-art about α-quartz materials

In most instances, the term quartz refers to α-quartz phase not only for α-quartz is the stable phase of quartz family but also for it is the most popular structure of quartz in application since ancient time. From the state-of-the-art, we can see that an improvement in the fabrication of α-quartz materials, especially for nanomaterials, is needed to open up new applications.

1.2.1. Traditional applications of α-quartz

Nowadays, α-quartz is used as the original material of precious jewelries and gemstones for its high transparency, stability and durability [15]. Another important application in daily life is as the oscillator of watch and clock for its capability of vibrating at a precise frequency without losses as it will discussed in more detail

below [16]. In industry and manufacturing, α-quartz is a common material used in construction as the main component of most types of sand and thus, it is present in cement, the strong blocks and decorative tiles in modern high-rise office buildings, traction on roadways and railroads and, as a filler, it is used in the manufacturing of paints, rubber and putty. [17-20] Even for petroleum industry, α-quartz also plays an important role as a key ingredient in hydraulic fracturing. In this application, α-Quartz sand can form a slurry [21], which is pumped at high pressure to form fractures in reservoir rocks, by mixing with water and then sandy slurry lodges into the fractured rock. The hard, durable sand grains hold the fractures open. These open fractures facilitate the flow of natural gas into the well bore. Besides, α-quartz can be used as an ideal foundry material by taking advantage of its high melting point [22]. Also, it is an excellent abrasive material, which is used for sand blasting, scouring cleansers, grinding media, and grit for sanding and sawing, due to its very high hardness (the hardness level is seven on the Mohs scale which range is 1 ~ 10) [10].

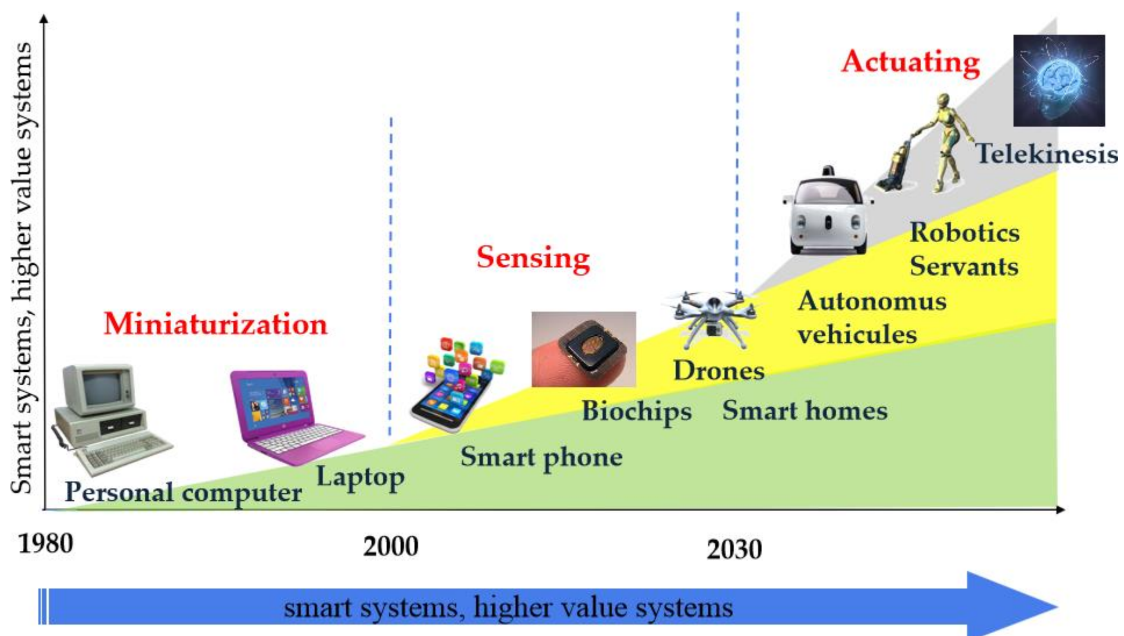

Figure 1.4. The development of electronic industry which prompts the fabrication of functional α-quartz materials.

At the same time, α-quartz is also widely used in the glass fabrication as the main raw material for the production of container glass, flat plate glass, specialty glass, and fiberglass for the further use in electronic and information fields, such as telescopes, microscopes, prisms, sensors, and other electronic and scientific instruments [23-26]. As **Figure 1.4** shows, the electronic industry has been lately following a miniaturization trend which is expected to evolve towards the development of ever-smarter systems for which will require the development of new sensors and actuators. In particular, the widespread deployment of millions of sensors wirelessly interconnected is starting to

become a reality in what is known as the Internet of Things. Such deployment poses important challenges to which environmentally friendly (*i.e.* Pb-free) piezoelectric materials are called to bring solutions, both in energy harvesting systems and, more relevant to this PhD, in smart sensing systems. In this context, there are plenty of opportunities for quartz-based functional materials exploiting its piezoelectricity.

1.2.2. Piezoelectric applications of α-quartz

Piezoelectricity is a phenomenon presented by non-centrosymmetric materials, by which these can develop a bound electric charge in response to the mechanical stress (see **Figure 1.5a**) [27]. Since piezoelectricity was initially observed for several substances including α-quartz by Pierre and Jacques Curie [28, 30], α-quartz has been not only a classical industrial raw material for its outstanding physical properties and chemical stability, but also used in electronics industry in modern time due to its piezoelectric response with a high-quality factor [30]. This implies that it can resonate at a very stable frequency with low losses. For this reason, a quartz resonator can be used as a frequency determining element to design electronic oscillators which represent an internal clock for electronic devices (see **Figure 1.5b**) [31].

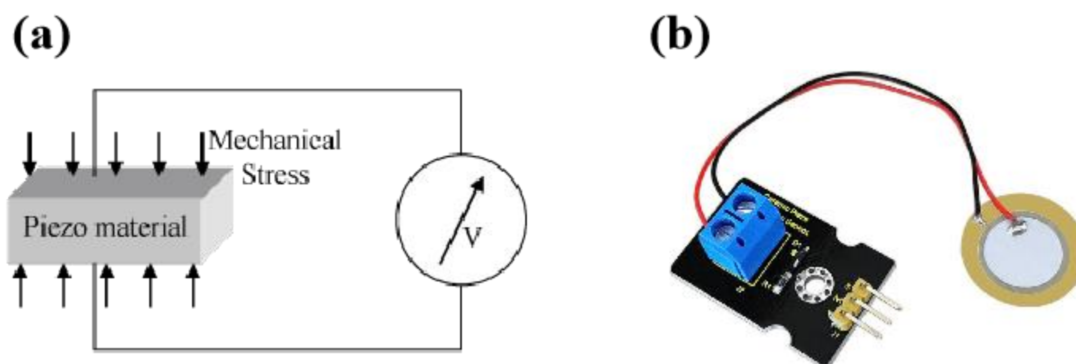

Figure 1.5. The schematic of **(a)** piezoelectricity and **(b)** α-quartz piezoelectric device.

Thanks to its piezoelectric properties with a high resonance quality factor, thin α-quartz plates are used as electric oscillators providing a stable clock frequency in virtually any electronic appliance. Since the resonant frequency of the plates is extremely sensitive to its mass and thickness, α-quartz crystals are also widely exploited in microgravimetric devices for sensing applications in chemistry and biology [32-35].

1.2.3. Optical properties of α-quartz

The trigonal symmetry of α-quartz crystals implies that these are optically uniaxial and thus display birefringence with two different refractive indices[36]. Moreover since the α-quartz structure is chiral, it also presents optical activity, that is different

refractive indices for right or left handed circularly polarized light [36]. Thanks to these properties α-quartz is also used in optical applications. In particular birefringence can be used to make optical low-pass filters which allow avoiding the formation of coloured Moiré fringes [37].

1.2.4. Fabrication of α-quartz materials

Quartz is used in applications that take advantage of its good piezoelectric and optical properties, as for instance in microbalance devices, sensors and chiral probes, especially in form of thin plates. However, the miniaturization of α-quartz into the sub-micron scale is still a big challenge. Indeed, for more than 60 years the industrial fabrication of quartz for electronics applications has been exclusively based in the same technology relying on a long time-consuming, highly specialized top-down processing of large quartz single crystals produced by hydrothermal growth. This involves the accurate cutting and polishing of the crystals along specific orientations, as illustrated in the manufacturing process displayed in **Figure 1.6**.

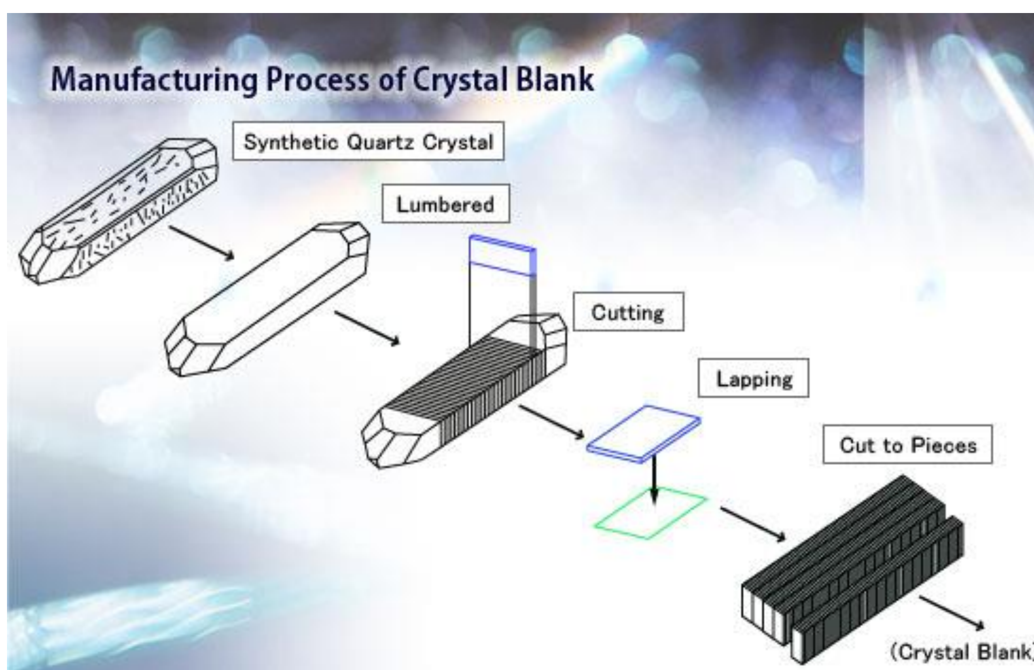

Figure 1.6. Manufacturing process of crystal blanks to produce α-quartz resonators (taken from the webpage of the Daishinku Corporation. www.kds.info).

Fully exploiting the potential of α-quartz in current and future applications requires controlling its microstructure down to the nanoscale. Yet, despite the importance of silicates in leading edge applications, fundamental aspects of their crystallisation are still poorly understood. A paradigmatic example of this is the highly empirical and poorly predictive devitrification of amorphous silicates. Indeed, even controlling the crystallization of SiO_2 is a long-standing problem connected with the remarkable stability of silica and the tiny differences in free energies of formation between all its

amorphous and crystalline forms [38].

In the context of the Internet of things, the main application of quartz is likely to be as a mass sensor. The mass sensitivity of quartz based sensors is inversely proportional to the square of its resonant frequency, and the resonant frequency increases as thickness of the quartz plate decreases [39]. Thus, in order to increase the sensitivity of the mass sensors it is necessary to decrease the thicknesses of the quartz plates below the current limit of 10 μm. However this cannot be achieved with the current top-down technologies of quartz processing but rather using a bottom-up approach. Moreover, in order to make the production of these sensors cost-competitive by taking advantage of the microelectromechanical processing technologies developed on silicon, the growth of quartz silicon substrates is a must [40].

advances in micro-/nano-fabrication technologies allow the implementation of a large-scale integration of miniaturized piezoelectric materials into innovative electromechanical devices with nano sized moving parts to achieve prospective sensor applications in electronics, biology and medicine [40-43]. One typical example is the fabrication of 2D photonic crystals slabs (2D CSBs) built on a glass substrate with Si nanomembrane by Laser Interference Lithography (LIL), which is shown in **Figure 1.7**. Firstly, the top Si layer of SOI wafer is etched by LIL patterning technique with the help of photoresist. Then, the patterned top Si layer is picked up and printed onto the glass substrate to build 2D CSBs via employing a polydimethylsiloxane (PDMS) stamp printing technique without using any adhesive layer [44].

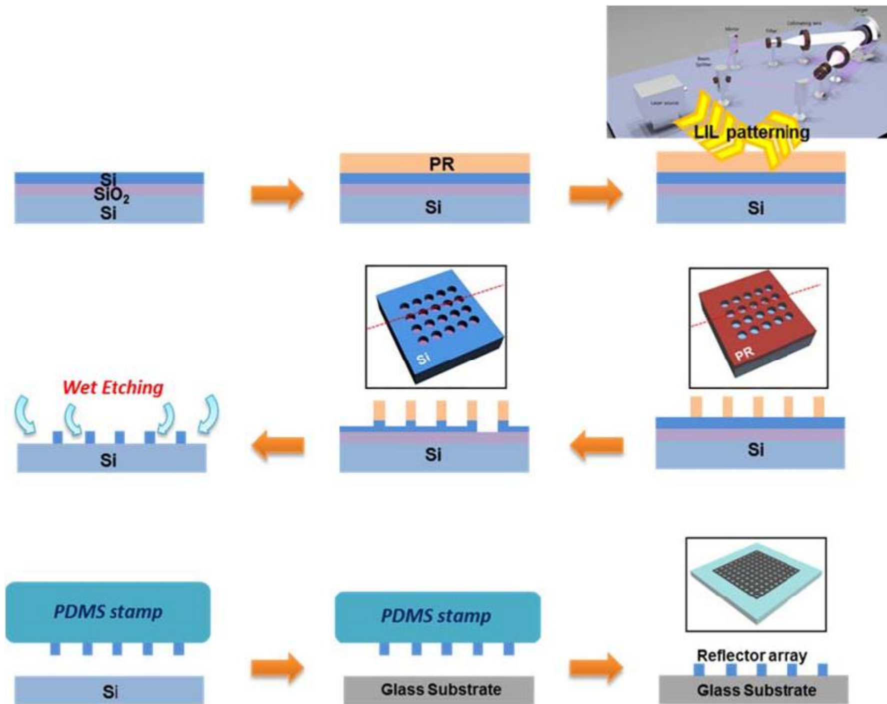

Figure 1.7 [44]. Sechematics of the process to prepare Si-membrane reflector on a glass substrate

using a transfer printing technique with an elastomeric stamp.

Another outstanding example is the soft nanoimprint lithography, which is a low-cost and flexible patterning method and is highly suitable for soft chemical synthesis. For instance (see **Figure 1.8**), different patterned silica macrostructures can be obtained by this approach by imprinting a suitable mask on the silica soft films made by sol-gel method.[45]

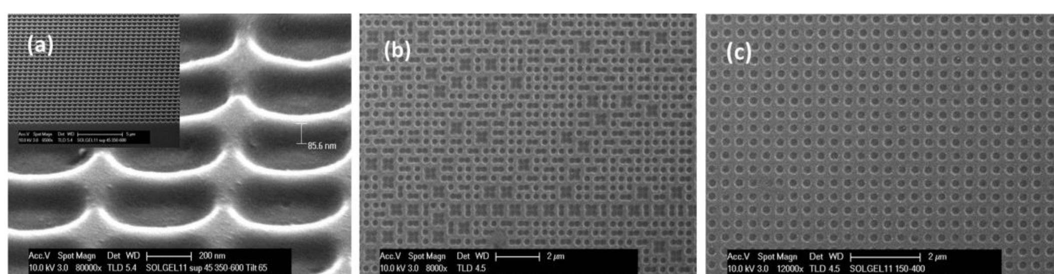

Figure 1.8 [45].SEM images of the imprint on SiO_2 sol-gel: diameter 350 nm and periodicity 600 nm **(a)**, diameter 200 nm and periodicity 400 nm with a collapse effect **(b)**, diameter 150 nm and periodicity 400 nm **(c)**.

These technologies open the door to obtaining nanostructured quartz-based piezoelectric devices but so far, few works have reported the sub-micron patterning of α-quartz surfaces or other technologically relevant oxides. For instance, α-quartz has been patterned by Laser Interference Lithography [46] and by Faraday cage angled-etching technique [47] or lithium niobiate nanostructures were synthetized by focused ion beam (FIB) technology [48]. However, in all these examples bulk single crystals were used, which indicates that the nanoengineering of functional oxide films prepared by bottom-up approaches is an open topic.

1.2.5. Crystallization of α-quartz nanomaterials from amorphous SiO_2

Lately, fundamental and application-driven interest in nanoscale SiO_2 provided new insights towards understanding and controlling silica devitrification in microporous, mesoporous and ultrathin silica [49-58]. Most of these works highlight the essential role of alkaline, alkaline earth and transition metal dopants for obtaining the desired crystallization. For instance, the formation of iron silicate seeds underpins the epitaxial growth of thermally evaporated ultrathin silica on Ru(0001). Other studies show that the controlled confinement of alkaline or alkaline earth melting agents at the nanoscale is essential for achieving a controlled crystallization of α-quartz.

In particular, superlattices of polycrystalline α-quartz nanospheres were prepared by impregnating preformed 3D stackings of mesoporous silica spheres with aqueous solutions of alkaline earth cations followed by thermal treatments above 800°C. However, by using a Li^{3+} solution, a straightforward crystallization of α-quartz and

Lithium silicate with a loss of the superstructure morphology was observed a temperature as low as 650°C.

In contrast, Matsuno *et al.* [54] obtained α-quartz nanosphere superlattices of improved crystallinity at 870°C after confining Li^+ between silica spheres and a reinforcing carbon coating. Ndayishimiye *et al.* [55] impregnated microporous SiO_2 nanoparticles with NaOH solutions and studied their hydrothermal sintering, finding an amorphous product below a concentration threshold (1 M) while dense polycrystalline α-quartz resulted from impregnations with more concentrated solutions.

The surfactants used in the synthesis of mesoporous silica can also have a strong influence on the devitrification. For instance, with the presence of amphiphiles the temperature of silica crystallization under high pressure was lower than in the case where the surfactants had been previously removed [57]. In this sense, Putz *et al.* have used sodium metasilicate solutions in microemulsions to obtain small α-quartz nanocrystals at room temperature or under mild hydrothermal conditions below 200ºC[58]. The above examples illustrate the complexity of controlling the crystallization and microstructure of nanostructured α-quartz and highlight the critical roles of the silica porosity, the concentration, distribution and confinement of devitrifying agents or the presence of surfactants.

1.3. Evaporation-induced self-assembly method

Evaporation-induced self-assembly (EISA), which is firstly reported by Ozin *et al*, is a two-step process including the preparation of initial solution and evaporation-induced deposition, has already became a popular route to fabricate various nanostructures of materials especially for nanofilms for its flexible and easy-to-use properties [59, 60]. For instance, both microstructures of mesoporous microspheres [61] and thin films [62] can be obtained via spray drying and coating processes respectively.

1.3.1. The preparation of initial solution

In general, self-assembly is achieved via the spontaneous organization of materials through noncovalent interactions with no external intervention, and typically employs asymmetric molecules that are pre-programmed to organize into well-defined supramolecular assemblies. Most common are amphiphilic surfactant molecules or polymers composed of hydrophobic and hydrophilic parts (CTAB, Pluronics, etc.) [63]. For instance (see **Figure 1.9**), in aqueous solution above the critical micelle concentration (CMC), CTAB assemble into micelles, spherical or cylindrical structures that maintain the hydrophilic parts of the surfactant in contact with water while shielding the hydrophobic parts within the micellar interior. Further increases in surfactant concentration result in the self-organization of micelles into periodic hexagonal, cubic, or lamellar mesophases. [64]

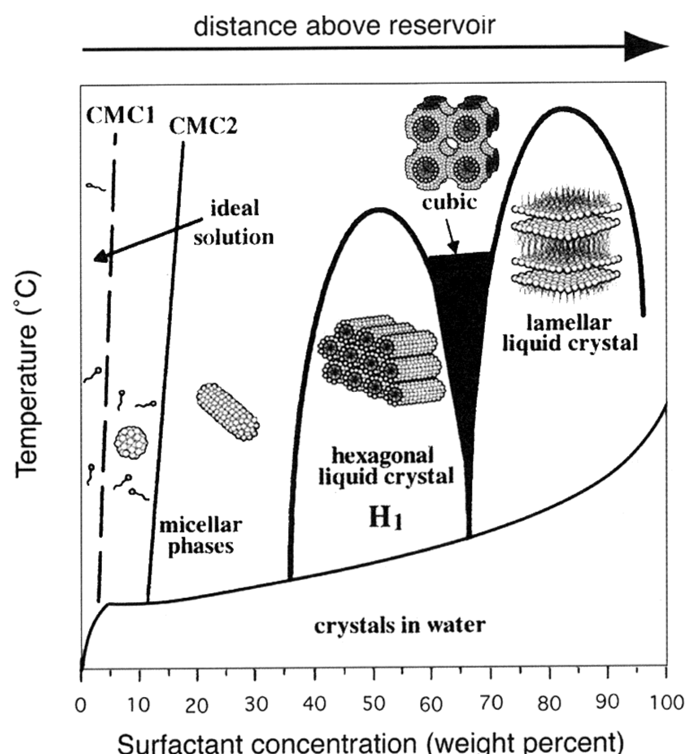

Figure 1.9. [64] Schematic phase diagram for CTAB in water. Arrow denotes evaporation-driven pathway during dip-coating, aerosol processing, etc.

As the chemical step of EISA process, the preparation of initial solution must play a role as an essential precondition for subsequent evaporation-induced deposition. In this step, the final phase of surfactant can be controlled via altering the sort of surfactant and the initial ratio of surfactant to solvent. For example, in my work, the as-prepared films can be hexagonal or lamellar depending on the sort of surfactant. Besides, the initial solution should have following features: The components are homogeneous, the surfactant inside solution cannot change the reactions (normally are hydrolysis and condensation in sol-gel process) and the initial solution can wet the substrate and highly volatile. [65]

1.3.2. The evaporation-induced deposition

The evaporation-induced deposition is the real moment to achieve the self-assembly of materials during the formation. In this physic step, the concentration of surfactant is increased sharply with the evaporation of solvent during the formation process of materials (such as spray drying, dip-coating and spin-coating). Thus, the surfactant inside material can make different phases depends on the finial concentration. So, in this step, the evaporation rate (which can be controlled by solvent of initial solution, relative humidity and temperature during the formation) is very essential for the final nanostructure of material. [63, 65]

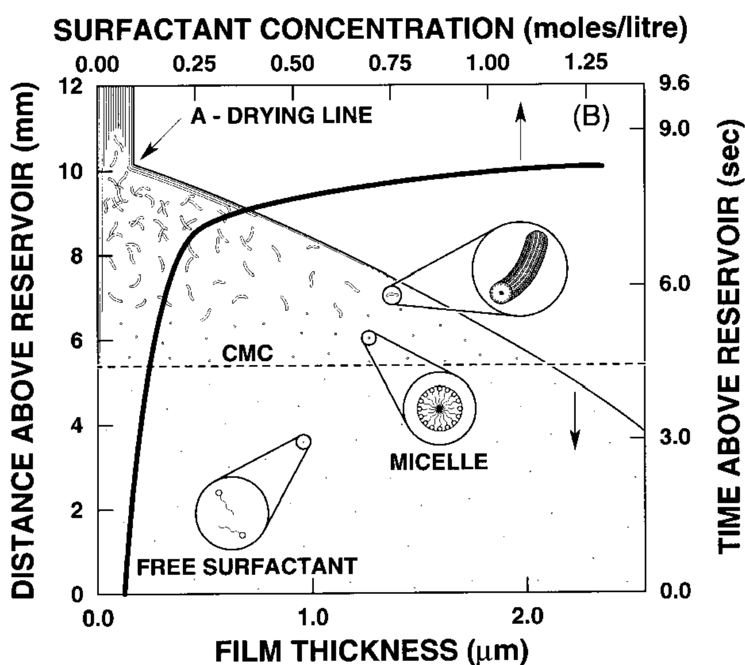

Figure 1.10. [66] Steady-state film thinning profile established during dip-coating of a complex fluid comprising soluble silica, surfactant, alcohol, and water. Initial surfactant concentration is much lower than CMC. Surfactant concentration increases with distance above the reservoir surface.

Figure 1.10 shows a typical evaporation-induced self-assembly process of silica ethanol solution during dip-coating period. The initial solution is with a surfactant concentration much lower than CMC [66]. During the withdrawal, with the rapid evaporation of ethanol, the progressively increasing surfactant concentration along the distance of solution surface drives self-assembly of silica/surfactant micelles and their further organization into liquid crystalline mesophases. The result is rapid formation of thin film mesophases that are highly oriented with respect to the substrate surface. With the variation of the initial surfactant concentration, it is possible to follow different trajectories in composition space and to arrive at different final mesostructures. For example, cetyltrimethylammonium bromide (CTAB) can form 1-D hexagonal, cubic, 3-D hexagonal and lamellar silica/surfactant mesophases via using different quantities.

1.3.3. Sol-gel method

Sol-gel method is a popular way to prepare thin films by EISA route [67, 68]. (see **Figure 1.11**). In this way, a solution (or sol) is prepared containing the precursors of the required material. The precursors typically undergo hydrolysis and condensation reactions, often in the presence of acid or basic catalysts, and eventually yield to the formation of a gel (*i.e.* an extended solid network resulting from the condensation reactions). Before gelation, the sol can be deposited on a substrate to form a thin gel film as the solvent evaporates and the condensation is accelerated. Normally, an

annealing treatment is needed after the coating process to complete the formation and crystallization of films.

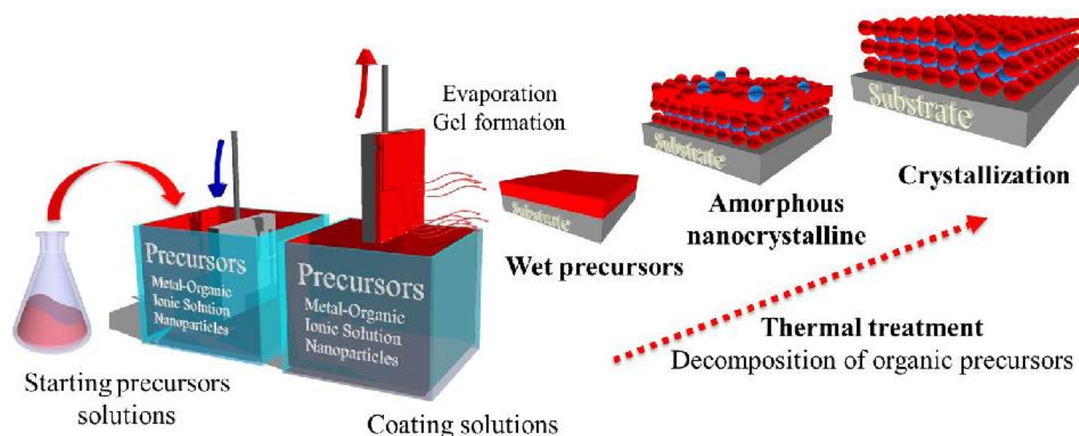

Figure 1.11. Schematics of the preparation of thin films by the sol-gel method.

Sol-gel process can ensure that the different precursors are homogeneously distributed in the solution, which is important for achieving a homogeneous microstructure and stoichiometry of the crystallized films. There are several techniques for the chemical solution deposition of films. In particular, dip-coating deposition is a useful method to keep the as-prepared film flat and continuous which is an important precondition for obtaining nanoscale films. Moreover, dip-coating process allows controlling the thickness of the films conveniently and making a large number of depositions with the same solution minimizing the waste of precursors. Considering all these advantages, the soft chemical approach combining sol-gel method and dip-coating technology is becoming more and more popular in the fabrication of nano-/micro-structures.

1.4. Sr-assisted sol-gel method to grow epitaxial α-quartz films

Inspired by the well-known property of alkaline metals as glass melting agents and its ability to induce the devitrification of silica and considering the convenience of sol-gel method, we attempted the fabrication α-quartz nanofilms on Si(100) substrates by combining these two technologies. It was found that alkaline earth rather than alkaline metals allowed obtaining epitaxial α-quartz films [51]. However, the mechanisms of crystallization still need to be properly understood in order to control the microstructure and properties of films. Achieving this control is a key step towards bringing this new quartz-based nanomaterial one step closer to applications.

1.4.1. Our previous studies on the Sr-assisted synthesis of α-quartz films

This chemical solution deposition method for preparing epitaxial α-quartz films on Si(100) substrates consisted in the thermal devitrification of dip-coated mesoporous silica films, assisted by alkaline earth cations in amphiphilic molecular templates [51].

The basic mechanism of this epitaxial crystallization is represented in **Figure 1.12a**. Thanks to the surfactant, the Sr^{2+} is packed and homogeneously distributed throughout the film and at high temperature assists the nucleation of quartz at the Si(100) interface, which is favoured thanks to a good epitaxial matching of the quartz(100) and the Si(100) planes (see **Figure 1.12b**). Playing with the surfactants and the synthesis conditions the porosity of the mesoporous silica can be tailored to range from 1 μm to a few tens of nm and is preserved upon crystallization, and the films are piezoelectric (see **Figure 1.12c**). However, pore sizes below 40 nm cannot be retained in the crystalline replica. In this latter case, the films display rough surfaces of densely packed crystals with lateral sizes of 500 nm or less, coexisting with significantly larger single crystalline domains which can attain several tens of μm.

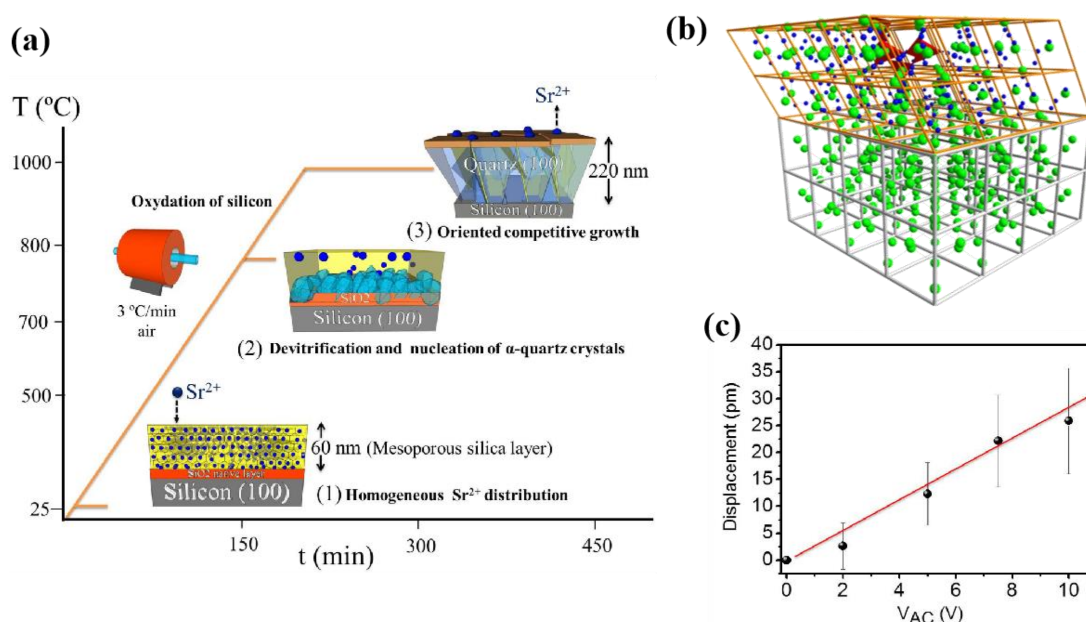

Figure 1.12.[51] Previous research on for the synthesis of epitaxial α-quartz films on Si(100) substrates: **(a)** Illustration of α-quartz phase growth via Sr-assisted devitrification. **(b)** The simulation of epitaxial α-quartz(100)//Si(100) microstructure. (the green dots are Si atom; the blue dots are O atom.). **(c)** Linear dependence of the film displacement vs applied voltage as obtained by Piezoelectric Force Microscopy demonstrating the piezoelectricity of as-prepared α-quartz films.

While these dense, non-homogeneous films with low planarity may be detrimental to some applications, the large single crystalline macrodomains could be appealing for other developments. For instance, for microgravimetric sensors it would be advantageous to use low roughness films (enabling the fabrication of surface acoustic wave devices by lithography) and displaying some degree of porosity (to achieve an increased mass sensitivity). In contrast, films with large single crystals in the in-plane dimensions would be preferred for fabricating nanostructured optical metamaterials to minimize the scattering losses. Moreover, for both application scenarios, controlling

the film thickness from hundreds of nm to above 1 μm is also necessary.

1.4.2. Aims of my PhD work

The former works show a convenient way to obtain nano size epitaxial α-quartz films but the crystallization mechanism is not well understood and thus the film microstructure cannot be properly controlled. For instance, a systematic investigation on the influence of the thickness of film, the amount of devitrifying agent and the annealing conditions is so far missing. All these parameters can play an important role in the crystallinity of as-prepared films. To address these shortcomings, this PhD work undertakes a systematic study aiming at controlling the microstructure of epitaxial α-quartz films on Silicon. This thesis is focusing on understanding the roles of the devitrifying agent (Sr), the relative humidity and the film roughness and thickness, which have been poorly studied so-far. These proved to be crucial for tailoring the film microstructures for specific applications and implementing a procedure for increasing film thickness up to the micron range. We could obtain highly flat porous films and we found that by increasing the concentration of Sr^{2+} solution we can switch to a microstructure characterized by large single crystals of fully dense α-quartz which are formed in a process of densification by recrystallization. Simultaneously, we exploited this enhanced control over the crystallization to prepare high-quality patterns of epitaxial quartz films by lithography techniques.

1.4. Chapter references

1. Götze, J., Chemistry, Textures and Physical Properties of Quartz-Geological Interpretation and Technical Application. *Mineralogical Magazine* **2009,** *73* (4), 645-671.

2. Melcher, C. L.; Schweitzer, J. S., CERIUM-DOPED LUTETIUM OXYORTHOSILICATE - A FAST, EFFICIENT NEW SCINTILLATOR. *Ieee Transactions on Nuclear Science* **1992,** *39* (4), 502-505.

3. Bonacci, F.; Di Michele, A.; Caponi, S.; Cottone, F.; Mattarelli, M., High Charge Density Silica Micro-Electrets Fabricated by Electron Beam. *Smart Materials and Structures,* **2018,** *27* (7), 075052

4. Han, Y.; Hu, M., Ground State of Bilayer Halpha-Silica: Mechanical and Electronic Properties. *Nanotechnology* **2015,** *26*(50), 505702.

5. Hello, K. M.; Fahad, N. G., In-situ Nitrous Acid Generation over Silica Imidazole Catalyst for Dyes Production. **2019,** *13*, 247-259.

6. Huo, L.; Liu, B.; Li, H.; Cao, B.; Hu, X.; Fu, X.; Zhang, J., Component Synergy and Armor Protection Induced Superior Catalytic Activity and Stability of

Ultrathin Co-Fe Spinel Nanosheets Confined in Mesoporous Silica Shells for Ammonia Decomposition Reaction. *Applied Catalysis B: Environmental* **2019,** *253*, 121-130.

7. Yu, B.; Chen, Y.; Pan, J.; Zhang, B.; Li, F.; Wan, L.; Li, Z., Silica-Microsphere-Cavity-Based Microwave Photonic Notch Filter with Ultra-Narrow Bandwidth and High Peak Rejection. *Optics Letters* **2019,** *44*(6), 1411-1414.

8. Liebau, F., Structural Chemistry of Silicates. Structure, Bonding, and Classification. *New York: Springer* **1985**.

9. Wenk, H.R.; Bulakh. A., Minerals: Their Constitution and Origin 1st Edition. *Cambridge University Press* **2004**.

10. Brinker, C. J.; Clem, P. G., Quartz on Silicon. *Science* **2013,** *340* (6134), 818-819.

11. Iwasaki, F.; Iwasaki, H., Historical review of quartz crystal growth. *J. Cryst. Growth* **2002,** 820, 237–239.

12. Strunz, H.; Tennyson, C., Mineralogical Tables. Akademische Verlagsgesellschaft Geest & Portig, Leipzig, Germany, (1982) 621 pp.

13. Carretero-Genevrier, A.; Gich, M.; Picas, L.; Sanchez, C.; Rodriguez-Carvajal, J., Chiral Habit Selection on Nanostructured Epitaxial Quartz Films. *Faraday Discussions* **2015,** *179*, 227-233.

14. Evgenii, K.; Wolfram, T., The Role of Quartz in The Origin of Optical Activity on Earth. *Origins Life Evol. Biospheres* **2000,** 30, 431–434.

15. Shumyatsky, P.; Alfano, R.R., Terahertz Sources, *Journal of Biomedical Optics* **2011,** *16*(3), 033001

16. Lombardi, A. M., The evolution of time measurement, Part 2: quartz clocks. *IEEE INSTRUMENTATION & MEASUREMENT MAGAZINE* **2011,** *14*(5), 41-49.

17. MCBRIDE, E.F., QUARTZ CEMENT IN SANDSTONES - A REVIEW. *EARTH-SCIENCE REVIEWS* **1989,** *26* (2), 69–112.

18. BEALL, G. H.; DUKE, D. A., TRANSPARENT GLASS-CERAMICS. *JOURNAL OF MATERIALS SCIENCE* **1969,** *4* (4), 340.

19. Cheng, X. S.; Ke, S. J.; Wang, Q. H.; Wang, H.; Shui, A. Z.; Liu, P. G., Fabrication and characterization of anorthite-based ceramic using mineral raw materials. *CERAMICS INTERNATIONAL* **2012,** *38* (4), 3227-3235.

20. Pasbakhsh, P.; Churchman, G. J.; Keeling, J. L., Characterisation of properties of various halloysites relevant to their use as nanotubes and microfibre fillers. *APPLIED CLAY SCIENCE* **2013,** *74*, 47-57.

21. Desale, G. R.; Gandhi, B. K.; Jain, S. C., Slurry erosion of ductile materials

under normal impact condition, *WEAR* **2008,** *264*(3-4), 322-330.

22. Zhang, S. J.; Yu, F. P., Piezoelectric Materials for High Temperature Sensors, *Journal of the American Ceramic Society* **2011,** *94*(10), 3153-3170.

23. Lambelet, P.; Sayah, A.; Pfeffer, M.; Philipona, C.; Marquis-Weible, F., Chemically etched fiber tips for near-field optical microscopy: a process for smoother tips, *Applied Optics* **1998,** *37*(31), 7289-7292.

24. Reitboeck, H.J., Fiber microelectrodes for elecrophysiological recordings, *Journal of Neuroscience Methods* **1983,** *8*, 249-262.

25. Zhang, S.; Li, M.; Su, B.; Shao, Y., Fabrication and Use of Nanopipettes in Chemical Analysis, *Annual Review of Analytical Chemistry* **2018,** *11*, 265-286.

26. Dukel'skii, K. V.; Ermolaeva, G. M.; Eron'yan, M. A.; Komarov, A. V.; Reutskii, A. A.; Shilov, V. B.; Shcheglov, A. A., Low-Dispersion Multimode Fibers with a Core Mae of Fluorine-Doped Quartz Glass, *Optics and Spectroscopy* **2018,** *125*(2), 281-284.

27. Manbachi, A.; Cobbold, R.S.C., Development and Application of Piezoelectric Materials for Ultrasound Generation and Detection. *Ultrasound* **2011,** *19* (4), 187–96.

28. Hlavay, J.; Guilbault, G.G., Applications of the Piezoelectric Crystal Detector in Analytical Chemistry. *Analytical Chemistry* **1977,** *49* (13), 1890–1898.

29. Curie, P.; Curie, J., Contractions and expansions produced by voltages in hemihedral crystals with inclined faces. *Comptes Rendus* **1881,** *93*, 1137–1140.

30. Galliou, S.; Goryachev, M.; Abbe, P.; Vacheret, X.; Tobar, M.; Bourquin, R., Quality Factor Measurements of Various Types of Quartz Crystal Resonators Operating Near 4 K. 2015; Vol. 63, p 1-1.

31. Kenji, U., The Development of Piezoelectric Materials and the New Perspective. **2017,** 10.1016/B978-0-08-102135-4.00001-1.

32. Benes, E.; Groschl, M.; Burger, W.; Schmid, M., SENSORS BASED ON PIEZOELECTRIC RESONATORS. *Sens. Actuator A-Phys.* **1995,** *48* (1), 1-21.

33. Sauerbrey, G., *Verwendung Von Schwingquarzen Zur Wagung Dunner Schichten Und Zur Mikrowagung*. 1959; Vol. 155, p 206-222.

34. Bunde, L. R.; Jarvi, J. E.; Resentreter J. J., Piezoelectric quartz crystal biosensors. *Talanta.* **1998,** *46*, 1223-1236

35. Fredriksson, C.; Kihlman, S.; Rodahl, M.; Kasemo, B., The Piezoelectric Quartz Crystal Mass and Dissipation Sensor: A Means of Studying Cell Adhesion. *Langmuir* **1998,** *14*, 248-251

36. Newnham, R. E., *Properties of Materials: Anisotropy, Symmetry, Structure*.

Oxford U. Press: New York 2005.

37. Optical Components-ndk. https://www.ndk.com/images/products/catalog/c_sq12_olpf1_e.pdf

38. Richet, P.; Bottinga, Y.; Denielou, L.; Petitet, J. P.; Tequi, C., THERMODYNAMIC PROPERTIES OF QUARTZ, CRISTOBALITE AND AMORPHOUS SIO2 - DROP CALORIMETRY MEASUREMENTS BETWEEN 1000-K AND 1800-K AND A REVIEW FROM 0-K TO 2000-K. *Geochimica Et Cosmochimica Acta* **1982,** *46* (12), 2639-2658.

39. Tadigadapa, S. & Mateti, K. Piezoelectric MEMS sensors: state-of-the-art and perspectives. Measurement Science and Technology 20, 092001 (2009)

40. Craighead, H. G., Nanoelectromechanical Systems. *Science* **2000,** *290* (5496), 1532-1535.

41. Ramesh, R.; Schlom, D. G., Orienting Ferroelectric Films. *Science* **2002,** *296* (5575), 1975-1976.

42. Warusawithana, M. P.; Cen, C.; Sleasman, C. R.; Woicik, J. C.; Li, Y.; Kourkoutis, L. F.; Klug, J. A.; Li, H.; Ryan, P.; Wang, L.-P.; Bedzyk, M.; Muller, D. A.; Chen, L.-Q.; Levy, J.; Schlom, D. G., A Ferroelectric Oxide Made Directly on Silicon. *Science* **2009,** *324* (5925), 367-370.

43. Danel, J. S.; Delapierre, G., Quartz: a material for microdevices. *Journal of Micromechanics and Microengineering* **1991,** *1* (4), 187.

44. Seo, J.-H.; Park, J.; Kim, S.-I.; Ju Park, B.; Ma, Z.; Choi, J.; Ju, B.-K., Nanopatterning by Laser Interference Lithography: Applications to Optical Devices. 2015.

45. Hamouda, F.; Bryche, J.-F.; Aassime, A.; Maillart, E.; Gâté, V.; Zanettini, S.; Ruscica, J.; Turover, D.; Bartenlian, B., Soft nanoimprint lithography on SiO2 sol-gel to elaborate sensitive substrates for SERS detection. *AIP Advances* **2017,** *7* (12), 125125.

46. Santybayeva, Z.; Meghit, A.; Desgarceaux, R.; Teissier, R.; Pichot, F.; Marin, C. d.; Charlot, B.; Pedaci, F. In *Fabrication of quartz microcylinders by laser interference lithography for angular optical tweezers*, SPIE: 2016; p 5.

47. Young-Ik Sohn, R. M., Vivek Venkataraman, Marko Lončar, Mechanical and optical nanodevices in single-crystal quartz. *arXiv.org > cond-mat >* **2017**.

48. Lu, H.; Sadani, B.; Courjal, N.; Ulliac, G.; Smith, N.; Stenger, V.; Collet, M.; Baida, F. I.; Bernal, M. P., Enhanced electro-optical lithium niobate photonic crystal wire waveguide on a smart-cut thin film. *Opt. Express* **2012,** *20* (3), 2974-2981.

49. Freund, H. J., Controlling Silica in Its Crystalline and Amorphous States: A

Problem in Surface Science. *Acc Chem Res* **2017,** *50* (3), 446-449.

50. Buchner, C.; Lichtenstein, L.; Yu, X.; Boscoboinik, J. A.; Yang, B.; Kaden, W. E.; Heyde, M.; Shaikhutdinov, S. K.; Wlodarczyk, R.; Sierka, M.; Sauer, J.; Freund, H. J., Ultrathin silica films: the atomic structure of two-dimensional crystals and glasses. *Chemistry* **2014,** *20* (30), 9176-83.

51. Carretero-Genevrier, A.; Gich, M.; Picas, L.; Gazquez, J.; Drisko, G. L.; Boissiere, C.; Grosso, D.; Rodriguez-Carvajal, J.; Sanchez, C., Soft-chemistry-based routes to epitaxial alpha-quartz thin films with tunable textures. *Science* **2013,** *340* (6134), 827-31.

52. Drisko, G. L.; Carretero-Genevrier, A.; Gich, M.; Gàzquez, J.; Ferrah, D.; Grosso, D.; Boissière, C.; Rodriguez-Carvajal, J.; Sanchez, C., Water-Induced Phase Separation Forming Macrostructured Epitaxial Quartz Films on Silicon. *Advanced Functional Materials* **2014,** *24* (35), 5494-5502.

53. Drisko, G. L.; Carretero-Genevrier, A.; Perrot, A.; Gich, M.; Gazquez, J.; Rodriguez-Carvajal, J.; Favre, L.; Grosso, D.; Boissiere, C.; Sanchez, C., Crystallization of hollow mesoporous silica nanoparticles. *Chem Commun (Camb)* **2015,** *51* (20), 4164-7.

54. Matsuno, T.; Kuroda, Y.; Kitahara, M.; Shimojima, A.; Wada, H.; Kuroda, K., A Single-Crystalline Mesoporous Quartz Superlattice. *Angew Chem Int Ed Engl* **2016,** *55* (20), 6008-12.

55. Ndayishimiye, A.; Largeteau, A.; Prakasam, M.; Pechev, S.; Dourges, M.-A.; Goglio, G., Low temperature hydrothermal sintering process for the quasi -complete densification of nanometric α-quartz. *Scripta Materialia* **2018,** *145*, 118-121.

56. Li, L.; Tissot, H.; Shaikhutdinov, S.; Freund, H.-J., Transition Metal Induced Crystallization of Ultrathin Silica Films. *Chemistry of Materials* **2017,** *29* (3), 931-934.

57. Mandal, M.; Stagno, V.; Fei, Y.; Landskron, K., Investigation of High-Pressure and Temperature Behavior of Surfactant-Containing Periodic Mesostructured Silicas. *Crystal Growth & Design* **2012,** *13* (1), 15-18.

58. Putz, F.; Scherer, S.; Ober, M.; Morak, R.; Paris, O.; Hüsing, N., 3D Printing of Hierarchical Porous Silica and α-Quartz. *Advanced Materials Technologies* **2018**.

59. Yang, H.; Coombs, N.; Sokolov, I.; Ozin, G. A., Free-standing and oriented mesoporous silica films grown at the air–water interface. *Nature* **1996,** *381*, 589-592.

60. Yang, H.; Kuperman, A.; Coombs, N.; Mamiche-Afara, S.; Ozin, G. A., Synthesis of oriented films of mesoporous silica on mica. *Nature* **1996,** *379*, 703-705.

61. Lu, Y.; Fan, H.; Stump, A.; Ward, T. L.; Rieker, T.; Brinker, C. J., Aerosol-

assisted self-assembly of mesostructured spherical nanoparticles. *Nature* **1999,** *398*, 223-226

62. Brinker, C. J.; Frye, G. C.; Hurd, A. J.; Ashley, C. S., Fundamentals of sol-gel dip coating. *Thin Solid Films* **1991,** *201*(1), 97-108

63. Brinker, C. J.; Lu, Y.; Sellinger, A.; Fan, H., Evaporation-Induced Self-assembly: Nanostructures Made Easy. *Adv. Mater.* **1990,** *11*(7), 579-585.

64. Raman, N.; Anderson, M.; Brinker, C., Template-Based Approaches to the Preparation of Amorphous, Nanoporous Silicas. *Chem. Mater.* **1996,** *8*(8), 1682-1701.

65. Grosso, D.; Cagnol, F.; Soler-Illia, G. J. A. A.; Crepaldi, E. L.; Amenitsch, H.; Brunet-Bruneau, A.; Bourgeois, A.; Sanchez, C., Fundamentals of Mesostructuring Through Evaporation-Induced Self-Assembly. *Adv. Funct. Mater.* **2004,** *14*(4), 309-322.

66. Lu, Y.; Ganguli, R.; Drewien, C.; Anderson, M.; Brinker, C.; Gong, W.; Guo, Y.; Soyez, H.; Dunn, B.; Huang, M.; Zink, J., Continuous formation of supported cubic and hexagonal mesoporous films by sol–gel dip-coating. *Nature* **1997,** *389*, 364-368.

67. Brinker, C. J.; Scherer, G. W., Sol-gel science: The physics and chemistry of sol-gel processing, *Academic Press London*, **1990**.

68. Wright, J. D.; Sommerdijk, N. A.J.M., Sol-Gel Materials Chemistry and Applications, *CRC Press*, **2000,** Advanced Chemistry Texts *Volume 4*.

Chapter 2. Motivation & Objectives

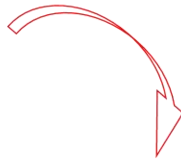

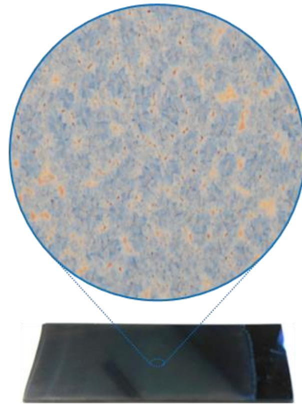

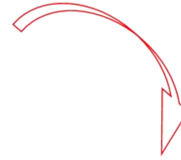

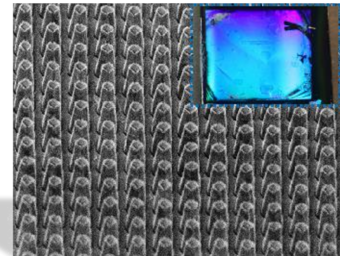

Chapter 2

2.1. Motivation

Quartz represents the second largest single crystal production for electronic applications. It is marketed after an expensive top-down miniaturization to transform large hydrothermally grown crystals into ever thinner plates, aiming to push higher and higher their resonance frequencies. However, α-quartz plates or films cannot be thinned below 10 µm via traditional physical routes and moreover, it is necessary to bond it on Si substrates for most applications. For all these reasons, the integration of high quality α-quartz nanomaterials on silicon is not yet developed, hindering the production of quartz-based devices with improved sensitivities, faster operation and compatible with microfabrication techniques. In this light, the scientific community is still interested in the production of α-quartz nanomaterials by using the devitrification and crystallization of glass silica driven by alkaline, alkaline earth and transition metal dopants [1-9].

In 2013, Carretero-Genevrier *et al*. developed a novel chemical solution deposition method for preparing epitaxial α-quartz films on Si(100) substrates [3, 4]. The method relies on the thermal devitrification of dip-coated mesoporous silica films, assisted by alkaline earth cations in amphiphilic molecular templates. However, we still need to address the challenge of understanding in depth the mechanism of epitaxial α-quartz growth on silicon by this method. This would allow achieving a control of crystallization parameters and enable the fabrication of sensors with unprecedented sensitivity for prospective applications in electronics, biology and medicine.

The aim of this thesis was bring new insights into the crystallization of epitaxial α-quartz films on Silicon(100) to enhance their piezoelectric properties. For this purpose, during this thesis, I studied the thermal devitrification of porous silica assisted by Sr which act as silica network modifiers, thereby controlling the film microstructures and its crystallinity. The novelty of the work here presented is two-fold since it deals with the emergent field of epitaxial piezoelectric oxide nanostructures and demonstrates the possibility of combining soft chemistry with micro and nanofabrication techniques. Hence, I aim to study growth parameters such as film thickness, relative humidity, temperature, deposition conditions and the nature of surfactant which play an important role in the control of the final microstructure and crystal homogeneity of α-quartz films.

A novel multilayer deposition method has been developed to prove the validity and generality of sol-gel precursor solution to extend the maximum thickness of the α-quartz films from a few hundreds of nm into the µm range. Finally, an original method which combines this multilayer approach with soft lithography has been validated to produce 1-Dimentional epitaxial α-quartz nanocolumn patterns while preserving the piezoelectric properties.

The improvements developed in this systematic work on the crystallization of epitaxial α-quartz can be relevant to other systems. Moreover, the possibility to generate vertical α-quartz nanorods, taking advantage of the good compatibility between cost-effective lithographic techniques and soft-chemistry, may extend the procedure to other functional oxides. Hence, the methodology presented exhibits a great potential and offers a pathway to design new nanodevices based on functional oxides on silicon technology by chemical routes with unique piezoelectric, optical, or electrical properties.

In particular, this thesis is a successful example of sol-gel chemistry. It explores the possible microstructures of Sr-doped xerogel film and their crystal evolution behaviours at high temperature, which lead to many pathways for synthesizing new α-quartz-based materials and a large variety of devices at the nanoscale. The case of the epitaxial α-quartz system investigated may establish the basis for the development of a new generation of functional piezoelectric sensor devices.

2.2. Objectives

The main objectives of this thesis were to disentangle the growth mechanism of epitaxial α-quartz films on silicon(100) substrates synthetized by the sol-gel method. In this sense, the work was mainly focused on studying the role of Sr^{2+} during the devitrification and crystallization of α-quartz films. The final target was producing piezoelectric epitaxial quartz films of controlled microstructure, crystallinity and nanostructures. α-quartz nanostructures were obtained using soft lithographic techniques therefore, inducing nanostructuration across the whole silicon surface. Lithographic techniques and thin film nanostructuration were developed in collaboration with the University of Montpellier, specially designed for this work in the framework of the European project SENSiSOFT No 803004 to which this thesis is linked together with the national Chinese grant No.201506060170. To achieve these main objectives, we divided the work into the following parts:

1. ***Investigation of α-quartz film crystal growth on silicon via Strontium-assisted devitrification***.

2. ***Comprehensive control of α-quartz film microstructures***.

3. ***Nanostructure engineering on epitaxial α-quartz thick films***.

2.3. Chapter references

1. Freund, H. J., Controlling Silica in Its Crystalline and Amorphous States: A Problem in Surface Science. *Acc Chem Res* **2017,** *50* (3), 446-449.

2. Buchner, C.; Lichtenstein, L.; Yu, X.; Boscoboinik, J. A.; Yang, B.; Kaden, W. E.; Heyde, M.; Shaikhutdinov, S. K.; Wlodarczyk, R.; Sierka, M.; Sauer, J.; Freund, H. J., Ultrathin silica films: the atomic structure of two-dimensional crystals and glasses. *Chemistry* **2014,** *20* (30), 9176-83.

3. Carretero-Genevrier, A.; Gich, M.; Picas, L.; Gazquez, J.; Drisko, G. L.; Boissiere, C.; Grosso, D.; Rodriguez-Carvajal, J.; Sanchez, C., Soft-chemistry-based routes to epitaxial alpha-quartz thin films with tunable textures. *Science* **2013,** *340* (6134), 827-31.

4. Drisko, G. L.; Carretero-Genevrier, A.; Gich, M.; Gàzquez, J.; Ferrah, D.; Grosso, D.; Boissière, C.; Rodriguez-Carvajal, J.; Sanchez, C., Water-Induced Phase Separation Forming Macrostructured Epitaxial Quartz Films on Silicon. *Advanced Functional Materials* **2014,** *24* (35), 5494-5502.

5. Li, L.; Tissot, H.; Shaikhutdinov, S.; Freund, H.-J., Transition Metal Induced Crystallization of Ultrathin Silica Films. *Chemistry of Materials* **2017,** *29* (3), 931-934.

6. Drisko, G. L.; Carretero-Genevrier, A.; Perrot, A.; Gich, M.; Gazquez, J.; Rodriguez-Carvajal, J.; Favre, L.; Grosso, D.; Boissiere, C.; Sanchez, C., Crystallization of hollow mesoporous silica nanoparticles. *Chem Commun (Camb)* **2015,** *51* (20), 4164-7.

7. Matsuno, T.; Kuroda, Y.; Kitahara, M.; Shimojima, A.; Wada, H.; Kuroda, K., A Single-Crystalline Mesoporous Quartz Superlattice. *Angew Chem Int Ed Engl* **2016,** *55* (20), 6008-12.

8. Ndayishimiye, A.; Largeteau, A.; Prakasam, M.; Pechev, S.; Dourges, M.-A.; Goglio, G., Low temperature hydrothermal sintering process for the quasi -complete densification of nanometric α-quartz. *Scripta Materialia* **2018,** *145*, 118-121.

9. Putz, F.; Scherer, S.; Ober, M.; Morak, R.; Paris, O.; Hüsing, N., 3D Printing of Hierarchical Porous Silica and α-Quartz. *Advanced Materials Technologies* **2018**.

Chapter 3. Experimental Procedures

Chapter 3

This chapter describes the preparation of epitaxial α-quartz films on silicon substrate and all the techniques used to characterize the structural, chemical, physical properties of this material.

3.1. General synthetic process

The methodology here presented demonstrated major advantages when taking into account its versatility and low cost. In this light, The synthesis method used along this thesis combines a soft chemistry method, such is the sol-gel method, and the use of dip-coating process for the synthesis of epitaxial piezoelectric α-quartz thin films. This synthesis of α-quartz films can be divided into three steps: 1) Preparation of silica sol; 2) Formation of gel film by dip-coating; 3) Thermal treatment of as-prepared gel film to crystalize the α-quartz phase. **Figure 3.1** illustrates the general synthetic process used along this thesis:

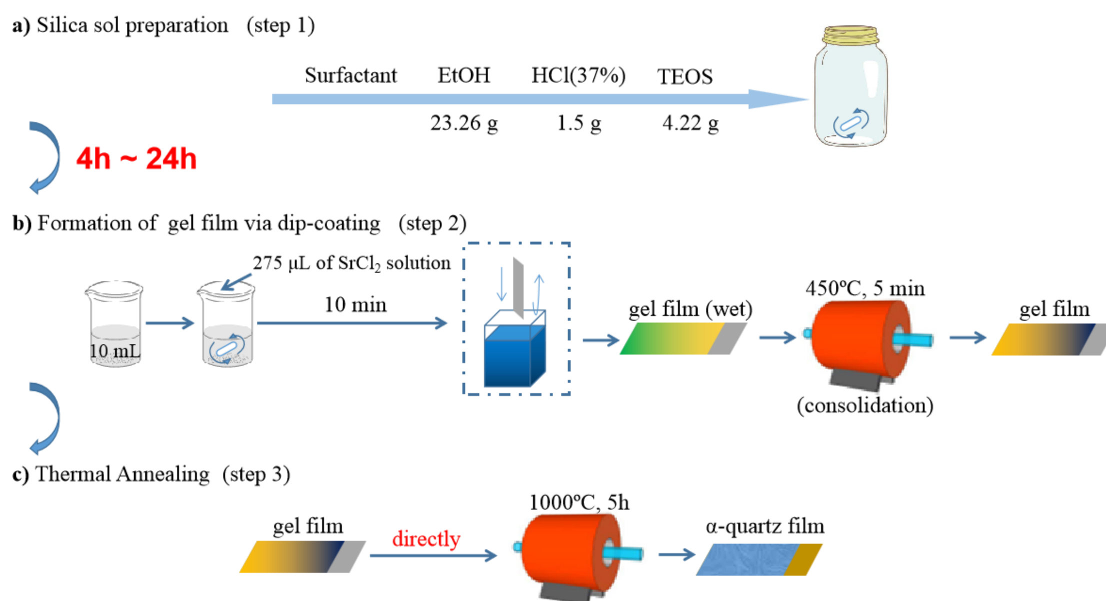

Figure 3.1. General synthetic process of quartz films studied during this PhD work.

3.2. Experimental section

3.2.1. Silica sol preparation

1) Prepare a solution of prehydrolyzed tetraethyl orthosilicate (TEOS) the day before the preparation of the gel films in a fume hood in which a lab balance and a magnetic stirrer are placed. In this step and throughout the protocol wear a lab coat, gloves and safety googles.

2) In a 50 mL glass bottle containing a Teflon coated magnetic stirring bar weigh 0.7 g of Brij-58, add 23.26 g of ethanol and 1.5 g of HCl (37%), cover the beaker with a watch glass (see **Figure 3.2a**) and stir until the Brij-58 is completely dissolved. For

the study of perforation in **Section 5.3** of **Chapter 5**, we also used sols with F127 and CTAB by adding 1.032 g and 1.4 g of them respectively. The final compositions of silica sols with these three different surfactants are shown in **Table 3.1** ~ **Table 3.3**:

Table 3.1 The composition of silica sol when the surfactant is Brij-58

Reagent	TEOS		EtOH		HCl(37%)		Brij-58
Dosage	4.22 g		23.26 g		1.5 g		0.7 g
Molar ratio	1	:	25	:	0.7	:	0.3

Table 3.2 The composition of silica sol when the surfactant is F127

Reagent	TEOS		EtOH		HCl(37%)		F127
Dosage	4.22 g		23.26 g		1.5 g		1.4 g
Molar ratio	1	:	25	:	0.7	:	0.0055

Table 3.3 The composition of silica sol when the surfactant is CTAB

Reagent	TEOS		EtOH		HCl(37%)		CTAB
Dosage	4.22 g		23.26 g		1.5 g		1.032 g
Molar ratio	1	:	25	:	0.7	:	0.14

3) Add 4.22 g of TEOS to the bottle dropwise (at a rate of about 1-2 drops per second) while stirring, then seal the bottle with a cover and leave it to stir overnight.

Here, one important thing should to be mentioned: If the hydrolysis time is not sufficiently long the as-prepared film will contain many defects after the solution deposition see the topographic AFM images of **Figure 3.2**. The film of **Figure 3.2b** is prepared from a sol stirred during 16 h and presents a well-crystallized surface. conversely, the film of **Figure 3.2c** was made from a sol stirred during 2 h presenting defects at the surface in form of pores. The reason of this behavior is that partially hydrolyzed TEOS can generate gases so that produces pores during annealing according to the following oxidation equation:

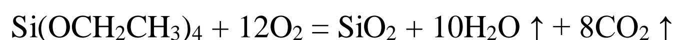

$$Si(OCH_2CH_3)_4 + 12O_2 = SiO_2 + 10H_2O \uparrow + 8CO_2 \uparrow$$

In the other hand, the stirring time cannot exceed 24 h,. because the condensation of the orthosilicic acid units formed during the hydrolysis produces large SiO_2 particles which avoiding a perfect crystallization of the silica film. As a consequence the optimum hydrolysis time of TEOS must be between 14 h and 16 h.

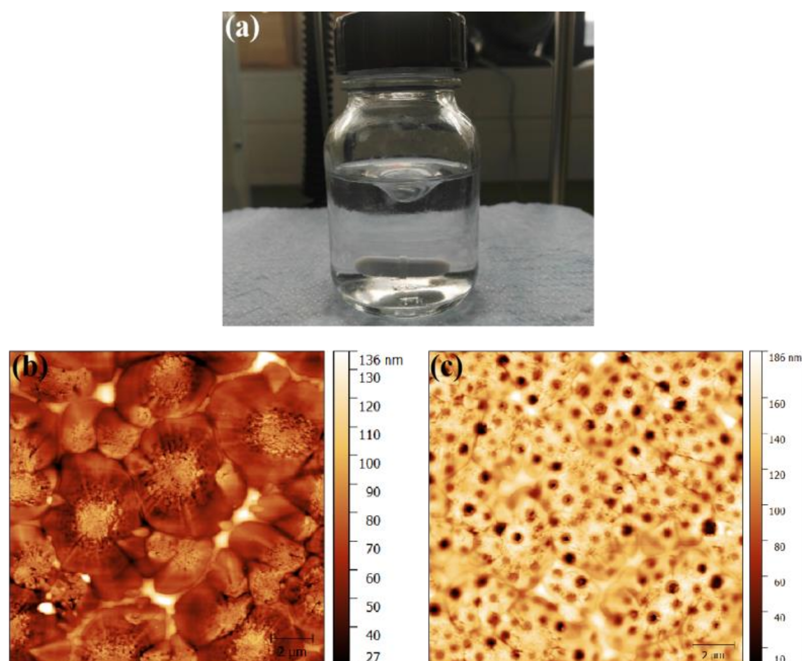

Figure 3.2. **(a)** Silica sol. **(b)** AFM topography image of a α-quartz film obtained from a silica sol stirred for 16 h. **(c)** The porous topography of as-prepared α-quartz after 2 h of condensation of TEOS.

4) The next day, prepare $SrCl_2$ aqueous solution with different Molar concentrations ($\boldsymbol{C}_{Sr}$) to obtain different final solutions with various ratios of Sr to Si ($\boldsymbol{R}_{Sr}$) for investigating Sr control of crystallization which is the content of **Chapter 4**. The Correspondence between $\boldsymbol{C}_{Sr}$ and $\boldsymbol{R}_{Sr}$ is shown as **Table 3.4**. Perform this and the following steps just before the preparation of the gel films because an aged solution is prone to re-precipitation of the Sr salt.

Table 3.4 Correspondence between the molarity of $SrCl_2$ aqueous solution and $\boldsymbol{R}_{Sr}$ in the final solutions used in the dip-coating process.

Concentration of $SrCl_2$ aqueous solution ($\boldsymbol{C}_{Sr}$)	**The Molar ratio of Sr to Si in the final solution ($\boldsymbol{R}_{Sr}$)**
0.4 M	0.02
0.5 M	0.025
0.6 M	0.03
0.65 M	0.0325 (shown as 0.033 in thesis)
0.7 M	0.035
0.75 M	0.0375 (shown as 0.038 in thesis)
1 M	0.05
1.5 M	0.075
2 M	0.1

5) Weigh different masses of $SrCl_2{\cdot}6H_2O$ salt into a 10 mL volumetric flask (see **Figure 3.3a**) respectively for obtaining different $\boldsymbol{C}_{Sr}$ shown in **Table 3.4**.

6) Add ultra-pure water (e.g., Milli-Q) up to 10 mL (meniscus tangent to the flask mark) and close the flask with a plastic cap and gently shake the flask to dissolve all the salt.

7) Take 10 mL of as-prepared silica sol from the glass bottle to a 25 mL glass beaker.

8) Add 275 μL of $SrCl_2$ aqueous solution to the 25 mL glass beaker containing the as-prepared sol and stir the solution for 10 minutes (see **Figure 3.3b**).

9) Dispose the residues that have been eventually generated according to the safety and environment protection protocols of the lab.

3.2.2. Formation of gel film via dip-coating

1) Preparation of the substrates

1.1) Cut Si slabs of about 2 cm by 5 cm out of a 2-inch p-type (100) silicon wafer with a thickness of 200 micron by cleaving the wafer in a direction parallel or perpendicular to the wafer flat using a diamond tip or a sharp-edged object. Perform this step in advance, for instance the day before the deposition of the gel films.

1.2) Just before the deposition of the gels, clean the substrates with ethanol and let them dry or use a nitrogen flow or compressed air to accelerate the drying. Perform this step while waiting for the completion of step **8** in **3.2.1**.

2) Coat the films.

2.1) In order to obtain a stable and controllable surrounding for dip-coating. this step is processed inside a cabin where can control the relative humidity (RH) at 40% and ambient temperature at 25ºC (see **Figure 3.3d**). Here, for the perforation study shown in **Section 5.3** of **Chapter 5**, other four RH including 50%, 60%, 70% and 80% were also attempted.

2.2) Establish a dip-coating sequence. Select the initial and final positions taking into account the actual length of the Si slab and the level of the solution in the beaker so that the slab is at least 2 cm above the solution level at the starting position and 1 cm above the bottom of the beaker at the end of the immersion. Set both the immersion and withdrawal rates. Set the immersion time (time at the final position) to 0. Here, the immersion rate is fixed as 5 mm/s. But the withdrawal rate was controlled from 1 mm/s to 40 mm/s for investigating the control of film's thickness which will be shown in **Section 5.1** of **Chapter 5**. Specially, 1 mm/min condition was also attempted to know the influence of very slow speed.

2.3) Upon completion of step **8** in **3.2.1**, take the final solution from the glass beaker to a specific 10 mL Teflon container (see **Figure 3.3c**). Then place the container with the solution in a well-centered position beneath the Si slab hanging from the dip-coater arm.

2.4) Fix one end of the Si slab to the dip-coater arm with the clip, ensuring the slab is as perpendicular as possible with respect to the horizontal.

2.5) Execute the dip-coating sequence and unclip the Si slab from the dip-coater arm.

2.6) After step **2.5**, put the as-prepared wet film into the furnace which under 450ºC for 10 min for consolidation. Then, the final gel film were ready for crystallization.

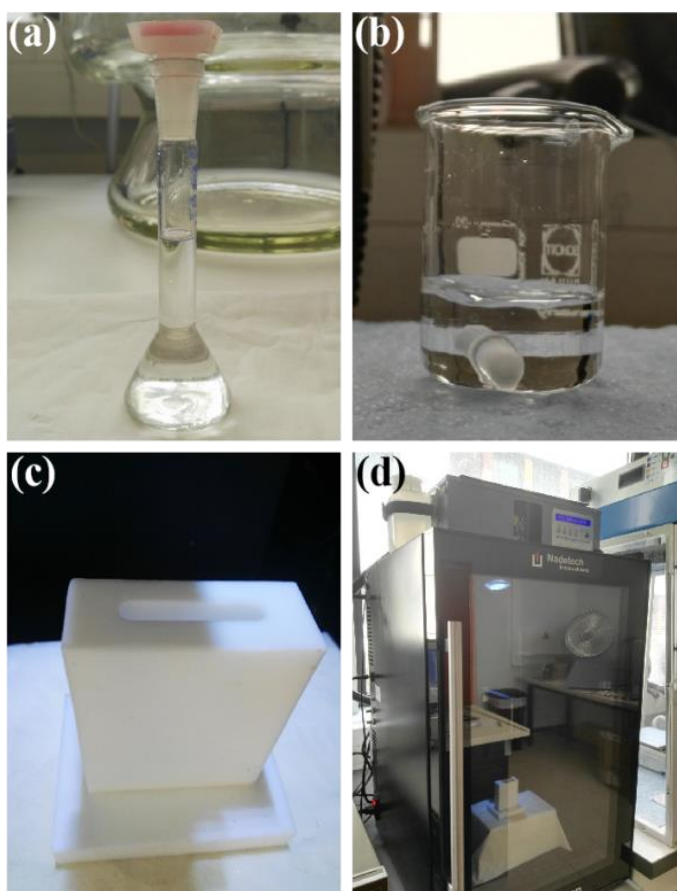

Figure 3.3. The lab ware and equipment used in the step of gel film deposition: **(a)** The 10 mL volumetric flask for preparing the $SrCl_2$ aqueous solution. **(b)** The 25 mL beaker for preparing the final solution. **(c)** The specific 10 mL Teflon container for dip-coating process. **(d)** The dip-coating equipment.

3) During deposition process, dispose the solutions staying longer than 40 min since preparation because the solutions are less effective. This process must be according to the safety and environment protection protocols of the lab.

4) For the multilayer deposition shown in **Section 6.1** of **Chapter 6**, repeat the step **2** in **3.2.2** for required times (see **Figure 3.4**).

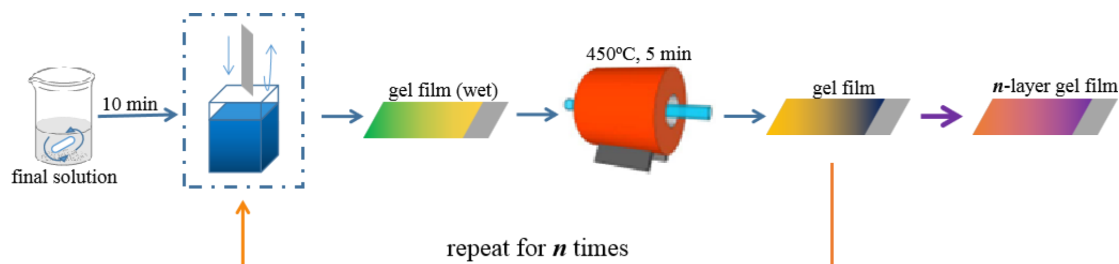

Figure 3.4. The schematic of multilayer deposition approach.

3.2.3. thermal annealing

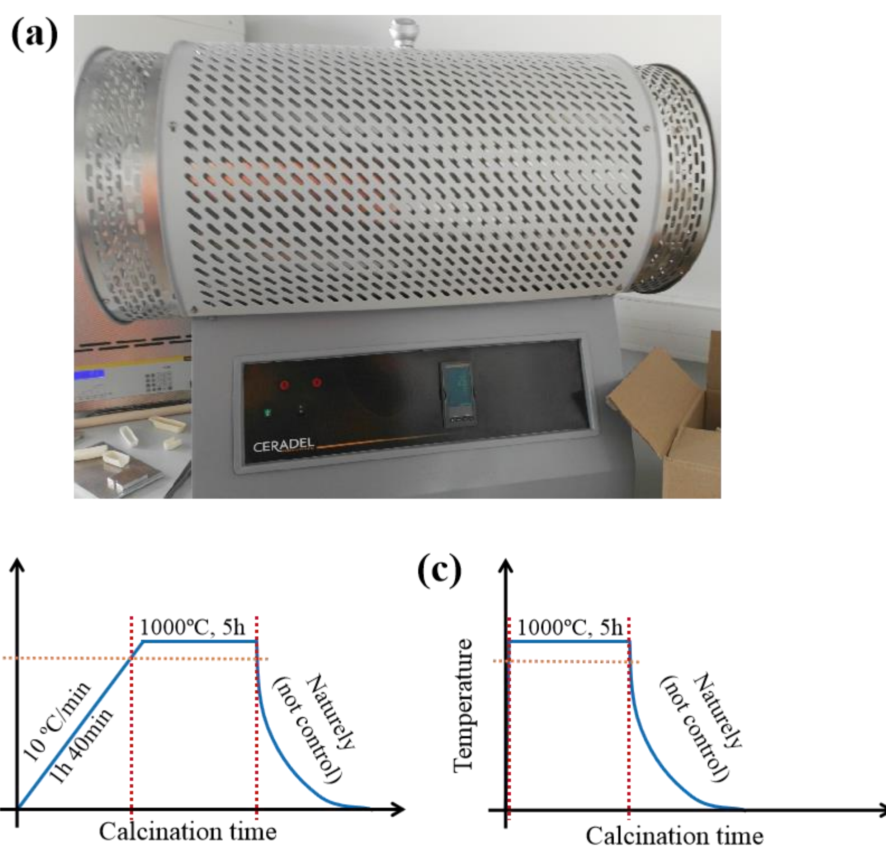

Figure 3.5. Thermal annealing step of film synthesis: **(a)** The furnace for the thermal treatments. **(b)** The temperature vs time dependence in a ramp-based treatment. **(c)** The temperature vs time dependence in the thermal treatments performed in this PhD.

In my work, except the study of annealing temperature (discussed later in **Section 5.2** of **Chapter 5**), the temperature is fixed at 1000ºC for 5 h. Thus, if the heating process contains a ramp, there is a heating period before 1000ºC (see **Figure 3.5b**). Here, one thing must be accounted is that the results in the following chapters tell us the

crystallization of α-quartz phase can occur since 925ºC and goes fast (For instance, the film containing high $SrCl_2$ will be crystallized within 30 min). However, the maximum of heating speed for the equipment is 10 ºC/min, which means it needs 1 h and 40 min to arrive the 1000ºC, also takes around 7.5 min from 925ºC to 1000ºC. With thinking of this, the crystallization should contain a 7.5 min of variable temperature annealing and 5 h of 1000ºC one, which is hardly to control.

For the purpose of controlling the annealing temperature, we chose to input the film at 1000ºC directly and the film is heated immediately (within 1 min) so that the heating process can be ignored (see **Figure 3.5c**). Combining with the natural cooling from 1000ºC to 925ºC is only need 2 minutes, the annealing in this way can be considered of at a constant temperature.

1) Program a furnace to perform the following thermal treatment in air atmosphere: heating from room temperature to 1000°C at 3°C/min, holding at 1000°C for 5 hours and cooling to room temperature naturely. For investigating the influence of annealing temperature to the crystallization of film, the holding temperature altered from 900°C to 1100°C. And for the annealing time study in **Chapter 4**, the short times were also attempted from 10 min to 60 min.

2) Place the gel film in an alumina boat, introduce it into the furnace once the temperature reaches to 1000°C and execute the thermal treatment.

3) Drag the alumina boat out from furnace by a metal bar once the temperature downs to room temperature to obtain the final crystallized films.

3.3. Characterization techniques

Throughout this work, the characterization of epitaxial quartz thin films and nanostructures were performed using the following techniques:

- X-ray diffraction analysis (XRD) was performed at Institut de Ciència de Materials de Barcelona (ICMAB) and IES by a specialized technicians.

- Atomic Force Microscopy (AFM) analysis was carried out at ICMAB and IES by a specialized technicians.

- Scanning Electron Microscopy (SEM) and Electron Back Scattered Diffraction (EBSD) images were acquired at ICMAB, and at the Institut des Matériaux de Paris Centre (IMPC FR2482).

- Electron Transmission Microscopy (TEM), High Resolution Electron Transmission Microscopy (HRTEM) and High-resolution Z-contrast scanning electron transmission microscopy (STEM) images were carried out by other group members and by specialized technician at SCT-UB, SMEUAB, ICMAB, STEM, and Group of Materials Science and Division (ORNL, Oak-Ridge).

- X-ray Photoelectron Spectrum (XPS) measurements and data analysis of epitaxial quartz thin films were performed at ICMAB.

- Dip-coating depositions of silica sol-gel films were performed at the IES (nanochemlab) during a 14 months stay in Montpellier.

- Piezoelectric measurements of quartz thin films and nanostructures were performed by Direct Piezoresponse Force Microscopy (DPFM) and Piezoresponse Force Microscopy (PFM) techniques at the ICMAB thanks to a collaboration with Andres Gomez.

- Nanoimprint lithographies (NIL) including laser inference lithography (LIL) and soft lithographic techniques were used to produced nanostructured quartz thin films, inducing nanostructuration across the entirety of silicon surface. All these lithographic processes were developed at the IES of the CNRS and the University of Montpellier.

3.3.1. Surface characterizations

Atomic Force Microscopy

AFM is especially used to obtain topographic images of surfaces, either insulating or conductive, in order to determine its roughness, grain size or other characteristics at micron and nanometric scale. Moreover, by studying other kinds of tip-sample interactions one can obtain information about other properties of the sample’s surface, such as electrical currents (Electrical Force Microscopy, EFM), magnetism (Magnetic Force Microscopy, MFM) or piezoelectric (Piezoelectric Force Microscopy, PFM).

The key elements of an AFM, and common to all SPMs, are the tip, which is the element that scans and interrogates the sample surface, and the piezoelectric scanner that positions the sample relative to the tip along the xyz-axis. The tip, typically with a pyramidal shape, is assembled at the extreme end of a flexible cantilever that will bend or twist in response to any tip-sample interaction.

AFM also includes an optical system consisting of a laser and a multi-faced position sensitive photo diode that allows the detection of the cantilever deflection, and a computer that drives the microscope and stores the surface contours.

The topographic image is then acquired by raster scanning the tip along the sample’s surface while the feed-back-loop drives the piezo-scanner in the z-axis, corresponding to the measured deflection in order to keep the cantilever deflection, i.e., the exerted force, constant. Finally, the error signal obtained by comparing the detector signal with the setpoint value will be the raw data used to generate the image of the sample’s topography.

Images captured for this work were done with a Park Systems NX-10 Scanning Probe Microscopy (SPM) unit installed at ICMAB-CSIC. A microscope 5500 from Agilent Technologies located at Matgas-AIE was used to localize a specific region of the sample, since it has an optical microscope with a micrometric positioning stage associated.

Images were taken in tapping mode and using silicon tips with a characteristic resonance frequency of 150-200 Hz and a stiffness constant of around 48 N/m. Surface was typically scanned at 1 line/s. Typical scans of 20x20 μm^2 were performed at distinct zones to study the microstructural evolution and rugosity. Image processing was done by using the software Gwyddion (http://gwyddion.net) which is a modular program for SPM (scanning probe microscopy), data visualization.

Scanning Electron Microscopy

Scanning electron microscope is a type of electron microscope that scans the sample's surface through a high-energy beam of electrons. The electrons interact with the atoms of sample thus, producing signals that contain information about the sample's surface topography, composition, and other properties such as the electrical conductivity.

The principal kinds of signals resulted from primary electrons (when a beam of electrons is focused on a sample placed in a vacuum chamber), secondary electrons, and back-scattered electrons (BSE). Secondary electrons imaging is the most common standard detection mode and detects the signal that results from the interactions of the electron beam with the atoms near the sample's surface. This mode can produce high-resolution images of a sample surface, revealing details less than 1 to 5 nm in size. Back-scattered electrons come from a beam electrons that is reflected from the sample by elastic scattering. BSE are often used for analytical details and surfaces features identification of inhomogeneous samples since the intensity of the BSE signal is strongly related to the atomic number (Z) of the specimen. The surface features include extensive faceting, phase separation, morphology of crystals, precipitates, and pores.

The operation principle of SEM is mainly the same as FESEM with the exception that in conventional SEM, samples must be electrically conductive, at least at the surface, and electrically grounded to prevent the accumulation of electrostatic charge at the surface. Therefore samples are usually coated with an ultrathin coating of electrically-conducting material, commonly gold, deposited on the sample either by low vacuum sputter coating or by high vacuum evaporation. However, an improvement of resolution while avoiding coating can be achieved using FESEM. In this case, electrons are accelerated under the influence of a strong electrical voltage gradient (or

field), which enables to generate narrow proving beams with low or high electro energy. As a result, the spatial resolution is improved (up to 10 nm), and sample charging and damage is minimized.

FESEM images were acquired using a FEI QUANTA 200 (FEG-ESEM) located at ICMAB and a FEG-SEM model Su-70 Hitachi, equipped with an EDX detector X-max 50 mm2 from Oxford instruments located at Paris. Nanostructures of less than 100 nm lateral size were imaged without coating and working at 5-10 kV in high vacuum. FESEM was the most useful electron optical system for surface imaging and was applied routinely to characterize all morphologies of the samples produced along this thesis.

3.3.2. Structural characterizations

X-ray diffraction

Along this thesis, ordinary θ-2θ and ω-scan analysis were carried out using Siemens D5000 diffractometers with Cu-Kα λ =1.5418Å and a Bruker D8 Gadds 2D diffractometer (XRD2) located at ICMAB.

XRD is a very important experimental technique to solve all issues related to the crystal structure including lattice constants and crystallography, identification of unknown materials, orientation of single crystals and preferred orientation of poylcrystals defects, stresses, grain size, etc.

Crystals can be decomposed into any number of different plane configurations separated by a constant parameter d (Bragg plane), due to the periodicity of the crystal lattice. Moreover, X-ray wavelength is comparable to this constant parameter d in a crystal (~Å). Then, when an X-ray beam is directed towards a sample, some photons primarily collide with electrons in atoms and are diffracted in all directions.

Elastically scattered waves can interfere constructively. If the atoms within the sample are arranged in a periodic fashion, the diffracted wave will reflect the symmetry of the atoms' distribution. The condition that must be fulfilled to obtain a constructive interaction between beams diffracted by parallel planes of atoms is known as the Bragg condition or Bragg's law:

$$2d \sin\theta = n\lambda$$

where d is the spacing of the atomic layers of the crystal, n is the period, λ is the wavelength and θ the angle of the incoming X-ray beam. Modifying the incidence angle θ, one obtains a diffraction pattern, which is characteristic for each crystalline phase. Moreover, relative rotation of the sample with respect to the detector enables to explore diffraction in distinct configurations and get information about preferred

alignment of crystallites (2θ-scan), their out-of-plane (ω-scan) or in-plane (Φ-scan) texture, etc.

The diffraction pattern obtained when the Bragg law is fulfilled, contains information about the structural arrangement of atoms in the material. For example, comparing a powder diffractogram with an internationally recognized data base powder diffraction file (PDF) reference patterns, it is possible identify crystalline phases present in the sample.

Two-dimensional X-Ray Diffraction (XRD2)

Compared to a conventional 1D diffraction system, XRD2 system has many advantages in various applications, especially when extremely fast texture data for multiple poles and multiple directions is required.

XRD2 is a diffraction system with the capability of acquiring diffraction patterns in 2D space simultaneously. Texture analysis was performed using a diffractometer equipped with a 2D detector GADDS D8 Advance XRD2 system from Bruker, located at ICMAB.

XRD2 technique was very suitable to identify secondary polycrystalline phases or resolve the epitaxial growth of quartz films on silicon. These results are not suitable to resolve using conventional X-ray. To establish the crystallographic orientation of quartz on silicon, a phi-scan (φ−scan) and pole figures mesurements were necessary. They provide information about the in-plane and out of plane texture of the epitaxial quartz films.

Transmission Electron Microscopy (TEM) and Scanning Transmission Electron Microscopy (STEM)

TEM and STEM are related techniques that use an electron beam to image a sample. High energy electrons, incident on ultra-thin samples allow image resolutions in the order of 1 or 2 Å.

Compared to SEM, STEM has better spatial resolution, is capable of additional analytical measurements, and requires significantly more sample preparation. Moreover, it is possible to obtain outstanding image resolution, characterize crystallographic phase, crystallographic orientation (both by diffraction mode experiments (ED), know the elemental composition as well as produce elemental maps (using EDS), and images that highlight elemental contrast (dark field mode) all from nm sized areas precisely located. STEM and TEM were an ultimate failure analysis tools for the nanostructures synthetized in this work.

Samples were cut to look at epitaxial quartz and the Quartz/Si interface from side view (cross-section). Samples were prepared by using the mechanical tripod polisher technique followed by Ar milling. In addition, nanopillars were prepared by dispersion in methanol and deposition of a droplet of this suspension on a carbon-coated film supported on a copper grid.

Direct electron images provided information about shape, size, lateral facets, interface, etc. of quartz nanopillars. Electron diffraction patterns were used to identify the crystallographic structure determine the cell parameters.

Low magnification TEM images and electron diffraction patterns were acquired with a 200 KV Jeol JEM-2011 microscope at UAB and a 300 KV Philips CM30 microscope at “Serveis Cientifico-Tècnics” of the Universitat de Barcelona (UB).

High-resolution Z-contrast scanning electron transmission microscopy (STEM) imaging

Aberration corrected Z-STEM microscopes can be used to produce atomic resolution images with unprecedented detail. In fact, Z-STEM imaging has been routinely used for the last few years to produce images with resolution down to 1 Å. In this work a 100 kV aberration-corrected Z-STEM VG Microscope HB501UX equipped with an Enfina EEL spectrometer and a NION aberration-corrector microscope that has a 0.78 Å resolution was used at STEM group of Oak Ridge National Laboratory (ORNL).

3.3.3. Physical characterizations

Piezoelectric Force Microscopy (PFM) and DPFM

We used Atomic Force Microscopy (AFM) more preciously "Piezoresponse Force Microscopy" (PFM) mode to study the piezo response of epitaxial quartz films and 1D nanostructures. PFM method measures displacement in piezoelectric materials as a result of the "converse piezoelectric effect" which takes place when a strain (stress) is produced upon application of an electric field. However, in some cases, this technique presents problems for quantitative analysis of the piezoelectric coefficient d_{33} based on wrong electromechanical response of the AFM tip that not exclusively depends on the piezo signal, but on other physical effects. In a complementary way, we used a new method that obtains a direct quantitative measurement of the piezoelectric constant in piezoelectric thin films developed at (ICMAB) [1]. DPFM was used during this thesis for direct measurements of d_{33} in epitaxial thick quartz films on silicon substrate. This new method uses a specific amplifier for measuring the charge generated by piezoelectric materials when a force is applied on them. The amplifier is an electronic circuit capable of converting electric charge into a voltage signal, readable by any commercial microscope. Piezoelectric characterization

through the direct piezoelectric effect was made by Direct Piezoelectric Force Microscopy [1, 2] in an Agilent 5500LS instrument using a low leakage amplifier (Analog Devices ADA4530) with Pt/Ir tips (Rockymountain Nanotechnology RMN-25 PtIr200H). A Periodically Poled Lithium Niobate from Bruker AFM was used as a calibrating reference. Roughness of films was obtained from a 50 µm × 50 µm AFM images by using the Gwyddion software [3].

3.4. Chapter references

1. Gomez, A.; Gich, M.; Carretero-Genevrier, A.; Puig, T.; Obradors, X., Piezo-generated charge mapping revealed through direct piezoelectric force microscopy. *Nature Communications* **2017,** *8* (1), 1113.

2. Vila-Fungueiriño, J.M.; Gómez, A.; Antoja-Lleonart, J.; Gázquez, J.; Magén, C.; Noheda, B.; Carretero-Genevrier, A., Direct and converse piezoelectric responses at the nanoscale from epitaxial $BiFeO_3$ thin films grown by polymer assisted deposition. *Nanoscale*, **2018**, *10*, 20155-20161.

3. Necas, D.; Klapetek, P., Gwyddion: an open-source software for SPM data analysis. *Central European Journal of Physics* **2012,** *10* (1), 181-188.

Chapter 4. Controlling α-Quartz Film Microstructures via Strontium-assisted Devitrification

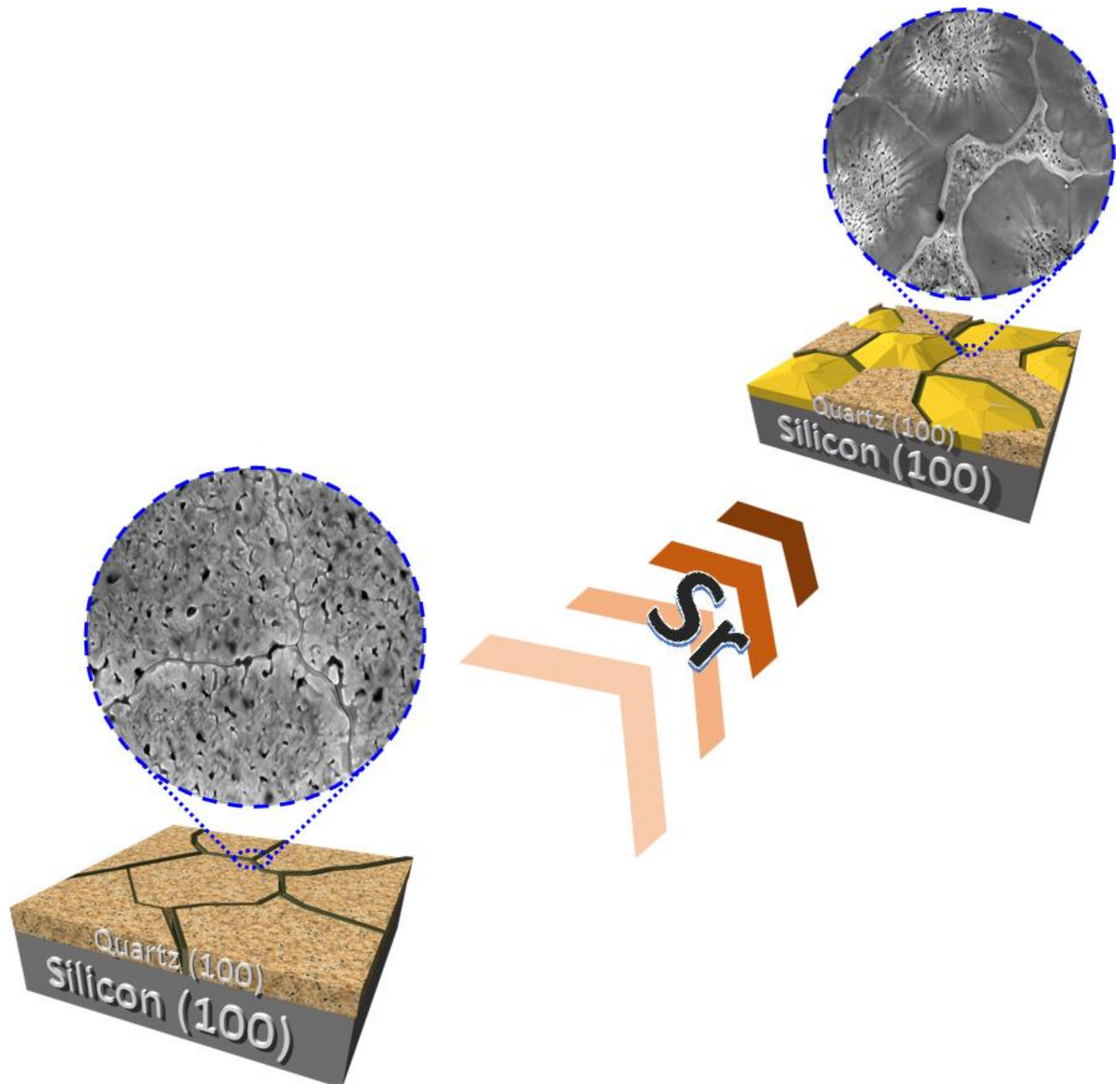

Chapter 4

For the crystallization of α-quartz films, Strontium (Sr), similarly to a catalyst in a reaction, is a key ingredient for the devitrification of amorphous silica. On this ground, the content of Sr inside gel film can influence not only the crystallinity of films by altering the rate of crystallization but also its microstructure and properties by changing the growth mechanism. Since Sr plays a central role in α-quartz crystallization, a first objective of my PhD is undertaking a systematic study on its role, despite the challenge of directly measuring and adjusting the amount of Sr inside the films. In my study, the selected way to control the quantity of Sr in the gel film is to adjust the concentration of $SrCl_2$ aqueous solution ($\boldsymbol{C}_{Sr}$) to make final solutions with different ratios of Sr^{2+} to SiO_2 ($\boldsymbol{R}_{Sr}$). This methodology has been already introduced in **Section 3.2.1** of **Chapter 3**.

In this chapter, the control of Sr inside gel films was achieved by using the final solutions containing different $\boldsymbol{R}_{Sr}$. To study the influence of $\boldsymbol{R}_{Sr}$ in the crystallization, the annealing procedure was fixed as 1000ºC for 5 hours. The microstructure and properties of all the as-prepared α-quartz films with different $\boldsymbol{R}_{Sr}$ were analyzed systematically in order to know how Sr can control the crystallization of films.

4.1. Different film microstructures controlled by $\boldsymbol{R}_{Sr}$

After establishing a method to control the Sr^{2+} concentration in the SiO_2 gel films, a series of films with different $\boldsymbol{R}_{Sr}$ was fabricated. The surfaces of these films were observed initially with an optical microscope. Representative images of those films are shown in **Figure 4.1**.

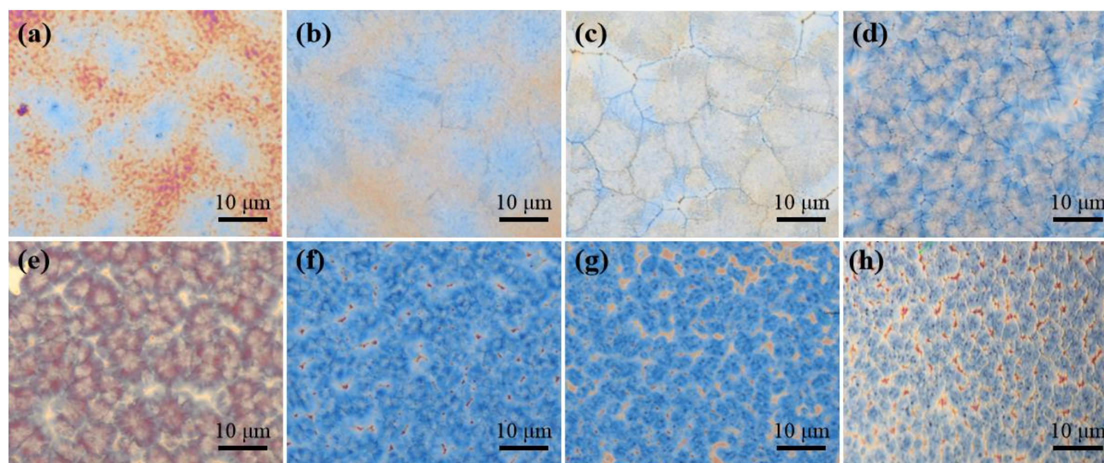

Figure 4.1. Optical pictures of as-prepared α-quartz films with different $\boldsymbol{R}_{Sr}$: **(a)** 0.025, **(b)** 0.03, **(c)** 0.033, **(d)** 0.035, **(e)** 0.038, **(f)** 0.05, **(g)** 0.075 and **(h)** 0.1.

Although these optical pictures only can be used as a preliminary characterization, there exist significant differences among the surfaces of films caused by $\boldsymbol{R}_{Sr}$. This result just confirms what has been expected at the beginning of this chapter: The film microstructure is very sensitive to $\boldsymbol{R}_{Sr}$. Aiming to know the influence of $\boldsymbol{R}_{Sr}$ on the

microstructure, films were classified according to the type of surface, and the microstructural features were investigated accordingly.

4.1.1. Partly crystalline films

When R_{Sr} is lower than 0.033, the films are inhomogeneous. By observing **Figure 4.2a** ~ **c**, the surfaces of films can be classified according to the characteristics of the speckled light color zone (yellow spots in **a** and **b**, pale blue spots in **c**) and the remaining dark color zone (pink areas in **a** and **b**, brown area in **c**). Very obviously, there is an increase of light color zone as R_{Sr} rises, which suggests that these zones correspond to α-quartz phase while the dark ones are still amorphous. To confirm this hypothesis, a single light color spot with a narrow shape on the surface of the R_{Sr} = 0.02 film was studied by electron back-scattering diffraction (EBSD) and the results are displayed in **Figure 4.2d** ~ **f**.

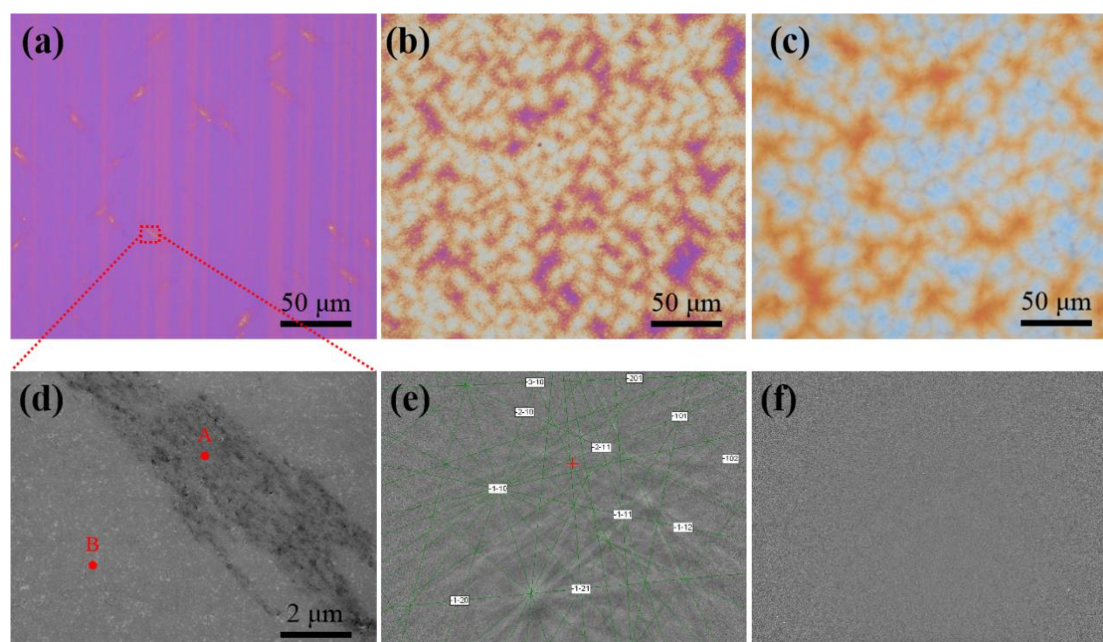

Figure 4.2. Optical images of partly crystalline films when R_{Sr} is **(a)** 0.02, **(b)** 0.025 and **(c)** 0.03. In these images, only the light color zones are crystallized to α-quartz phase, the remaining pink or brown zones are still amorphous. **(d)** is the SEM image of one selected zone of R_{Sr} = 0.02 film (indicated by the red dotted square) containing crystalline microstructure (dark area) and amorphous surface (light area) as analyzed by EBSD: **(e)** is the EBSD result of point A in **(d)** with α-quartz phase signals. **(f)** is the EBSD result of point B in **(d)** without any signal.

The selected single spot is presented as the dark part in the SEM image (see **Figure 4.2d**), and the Point A inside this part is the position in which the EBSD analysis was done. According to the result shown in **Figure 4.2e**, a response corresponding to α-quartz phase is detected, but very weak. At the same time, the Point B, which is outside of the selected spot, also was analyzed by EBSD without obtaining any

evidence of crystalline phase (see **Figure 4.2f**). The test of Point B indicates that outside the light spots which correspond to α-quartz , there is amorphous silica.

EBSD analysis identifies that only these light color spots in the optical images correspond to α-quartz phase. It is very clear that the crystallization of films with $\boldsymbol{R}_{Sr}$ < 0.033 condition is incomplete. In this partly crystalline region ($\boldsymbol{R}_{Sr}$ is 0.02 ~ 0.03), $\boldsymbol{R}_{Sr}$ = 0.02 can be regarded as the minimum Sr concentration for which extremely tiny and sparse zones with α-quartz can be observed. This means that Sr-induced crystallization has allready started but the level is trifling, and the films are mostly amorphous.

As mentioned, in this partly crystalline region, the α-quartz spots increase very obviously with $\boldsymbol{R}_{Sr}$. In order to understand the influence of $\boldsymbol{R}_{Sr}$ on the film crystallinity, for all the three partly crystalline compositions, larger optical pictures were taken at lower magnifications and the area coverages of α-quartz phase were calculated with the “Image J” image analysis software. Meanwhile, the film with $\boldsymbol{R}_{Sr}$ = 0.033, which is fully crystalline, was chosen as a reference. The results of these measurements are plotted in **Figure 4.3**.

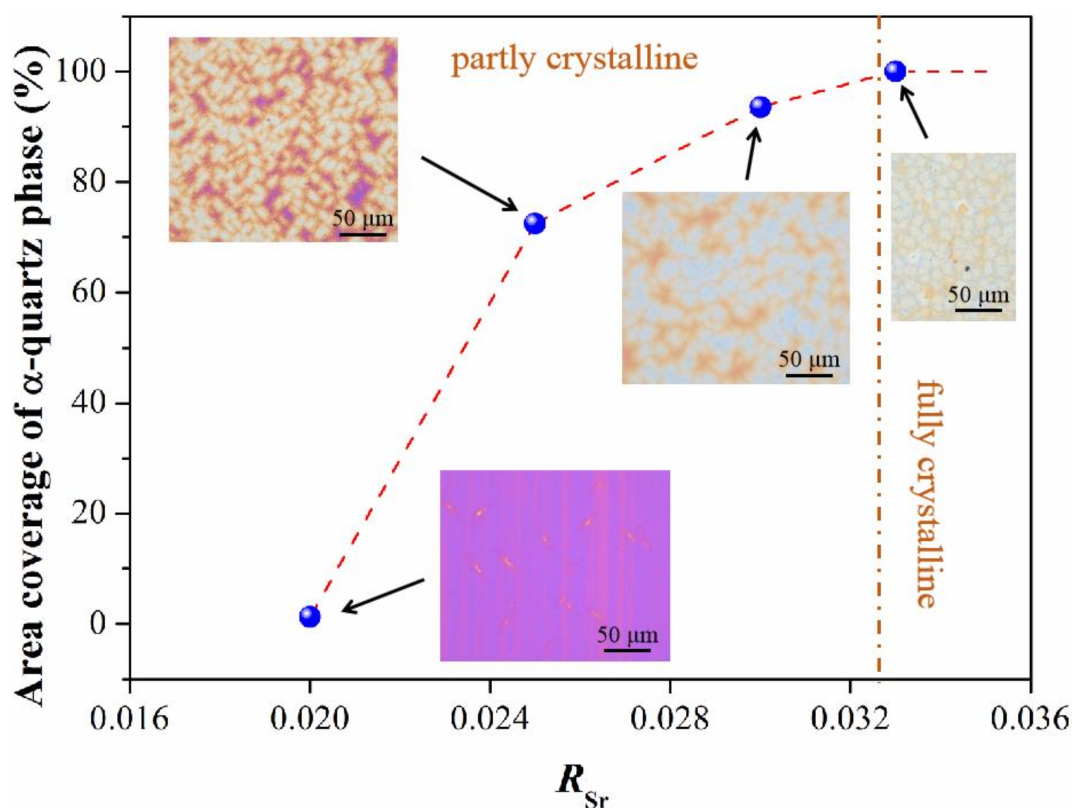

Figure 4.3. Relationship between the area coverage of α-quartz phase and $\boldsymbol{R}_{Sr}$. The inset images are the pictures of films with different $\boldsymbol{R}_{Sr}$ used to obtain the evolution of α-quartz phase coverage.

As observed in **Figure 4.3**, the area coverage of α-quartz spots is close to zero (1.3%)

for $\boldsymbol{R}_{\mathrm{Sr}}$ = 0.02 which ensures that the film is almost amorphous. But the coverage increases strongly (up to 72.9%) when $\boldsymbol{R}_{\mathrm{Sr}}$ raises a bit to 0.025. Then, the coverage keeps increasing with $\boldsymbol{R}_{\mathrm{Sr}}$ but more and more slowly until reaching 100% at $\boldsymbol{R}_{\mathrm{Sr}}$ = 0.033. This crystalline area measurement tells us that $\boldsymbol{R}_{\mathrm{Sr}}$ in this partly crystalline region is the main factor controlling the crystallinity of the films. In general, the crystalline fraction can increase to above 80% when $\boldsymbol{R}_{\mathrm{Sr}}$ just changes from 0.02 to 0.03 (*i.e.* increases by 30%). However, the films are still partly crystalline and inhomogeneous.

Even so, partly crystalline films are well suited to investigate the differences between the microstructures of α-quartz and amorphous zones. For instance, from the $\boldsymbol{R}_{\mathrm{Sr}}$ = 0.02 film, which presents small and isolated crystalline spots, one spot was chosen to take SEM images both in secondary electron (SE) and back-scattered electron (BSE) modes.BSE images are very helpful to know the distribution of Sr. In BSE mode, the zones containing Sr are much brighter and whiter because Sr atoms have more electrons than Si and O atoms. Simultaneously, atomic force microscopy (AFM) was also performed on a single crystalline zone. All these results are summarized as **Figure 4.4**.

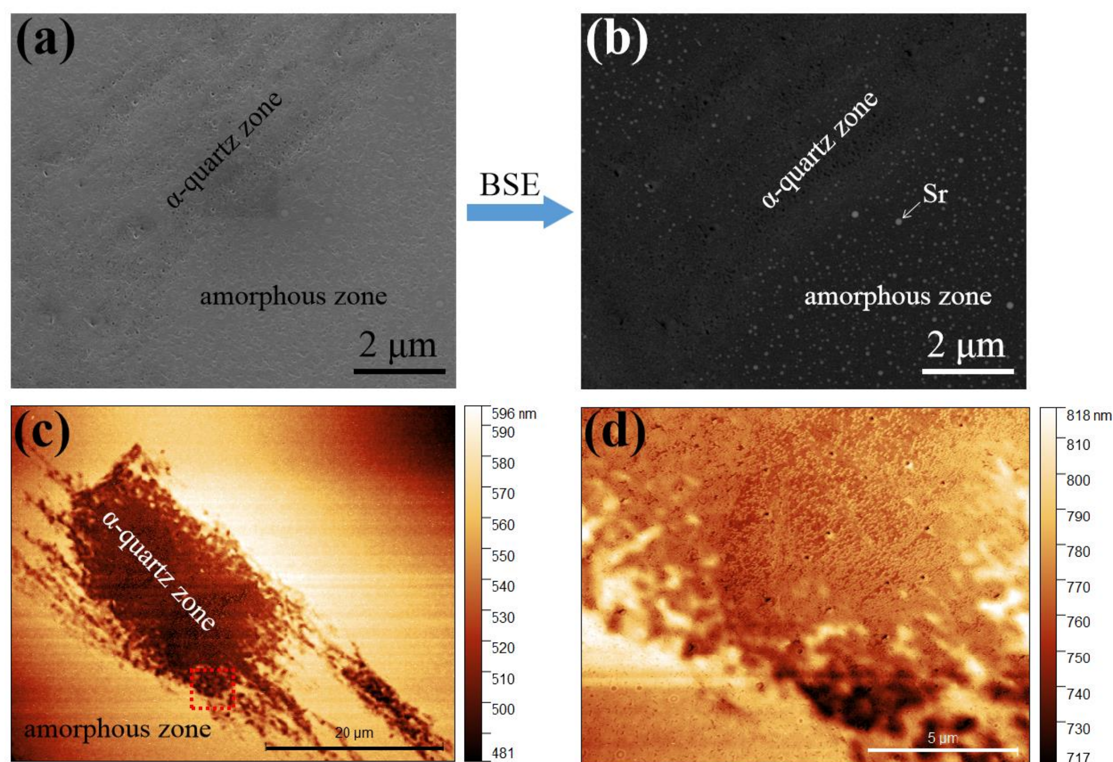

Figure 4.4. Microstructural study of $\boldsymbol{R}_{\mathrm{Sr}}$ = 0.02 film. **(a)** and **(b)** are the SEM images in SE and BSE modes respectively to show the microstructure of one selected area displaying an α-quartz zone and an amorphous zone. **(c)** is the corresponding AFM images to show the topography of the microstructure. **(d)** is the magnified AFM image of the selected red-dotted square area in **(c)**.

According to the SEM image in SE mode (**Figure 4.4a**), the difference of microstructures between α-quartz zone and amorphous zone is not obvious. But when the image is observed carefully, one can notice that the α-quartz zone appears a bit more porous and with a lower surface in the out of plane coordinate in comparison to the amorphous zone, as indicated by a darker contrast in SE mode image. However, the SEM image in BSE mode (see **Figure 4.4b**) can tell us clearly that only the amorphous microstructure contains Sr on the surface, which corresponds to the white dots in the image with a droplet shape. The distribution of Sr is an important evidence indicating that the crystalline microstructure due to α-quartz phase cannot coexist with Sr. Thus, the narrow crystalline zone can be easily identified by the absence of Sr inside it.

AFM is necessary to confirm the topography differences indicated by SEM. Indeed, **Figures 4.4c** and **d** show that the α-quartz microstructure is found at a lower level with respect to the amorphous one (Ca. 10 nm) and more porous. This is a normal phenomenon caused by phase transition: α-quartz phase (density is 2.65 g/cm^3) is denser than amorphous silica (density is 2.20 g/cm^3), so during the phase transition, the thickness decreased and pores were created to accommodate the volume shrinkage, resulting in a sort of loose microstructure which can release space and minimize surface tension.

4.1.2. Porous α-quartz films

When $\boldsymbol{R}_{Sr}$ is 0.033 or higher, the film can be fully crystallized, which means that α-quartz phase can grow everywhere in the film, since $\boldsymbol{R}_{Sr}$ is always high enough to complete the phase transition. Despite that, the control of $\boldsymbol{R}_{Sr}$ is still crucial to tune the microstructure of α-quartz phase in the films, as already shown in **Figure 4.1c** ~ **h**. In this fully crystalline region ($0.033 \leq \boldsymbol{R}_{Sr} \leq 0.1$), the crystallization results in films which are dominated by a porous microstructure when $\boldsymbol{R}_{Sr}$ is relatively low (*i.e.* for $\boldsymbol{R}_{Sr} = 0.033$ and 0.035). In order to see the porous microstructure in more detail, SEM images have been taken for the films of these two conditions, and the results are shown in **Figure 4.5**.

Although both the microstructures of $\boldsymbol{R}_{Sr} = 0.033$ and $\boldsymbol{R}_{Sr} = 0.035$ films are porous, there are significant differences between them. For $\boldsymbol{R}_{Sr} = 0.033$, the film is highly homogeneous and characterized by a porous microstructure (see **Figure 4.5a**), but it also displays many crevices which are observed more clearly with a higher magnification (see **Figure 4.5b**). It makes sense because the gel film normally shrinks itself and makes cracks or crevices during the annealing treatment.

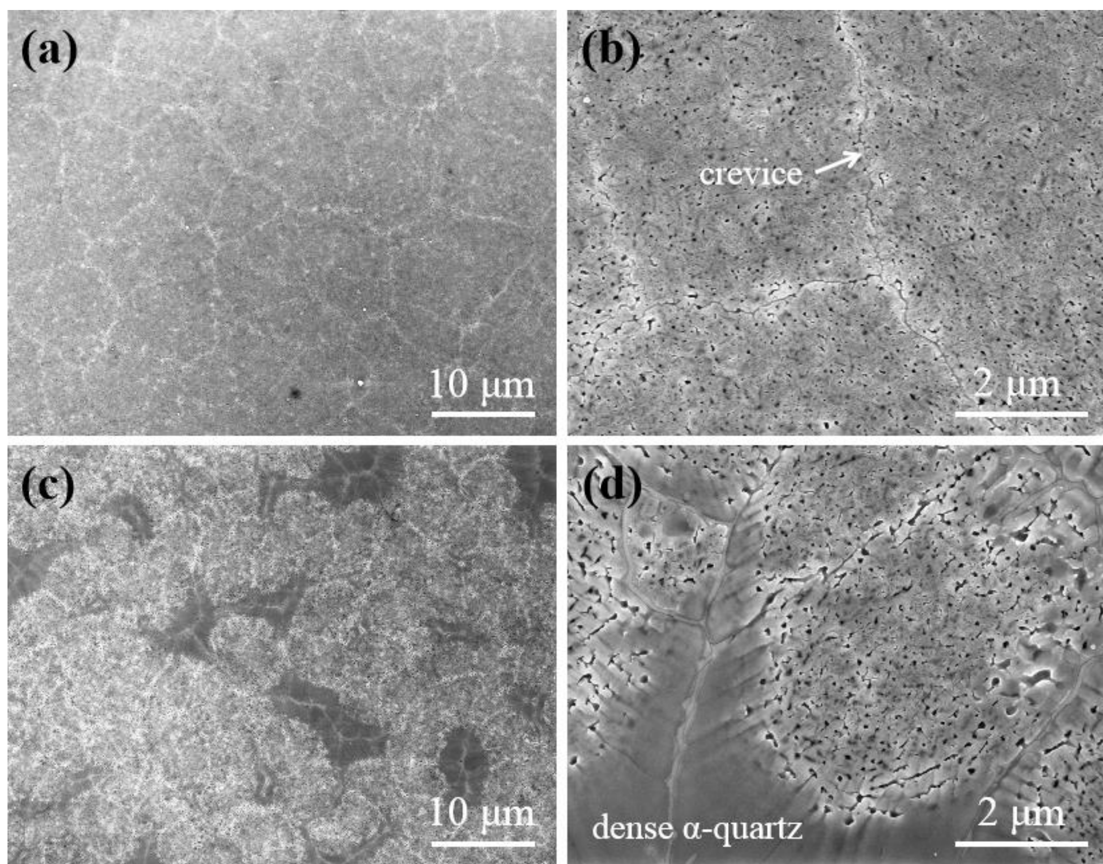

Figure 4.5. SEM images of porous α-quartz films in SE mode: **(a)** and **(b)** are the images of $\boldsymbol{R}_{\mathrm{Sr}}$ = 0.033 film at different magnifications. **(c)** and **(d)** are the images of $\boldsymbol{R}_{\mathrm{Sr}}$ = 0.035 film at different magnifications.

When $\boldsymbol{R}_{\mathrm{Sr}}$ reaches 0.035, we can observe that several zones of dense microstructure appear around some of the crevices, which can be found easily as dark areas in **Figure 4.5c**. Even so, for $\boldsymbol{R}_{\mathrm{Sr}}$ = 0.035 the film can still be considered as porous α-quartz because the area coverage of dense microstructures is small (14.96% in mean value, measured by Image J) and thus the film is dominated by porous microstructure. With the higher magnification image (see **Figure 4.5d**), we can see that the dense microstructure is a block of α-quartz without any fracture or porosity. Note that all the dense α-quartz zones are located at crevices which appear to be filled with a lighter phase with a liquid-like shape.

For the sake of understanding the reason why the dense α-quartz microstructure can be formed when $\boldsymbol{R}_{\mathrm{Sr}}$ rises from 0.033 to 0.035, one zone containing crevices was selected respectively for each $\boldsymbol{R}_{\mathrm{Sr}}$ condition to take SEM images in BSE mode, and the images are displayed in **Figure 4.6**.

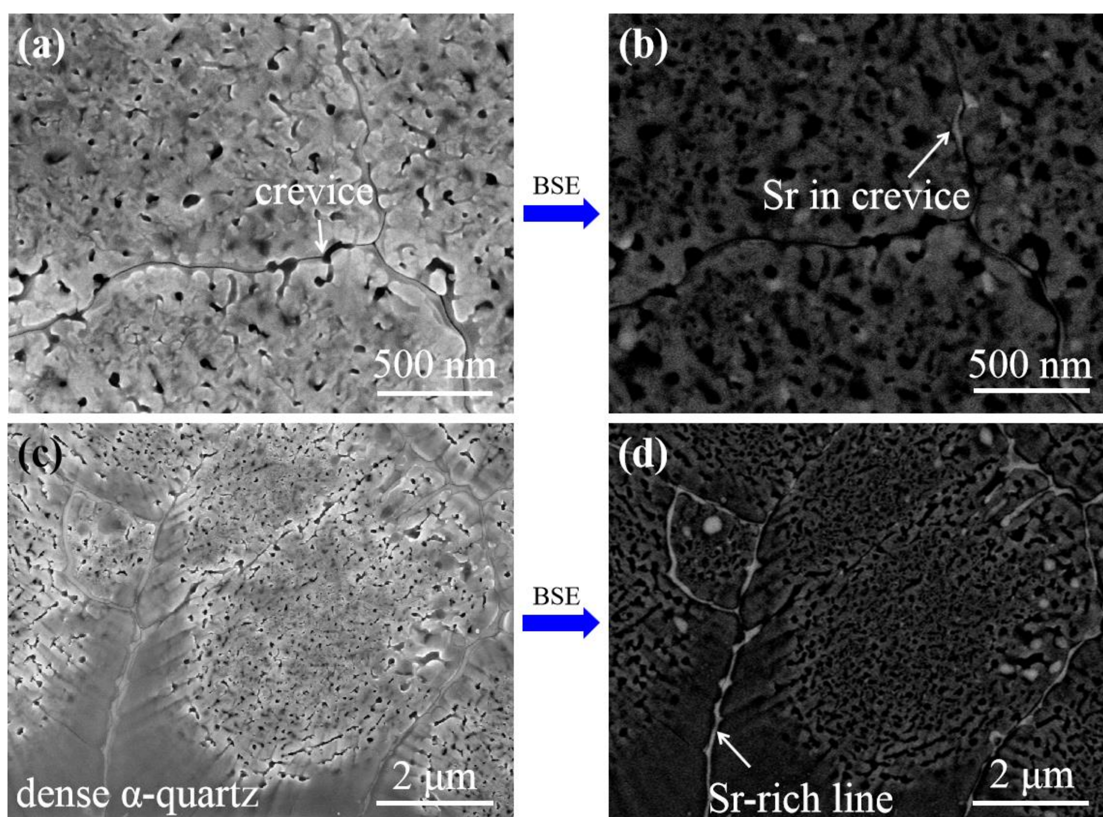

Figure 4.6. SEM images of two porous α-quartz films: **(a)** and **(b)** are the SE and BSE images of selected zone for $\boldsymbol{R}_{Sr}$ = 0.033 film. **(c)** and **(d)** are the SE and BSE images of selected zone for $\boldsymbol{R}_{Sr}$ = 0.035 film.

It should be emphasized again that the Sr-containing compound cannot coexist with α-quartz phase. So, in the case of fully crystalline film, most of the Sr only can aggregate into pores or crevices after crystallization. Comparing **Figures 4.6b** and **d**, it is obvious that more Sr aggregates into crevices when $\boldsymbol{R}_{Sr}$ increases from 0.033 to 0.035, so that the crevices of $\boldsymbol{R}_{Sr}$ = 0.035 film are filled with Sr and become a Sr-rich line. This appears to be the key point to explain why dense α-quartz microstructure can be grown at $\boldsymbol{R}_{Sr}$ = 0.035 condition. According to Ndayishimiye's work [1], further densification of porous α-quartz microstructure can be driven by concentrated devitrifying agent (which is Sr in this Thesis). Therefore, the porous α-quartz microstructure surrounding the Sr-rich lines can be densified into dense microstructure. But the densification cannot occur in the whole film because it is limited by the sparse distribution of crevices. Indeed, most of the surface is far from Sr-rich lines and maintains the porous microstructure.

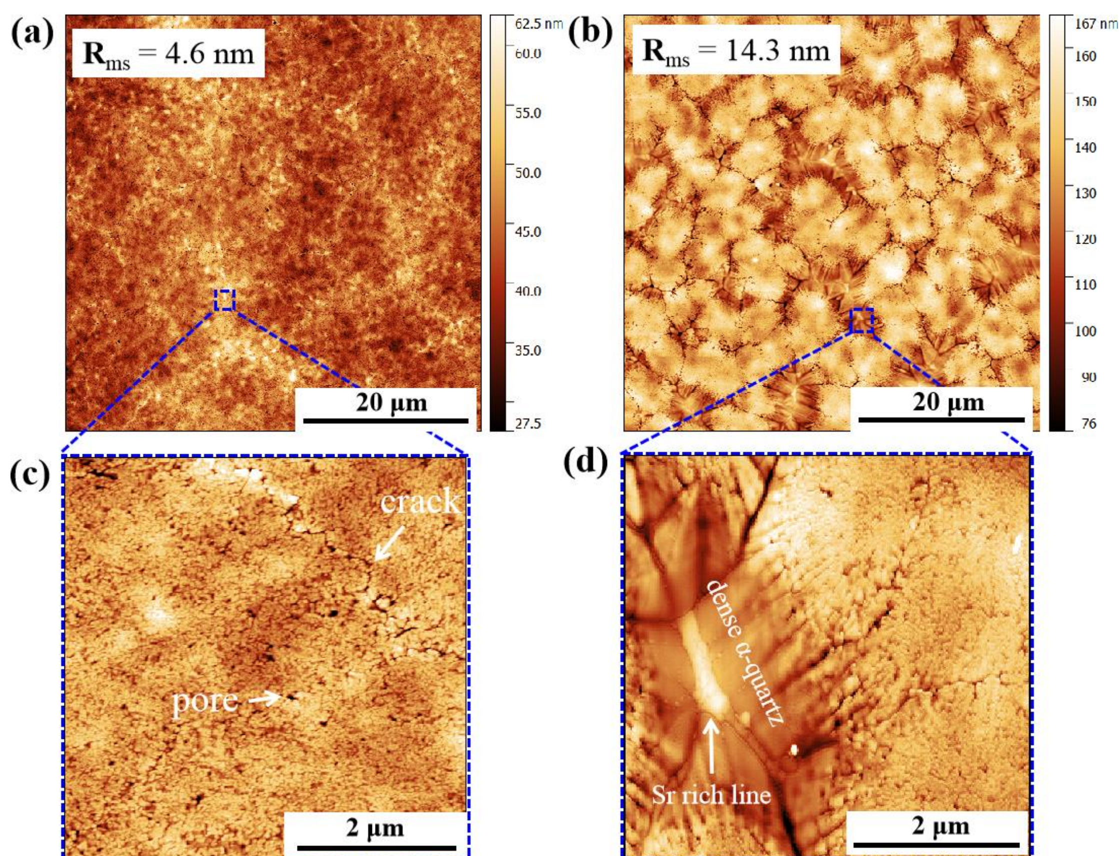

Figure 4.7. AFM images of two porous α-quartz films: **(a)** $\boldsymbol{R}_{\mathrm{Sr}}$ = 0.033. **(b)** $\boldsymbol{R}_{\mathrm{Sr}}$ = 0.035. **(c)** Zoomed-in image of the blue selected zone in **(a)** to show the topography of porous microstructure. **(d)** Zoomed-in image of the blue selected zone in **(b)** to show the topography of dense microstructure.

Simultaneously, AFM images of these two types of porous α-quartz films were taken to have more information about their microstructure. Besides, for the purpose of a better understanding of the film's roughness, we also measured a silica film prepared without adding Sr^{2+} but having undergone the same thermal treatment. In the case of this amorphous film, which we will use as a reference for the topography, we found that the root mean square roughness ($\mathbf{R}_{\mathrm{ms}}$) was as low as 1.3 nm, which means that the film is highly flat.

Then, from **Figure 4.7a**, the surface of $\boldsymbol{R}_{\mathrm{Sr}}$ = 0.033 film is still homogeneous and flat because the densification cannot be initiated in this condition and porous microstructure only has a small effect on the film topography. The $\mathbf{R}_{\mathrm{ms}}$ is just 4.6 nm and the increase with respect to the reference amorphous film ($\mathbf{R}_{\mathrm{ms}}$ =1.3 nm) is mainly due to the formation of pores and crevices. This can be illustrated in detail by **Figure 4.7c**, which shows a loose surface with small pores and narrow crevices.

In contrast, $\mathbf{R}_{\mathrm{ms}}$ increases a lot, to 14.3 nm, when $\boldsymbol{R}_{\mathrm{Sr}}$ is 0.035, as displayed in **Figure 4.7b**. The dense α-quartz microstructure built by densification plays the biggest role

to increase the roughness because the dense zone is obviously lower than the porous surface, while the middle Sr-rich line, which is alike a ridge, is much higher than other parts (see **Figure 4.7d**). Besides the increased roughness, the film is less homogeneous as there are two different parts in the film with different topographies: dense structures containing Sr-rich lines and porous structures containing crevices.

To confirm that the inner part of the film (not visible from the surface) presents a porous α-quartz microstructure similar to that of the surface, we prepared a cross-section for Z-contrast STEM analysis for the film with $\boldsymbol{R}_{\mathrm{Sr}}$ = 0.033 (see **Figure 4.8**).

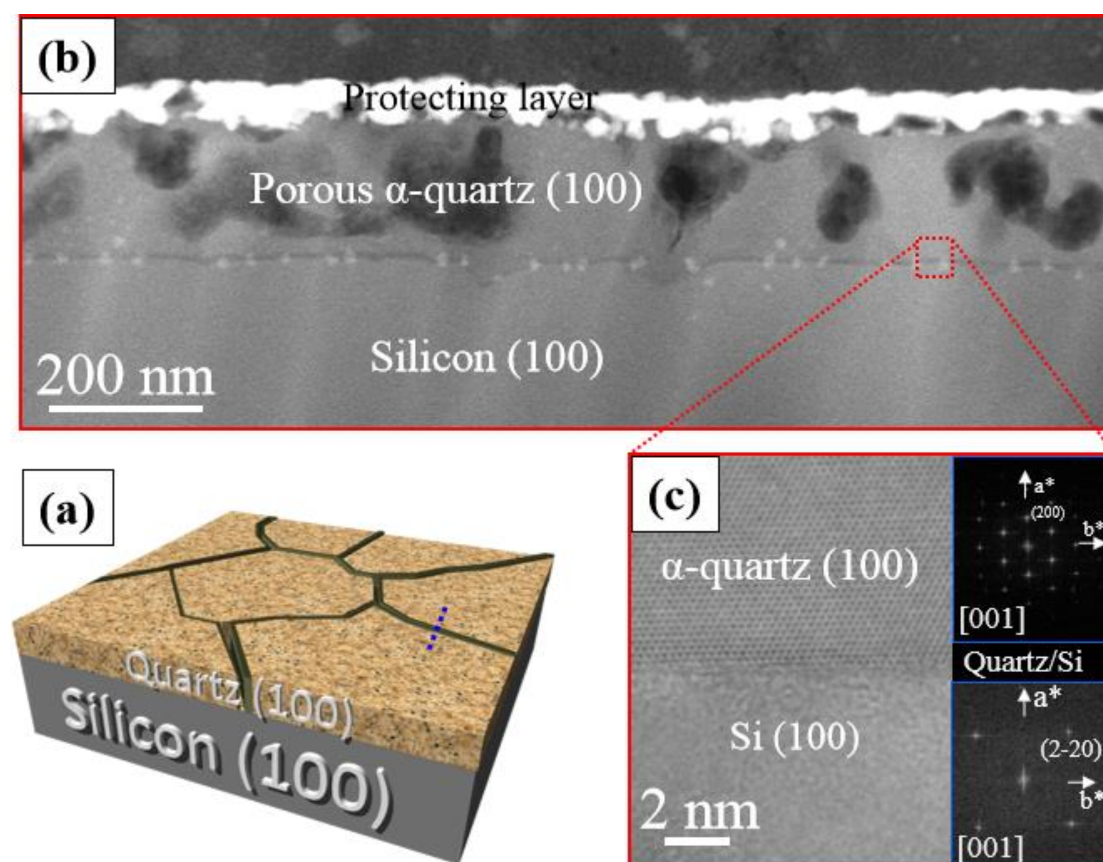

Figure 4.8. Z-contrast STEM images for a $\boldsymbol{R}_{\mathrm{Sr}}$ = 0.033 film: **(a)** is the 3D representation of porous microstructures with a blue dotted line indicating the cross-section to which the images correspond. **(b)** Low magnification cross-section image. **(c)** Atomic resolution image of the cross-section showing the interface between α-quartz (100) film and Silicon (100) substrate. The insets are the FFT patterns of film (top) and substrate (bottom), respectively.

Figure 4.8b presents a representative Z-contrast low magnification image of film cross sections of the zones indicated by blue dotted line in a 3D sketches (see **Figures 4.8a**) representing the salient characteristics of the porous films. The image shows that the inner part of the film is also porous and presents interconnected pores with diameters in the range of 50 ~100 nm. Distributed within the pores there are small whitish features of about 10 ~ 20 nm which correspond to Sr agglomerates. The

atomic resolution images of **Figure 4.8c** and the corresponding fast Fourier transform (FFT) patterns (shown in the insets) indicate that the porous microstructure is α-quartz phase with well-defined orientations. In particular, the FFT patterns in **Figure 4.8c**, which correspond to an orientation of the Si(100) substrate and α-quartz crystals along their [100] zone axes, are indicative of an epitaxial growth with Si(100)//α-quartz(100) and Si(010)//α-quartz(010), in agreement with a previous report [2].

4.1.3. Dense α-quartz films

When $\boldsymbol{R}_{Sr}$ is 0.038 or higher, the microstructures of the films become more complex. This is because the densification is more important and has a larger influence on the crystallization. Indeed, in this high $\boldsymbol{R}_{Sr}$ region, dense α-quartz microstructure becomes more dominant. Notwithstanding, the details of these dense microstructures still depend on $\boldsymbol{R}_{Sr}$.

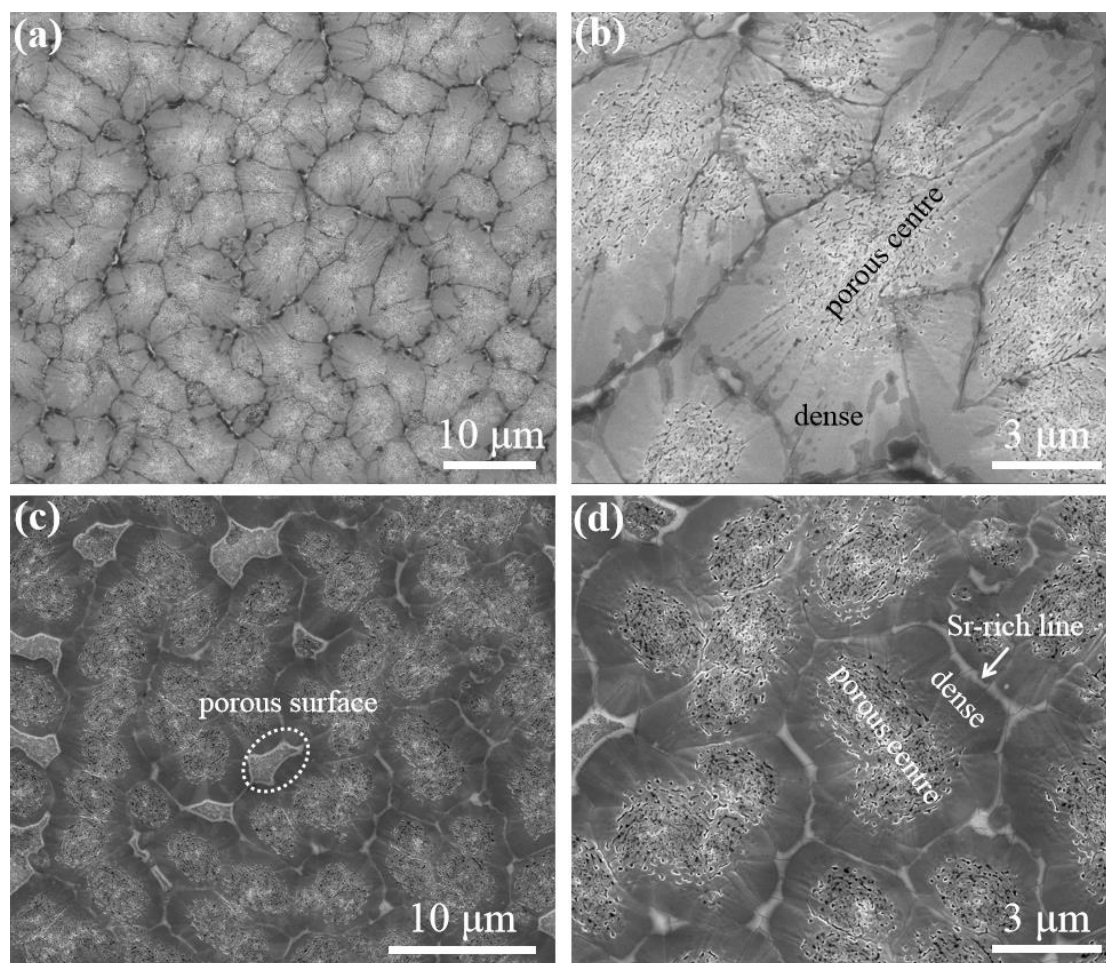

Figure 4.9. SEM images of $\boldsymbol{R}_{Sr}$ = 0.038 and 0.05 films: **(a)** and **(b)** are the SE images of $\boldsymbol{R}_{Sr}$ = 0.038 film at different magnifications. **(c)** and **(d)** are the SE images of $\boldsymbol{R}_{Sr}$ = 0.05 film at different magnifications.

For investigating these dense α-quartz microstructures, optical pictures (**Figure 4.1e ~ h**) are not effective at all for its low magnification. SEM and AFM were used to all

the four conditions corresponding to dense film region ($\boldsymbol{R}_{Sr}$ = 0.038, 0.05, 0.075 and 0.1) as main methods to describe the microstructures of films and the tendency controlled by $\boldsymbol{R}_{Sr}$.

As discussed before, a slight densification has already started when $\boldsymbol{R}_{Sr}$ = 0.035. However, once $\boldsymbol{R}_{Sr}$ increases a bit to 0.038, the microstructure undergoes a distinct change (shown in **Figure 4.9a** and **b**). The distribution of crevices is very dense, which is alike a network, and the whole film is divided into pieces by these crevices. Densification can occur more widely since Sr-rich lines reach almost everywhere via the crevice network. Despite this, still some parts of crevice network have not been filled by Sr and thus densification cannot occur in those zones. Nevertheless, the densification is important and occurs widely at this $\boldsymbol{R}_{Sr}$ condition, which makes the area coverage of dense α-quartz microstructure rise sharply to 53.3%.

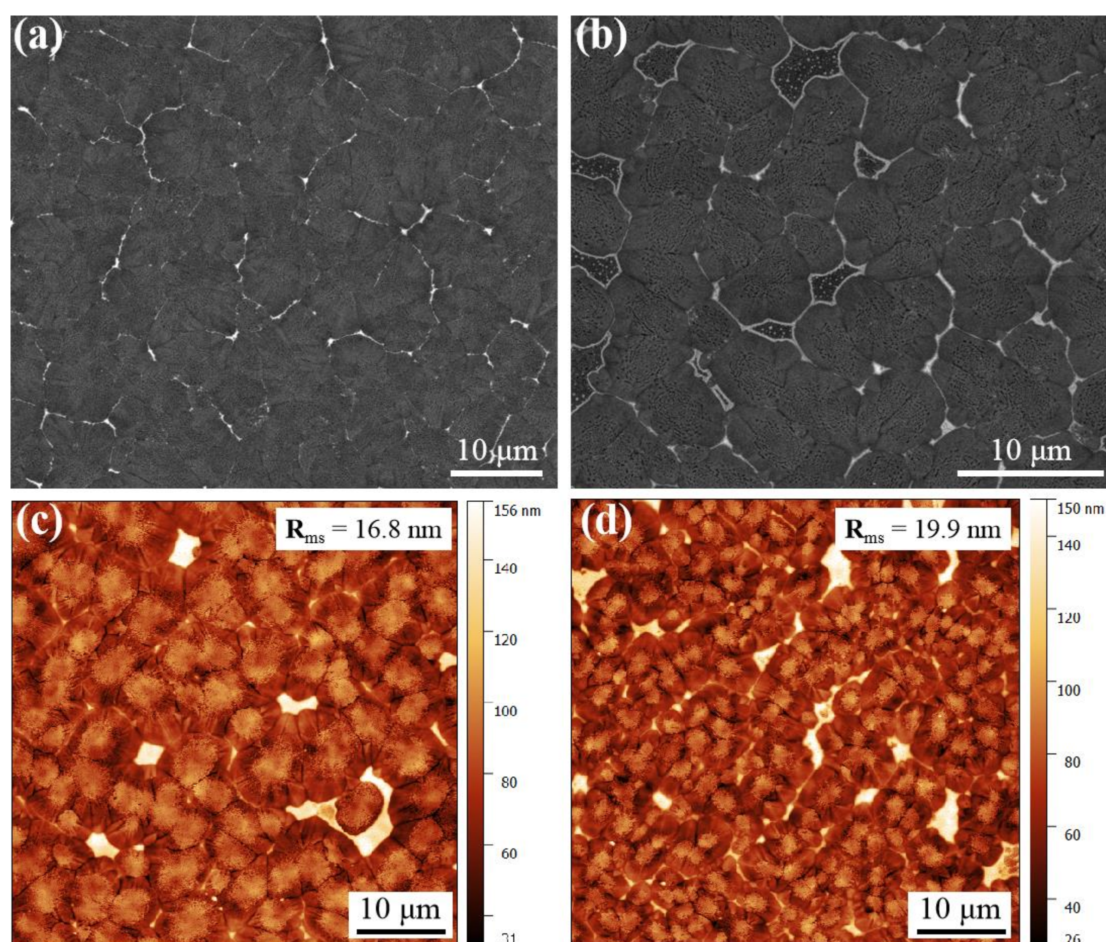

Figure 4.10. BSE images for investigating the Sr-rich line: **(a)** $\boldsymbol{R}_{Sr}$ = 0.038 film, **(b)** $\boldsymbol{R}_{Sr}$ = 0.05 film. AFM images for knowing the topography: **(c)** $\boldsymbol{R}_{Sr}$ = 0.038 film, **(d)** $\boldsymbol{R}_{Sr}$ = 0.05 film.

The Sr-rich line can be formed at almost every part of the crevice network when $\boldsymbol{R}_{Sr}$ increases to 0.05 (see **Figure 4.9c** and **d**). In this case, Sr-rich lines are longer and, in some places, thicker as can be even seen in SE mode. All the surfaces bordering Sr-

rich lines are densified, and the area coverage of dense structure increases to 63.8%.

The BSE figures (see **Figure 4.10a** and **b**), which respectively correspond to the same zone of **Figure 4.9a** and **c**, also confirm the tendency of Sr distribution. By comparing these two figures, we can confirm that the Sr-rich lines are longer and thicker for the $\boldsymbol{R}_{Sr}$ = 0.05 film because the larger amount of Sr available in this case can better fill the crevice network.

One interesting thing is that for $\boldsymbol{R}_{Sr}$ = 0.05, there are two types of porous microstructures. One is surrounded by a dense α-quartz microstructure, which is alike a porous elliptic center (as it can be observed in **Figure 4.10b** and **d**). This sort of porous center is relatively far away from Sr-rich line and not affected by densification. This porous center exists commonly in all the dense α-quartz films. The other type of porous microstructure is a small area without a regular shape (marked with a white dotted circle in **Figure 4.9c**) and surrounded by an extra thick Sr-rich line (see **Figure 4.10b**). From the AFM image of **Figure 4.10d** it is obvious that these zones are higher than nearby dense structures. The main feature of this porous area is that despite being surrounded by Sr-rich lines it has not been densified. However, outside this region, we find a dense microstructure. Thus, in this case we have a dense α-quartz structure in only one side of the Sr-rich line in contrast to what occurs for the dense crystals originating from the crevices filled with Sr, which grow at both sides of these Sr-rich lines. Hereafter we will refer to the crystallization of dense crystals at only one side of extra thick Sr-line as "one-side densification".

This one-side densification is unique and not well understood. But considering that the Sr-rich line in this part is much thicker, we can propose the following hypothesis: During the crystallization, the primary crystallization into porous α-quartz and the microstructure densification are not coincident in different places of the film. Thus, in some places, densification occurs earlier and a big amount of Sr is released from dense α-quartz crystals and aggregates into this kind of thicker line. However, the Sr inside this line cannot promote the densification in the other side (arguably because the Sr concentration is too high). Based on this hypothesis, this sort of porous area seems to be a residual area of the primary crystallization into a porous α-quartz microstructure before densification by recrystallization occurs, but enriched with Sr that has been expulsed in all the recrystallization events which have occurred around it.

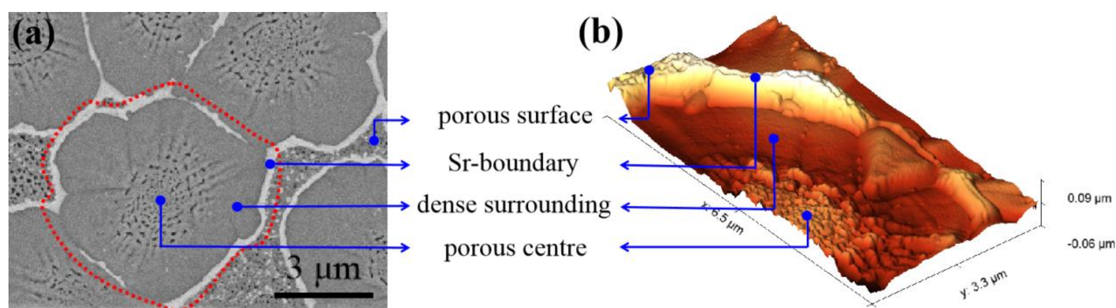

Figure 4.11. Dense crystals for a dense α-quartz film with $\boldsymbol{R}_{\mathrm{Sr}}$ = 0.05 condition: **(a)** SEM image in BSE mode, **(b)** 3-Dimensional image of a single dense crystal based on an AFM image.

After all the analysis of the specific microstructure for dense α-quartz films, it is easy to realize that the distribution of this microstructure is generally based on the crevice network which evolves into Sr-rich lines during the crystallization, and the whole film is divided into pieces. Visually, each piece can be considered as one "*unit*" of dense microstructure and named as "dense crystal". **Figure 4.11** is intending to clearly illustrate what are dense crystals. A single dense crystal (shown as the area inside red dotted circle in **Figure 4.11a**) consists of a porous center, a dense surrounding and a Sr-boundary made by Sr-rich line. The outside porous part can be considered as porous surface. Although the concept of "dense crystals" is artificial and sometimes they are difficult to be distinguished because the distribution of them is very close from one another and the shape of them is irregular, "dense crystal" still can be used to describe the microstructure of dense α-quartz films.

Back to the study of dense α-quartz microstructure, when $\boldsymbol{R}_{\mathrm{Sr}}$ is increased to 0.075, the distribution of dense α-quartz microstructure is a little less predominant (see **Figure 4.12a** and **b**). The size of dense crystal has become smaller which indicates that the crevice network becomes denser. Moreover, the fact that the area of porous surface is increased indicates that the one-side densification occurs more often. The main reason is that a larger amount of Sr can be used to build the extra thick Sr-rich line when $\boldsymbol{R}_{\mathrm{Sr}}$ is increased, which is confirmed by BSE images. In **Figure 4.13a**, extra thick Sr-line is more predominant, building more porous surface zones via one-side densification. In addition, since Sr is quite abundant for $\boldsymbol{R}_{\mathrm{Sr}}$ = 0.075, some bulk Sr-aggregating areas appear instead of Sr-rich line. All this makes the film topography more complex and the $\mathbf{R}_{\mathrm{ms}}$ increases to 24.6 nm (see **Figure 4.13c**). In spite of the presence of porous surface areas resulting from one-side densification, the area coverage of dense microstructures is slightly increased to 68.1%. This is mainly caused by the decrease of porous center area. This decrease is not unexpected because when the sizes of dense crystals are smaller, all the points inside a dense crystal are closer to the Sr-boundary which enables the densification of the center to a larger extent.

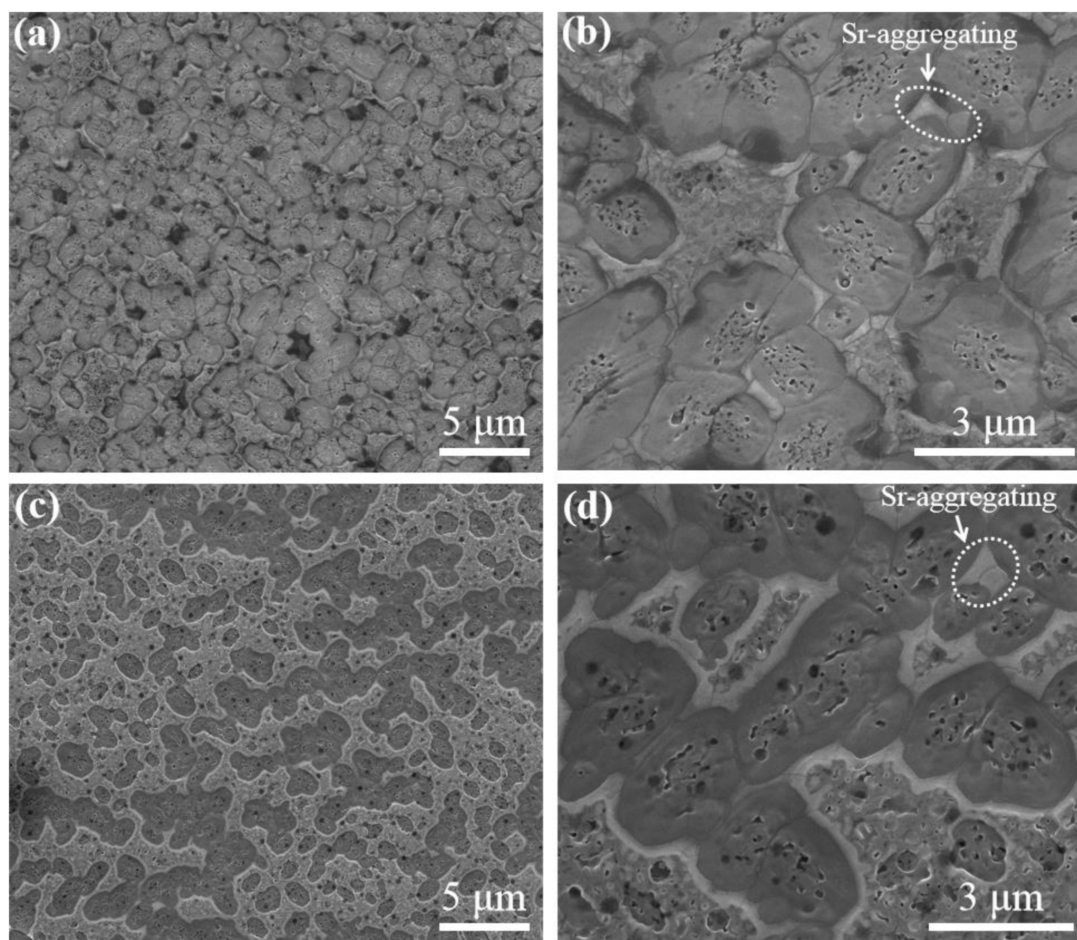

Figure 4.12. SEM images of $\boldsymbol{R}_{Sr}$ = 0.075 and 0.1 films: **(a)** and **(b)** are the SE images of $\boldsymbol{R}_{Sr}$ = 0.075 films at different magnifications. **(c)** and **(d)** are the SE images of $\boldsymbol{R}_{Sr}$ = 0.1 films at different magnifications.

When $\boldsymbol{R}_{Sr}$ reaches 0.1, which is the maximum Sr concentration studied in my PhD work, the formation of extra thick Sr-line and one-side densification are the dominant features of the film microstructure (see **Figure 4.12c**, **d** and **Figure 4.13b**). The sizes of dense crystals are even smaller and almost all the Sr-boundaries are extra thick Sr-lines, which makes the distribution of dense crystals much more isolated and sparser. However, the area coverage of dense α-quartz zones increases stably to 71.6%, which is due to the fact that the dense crystals are even more dense. However, the $\mathbf{R}_{ms}$ remains as high as 25.7 nm due to the small size of dense crystals and the increase of porous surface areas (see **Figure 4.13d**).

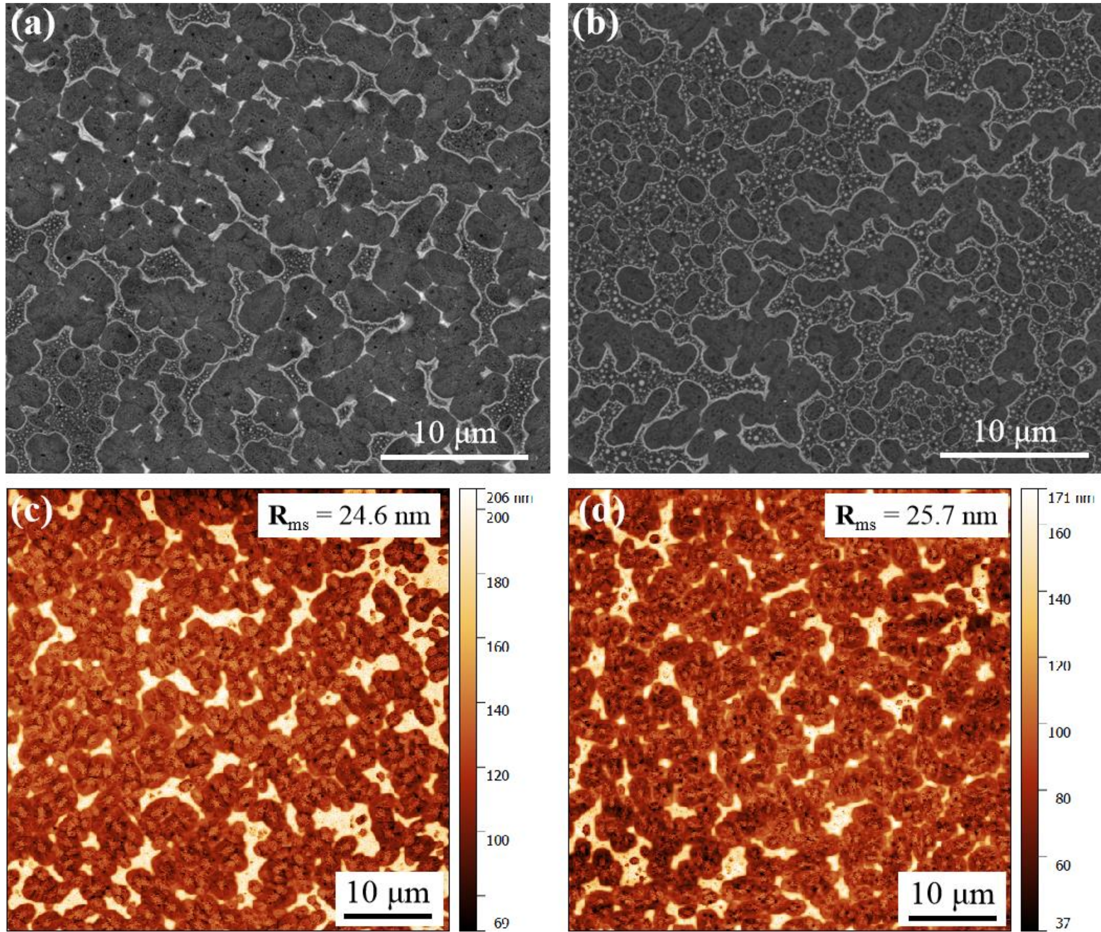

Figure 4.13. BSE images to investigate the distribution of Sr-rich line for **(a)** $\boldsymbol{R}_{\mathrm{Sr}}$ = 0.075 film, **(b)** $\boldsymbol{R}_{\mathrm{Sr}}$ = 0.1 film. AFM images displaying the topography of **(c)** $\boldsymbol{R}_{\mathrm{Sr}}$ = 0.075 film, **(d)** $\boldsymbol{R}_{\mathrm{Sr}}$ = 0.1 film.

Unlike porous films, dense α-quartz films are less homogeneous and present a more complex microstructure. To investigate the microstructure inside the films, we studied the $\boldsymbol{R}_{\mathrm{Sr}}$ = 0.05 film, which presents large and well-ordered dense crystals, by Z-contrast STEM. The studied cross section corresponds to an edge area of a dense crystal which contains porous surface, Sr-boundary and dense crystal (marked by the blue dashed line in **Figure 4.14a**). The results are displayed in **Figure 4.14**.

The left part of **Figure 4.14b** shows interconnected pores, which correspond to the same microstructure as in the previously discussed porous films without any densification ($\boldsymbol{R}_{\mathrm{Sr}}$ = 0.033 film, see **Figure 4.8b**). On the right-hand side of the image, the microstructure of α-quartz phase shifts to a thinner but flat dense microstructure. The atomic resolution images of **Figure 4.14c**, and the corresponding FFT patterns (shown in the insets) indicate that the α-quartz of dense crystals are with a well-defined orientation. In particular, the FFTs of **Figure 4.14c**, which correspond to an orientation of the Si(100) substrate and α-quartz crystals along their [100] zone axes, are indicative of an epitaxial growth with Si(100)//α-quartz(100) and Si(010)//α-quartz(010), which is same to the porous film (see **Figure 4.8c**). Then, the Sr-

boundary, which separates the dense crystal and porous surface, sits in the middle of **Figure 4.14b**. According to the Z-contrast, the Sr-boundary is an extra dense aggregate of Sr and penetrates throughout the film. This fact, could explain the mechanism of one-side densification as the thick Sr accumulation may act as a barrier specially if it becomes solid upon carbonation, as will be discussed later in **section 4.3**.

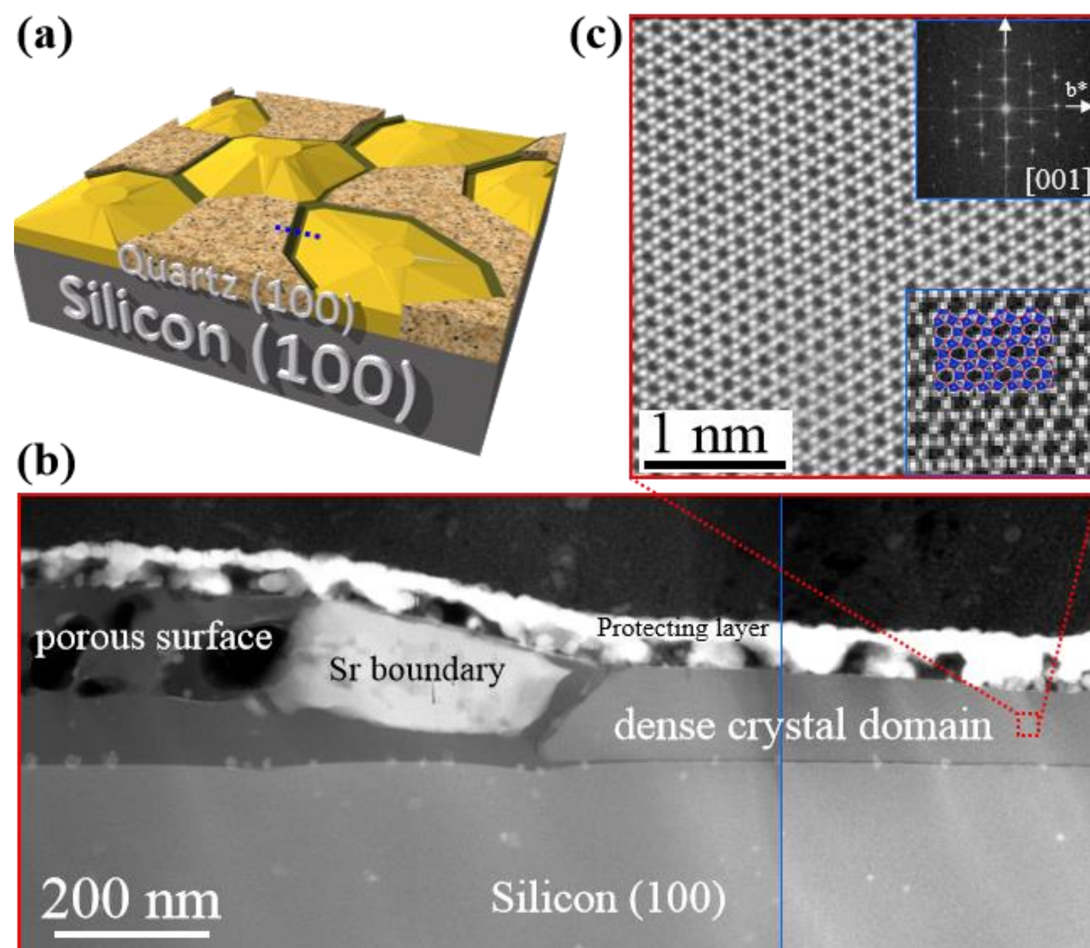

Figure 4.14. Z-contrast STEM images for $\boldsymbol{R}_{Sr}$ = 0.05 film: **(a)** is the 3D representations of dense dominating microstructures with a blue dotted line indicating the cross-section to which the images correspond. **(b)** Low magnification cross-section image. **(c)** Atomic resolution image of the of dense film cross-section. The upper inset is the FFT pattern and the lower inset a higher magnification image displaying the model structure with the Si tetrahedral in blue, surrounded by oxygens in red.

We also prepared specimens for a TEM study in planar view (see **Figure 4.15**) which confirmed, thanks to the phase contrast images, that the orientation of α-quartz phase is uniform. This can be appreciated in **Figure 4.15a**. corresponding to a dense crystal and in **Figure 4.15b** displaying a zone of both dense crystal and a porous surface. The similar contrast of both zones confirms that these correspond to the same quartz epitaxial orientations no matter the microstructure is porous or dense, and that the

densification doesn't change this.

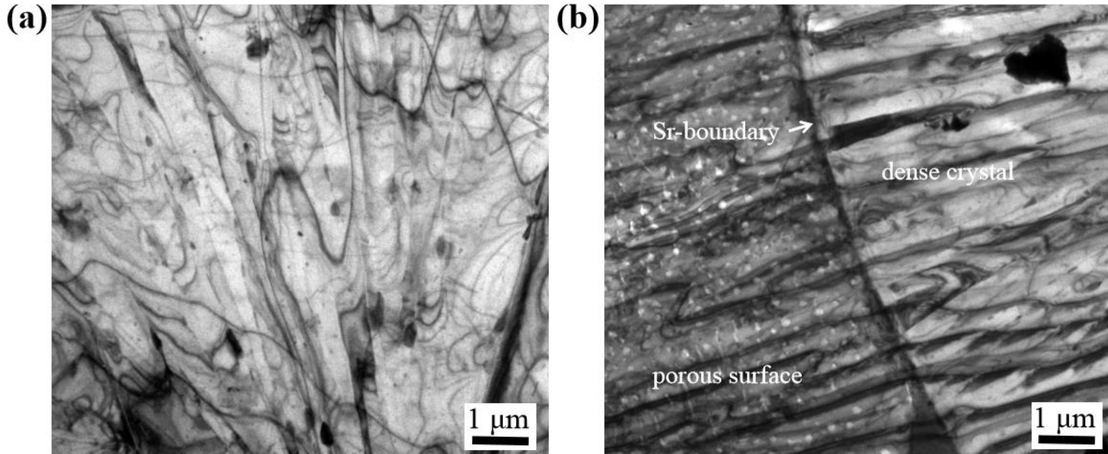

Figure 4.15. The TEM image in planar view of $\boldsymbol{R}_{Sr}$ = 0.05 film: **(a)** The image shows the signal of a dense crystal. **(b)** The image shows the same signal for both the dense microstructure inside dense crystal and porous surface.

Besides studying the TEM planar view, NaOH etching treatment is also an excellent method to show that both the porous and dense α-quartz microstructures present the same crystallinity. Thanks to the fact that dense α-quartz films are based on the crevice network, the whole film can be peeled off into pieces after NaOH etching (see the SEM images of the etched film for $\boldsymbol{R}_{Sr}$ = 0.05). The NaOH etching treatment is explained in **Section 3.5.9** of **Chapter 3** and the TEM analysis of the peeled off fragments is shown as **Figure 4.16a**. Both the porous surface and dense crystals of the film are broken into fragments. Then, the pieces of porous (porous surface fragment, **Figure 4.16b**) and dense microstructures (dense crystal, **Figure 4.16c**) can be peeled-off by using ultrasonic bath.

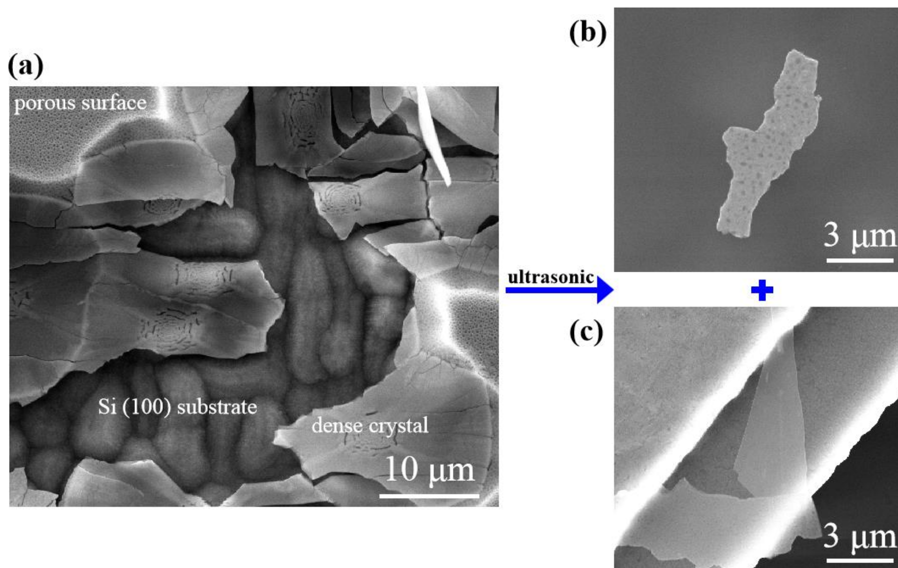

Figure 4.16. Images showing the NaOH etching treatment for $\boldsymbol{R}_{Sr}$ = 0.05 film: **(a)** SEM image of

film's surface after NaOH etching. **(b)** The TEM image of one piece of porous surface. **(c)** TEM image of fragments of a dense crystal.

The TEM images (see **Figure 4.17**) certify again that the dense α-quartz microstructure is a flat and thin piece with a shape of glass sheet. But the porous microstructure is a loose area with pores and cracks, the topography is rugged because the contrast is not homogeneous. The inset Selected Area Diffraction pattern (SAED) of the two pieces present typical patterns corresponding to the lattice planes of quartz phase ([-21-1] for dense microstructure, [-210] for porous one) indicating that both are single crystals of α-quartz phase. However, this treatment can not verify the orientation of α-quartz growth because the fragments are not fixed on the Si(100) substrate anymore and can be rotated freely. Even so, this NaOH etching analysis can still show us that the densification has an impact on the formation of α-quartz microstructures but does not affect the overall crystallinity of the films.

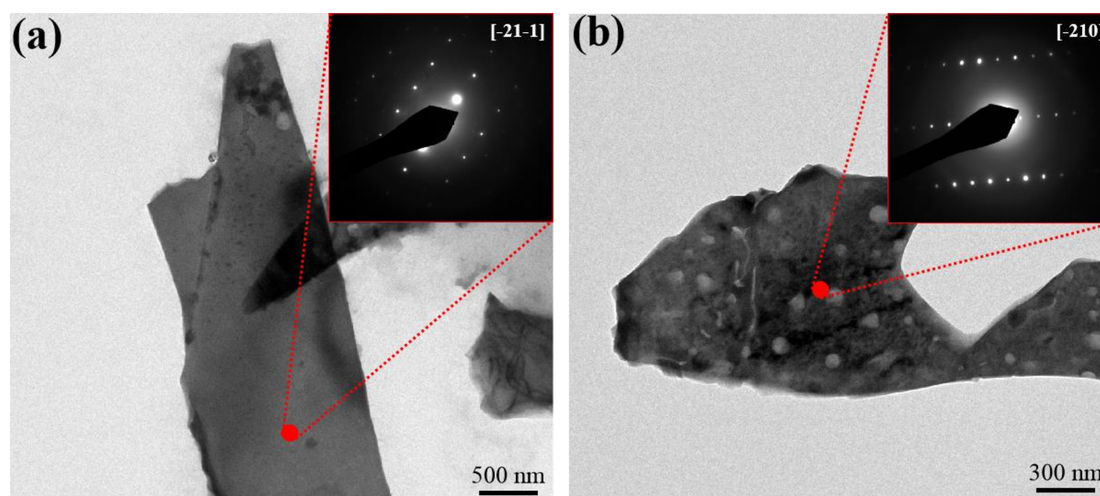

Figure 4.17. TEM analysis of fragments from $\boldsymbol{R}_{Sr} = 0.05$ film after NaOH etching: **(a)** TEM image of one fragment from the dense crystal. The inset image is the SAED pattern from the position marked as a red point. **(b)** TEM image of one fragment of porous surface. The inset image is the SAED pattern from the position marked as a red point.

4.1.4. Analysis of Sr compounds present in the films

After watching all the SEM and AFM figures which contain Sr-rich regions (Sr-rich line for porous films, Sr-boundary of dense crystal, Sr dots on the surface and so on), an important and common phenomenon is discovered: These Sr-rich regions present either irregular shapes reminiscent of a river in the Sr aggregates or the shape of droplets on the surface of porous microstructures, suggesting that Sr-rich phase had been a liquid at the annealing temperature. It makes sense because the melting point of $SrCl_2$, which is the Sr precursor used in my PhD work, is 874ºC at ambient

pressure.

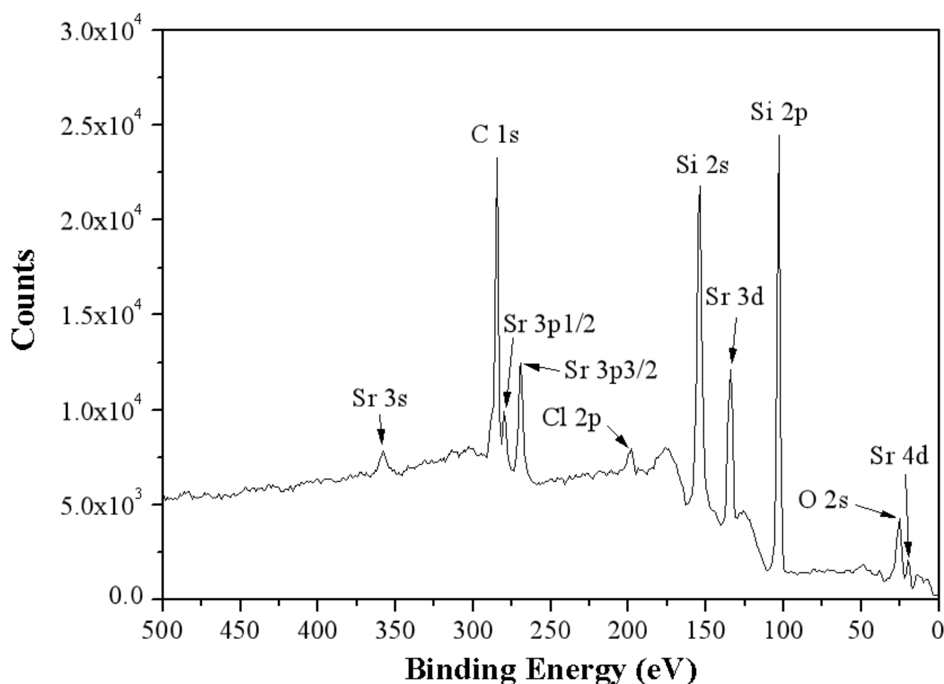

Figure 4.18. XPS overview of $\boldsymbol{R}_{Sr}$ = 0.05 film to show the presence of Sr, Cl, C, Si and O atoms.

The α-quartz films were analysed by X-ray Photoelectron Spectroscopy (XPS) to get more insight on the Sr compounds which might have been formed during and after the annealing treatment. Here, a film with $\boldsymbol{R}_{Sr}$ = 0.05 was chosen for its relatively high quantity and regular distribution of Sr. XPS overview result (see **Figure 4.18**) indicates that Sr-containing compounds are $SrCO_3$, SrO and $SrCl_2$. Interestingly, there is not a trace of Sr/Si compounds such as $SrSiO_3$, and most likely, Sr just prompts the melting of SiO_2 without any chemical reaction during annealing treatments.

For the further quantification of these three Sr components, corresponding peaks were verified and calculated by the software CasaXPS. Thinking into account the binding energies previously reported for different Sr compounds, Sr 3d multi-peak was fit considering the presence of SrO and $SrCO_3$ (**Figure 4.19a**), C 1s peak was accounted for considering the presence of $SrCO_3$ (**Figure 4.19b**), while for Cl 2p multi-peak we considered that this could correspond to $SrCl_2$ (**Figure 4.19c**) and finally the O1s peak could be assigned SrO (**Figure 4.19d**). The final composition of the the Sr-containing compounds as obtained from this XPS analysis is presented in **Table 4.2**.

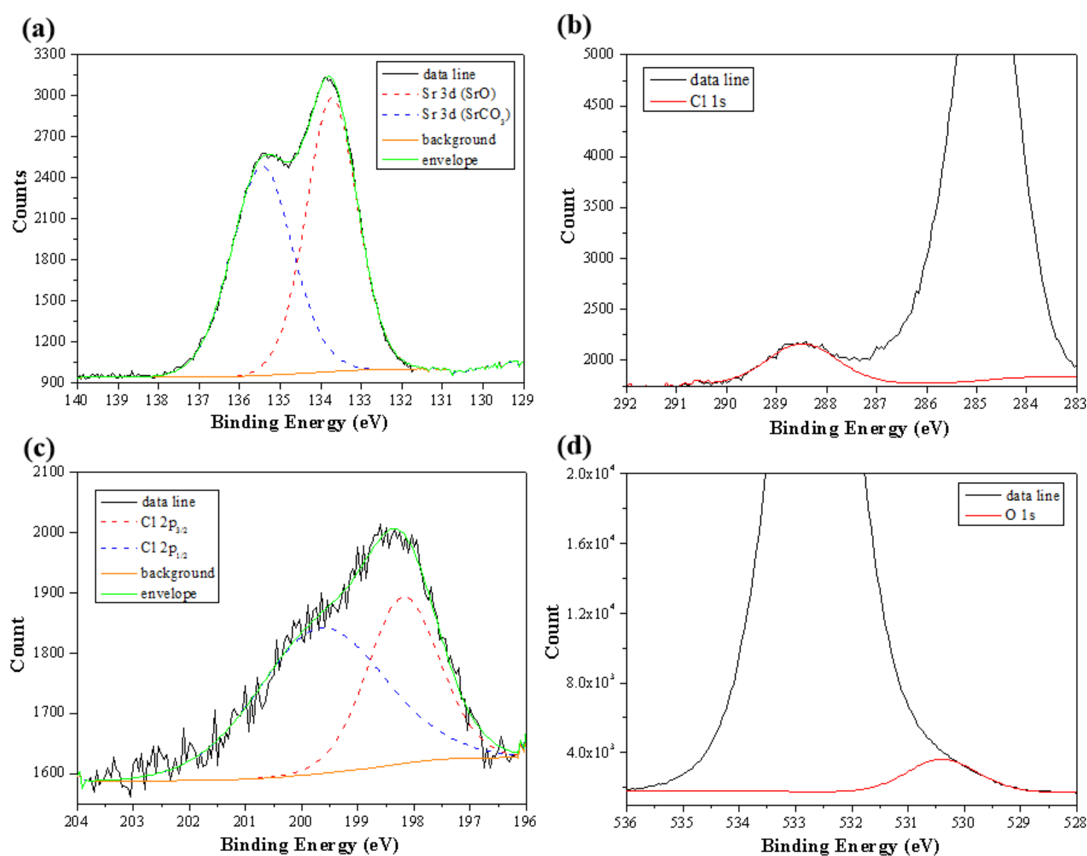

Figure 4.18. Study of the Sr compounds present in the films by XPS peak measurement: **(a)** Sr 3d multi-peak for SrO and $SrCO_3$, **(b)** C 1s peak for $SrCO_3$, **(c)** Cl 2p multi-peak for $SrCl_2$, **(d)** O 1s peak for SrO.

In **Table 4.1**, atomic concentrations (AC) of elements in different chemical situations can indicate the Molar ratio of the corresponding Sr components. According to the Sr 3d measurements for SrO and $SrCO_3$, the Molar contents of them are almost equal. However, the AC of relative C 1s (which should be equal to $SrCO_3$ one) and O 1s (which should be equal to SrO one) are higher, possibly due to other components containing these two elements, most likely related to surface contamination by organic compounds. Then, Cl 2p measurement shows that the AC of $SrCl_2$ is around 7, therefore the final Molar ratio of $SrCl_2$: SrO : $SrCO_3$ is expected to be 1: 2.5 : 2.5.

Table 4.1 The result for Sr component based on XPS peak measurement

Peak	Sr 3d (SrO)	Sr 3d ($SrCO_3$)	C 1s	Cl $2p_{1/2}$	Cl $2p_{3/2}$	O 1s
Peak Area*	565.332	518.804	648.82	177.502	273.933	1013.24
Atomic Concentration (%)	17.7	16.2	20.3	5.5	8.6	31.7

* All results are modified by relative sensitivity factor (RSF) and standard deviation (St-Dev).

In spite of being approximate, this quantification of the different Sr compounds that we expect to be present in the films tells us that the Sr compounds present in the film surface mainly consist of SrO and $SrCO_3$ instead of $SrCl_2$. Notice that the SEM images suggest that the Sr-rich phase was in liquid state during the annealing treatment at 1000ºC, but the melting points of both SrO and $SrCO_3$ are much higher (2531ºC for SrO, 1494ºC for $SrCO_3$), leaving $SrCl_2$ (melting point is 874ºC) as the sole molten Sr phase which can be present during the thermal treatment s of crystallization.

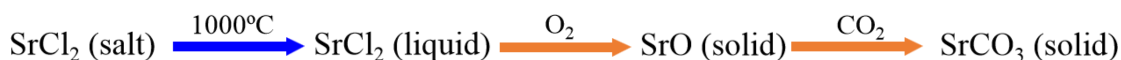

Figure 4.20. The fate Sr containing phases during the annealing treatment.

Thus, the fate of Sr inside the films during the annealing can be summarized by **Figure 4.20**: Before the film is put into furnace, Sr is present as $SrCl_2$ salt inside gel film. Once the film is at 1000ºC, $SrCl_2$ salt is already molten and plays an important role in the devitrification of amorphous SiO_2 into α-quartz. With the growth of α-quartz phase, $SrCl_2$ liquid is expulsed from the silica rich zones and is more exposed to air being more prone to undergo processes of oxidation by O_2 to form SrO or carbonation by reacting with CO_2 to form $SrCO_3$. After these reactions and the lowering of temperature, Sr is found in solid phases and fixed in the Sr aggregates we have observed by SEM. This study also can be the proof of one-side densification for high $\boldsymbol{R}_{Sr}$ films if the extra thick Sr rich lines are mainly composed of SrO and $SrCO_3$, since both of them are solid phases which cannot assist in the densification process.

4.2. Influence of $\boldsymbol{R}_{Sr}$ on film crystallinity

After determining the different microstructures of films, we have found that $\boldsymbol{R}_{Sr}$ affects the microstructures that result from the film crystallization, essentially by modifying the distribution of Sr inside film during crystallization treatment. Although it is hard to investigate the dynamics of Sr inside the film because its relative quantity is low, the impact of Sr to crystallization can still be understood by analyzing the Sr compounds and performing a dynamic study of the time dependence of film crystallization. At the same time, the mechanism of crystallization based on $\boldsymbol{R}_{Sr}$ is also estimated via these two studies.

4.2.1. Dynamic study of crystallization

In order to understand the routes of crystallization for both porous (including partly crystalline ones) and dense α-quartz films, we performed time dependent dynamic experiments with films of selected compositions presenting markedly different microstructures (**Section 3.2.3** in **Chapter 3** describes the experimental process). For porous microstructure, we made the experiments for the $\boldsymbol{R}_{Sr}$ = 0.035 film, which is the

minimum concentration which allows obtaining dense microstructures, and at the same time its crystallization is sufficiently slow to allow monitoring it by quenching films at different annealing times (see **Figure 4.21a**). On the other hand, for the dense α-quartz microstructure we chosen the $\boldsymbol{R}_{\mathrm{Sr}}$ = 0.05 film to reveal a primary crystallization of the characteristic porous microstructure. However, we found that due to its higher Sr content the densification occurs well before the porous microstructure can cover the whole film surface (see **Figure 4.21b**).

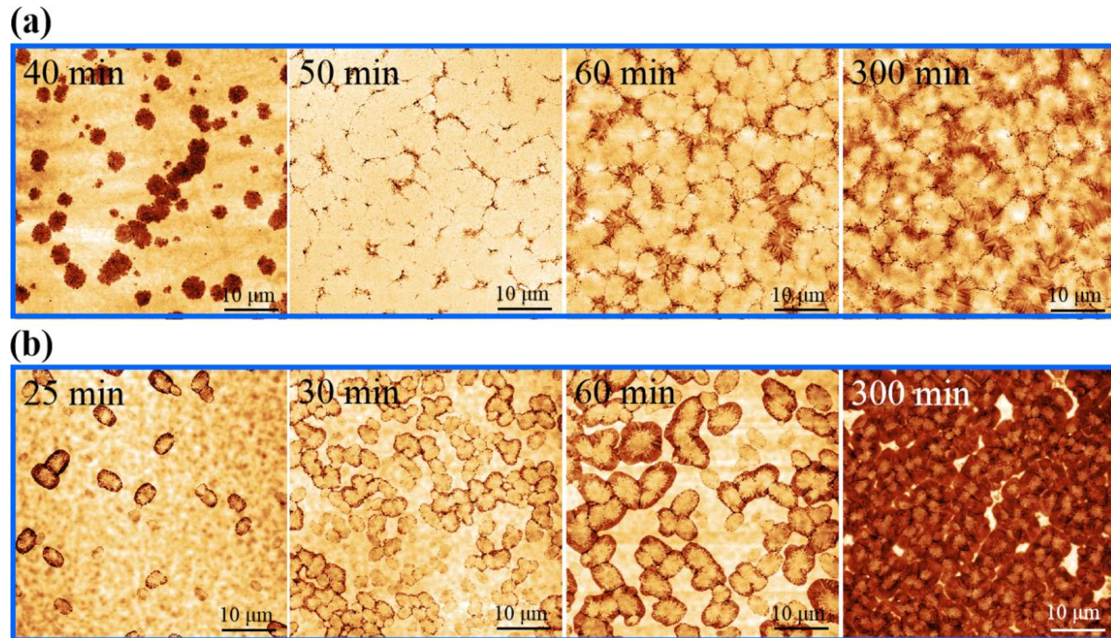

Figure 4.21. Topographic AFM images showing the influence of annealing time at 1000ºC for **(a)** porous microstructure (obtained with $\boldsymbol{R}_{\mathrm{Sr}}$ = 0.035), **(b)** dense α-quartz microstructure (obtained with $\boldsymbol{R}_{\mathrm{Sr}}$ = 0.05).

The BSE images of $\boldsymbol{R}_{\mathrm{Sr}}$ = 0.035 film quenched after annealing at 1000ºC for 40, 50 and 60 minutes are presented in **Figure 4.22**. At 40 min, some isolated or a few aggregated spots of the primary porous crystalline phase without Sr are surrounded by non-porous zones containing Sr. The image for 50 min displays a full coverage of the film surface by porous microstructure and the beginning of densification from limited portions of the dense microstructure in which Sr has accumulated. At 60 min, we can see a more advanced stage of the inward growth from larger portions of the dense zone.

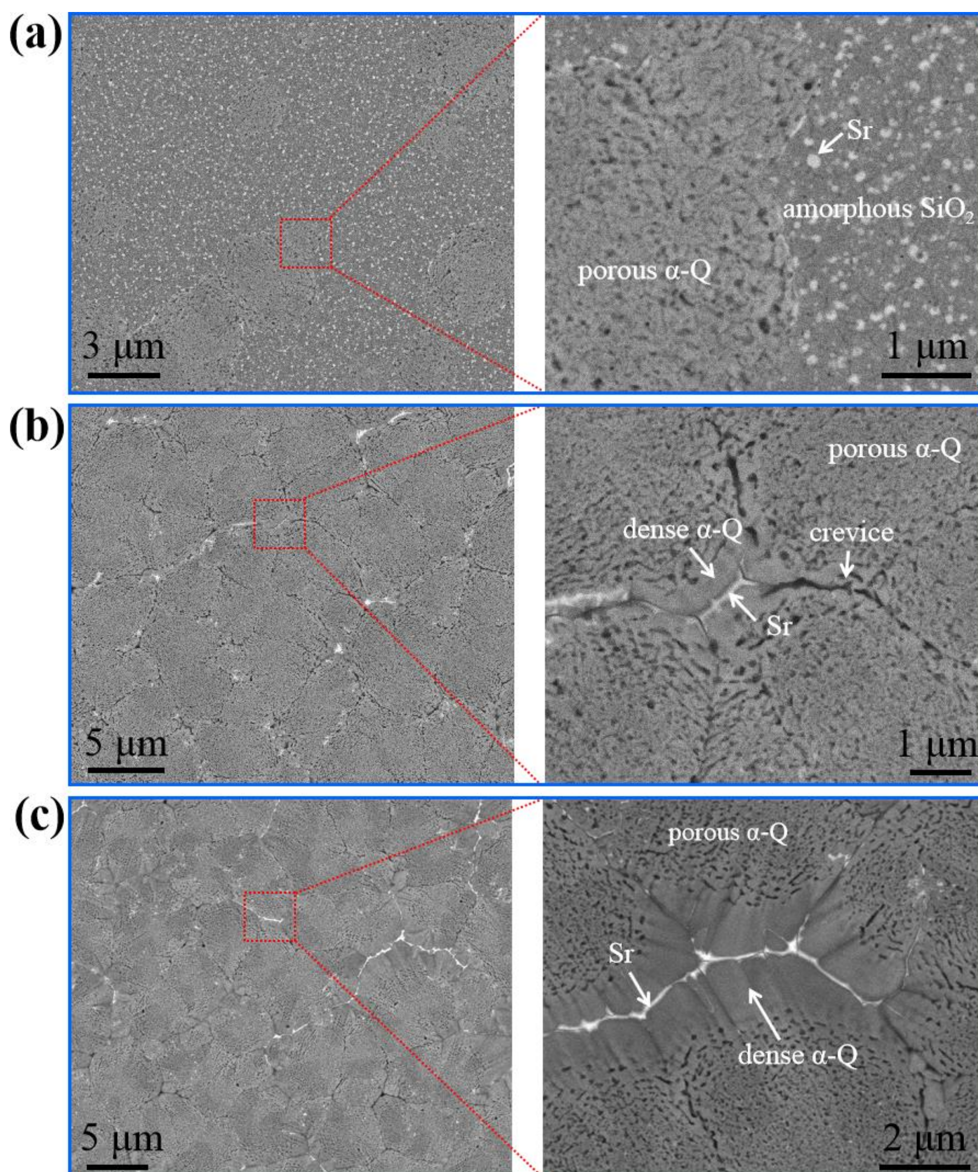

Figure 4.22. BSE images of $\boldsymbol{R}_{\mathrm{Sr}}$ = 0.035 films crystallized with different times: **(a)** 25 min. **(b)** 30 min. **(c)** 60 min.

The BSE images of the $\boldsymbol{R}_{\mathrm{Sr}}$ = 0.05 film quenched after annealing at 1000ºC for 25, 30 and 60 minutes are presented in **Figure 4.23**. In contrast to the porous film, porous crystalline spots appeared as early as at 25 min and were already surrounded by a thin Sr-rich line due to the higher content of Sr. This indicates that the Sr liquid inside the film can “flow” somewhat freely and form a Sr-rich area to begin the α-quartz transition. With the growth of porous α-quartz microstructure, Sr liquid is pushed away to form the thin Sr-rich line. The image for 30 min shows that the densification had already started with the growth of spots. This is because the Sr-rich line grows quickly by absorbing all the expelled Sr and becomes concentrated enough to make a simultaneous densification. This is the main route of one-side densification. At 60 min, the crystallization of film is very complex: we can observe some zones with

dense crystals and other zones with either porous quartz or amorphous silica which indicates that the crystallization is not homogeneous (see **Figure 4.23c**).

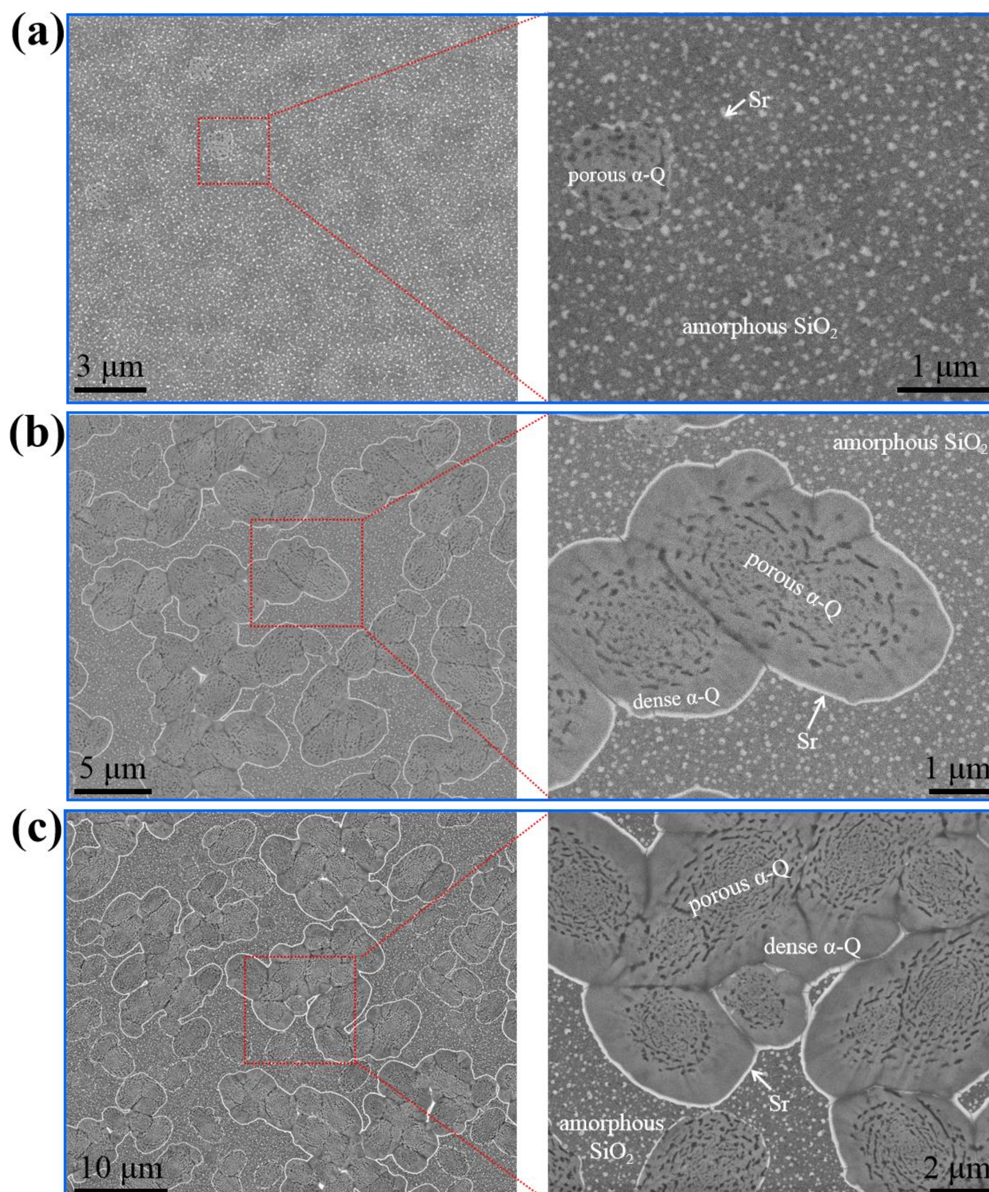

Figure 4.23. BSE images of $\boldsymbol{R}_{Sr}$ = 0.05 films crystallized with different times: **(a)** 20 min. **(b)** 30 min. **(c)** 60 min.

From the dynamic study and the XPS characterization we can conclude that the primary crystallization of α-quartz from amorphous silica is made possible by mobile Sr^{2+} ions from the Sr-rich droplets (most likely consisting of $SrCl_2$) which weaken Si-O bonds, increasing the flexibility of [SiO_4] tetrahedral units and the migration of oxygen. This mechanism has been studied thoroughly in the recrystallization of α-quartz previously amorphized by the implantation of alkaline and alkaline earth ions[3-6]. In the case of recrystallization, our observations suggest that the role of the Sr-rich liquid is akin to that of the fluxes widely used in solid state chemistry to improve

sintering or crystal growth. There are recent examples of solid-liquid crystallization by an Ostwald ripening mechanism assisted by a flux [7-10], which leads us to hypothesize that an analogous mechanism could be at play in epitaxial α-quartz films obtained from silica gels with $\boldsymbol{R}_{Sr} > 0.033$.

4.2.2. $\boldsymbol{R}_{Sr}$ dependent crystallization

After the dynamic study, we know that both the primary phase transition and densification critically depend on the content and distribution of Sr inside film, which is directly controlled by $\boldsymbol{R}_{Sr}$. However, considering that all the films are annealed for the same time (5 hours). One can consider the possibility that $\boldsymbol{R}_{Sr}$ mostly influences the crystallization rate. If this was the case, it would be possible to obtain the same crystallinity with different $\boldsymbol{R}_{Sr}$, using longer thermal treatments for lower $\boldsymbol{R}_{Sr}$. Or alternatively, for a given $\boldsymbol{R}_{Sr}$, it would be possible to achieve different crystalline fractions depending on the crystallization time.

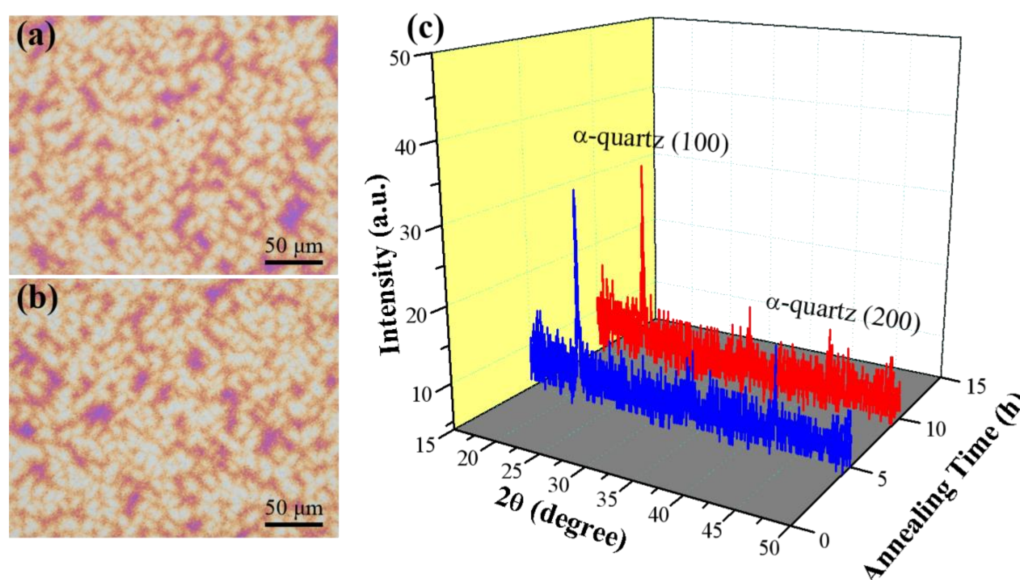

Figure 4.24. Study performed on $\boldsymbol{R}_{Sr} = 0.025$ films with different annealing times: **(a)** Optical picture of the film crystalized for 5 h. **(b)** Optical picture of the film crystalized for 10 h. **(c)** XRD results for the two films with different annealing times.

To verify this hypothesis, we investigated the influence of different crystallization times (5 h and 10 h) for a film with $\boldsymbol{R}_{Sr} = 0.025$, which makes a typical partly crystalline film. The results are shown in **Figure 4.24**. Two optical microscopy images reveal that the film is only partly crystalline even in the case of the longest annealing time (10 h). The XRD patterns of these two films confirm that the crystallinity is not improved at all. Therefore, we can conclude that the primary crystallization cannot be completed by extending the crystallization time.

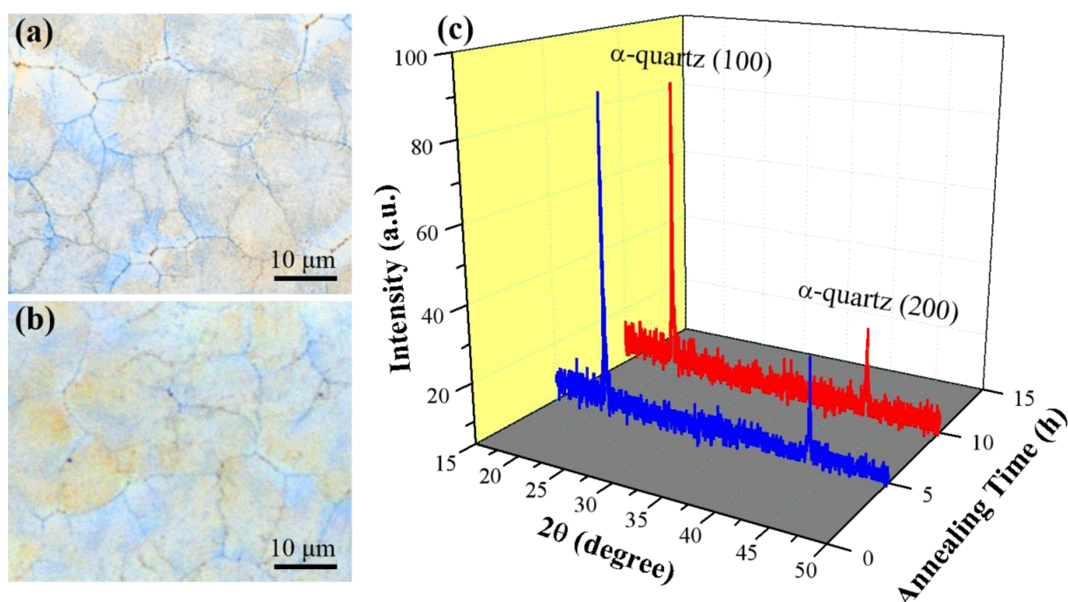

Figure 4.25. Study on $\boldsymbol{R}_{\mathrm{Sr}}$ = 0.033 films with different annealing times: **(a)** Optical picture of the film annealed for 5 h. **(b)** Optical picture of the film annealed for 10 h. **(c)** XRD results for the two films with different annealing times.

Secondly, the films with $\boldsymbol{R}_{\mathrm{Sr}}$ = 0.033 were selected to check if the densification can be improved and films turn from a porous microstructure to a characteristic dense quartz microstructure when the annealing time is doubled. However, according to the results presented in **Figure 4.25**, the surfaces of the two films present the same features and the intensity of α-quartz phase in the diffractograms is not increased, which means that performing an extended thermal treatment is useless.

These tests on the influence of the crystallization time, confirm that the process of crystallization and the resulting microstructure of the quartz epitaxial films are mostly controlled by the Sr content of the film. As a result, the parameters which can control the film crystallization should change the content of Sr inside film (for instance $\boldsymbol{R}_{\mathrm{Sr}}$).

4.3. Microstructural characteristics and properties of films controlled by $\boldsymbol{R}_{\mathrm{Sr}}$

Since the microstructure of film can be controlled by $\boldsymbol{R}_{\mathrm{Sr}}$, we have made a systematical examination of how different film microstructural aspects change with different $\boldsymbol{R}_{\mathrm{Sr}}$ region (0.02 ~ 0.1).

4.3.1. Densification & roughness

As **Section 4.1** describes, films can be generally classifyed into porous films (including the partly crystalline ones) and dense films. Therefore, the coverage of dense microstructure is a key feature to distinguish the different types of films. Considering that a dense microstructure has a different topography compared to the porous one, one can foresee that roughness will also be impacted with the content of

dense microstructures.

The area coverage of dense microstructure was measured using 50 × 50 μm AFM images of all the films with different $\boldsymbol{R}_{Sr}$, and the result is shown in **Figure 4.26a**. The brown background color corresponds to porous film region and blue one results from a dense film region. As the tendency shows, all the partly crystalline films only present porous α-quartz microstructures because the Sr content is even not enough to complete the primary α-quartz crystallization. The fully crystalline but porous films already contain a small part of dense microstructure due to the sparse aggregation of Sr in crevices. However, when $\boldsymbol{R}_{Sr}$ turns into dense film region, the area coverage by dense regions suddenly increases above 50%. Then, it can still slightly increase with $\boldsymbol{R}_{Sr}$ but never reaching 100%. The maximum is limited around 70% because the dense films always have some porous α-quartz microstructures such as the porous center of dense crystals and porous surface due to one-side densification.

The important thing is that the large change in the coverage by dense α-quartz occurs in a narrow range of $\boldsymbol{R}_{Sr}$ (0.033 ~ 0.038). This indicates that $\boldsymbol{R}_{Sr}$ control is like a "switch" because there is a threshold $\boldsymbol{R}_{Sr}$ above which it is possible to jump from one zone to the other without a transition region, just by adjusting $\boldsymbol{R}_{Sr}$. This switching control of $\boldsymbol{R}_{Sr}$ is a common way to influence other characteristics of the film which will be illustrated later.

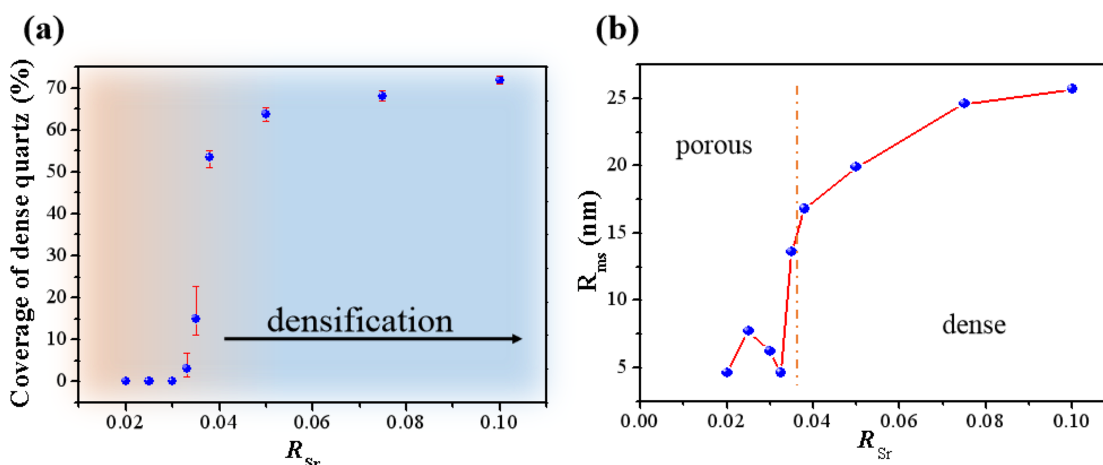

Figure 4.26. Influence of $\boldsymbol{R}_{Sr}$ on different microstructural features of the films: **(a)** area coverage by dense α-quartz microstructure, **(b)** film roughness.

Similar to the tendency of dense microstructure coverage, the root mean square roughness ($\mathbf{R}_{ms}$) of films with different $\boldsymbol{R}_{Sr}$ also displays a step-like increase. Although $\mathbf{R}_{ms}$ has already been discussed in **Section 4.1**, **Figure 4.26b** summarizes the results for all the studied films. In porous film zone (left side of the orange dash-dot line), the films present a low $\mathbf{R}_{ms}$ because the porous microstructure is less rugged. in the case of the $\boldsymbol{R}_{Sr}$ = 0.02 film, whose $\mathbf{R}_{ms}$ is closest to gel film ($\mathbf{R}_{ms}$ = 2.1 nm) its surface is almost amorphous and its roughness is close to that of a gel film. Then $\mathbf{R}_{ms}$ rises a bit

for partly crystalline films because the surface is inhomogeneous. When film has a typical porous surface, $\mathbf{R}_{ms}$ goes down to 4.6 nm which means the porous microstructure is highly flat. Then $\mathbf{R}_{ms}$ sharply increases at $\boldsymbol{R}_{Sr}$ = 0.035 due to the formation of some dense microstructure which creates a more rugged surface.

When $\boldsymbol{R}_{Sr}$ runs into the dense film region (right side of the orange dash-dot line), $\mathbf{R}_{ms}$ shifts to high values and keeps increasing steadily. The reason is that all the dense films contain a complex surface. Dense crystals are specific 3D structures which change their own sizes and distribution controlled by $\boldsymbol{R}_{Sr}$., which also can apply a bumpy topography.

4.3.2. Crystallinity & epitaxy

The crystallinity of films with different $\boldsymbol{R}_{Sr}$ can be studied by XRD θ-2θ scans and pole figure analysis. XRD θ-2θ scan plots for all the porous films were obtained as **Figure 4.27a**. Any peak of α-quartz phase is observed in the pattern of $\boldsymbol{R}_{Sr}$ = 0.02 film because the α-quartz growth is very slight. For partly crystalline films, the intensities of α-quartz peaks increase steadily until the film is fully crystalline at $\boldsymbol{R}_{Sr}$ = 0.033, which corresponds to the increase of α-quartz coverage (see **Figure 4.3**).

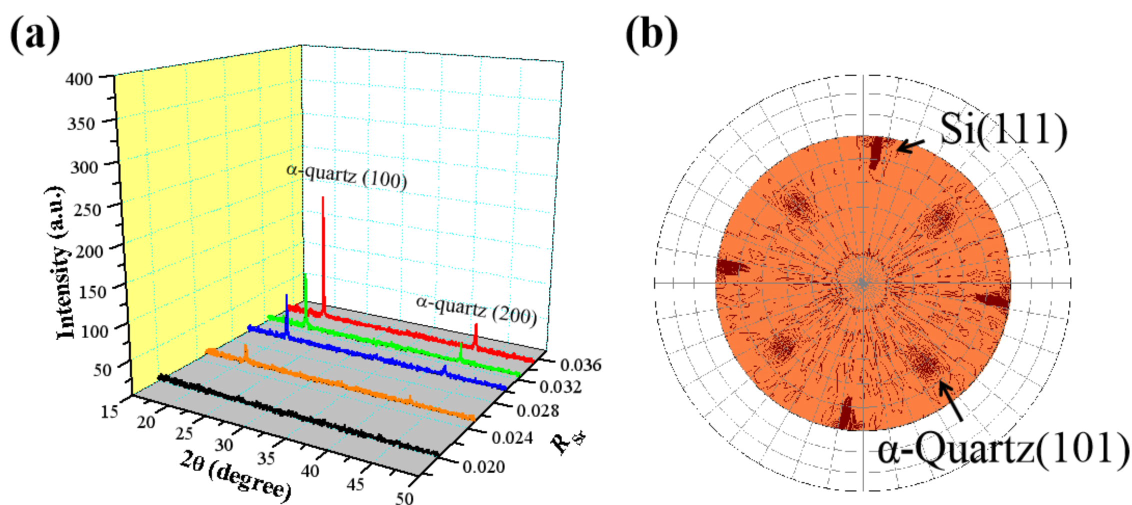

Figure 4.27. X-ray diffraction study for porous films region: **(a)** the XRD θ-2θ result of porous films, **(b)** the pole figure of $\boldsymbol{R}_{Sr}$ = 0.033 film.

The intensities for $\boldsymbol{R}_{Sr}$ = 0.035 film are obviously higher than others because the film contains a certain amount of dense α-quartz microstructure which can increases the intensity significantly. The pole figure of $\boldsymbol{R}_{Sr}$ = 0.033 film (see **Figure 4.27b**) shows the Si{111} and α-quartz{101} reflections and confirms the epitaxial relationships also obtained from the SAED result of STEM (see the inset SAED image of **Figure 4.8c**).

The XRD θ-2θ patterns for dense α-quartz films are presented in **Figure 4.28a**. Unlike

porous films, all the dense films have a stronger diffraction signal because the dense α-quartz microstructure is dominant. In these regards we can see how, as expected, the intensities of quartz peaks keep increasing with $\boldsymbol{R}_{Sr}$ because the quantity of dense α-quartz microstructure follows the same trend. But this increase levels off when $\boldsymbol{R}_{Sr}$ reaches 0.075. The pole figure of the $\boldsymbol{R}_{Sr}$ = 0.05 film (see **Figure 4.28b**) also shows the epitaxial signal of Si{111} and α-quartz {101} reflections which are also in agreement with the SAED result of STEM (see the inset SEAD images of **Figure 4.14c**).

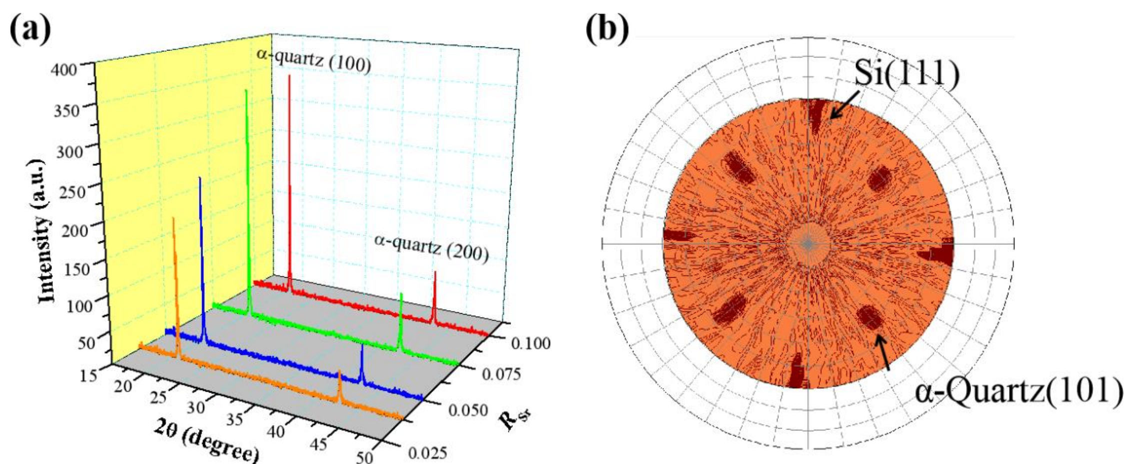

Figure 4.28. X-ray diffraction study for dense films region: **(a)** the XRD θ-2θ result of dense films, **(b)** the pole figure of $\boldsymbol{R}_{Sr}$ = 0.05 film.

To sum up all the results of XRD and pole figure, the crystallinity of films is also under the "switching" control of $\boldsymbol{R}_{Sr}$. The intensities of α-quartz peaks present a big jump when $\boldsymbol{R}_{Sr}$ shifts from porous α-quartz region to the dense one (0.033 ~ 0.038). But the films of both two regions are epitaxial.

The mosaicity of the epitaxial films with different $\boldsymbol{R}_{Sr}$ was analyzed by measuring the full widths at half maximum (FWHM) of the α-quartz(100) reflections in θ-ω measurements. The inset of **Figure 4.29** presents the θ-ω measurements of α-quartz(100) reflection (rocking curves) for films with different $\boldsymbol{R}_{Sr}$, showing how FWHMs are lowered by increasing $\boldsymbol{R}_{Sr}$. The FWHM decreases steeply when $\boldsymbol{R}_{Sr}$ rises from 0.025 to 0.035 (left side of orange dash-dot line, which corresponds to porous film region) but much more slowly and tending to level off for the dense film region (0.038 ~ 0.1, right side of orange dash-dot line).

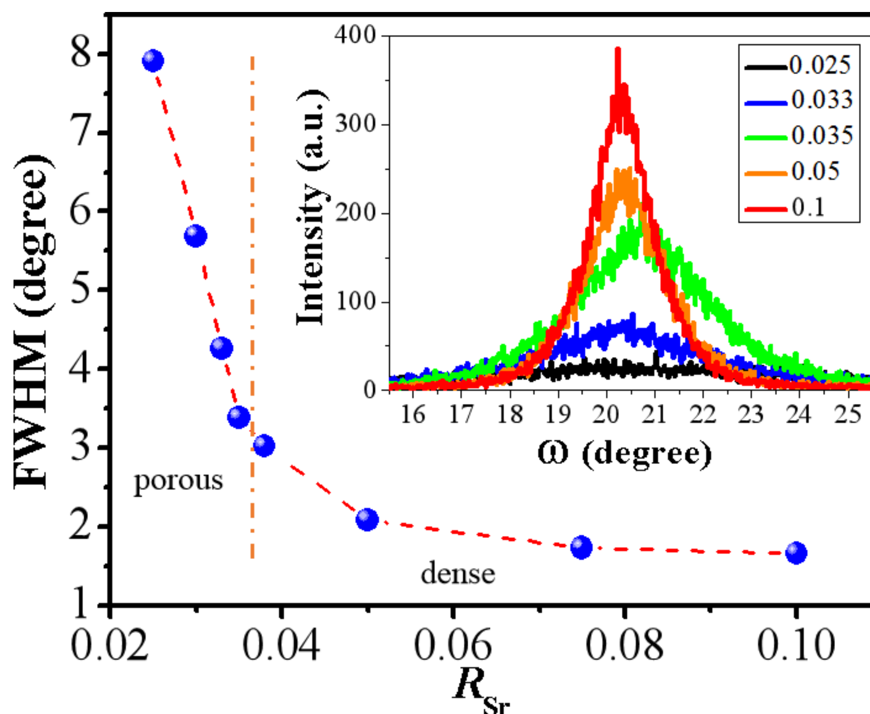

Figure 4.29. Relationship between the FWHM of rocking curves of α-quartz(100) and $\boldsymbol{R}_{\mathrm{Sr}}$. The inset image displays the rocking curves of films.

This indicates that the effect of $\boldsymbol{R}_{\mathrm{Sr}}$ on the misorientation of α-quartz crystals follows two differentiated regimes delimited by $\boldsymbol{R}_{\mathrm{Sr}}$ between 0.033 ~ 0.035. It coincides with the threshold concentration range above which dense films can be stabilized over the porous morphologies, as is evidenced in the plot of surface coverage by dense crystals vs $\boldsymbol{R}_{\mathrm{Sr}}$ (see **Figure 4.26a**).

4.3.3. DPFM test of piezoelectricity

The piezoelectric response for both porous ($\boldsymbol{R}_{\mathrm{Sr}}$ = 0.033) and dense ($\boldsymbol{R}_{\mathrm{Sr}}$ = 0.05) films were measured via a novel technique named direct piezoelectric force microscopy (DPFM) [11]. This technique is based on a conductive AFM tip which strains a piezoelectric while measuring the charge that is built-up by the mechanical stress induced to the material.

To characterize the piezoelectric response of α-quartz films we performed a step-like force function applied to the material under test (see **Figure 4.30a**): The force profile starts with a constant value, while at 1s the force is increased to a value of 380 μN in a 5 ms time step. Following this step, a constant force is re-settled for an additional 1s, while at 2 s, an unloading ramp is performed, reducing the applied force. While force is varied, the current channel is recorded simultaneously; current is depicted in green squares in **Figure 4.30a**.

Due to the piezoelectric effect, a constant force builds up a constant charge, hence the

recorded current remains zero. However, when the force is varied, through a loading or unloading event, there is an increase or decrease of the charge build up, whereas a constant current can be seen at a constant force rate applied (see **Figure 4.30b**). The system current is calibrated using a known resistance, while the force applied is calibrated using standard procedures available for AFM. To increase homogeneity, the results of our experiments are depicted by averaging 10 curves obtained in 10 different randomized spots of the sample (see **Figure 4.30c**).

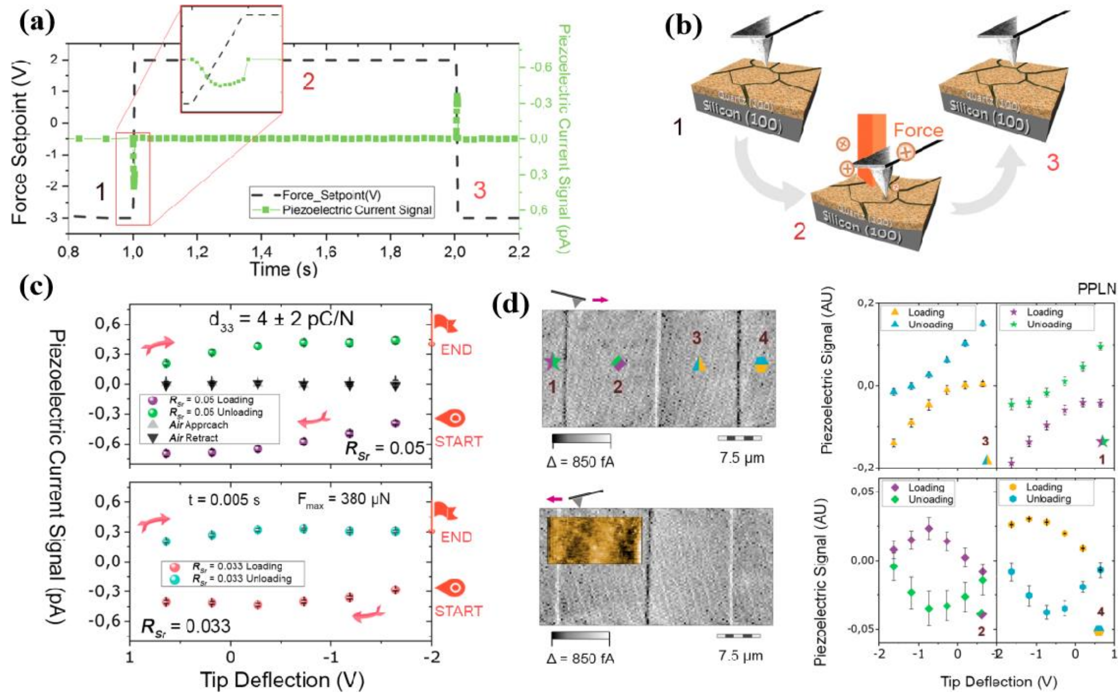

Figure 4.30. Force and piezoelectric current vs Time (s) for different applied forces for $\boldsymbol{R}_{\mathrm{Sr}}$ = 0.033 and 0.05 films respectively. **(a)** The current peaks are seen when DPFM-Si and DPFM-So of a Periodically Poled Lithium Niobate (PPLN) showing the ferroelectric domain configuration of the test sample that is used as a reference for calibration. **(b)** Scheme of the spectroscopy experiments carried out in which the AFM tip applies a suitable force, within a given time, collecting the charges generated by the direct piezoelectric effect. **(c)** Curves performed in α-quartz films with $\boldsymbol{R}_{\mathrm{Sr}}$ = 0.05 and 0.033 showing its piezoelectric response. The graphs were obtained by averaging 4x4 matrix volume spectroscopy experiments in an area of 10 microns, in order to depict the homogeneity of the sample. **(d)** Results of the spectroscopy experiments obtained in four different locations on the PPLN tests sample, indicated by the numbers 1 to 4 and the corresponding spots where the curves were recorded.

We were able to obtain the d_{33} value of the material by simply dividing the collected current, in pC/s units, by the force rate applied (0.078 N/s), obtaining the piezoelectric constant in pC/N. Independently of the $\boldsymbol{R}_{\mathrm{Sr}}$ value, a similar piezoelectric response is measured for crystallized films. As a negative test, we repeated the movement of the Z-piezo of the AFM (see black-and-grey triangles of **Figure 4.30c**), obtaining a zero-current response. We performed another test experiment in a ferroelectric Periodically

Poled Lithium Niobate (PPLN) sample of known piezoelectric coefficient as a reference (see **Figure 4.30d**). For obtaining the location of ferroelectric domains, DPFM-Si (Signal Input) and DPFM-So (Signal Output) scans are recorded, revealing the expected antiparallel domain configuration. A similar force ramp consisting of loading and unloading the sample surface with the AFM tip is repeated in each of the domains position (see **Figure 4.30d** in which the numbers are correlated with right panel graphs). It is seen that the current reverses depending on which domain polarization direction is mechanically stressed. Such behavior is expected for a ferroelectric known sample, leading us to conclude that the recorded current signal arises from the piezoelectric property inherent to our films. From these measurements we obtained a d_{33} of 4 ± 2 pC/N in agreement with the piezoelectric coefficient of α-quartz obtained via other relative works [12].

4.4. Chapter conclusion

In this chapter, the crystallization mechanism and the role of thedevitrifying agent (Sr) is investigated by controlling $\boldsymbol{R}_{Sr}$. It has been found that $\boldsymbol{R}_{Sr}$ needs to be higher than 0.02 in order to trigger the crystallization but cannot be larger than 0.1 due to the low solubility of corresponding $SrCl_2$ salt inside gel film.

For Sr-induced crystallization, we have found evidences indicating that that Sr performs its function of devitrifying agent in liquid phase which indicates that Sr would “flow” within the film during the devitrification. During crystallization, the control of $\boldsymbol{R}_{Sr}$ is embodied in two aspects. The first one is a primary crystallization of amorphous silica into α-quartz which results in a porous microstructure because α-quartz phase is denser than amorphous silica. The second is a recrystallization process consisting of a densification of the primary porous α-quartz to give a microstructure characterized by dense crystals. However, unlike the primary α-quartz crystallization, the densification only occurs in zones with high concentrations of Sr, which in turn are only found in films with high $\boldsymbol{R}_{Sr}$.

It can be stated that the crystallization of α-quartz films can be controlled by $\boldsymbol{R}_{Sr}$ for which a clear threshold allows switching between two contrasting microstructures: a porous and low roughness highly homogeneous microstructure and a rougher and more complex microstructure characterized by the presence of dense crystals and some porous zones. The films prepared with $\boldsymbol{R}_{Sr} < 0.033$ are partly crystalline for porous α-quartz microstructure because the Sr content is not enough to complete the α-quartz phase transition. The films with $\boldsymbol{R}_{Sr} = 0.033$ and 0.035 show a typical fully crystalline porous microstructure because the Sr is effective everywhere on the film. The films fabricated with $\boldsymbol{R}_{Sr} = 0.038$ or higher present a microstructure dominated by dense α-quartz because the quantity of Sr allows a significant and active densification. In this region, the Sr aggregates either create spots or fill the crevices network, with

the primary crystallization and densification by recrystallization occurring simultaneously in different zones of the film. This contributes to the complexity and inhomogeneity of these films. Visually, the surface of films consists of elliptical dense crystal domains and porous surfaces.

Accompanying the switching control of $\boldsymbol{R}_{Sr}$ the microstructural characteristics of the films also present step-like changes. The crystallinity of films can be improved when $\boldsymbol{R}_{Sr}$ goes into dense region for dense microstructure, presenting a better response for X-ray diffraction analysis. Simultaneously, the mosaicity of α-quartz phase decreases upon densification and recrystallization, but the roughness increases substantially. Nevertheless, the film is always epitaxial and piezoelectric no matter which microstructure it presents.

To sum up all the results in this chapter, it is clear that the quantity and state of Sr inside film is crucial to determine the microstructure of the films, to be either porous and with low roughness or rougher and more dominated by the presence of dense α-quartz domains.

4.5. Chapter references

1. Ndayishimiye, A.; Largeteau, A.; Prakasam, M.; Pechev, S.; Dourges, M.-A.; Goglio, G., Low temperature hydrothermal sintering process for the quasi -complete densification of nanometric α-quartz. *Scripta Materialia* **2018,** *145*, 118-121.

2. Buchner, C.; Lichtenstein, L.; Yu, X.; Boscoboinik, J. A.; Yang, B.; Kaden, W. E.; Heyde, M.; Shaikhutdinov, S. K.; Wlodarczyk, R.; Sierka, M.; Sauer, J.; Freund, H. J., Ultrathin silica films: the atomic structure of two-dimensional crystals and glasses. *Chemistry* **2014,** *20* (30), 9176-83.

3. Gomez, A.; Gich, M.; Carretero-Genevrier, A.; Puig, T.; Obradors, X., Piezo-generated charge mapping revealed through direct piezoelectric force microscopy. *Nat Commun* **2017,** *8* (1), 1113.

4. Necas, D.; Klapetek, P., Gwyddion: an open-source software for SPM data analysis. *Central European Journal of Physics* **2012,** *10* (1), 181-188.

5. Gustafsson, M.; Roccaforte, F.; Keinonen, J.; Bolse, W.; Ziegeler, L.; Lieb, K. P., Oxygen-activated epitaxial recrystallization of Li-implanted alpha-SiO_2. *Physical Review B* **2000,** *61* (5), 3327-3332.

6. Gąsiorek, S.; Dhar, S.; Lieb, K. P.; Schaaf, P., Laser-induced epitaxial recrystallization after alkali-ion implantion into α-quartz. *Applied Surface Science* **2005,** *247* (1-4), 396-400.

7. Dhar, S.; Sahoo, P. K.; Gąsiorek, S.; Vetter, U.; Kulkarni, V. N.; Lieb, K. P., Cathodoluminescence and solid phase epitaxy in Ba-irradiated α-quartz. *Journal of Applied Physics* **2005,** *97* (1).

8. Keinonen, J.; Gąsiorek, S.; Sahoo, P. K.; Dhar, S.; Lieb, K. P., Light-emitting defects and epitaxy in alkali-ion-implanted α-quartz. *Applied Physics Letters* **2006,** *88* (26), 261102.

9. Hayashi, S.; Sugai, M.; Nakagawa, Z.; Takei, T.; Kawasaki, K.; Katsuyama, T.; Yasumori, A.; Okada, K., Preparation of $CaSiO_3$ whiskers from alkali halide fluxes. *Journal of the European Ceramic Society* **2000,** *20* (8), 1099-1103.

10. Tas, A. C., Molten salt synthesis of calcium hydroxyapatite whiskers. *Journal of the American Ceramic Society* **2001,** *84* (2), 295-300.

11. Gomez, A.; Gich, M.; Carretero-Genevrier, A.; Puig, T.; Obradors, X., Piezo-generated charge mapping revealed through direct piezoelectric force microscopy. *Nat Commun* **2017,** *8* (1), 1113.

12. Newnham, R. E., *Properties of Materials: Anisotropy, Symmetry, Structure*. Oxford U. Press: New York 2005.

Chapter 5. Microstructural Control of Film During Synthesis

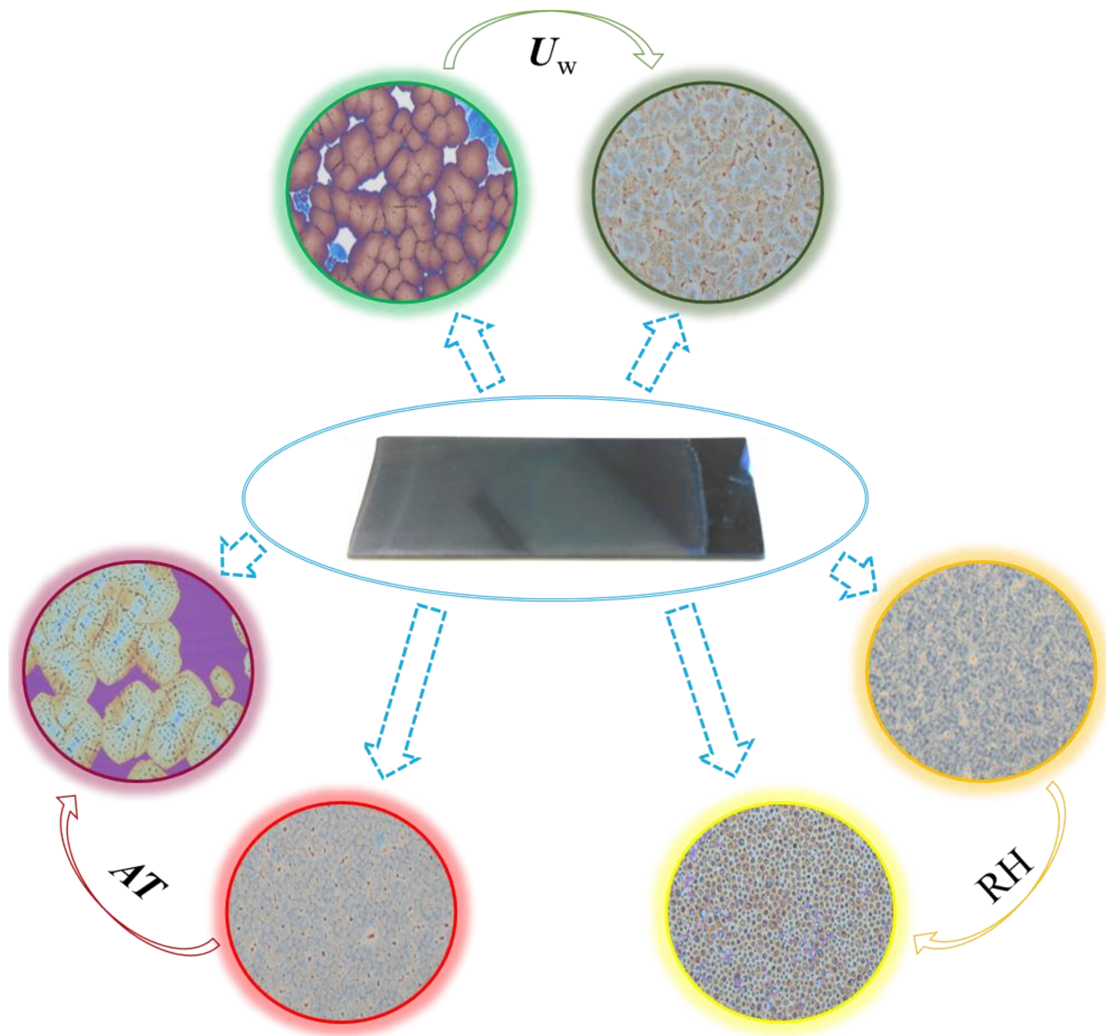

Chapter 5

As we have seen in the previous chapter, the content and distribution of Sr inside the gel films plays a central role to control the microstructure of epitaxial quartz films. This can be achieved by adjusting the content of Sr inside the films through $\boldsymbol{R}_{Sr}$. However, the whole synthesis is a three-step process consisting of sol preparation, film deposition and annealing, and there are other important parameters which can influence the distribution of Sr inside gel film. Therefore, controlling thefilm crystallization requires simultaneously managing several synthesis conditions in each step.

In this chapter, several parameters considered to be relevant at different stages of the α-quartz film preparation were investigated systematically. Thereby, the studies of these parameters can provide important clues to achieve a comprehensive control of the microstructure of as-prepared film.

5.1. Thickness of gel films

The thickness of gel films ($\boldsymbol{T}_{gel}$), defined as the thickness of the film just before annealing treatment but after consolidation, was taken into account firstly for it is the main way to change the content of Sr inside film once the $\boldsymbol{R}_{Sr}$ is fixed. $\boldsymbol{T}_{gel}$ is regulated by controlling withdrawal rate ($\boldsymbol{U}_{w}$) during dip-coating operation. As many relative studies have previously reported [1-3], also in this work the relationship between $\boldsymbol{T}_{gel}$ and $\boldsymbol{U}_{w}$ can be described by the so-called “Landau-Levich Model” [4].

The general principle of this model is that the film thickness is affected by two different $\boldsymbol{U}_{w}$ regimes. When $\boldsymbol{U}_{w}$ is low enough, the thickness of film decreases when $\boldsymbol{U}_{w}$ increases and this is called the capillarity regime because the capillary force dominates the fluid behavior. However, when $\boldsymbol{U}_{w}$ is as high enough, the film thickness increases with $\boldsymbol{U}_{w}$ and the system is in the so-called draining regime because the fluid behavior results from the balance between the entraining forces (depending on viscosity and $\boldsymbol{U}_{w}$) and the draining forces (depending on gravity and fluid density). In both of these two cases, the dependencies of the gel thickness on $\boldsymbol{U}_{w}$ are linear in a *log-log* coordinate system. Between these two $\boldsymbol{U}_{w}$ regimes, there is a mixed regime where the thickness is impacted by both capillarity and draining effects. Since $\boldsymbol{U}_{w}$ has opposite effects on the film thickness for the capillary and draining regimes, a minimum is expected in the mixed regime.

Based on the Landau-Levich Model, the films with different $\boldsymbol{T}_{gel}$ can be achieved via controlling $\boldsymbol{U}_{w}$ during dip-coating. All the other conditions were fixed to the most suitable values to promote crystallization. Particularly, $\boldsymbol{R}_{Sr}$ was fixed to 0.05 for the measurement of $\boldsymbol{T}_{gel}$ because $\boldsymbol{R}_{Sr}$ does not affect the $\boldsymbol{U}_{w}$-$\boldsymbol{T}_{gel}$ dependence. The experimental operation is described in **Section 3.2.2** of **Chapter 3**.

5.1.1. The relationship between $\boldsymbol{T}_{gel}$ and $\boldsymbol{U}_{w}$

In my work, the gel films with different $\boldsymbol{T}_{\mathrm{gel}}$ were fabricated at 8 different $\boldsymbol{U}_{\mathrm{w}}$ values, from 1.0 to 15.0 mm/s, and $\boldsymbol{T}_{\mathrm{gel}}$ of the resulting films were measured by SEM cross-section images after the film consolidation. The final relationship between $\boldsymbol{T}_{\mathrm{gel}}$ and $\boldsymbol{U}_{\mathrm{w}}$ is plotted in **Figure 5.1**.

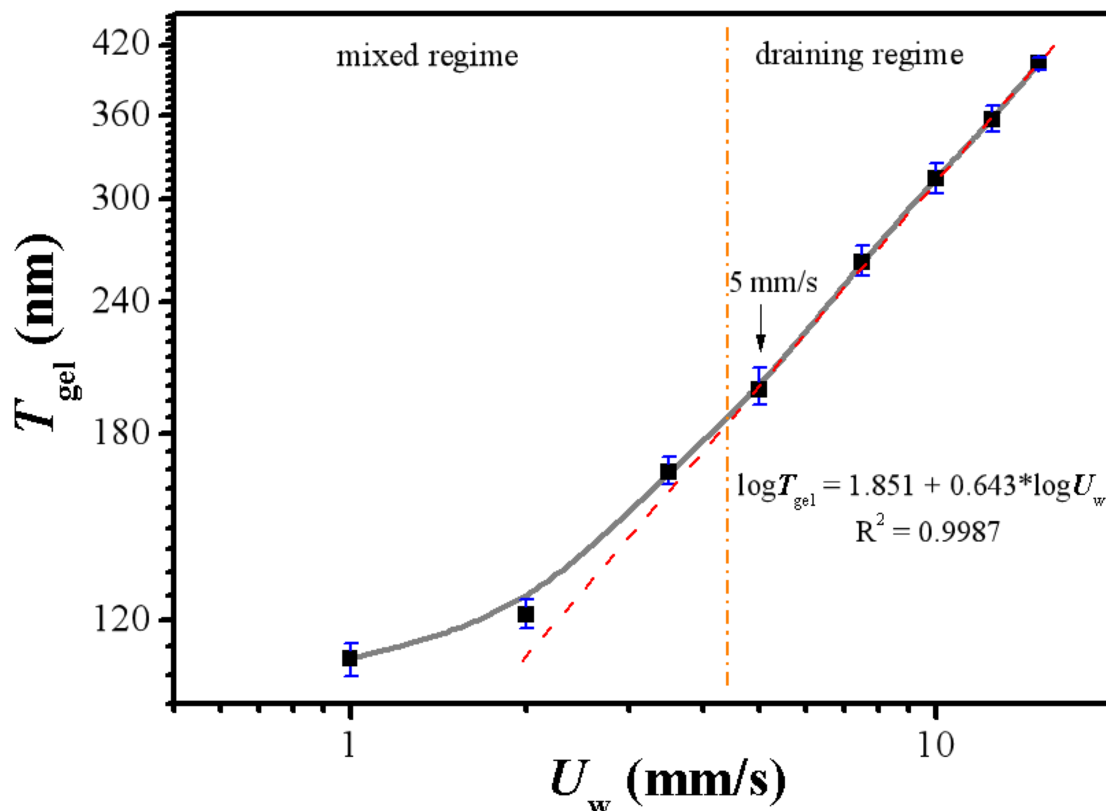

Figure 5.1. The relationship between $\boldsymbol{T}_{\mathrm{gel}}$ and $\boldsymbol{U}_{\mathrm{w}}$ as obtained by measuring the SEM cross-section images for gel films with $\boldsymbol{R}_{\mathrm{Sr}}$ = 0.05. The inset function is a fit (red dashed line) of the last five points in the figure considering the draining regime model.

The $\boldsymbol{T}_{\mathrm{gel}}$ dependence on $\boldsymbol{U}_{\mathrm{w}}$ is in agreement with the Landau-Levich Model and $\boldsymbol{T}_{\mathrm{gel}}$ is dominated by draining effect because $\boldsymbol{T}_{\mathrm{gel}}$ keeps increasing with $\boldsymbol{U}_{\mathrm{w}}$. In **Figure 5.1**, the three left-most points ($\boldsymbol{U}_{\mathrm{w}}$ = 1, 2 and 3.5 mm/s, the left side of the orange dashed dot line) belong to the mixed regime, which means that $\boldsymbol{T}_{\mathrm{gel}}$ in this regime is influenced simultaneously by draining and capillarity effects. According to the tendency, $\boldsymbol{U}_{\mathrm{w}}$ = 1 mm/s can be considered as the minimum in my work and the corresponding $\boldsymbol{T}_{\mathrm{gel}}$ value is 110 nm. For $\boldsymbol{U}_{\mathrm{w}}$ between 5 mm/s and 15 mm/s, the system is in the draining regime (the right side of the orange dash-dot line) which means that $\boldsymbol{T}_{\mathrm{gel}}$ is only determined by draining effects. The experimental fitting of the draining model line (which is the red dashed line) based on the five points of draining regime is in agreement with the model, in which $\boldsymbol{T}_{\mathrm{gel}}$ and $(\boldsymbol{U}_{\mathrm{w}})^{2/3}$ are in direct proportion. Hence, the maximum of this series appears at $\boldsymbol{U}_{\mathrm{w}}$ = 15 mm/s, which gives a $\boldsymbol{T}_{\mathrm{gel}}$ of 404 nm. To sum up these measurements, in this chapter, $\boldsymbol{T}_{\mathrm{gel}}$ can be changed from 100 nm to 400 nm by controlling $\boldsymbol{U}_{\mathrm{w}}$ between 1.0 and 15.0 mm/s, and the relationship

between them fits the Landau-Levich Model very well.

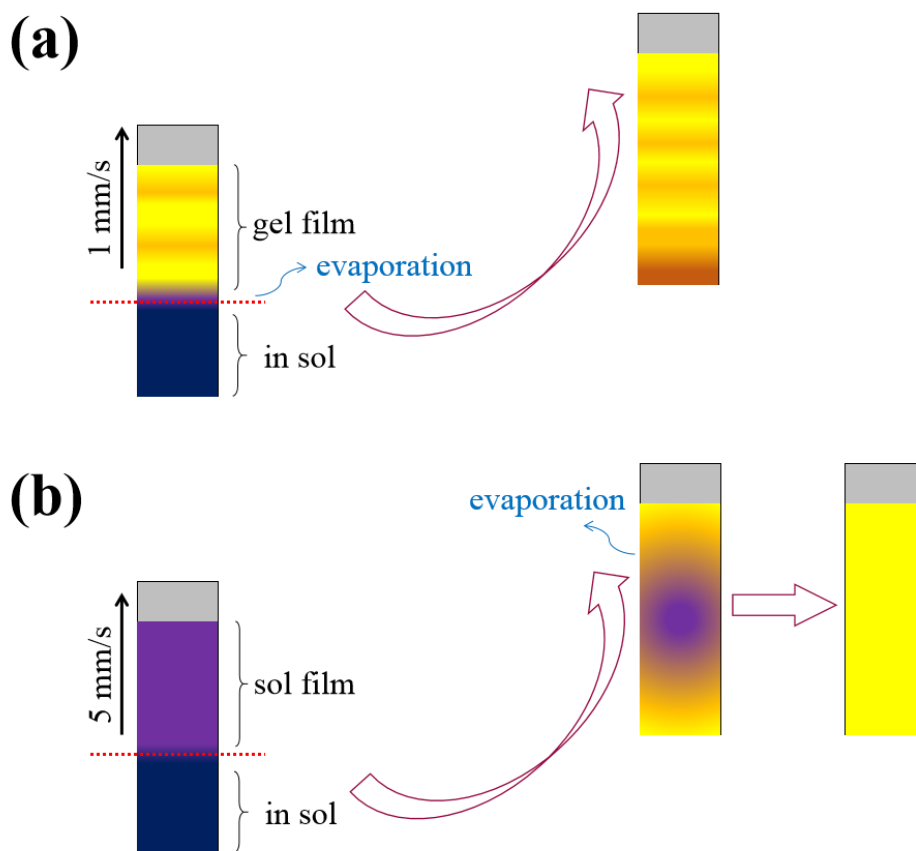

Figure 5.2. Two regimes for the formation of gel films: **(a)** mixed regime (U_w = 1 mm/s), **(b)** draining regime (U_w = 5 mm/s).

Although in both mixed and draining regimes T_{gel} increases with U_w, the gel film can present different characteristics due to the different formation mechanism of these two regimes, as is illustrated in **Figure 5.2**. In the mixed regime case (U_w = 1 mm/s is chosen for it has the biggest influence of capillarity effect), since the upward movement of the film is relatively slow, the evaporation of solvent takes place at the meniscus (shown in **Figure 5.2** by the red dot line) immediately after the substrate is dragged out from the sol. Due to the capillarity effect, the surface of the gel film contains top-down ripples (shown as the gel film parts with orange and yellow colors in **Figure 5.2a**), which can cause non-homogeneities in thickness along the withdrawal direction (Ca. 20 nm, according to measurements made by of ellipsometry). However, for the draining regime (see **Figure 5.2b**, U_w = 5 mm/s was chosen for its relatively slower movement so that easier to be observed), U_w is high enough to form a thick sol layer on the substrate and substantially decrease the withdrawal time, preventing that the evaporation is completed during withdrawal. Thus, the film is still wet when the withdrawal movement is completed. Then, the subsequent evaporation starts naturally and proceeds from the substrate outer borders towards the centre, which results in a very flat and homogeneous topography.

Therefore, according to my study, U_w not only changes the content of Sr inside gel film by controlling the T_{gel}, but also can affect the distribution of Sr inside gel film by building different topographies on it.

5.1.2. The influence of T_{gel} in mixed regime

After knowing the relationship between T_{gel} and U_w, we investigated the influence of T_{gel} in mixed regime (*i.e.* for U_w = 1.0, 2.0 and 3.5 mm/s) on the film crystallization for R_{Sr} fixed to 0.033 and 0.05. To make a comparison, a film prepared with U_w = 5.0 mm/s was chosen as a reference since it is the condition in draining regime in which most of the films of this Thesis have been prepared. The results are presented in **Figure 5.3**.

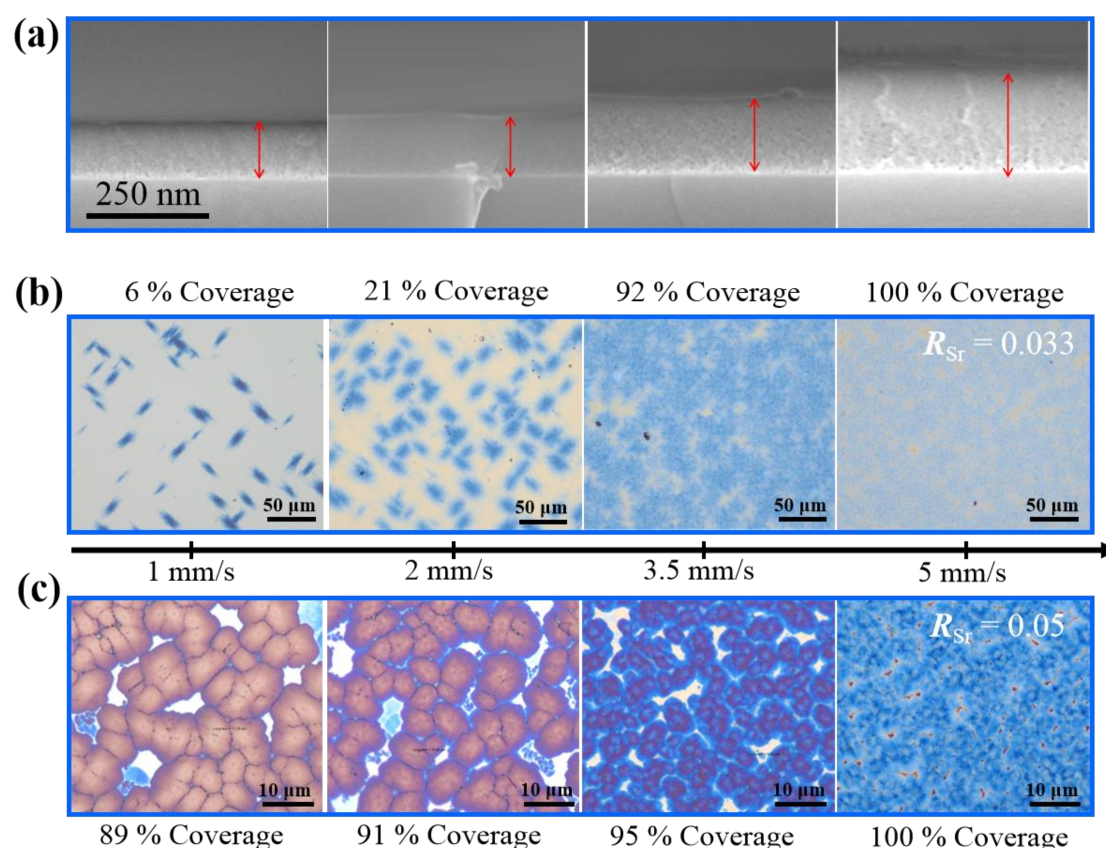

Figure 5.3. The influence of T_{gel} in mixed regime on the microstructure of films: **(a)** SEM cross-section images of gel films which show the increase of T_{gel} for higher U_w in the case of R_{Sr} = 0.05 films. **(b)** and **(c)** are the optical images of as-prepared α-quartz films with different U_w for R_{Sr} = 0.033 and 0.05 conditions, respectively. The area coverages of porous α-quartz phase for **(b)** and that of dense crystal domains for **(c)** are indicated above and below the images, respectively. The values of U_w are indicated in the black axis between **(b)** and **(c)**.

The cross-section images of gel films (see **Figure 5.3a**) tell us that U_w just controls T_{gel} and the topography but not the microstructure of films, since all the gel films

(including the draining regime one) are quite dense and homogeneous. Note that for the porous films ($\boldsymbol{R}_{Sr}$ = 0.033, see **Figure 5.3b**), the crystallization is not complete until $\boldsymbol{U}_w$ reaches the draining regime ($\boldsymbol{U}_w$ = 5 mm/s). Similarly to the partly crystalline films which were discussed in **Section 4.1.1**, here the coverage of α-quartz phase (blue tones in **Figure 5.3b**) is as low as 6% when $\boldsymbol{U}_w$ = 1.0 mm/s, and the coverage has an obvious improvement by increasing $\boldsymbol{U}_w$, to finally reach 92% for $\boldsymbol{U}_w$ = 3.5 mm/s, the maximum withdrawal rate of the mixed regime in this work. Therefore, for porous films ($\boldsymbol{R}_{Sr} \leq 0.035$), the effect of changing $\boldsymbol{T}_{gel}$ is analogous to that of varying $\boldsymbol{R}_{Sr}$ because the content of Sr can be adjusted by changing of $\boldsymbol{T}_{gel}$, and the crystallization of amorphous silica into α-quartz cannot be completed in this mixed regime.

For dense film conditions ($\boldsymbol{R}_{Sr} \geq 0.05$), the distribution and shape of dense crystals (darker contrast in **Figure 5.3c**) is impacted by $\boldsymbol{T}_{gel}$. When $\boldsymbol{U}_w$ is as low as 1 mm/s, the distribution of dense crystals is lower (the area coverage is 89%) but the shape of the single dense crystal is larger. For larger $\boldsymbol{T}_{gel}$, the coverage by dense crystals increases up to 95% while the size of single dense crystal is somewhat smaller. However, the distribution of dense crystals cannot reach 100% until $\boldsymbol{U}_w$ is not in the draining regime. So, under dense film conditions, $\boldsymbol{T}_{gel}$ mainly influences the homogeneity of dense crystals because as discussed previously, the surfaces of films in mixed regime present ripples (i.e. zones with varying thickness) which are responsible for a less homogeneous distribution of Sr inside film. The effect of ripples can be reduced by increasing $\boldsymbol{U}_w$ which allows obtaining a film crystallization more and more homogeneous.

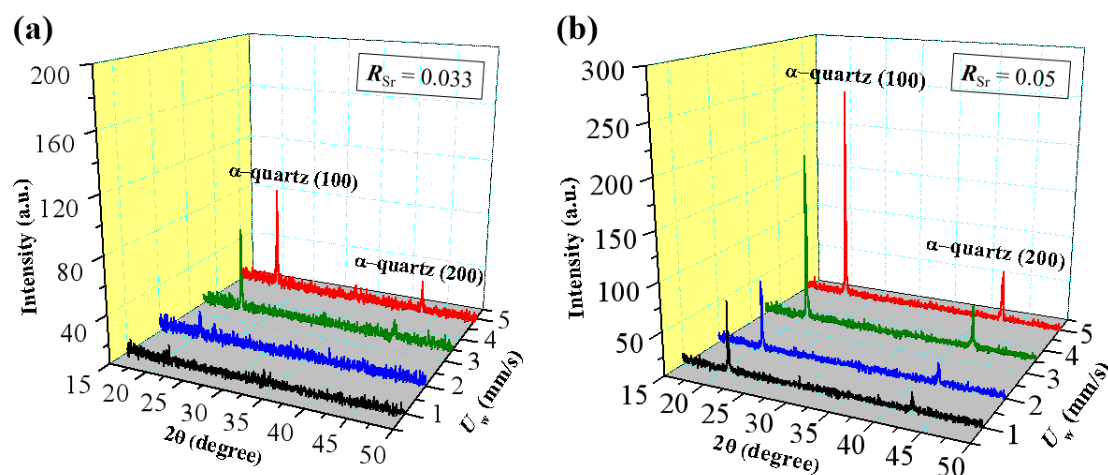

Figure 5.4. XRD θ-2θ measurements of as-prepared films with different $\boldsymbol{U}_w$ in mixed regime ($\boldsymbol{U}_w$ = 5 mm/s for draining condition is accounted as reference) for different $\boldsymbol{R}_{Sr}$ of **(a)** 0.033 and **(b)** 0.05, respectively.

The influence of $\boldsymbol{T}_{gel}$ in mixed regime on the crystallinities of the two kinds of films

were investigated by XRD θ-2θ measurements (see **Figure 5.4**) respectively. The diffraction peak intensities of porous films are relatively small (see **Figure 5.4a**). Especially for the films prepared with $\boldsymbol{U}_{w}$ = 1.0 and 2.0 mm/s, the signals are extremely weak due to the partial devitrification of silica into α-quartz phase (the areal coverages are 6% and 21%, respectively). The intensity is increased a lot when $\boldsymbol{U}_{w}$ reaches 3.5 mm/s because the crystalline fraction of the film is close to 100% ($\boldsymbol{U}_{w}$ = 5.0 mm/s, the red diffractogram in both figures).

When $\boldsymbol{R}_{Sr}$ = 0.05, the films are highly crystalline, and the intensity of α-quartz peaks is large. This is because the amount of Sr inside films is high enough to build dense crystals. The influence of $\boldsymbol{T}_{gel}$ is on the distribution and sizes of dense crystals which introduce changes in the areal coverage by a dense α-quartz microstructure. However, in contrast to what is observed for the films with $\boldsymbol{R}_{Sr}$ = 0.033, in the case of the films with $\boldsymbol{R}_{Sr}$ = 0.05 the diffraction peak intensity gradually increases with $\boldsymbol{U}_{w}$ (see **Figure 5.4b**) and accordingly with $\boldsymbol{T}_{gel}$. This is reasonable because the differences in areal coverage by dense α-quartz microstructure are not significant (89% *vs.* 95%), and thus the intensity is larger because of the increased thicknesses of films.

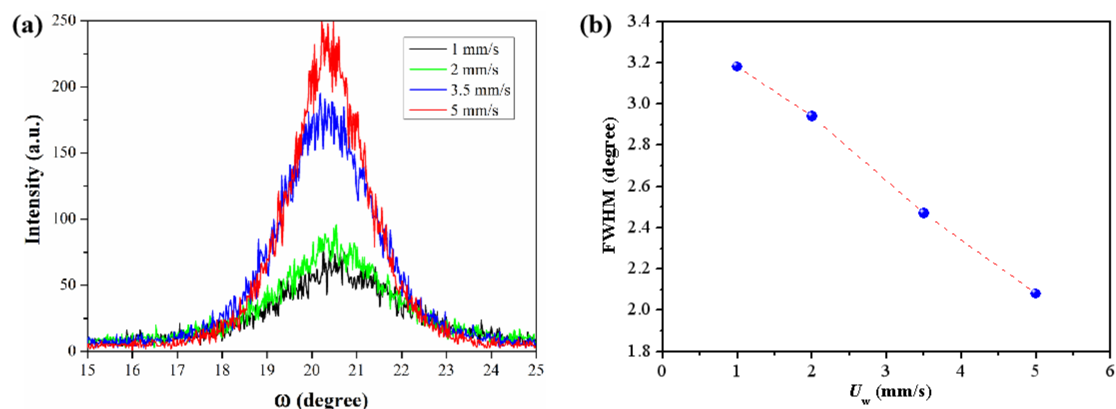

Figure 5.5. Rocking curves of α-quartz (100) reflections for films with $\boldsymbol{R}_{Sr}$ = 0.05 prepared under different $\boldsymbol{U}_{w}$ **(a)**. The dependence of the FWHM of these rocking curves on $\boldsymbol{U}_{w}$ are presented in **(b)**.

At the same time, FWHM values of rocking curves corresponding to α–quartz (100) peaks for films made at different $\boldsymbol{U}_{w}$ in mixed regime were obtained. Here, it has to be mentioned that it was not possible to obtain the FWHM for the porous film series ($\boldsymbol{R}_{Sr}$ = 0.033) because some of the peaks are too weak to have a reliable fitting result. Accordingly, only the FWHM results of dense films ($\boldsymbol{R}_{Sr}$ = 0.05) will be discussed. The FWHM analysis of dense films with different $\boldsymbol{U}_{w}$ is shown in **Figure 5.5**. The FWHM of films deceases with the increase of $\boldsymbol{T}_{gel}$, as the dense microstructures develop, which indicates that the α-quartz phase growth becomes more and more oriented in one direction reflecting the low mosaicity of the dense α-quartz microstructure.

5.1.3. The influence of T_{gel} in draining regime

For U_w = 5.0 mm/s, T_{gel} is already within the draining regime. Unlike in mixed regime, the gel films made in draining regime are only influenced by the draining effect which only changes the film thickness, the topography being fixed as a flat surface. Even so, the crystallization of films can be different because the quantity of Sr inside the gel can be altered by differences in T_{gel}.

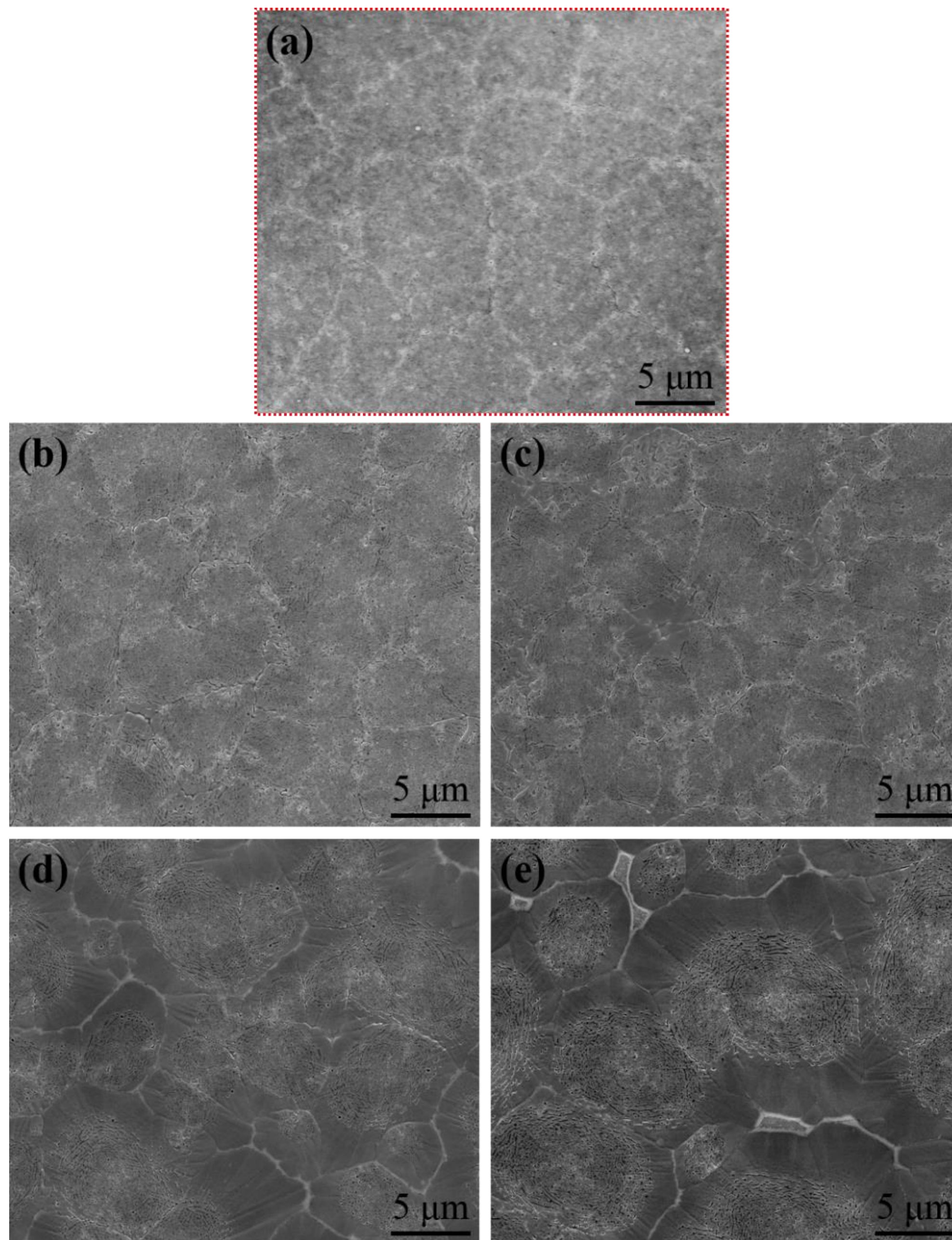

Figure 5.6. SEM secondary electron images of films under porous R_{Sr} condition (R_{Sr} = 0.033) with different U_w within the draining regime: **(a)** 5.0 mm/s, **(b)** 7.5 mm/s, **(c)** 10.0 mm/s, **(d)** 12.5 mm/s, **(e)** 15.0 mm/s.

For $\boldsymbol{R}_{Sr}$ values which allow preparing porous films, an SEM study was made on films with $\boldsymbol{R}_{Sr}$ = 0.033 and using different $\boldsymbol{U}_w$ within the draining regime. The secondary electron images are presented in **Figure 5.6**. Here, **Figure 5.6a** showing an image of the 5.0 mm/s film can be taken as a reference to show the influence of high $\boldsymbol{U}_w$. For $\boldsymbol{U}_w$ = 7.5 and 10.0 mm/s the film surfaces display a completely porous microstructure with crevices (see **Figure 5.6b** and **c**), which imply that the Sr has not been able to aggregate within the crevices to start densification. However, when $\boldsymbol{U}_w$ attains 12.5 mm/s, the increase in the total amount of Sr contained in the film (because the film is thicker) is large enough to flow into the crevices to form the Sr agglomerates. Thus, in the latter case dense microstructure appear surrounding the Sr-lines by the densification (see **Figure 5.6d**). Then, with $\boldsymbol{U}_w$ moving to the maximum (15.0 mm/s), the content of Sr is high enough to shift to a microstructure dominated by dense α-quartz (see **Figure 5.6e**) which results from a recrystallization of the primary porous α-quartz. It is interesting to note that this dense microstructure has been achieved with a low $\boldsymbol{R}_{Sr}$ which is typically used to prepare ultra-flat porous quartz films. In this condition, dense crystals are basically formed and even the porous surfaces caused by one-side densification are present in some places with dense aggregates of Sr (see bottom part of **Figure 5.6e**).

Simultaneously, corresponding BSE images were also recorded (see **Figure 5.7**). Also in this case, **Figure 5.7a** which corresponds to the $\boldsymbol{U}_w$ = 5.0 mm/s sample is taken as a reference see the effects of higher $\boldsymbol{U}_w$. For $\boldsymbol{U}_w$ = 7.5 and 10.0 mm/s conditions (see **Figure 5.7b** and **c**), there is no trace of Sr accumulations inside crevices, which proves that the films are totally porous. **Figure 5.7d**, which corresponds to a film prepared with $\boldsymbol{U}_w$ = 12.5 mm/s, illustrates a typical zone consisting of a Sr-rich line inside a crevice and a dense microstructure surrounding the line, indicating the occurrence of an initial aggregation of Sr which can start a local densification by recrystallization. Finally, **Figure 5.7e** shows that for $\boldsymbol{U}_w$ = 15.0 mm/s Sr forms agglomerates for one-side densification, which is only present in films dominated by dense α-quartz microstructures. These SEM study shows that by increasing $\boldsymbol{T}_{gel}$ through faster withdrawal rates within the draining regime one can achieve α-quartz film microstructures which are typically obtained with larger $\boldsymbol{R}_{Sr}$ at lower withdrawal rates. This is because the total amount of Sr inside the gel film both increases with $\boldsymbol{R}_{Sr}$ and $\boldsymbol{T}_{gel}$.

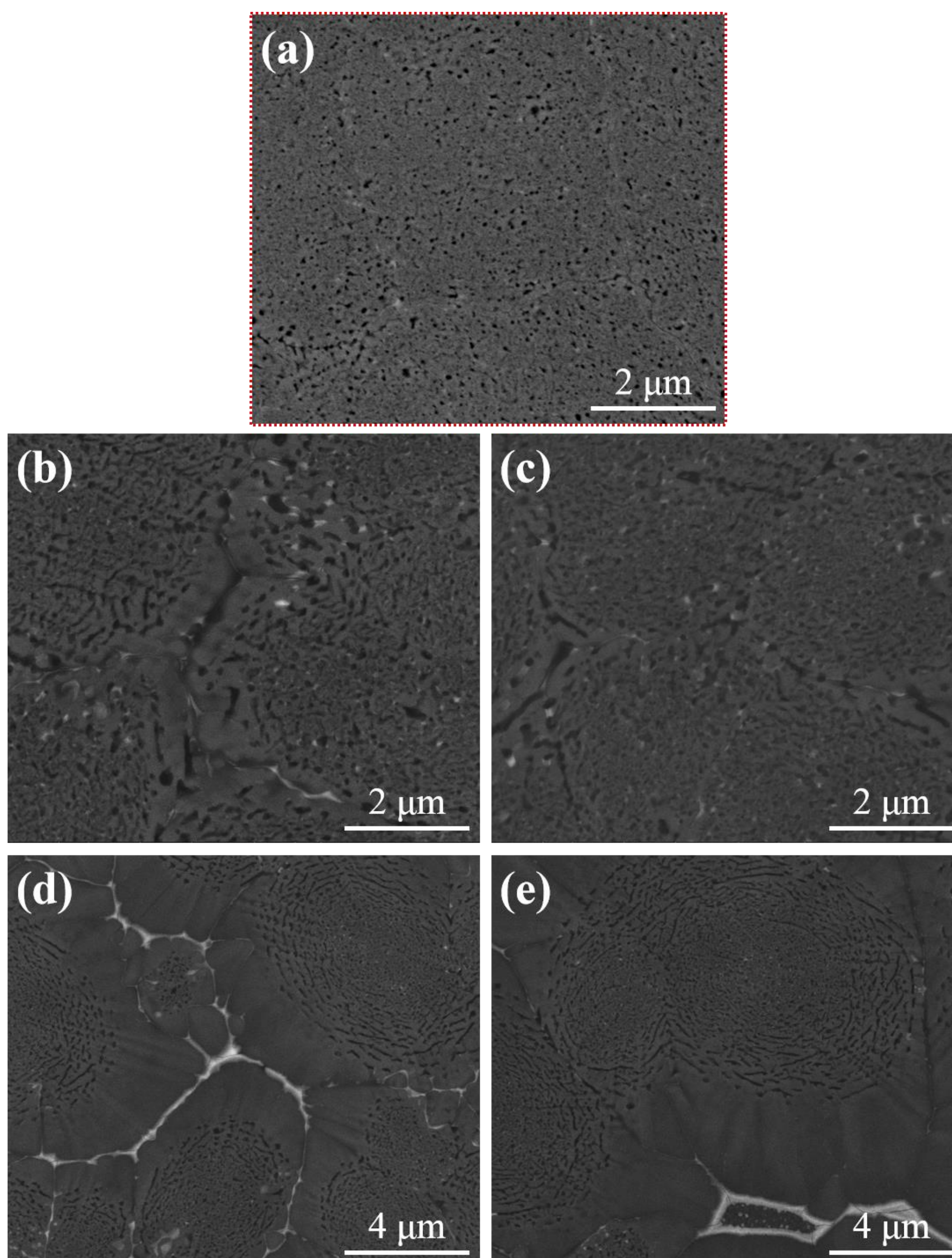

Figure 5.7. BSE images of quartz films prepared with $\boldsymbol{R}_{Sr}$ = 0.033 and different $\boldsymbol{U}_w$ within the draining regime **(a)** 5.0 mm/s, **(b)** 7.5 mm/s, **(c)** 10.0 mm/s, **(d)** 12.5 mm/s, **(e)** 15.0 mm/s to illustrate the influence of $\boldsymbol{U}_w$ on the content and distribution of Sr.

In order to know the influence of $\boldsymbol{U}_w$ (and thus $\boldsymbol{T}_{gel}$) on the crystallinity of films prepared with $\boldsymbol{R}_{Sr}$ = 0.033, XRD θ-2θ patterns and FWHM measurements were made for all the five films and the results are displayed in **Figure 5.8**. From XRD θ-2θ patterns (see **Figure 5.8a**), the intensities of the α-quartz(h00) reflections increase linearly with $\boldsymbol{U}_w$, as it is shown in **Figure 5.8b**. Nevertheless, since in the draining regime log($\boldsymbol{T}_{gel}$) is proportional to 0.643*log($\boldsymbol{U}_w$) (see **Figure 5.1**), $\boldsymbol{T}_{gel}$ is proportional to $(\boldsymbol{U}_w)^{0.643}$, and thus we can conclude that the linear increase in the intensity of the

(h00) reflections is not only caused by the increase in T_{gel}, but also influenced by the appearance of the dense microstructure at U_w = 12.5 and 15.0 mm/s conditions. **Figure 5.8c** shows that the FWHM of the of α-quartz(100) reflection in θ-ω measurements (rocking curves) decreases with increasing U_w, displaying a non-linear dependence which is equivalent to that already observed for R_{Sr} (see **Figure 4.29**). It is interesting to note that films which are completely porous (*i.e.* those obtained for U_w = 5.0 – 10.0 mm/s), also present a significant decrease of the rocking curve FWHM with respect to films prepared with lower withdrawal rates. This indicates that the misorientation of α-quartz phase growth is significantly reduced by increasing T_{gel}. Once U_w is higher than 10.0 mm/s and allows films to form dense microstructures, the decrease of FWHM is more moderate and is mainly related to the appearance of the dense α-quartz microstructures which present low mosaicity.

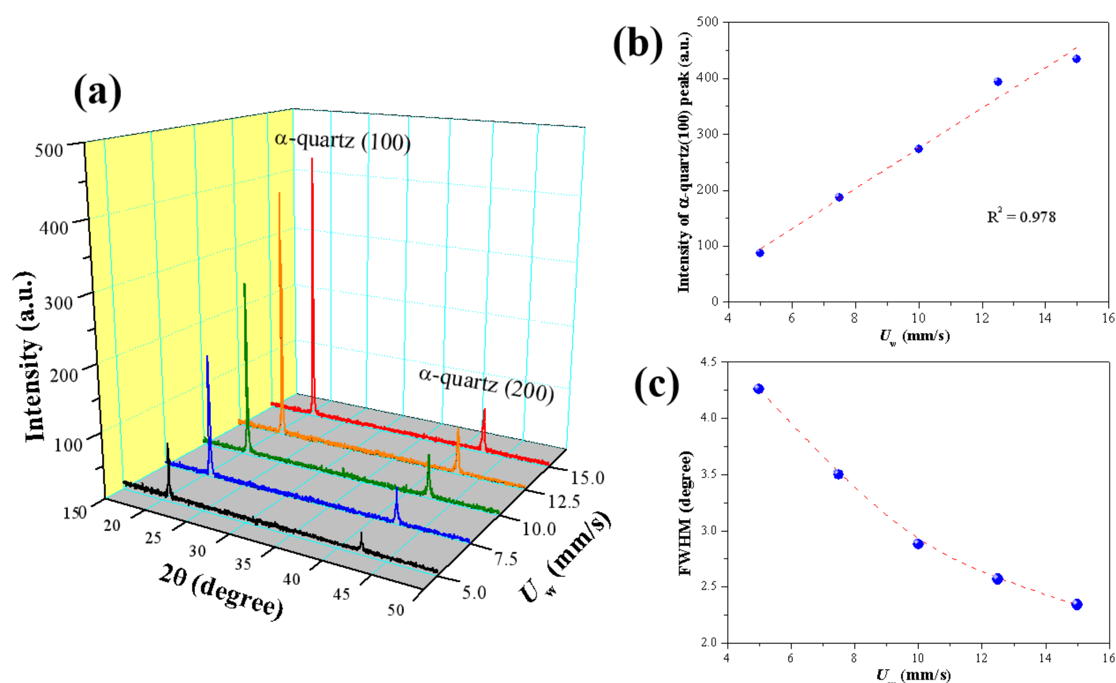

Figure 5.8. Crystallinity study of as-prepared films in porous R_{Sr} region (R_{Sr} = 0.033) with different U_w of draining regime: **(a)** XRD θ-2θ patterns, **(b)** the linear relationship between the intensity of α-quartz(100) peak and U_w. **(c)** FWHM of the α-quartz(100) reflection obtained in rocking curve measurements.

Subsequently, we studied the influence of U_w within the draining regime and T_{gel} on films with R_{Sr} values which typically result in dense microstructures (R_{Sr} ~0.038 - 0.1). This was investigated on a series of films prepared at different U_w values, with R_{Sr} = 0.05. **Figure 5.9** shows secondary electron images to analyse the microstructure of these films.

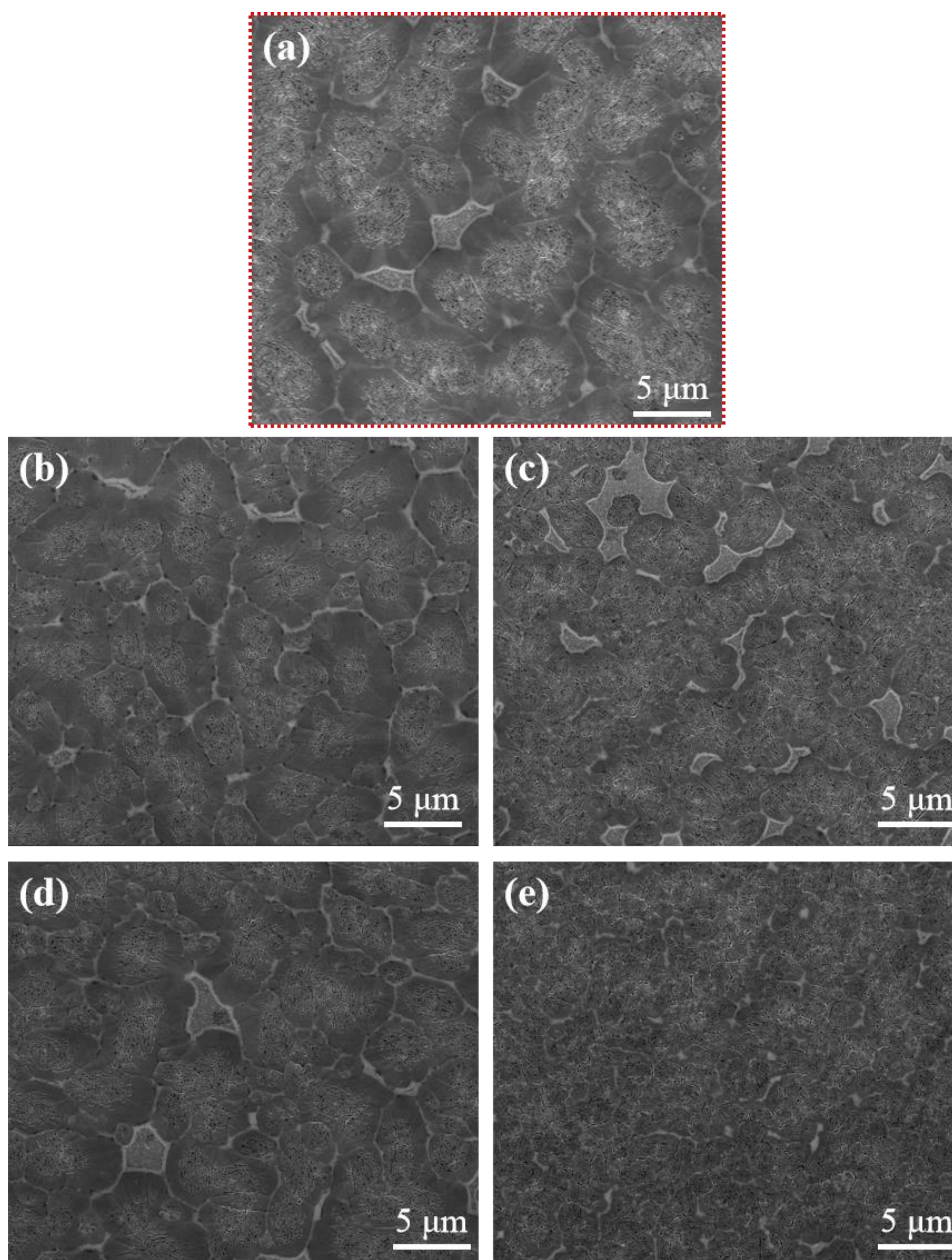

Figure 5.9. SEM secondary electron images of films presenting dense quartz structures ($\boldsymbol{R}_{\mathrm{Sr}}$ = 0.05) with the different $\boldsymbol{U}_{\mathrm{w}}$ within the draining regime: **(a)** 5.0 mm/s **(b)** 7.5 mm/s, **(c)** 10.0 mm/s, **(d)** 12.5 mm/s, **(e)** 15.0 mm/s.

The $\boldsymbol{U}_{\mathrm{w}}$ = 5.0 mm/s condition (see **Figure 5.9a**) is taken as the reference for comparing the influence of larger $\boldsymbol{U}_{\mathrm{w}}$ in this series. The images of **Figure 5.9** show that the films prepared at $\boldsymbol{U}_{\mathrm{w}}$ = 7.5, 10.0 and 12.5 mm/s display the typical microstructure dominated by dense α-quartz crystals with filling of dense crystals (see **Figure 5.9b-d**). However, by increasing $\boldsymbol{T}_{\mathrm{gel}}$ one cannot introduce into the film enough Sr to obtain smaller and more isolated dense crystals with a thicker Sr-boundary, in contrast to what is observed by increasing $\boldsymbol{R}_{\mathrm{Sr}}$ (*cf.* **Section 4.1.3**). So, the

dense crystals of **Figure 5.9b-d** are still hardly recognizable for their irregular shapes and poorly-defined Sr-boundaries. The main difference among them is that the areal coverage of porous surface zones becomes larger as $\boldsymbol{U}_{\mathrm{w}}$ is increased. An unexpected finding of this study is that for the maximum withdrawal rate ($\boldsymbol{U}_{\mathrm{w}}$ = 15.0 mm/s), the film is again dominated by a porous microstructure (see **Figure 5.9e**). The reason which could explain this result is that the crevices become deeper upon increasing $\boldsymbol{T}_{\mathrm{gel}}$ and, as a result, the Sr does not properly accumulate to induce the recrystallization. Both of these two changes make more difficult for Sr to fill the crevices and aggregate. In particular, this additional microstructural factor (the nature of the crevices) shows that a dense microstructure is not always achieved by arbitrarily increasing $\boldsymbol{T}_{\mathrm{gel}}$.

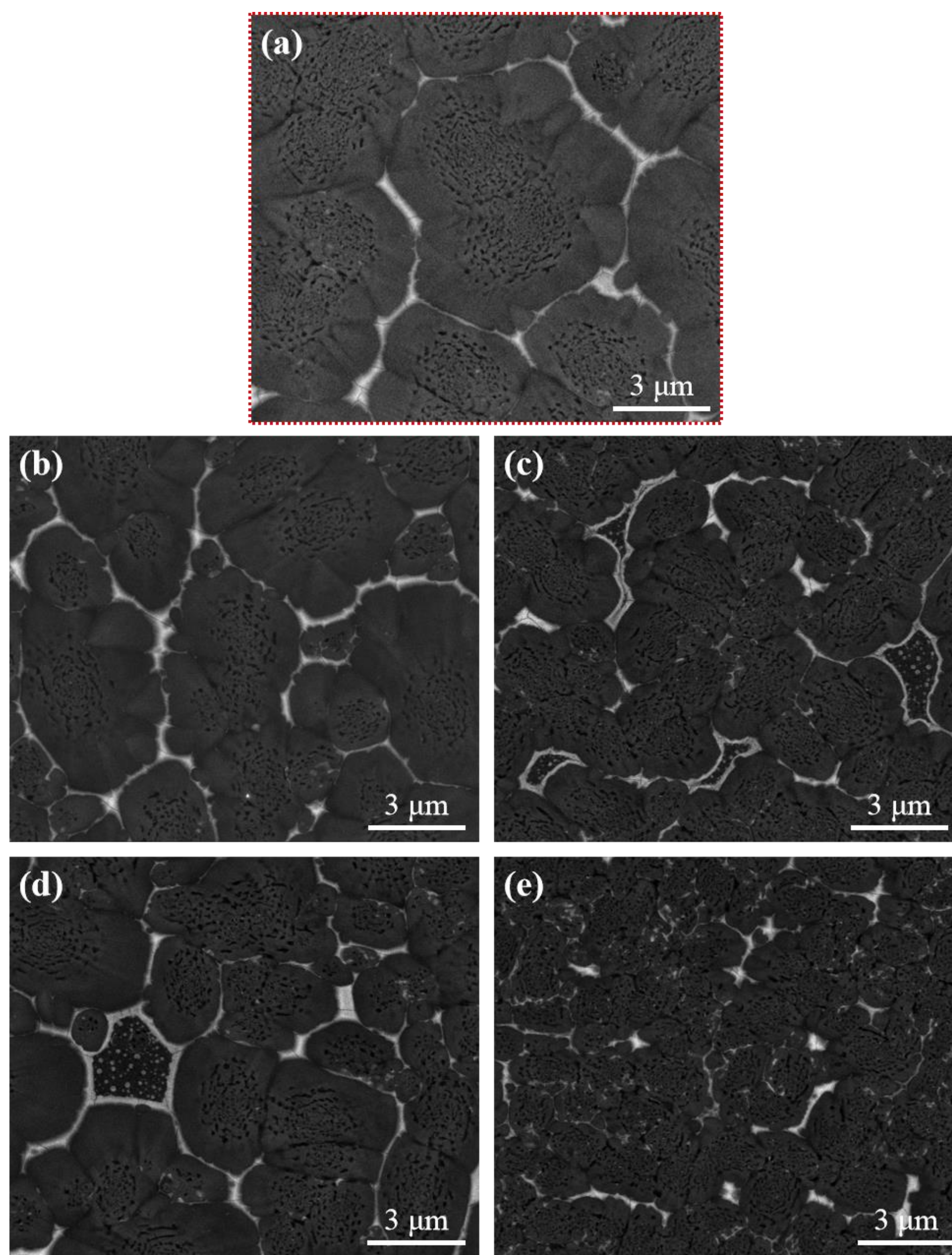

Figure 5.10. BSE images of quartz films prepared with $\boldsymbol{R}_{\mathrm{Sr}}$ = 0.05 and different $\boldsymbol{U}_{\mathrm{w}}$ within the draining regime **(a)** 5 mm/s, **(b)** 7.5 mm/s, **(c)** 10 mm/s, **(d)** 12.5 mm/s, **(e)** 15 mm/s) to illustrate the influence of $\boldsymbol{U}_{\mathrm{w}}$ on the content and distribution of Sr.

The corresponding BSE images of films (shown as **Figure 5.10**, with a reference of $\boldsymbol{U}_{\mathrm{w}}$ = 5.0 mm/s condition) points to the same conclusion. The images corresponding to $\boldsymbol{U}_{\mathrm{w}}$ = 7.5, 10.0 and 12.5 mm/s conditions (see **Figure 5.10b-d**) reveal a scenario of the Sr distribution which is analogous to the one already found in $\boldsymbol{R}_{\mathrm{Sr}}$ dependent study (see **Figure 4.10c**), evidencing that $\boldsymbol{U}_{\mathrm{w}}$ doesn't change the microstructure of films under $\boldsymbol{R}_{\mathrm{Sr}}$ = 0.05 condition. Then, the image of $\boldsymbol{U}_{\mathrm{w}}$ = 15.0 mm/s condition (see **Figure 5.10e**) shows a surface dominated by pores with a dense crevice network and Sr only can accumulate into some specific parts of the network, which shows us that the film microstructure that is obtained by increasing $\boldsymbol{T}_{\mathrm{gel}}$ can be again porous although for that $\boldsymbol{R}_{\mathrm{Sr}}$ value one would expect dense film microstructures.

Meanwhile, the crystallinity of films prepared with $\boldsymbol{R}_{\mathrm{Sr}}$ = 0.05 and different $\boldsymbol{U}_{\mathrm{w}}$ within draining regime were studied by XRD θ-2θ patterns and rocking curve measurements. The results are summarized in **Figure 5.11**. The XRD patterns of the films (see **Figure 5.11a**) show that the intensity of the α-quartz(h00) reflections increase with $\boldsymbol{U}_{\mathrm{w}}$ except for $\boldsymbol{U}_{\mathrm{w}}$ = 15 mm/s. This is reasonable because, as already discussed in **Chapter 4** (see **Figure 4.14b**), the dense microstructure runs throughout the whole film and thus can also increase with $\boldsymbol{T}_{\mathrm{gel}}$. The increased thickness of dense microstructure can give much stronger reflections even if the corresponding surface area doesn't change significantly. Then, the drop in the diffraction intensity for $\boldsymbol{U}_{\mathrm{w}}$ = 15 mm/s can be attributed to the previously discussed reappearance of the porous microstructure.

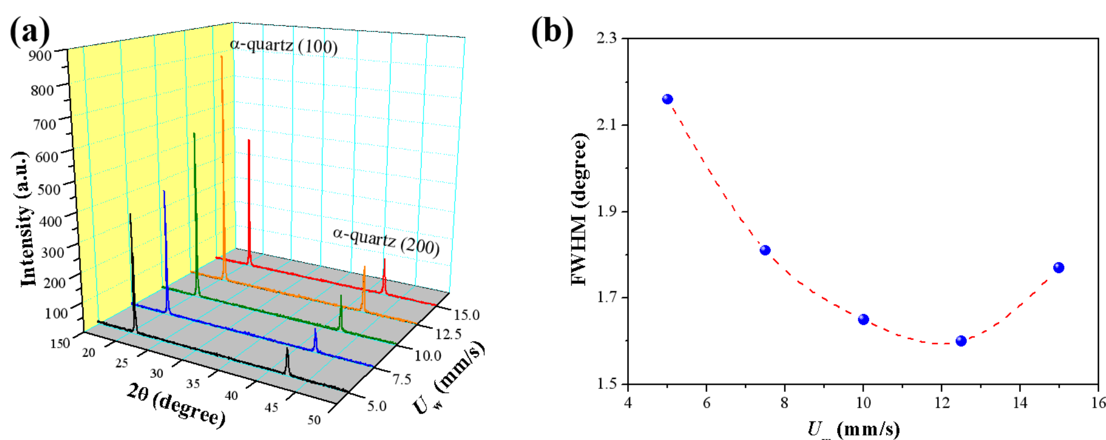

Figure 5.11. Crystallinity study of films prepared with $\boldsymbol{R}_{\mathrm{Sr}}$ = 0.05 films and different $\boldsymbol{U}_{\mathrm{w}}$ within the draining regime: **(a)** XRD θ-2θ patterns, **(b)** FWHM of the α-quartz(100) reflection obtained in rocking curve measurements.

The mosaicity of the α-quartz crystals, studied by rocking curves of the (100)

reflection of α-quartz, is decreasing when U_w increases from 5.0 mm/s to 12.5 mm/s. This is indicated by the falling down trend of FWHM of the rocking curves which displays a minimum at U_w = 12.5 mm/s (see **Figure 5.11b**). Then the mosaicity of the α-quartz crystals increases again when U_w rises to 15 mm/s and the porous microstructure, in which the crystals are less well-oriented, reappears.

5.1.4. Limitation of the T_{gel} study

The range of T_{gel}, covered in my study is also relevant. According to **Figure 5.1**, the experimental range of T_{gel} goes from 110 nm to 400 nm (corresponding to U_w = 1.0 and U_w = 15.0 mm/s, respectively) and partially contains the mixed regime and the whole of draining regime, which corresponds to the right-hand half of the complete Landau-Levich plot. This range was chosen not only because the dependence between T_{gel} and U_w presents a monotonous increase but also because it comprises the only effective conditions to fabricate good-quality gel films in the laboratory.

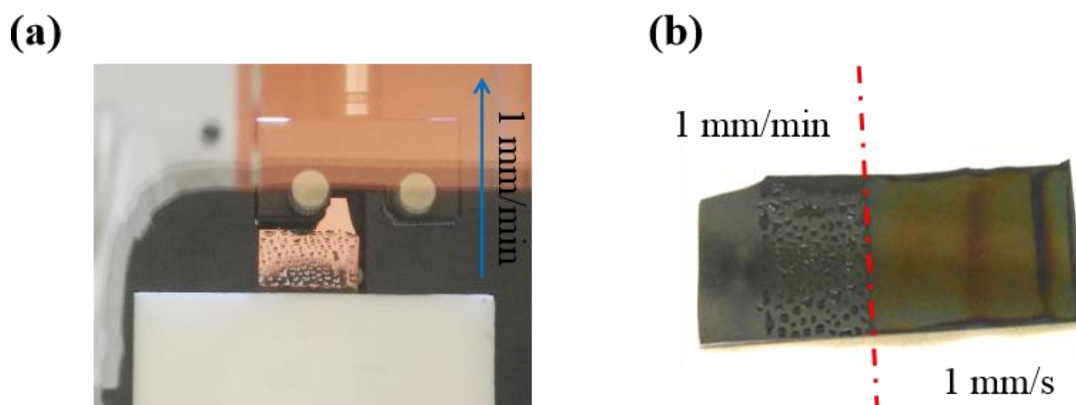

Figure 5.12. Attempt to fabricate a film with R_{Sr} = 0.05 within the capillarity regime by (U_w = 1 mm/min): **(a)** The image of the withdrawal process at a rate of 1 mm/min shows the failure in the formation of gel film **(b)** The image of the as-prepared sample presents a film-free area obtained at 1 mm/min withdrawal rate (left side of red dash-dot line) and a consecutive gel film area when U_w changed to 1 mm/s (right side of red dash-dot line).

The Landau-Levich Model tells us that T_{gel} can increase by decreasing U_w when the capillarity effect is dominant, and the relationship between them also can be linear when U_w is slow enough into the capillarity regime. However, as the shortage for all the common theorems, sometimes they are not practical because they cannot take into account all the relevant parameters during the experiment. My study also suffered from this.

I tried to make a gel film within the capillarity regime to know the influence of T_{gel} in this regime, but this attempt failed, as is shown in **Figure 5.12**. U_w = 1 mm/min was selected to make sure the condition is in capillarity regime. **Figure 5.12a** shows that the sol forms isolated droplets on the substrate (also described as the left part of

Figure 5.12b) instead of forming a continuous a gel film (shown as the right part of **Figure 5.12b**, which was obtained in draining regime condition of U_w= 1.0 mm/s). Therefore, the capillarity regime is not available in my work. The main reason that makes the experimental conditions inaccessible to the capillary regime is that the viscosity of my final solution is not high enough to support the sol layer staying as a film after evaporation.

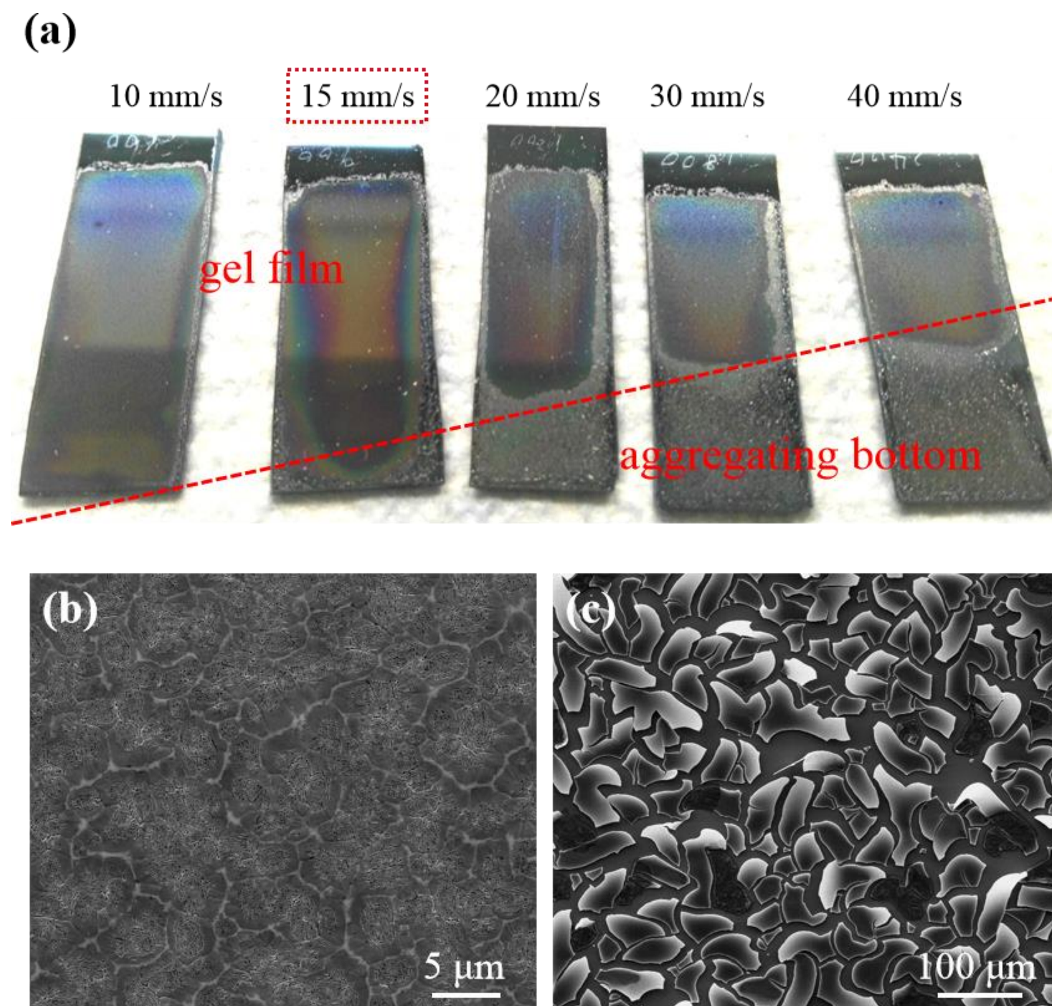

Figure 5.13. Attempt of making R_{Sr} = 0.05 α-quartz films by using U_w higher than 15.0 mm/s: **(a)** Images of as-prepared films with U_w = 10 - 40 mm/s. **(b)** SEM image to show the gel film zone of U_w = 40 mm/s film. **(c)** SEM image to show the aggregating bottom of U_w = 40 mm/s film.

Another limitation of this study was in the maximum U_w that could be used while preserving the homogeneity of as-prepared film. Actually, the maximum U_w of the dip-coater apparatus used in my work can be as high as 40 mm/s. And theoretically, T_{gel} could reach 750 nm according to draining law shown in **Figure 5.1**. However, in practice, for U_w above 15.0 mm/s the crystallized films are vertically inhomogeneous and display two completely different microstructures in the top and down parts of the substrates along the withdrawal direction (see **Figure 5.13**). The image of samples

prepared at $U_w \geq 20$ mm/s (see **Figure 5.13a**) shows that the films present an upper zone characterized by the typical dense microstructure (confirmed via **Figure 5.13b**). The bottom part of the substrates presents broken pieces of gel layer, as can be seen in **Figure 5.13c**. Thus, since the film only can be homogeneous when U_w is not higher than this value, $U_w = 15$ mm/s was chosen as the maximum limit for the T_{gel} dependence study in this chapter.

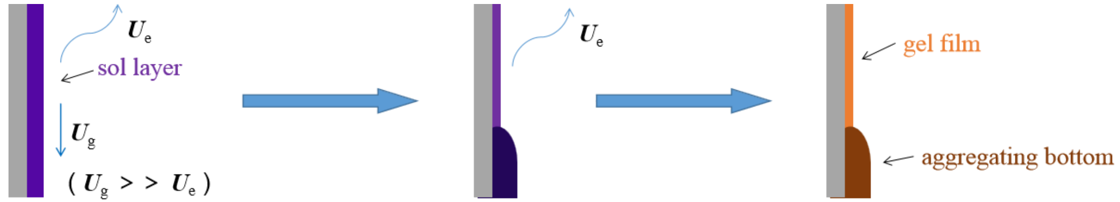

Figure 5.14. The schematics illustrating the zone separation of inhomogeneous films made by high U_w (20 ~ 40 mm/s).

The reason for the zone separation caused by high U_w (> 15 mm/s) is illustrated in **Figure 5.14**: When the sample is dragged out from final solution with a high U_w, the sol layer on the substrate is very thick. Such a thick liquid undergoes a large gravitational force which pulls the liquid with a downward rate (U_g). Meanwhile, the evaporation rate at the sol layer (U_e), which is independent of U_w, becomes slow compared to the fast withdrawal process. As a result, the sol layer can stay long enough without gelling, flowing downward and a sol excess is accumulated at the bottom of the withdrawn substrate, forming an aggregating zone. During the consolidation thermal treatment, the gel in this thicker aggregating zone is broken because it cannot withstand the increased stresses which develop upon drying or due to different thermal expansion of gel and substrate.

5.2. Investigating the influence of annealing temperature on the microstructures of epitaxial α-quartz films

The annealing temperature (***AT***) can be relevant to the crystallization in two aspects. On the one hand, ***AT*** offers the energy to induce the nucleation and keep the crystal growth running in progress, which indicates that ***AT*** can control the crystal density and the rate of crystallization. On the other hand, and more interesting, ***AT*** can influence the distribution and the diffusion dynamics of Sr inside film, thereby affecting the film microstructure. According to the results discussed in **section 4.1.4** of **Chapter 4**, Sr is found under a molten state during the film devitrification. This facilitates the Sr diffusion in the film, creating different microstructures depending on its distribution. For instance, if Sr forms large aggregates, we have seen that it triggers a recrystallization which yields to dense quartz structures. Hence, ***AT*** can control the activity of Sr inside film by the melting route. Considering these two points, I designed a systematic study about the influence of ***AT*** on the quartz crystallization. To

this aim, the $\boldsymbol{R}_{\mathrm{Sr}}$ conditions which allow preparing both porous ($\boldsymbol{R}_{\mathrm{Sr}}$ = 0.033) and dense ($\boldsymbol{R}_{\mathrm{Sr}}$ = 0.05) film were selected. Besides, in order to obtain a typical film, the withdrawal rate of all the films was fixed to 5.0 mm/s. Other relative parameters were also fixed at their optimal conditions, as is described in more detail in **Section 3.2** of **Chapter 3**.

5.2.1. The influence of ***AT*** in porous α-quartz films

Firstly, the influence of ***AT*** to the films with an $\boldsymbol{R}_{\mathrm{Sr}}$ which typically yields a porous microstructure ($\boldsymbol{R}_{\mathrm{Sr}}$ = 0.033) was investigated by preparing 9 samples with different ***AT*** ranging from 900ºC to 1100ºC. Optical microscopy images of these films are displayed in **Figure 5.15**.

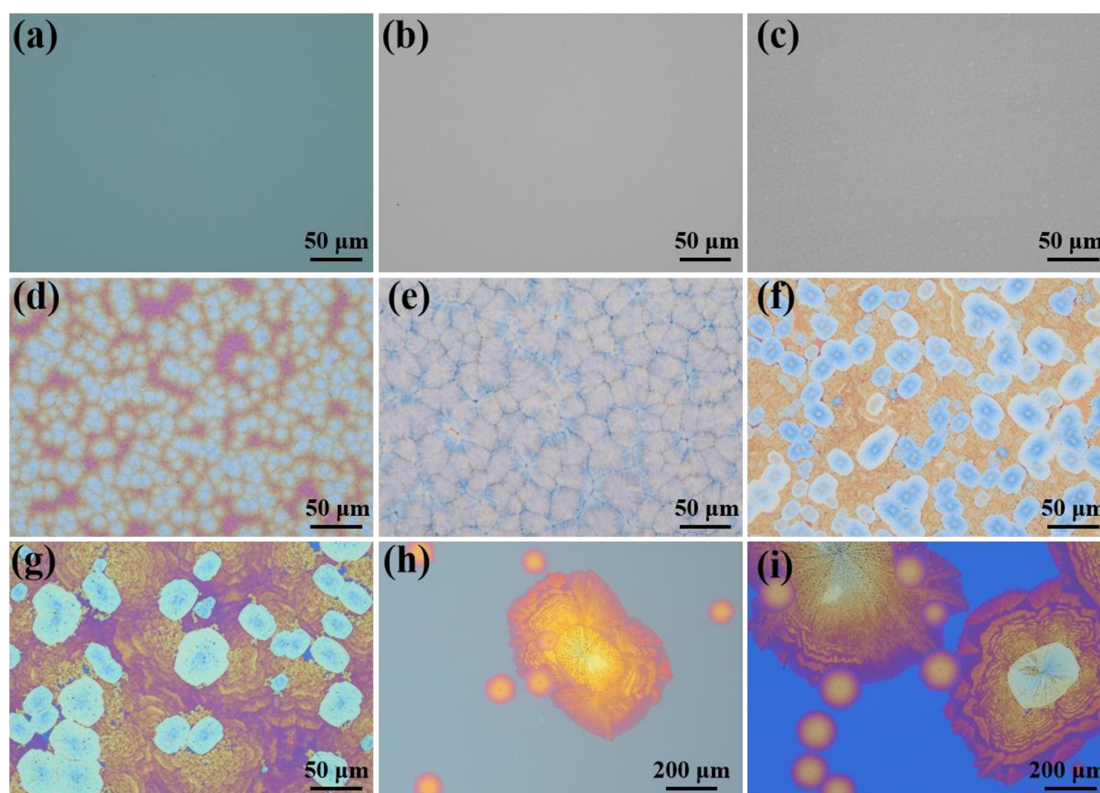

Figure 5.15. The optical images of films with $\boldsymbol{R}_{\mathrm{Sr}}$ = 0.033 at different ***AT***: **(a)** 900ºC, **(b)** 925ºC, **(c)** 950ºC, **(d)** 975ºC, **(e)** 1000ºC, **(f)** 1025ºC, **(g)** 1050ºC, **(h)** 1075ºC, **(i)** 1100ºC.

Under the Sr ratio for porous film ($\boldsymbol{R}_{\mathrm{Sr}}$ = 0.033), **Figure 5.15e** (***AT*** = 1000 ºC) shows a typical porous α-quartz microstructure, which has been discussed in **Section 4.1.2** and can be used as the reference. When ***AT*** is lower than 1000ºC, the crystalline zone does not appear until ***AT*** reaches 975ºC, and the film presents a partly crystalline microstructure (only the high contrast spots in the **Figure 5.15d** are crystalline zones). Once ***AT*** increases above 1000ºC, the film microstructures shift into different types of dense crystal patterns. However, these dense microstructures caused by higher ***AT*** are quite different from the typical dense films obtained by increasing $\boldsymbol{R}_{\mathrm{Sr}}$ (see detail in

Section 4.1.3). On the one hand, the sizes of dense crystals are larger (30 to 200 nm); on the other hand, the dense crystals are less overlapped and connected (see **Figure 5.15f-i**). Moreover, the outer porous surfaces surrounding the dense crystals present a specific pattern (yellow colour zones in **Figure 5.15f-i**) which is not found in the typical dense films obtained by controlling $\boldsymbol{R}_{Sr}$.

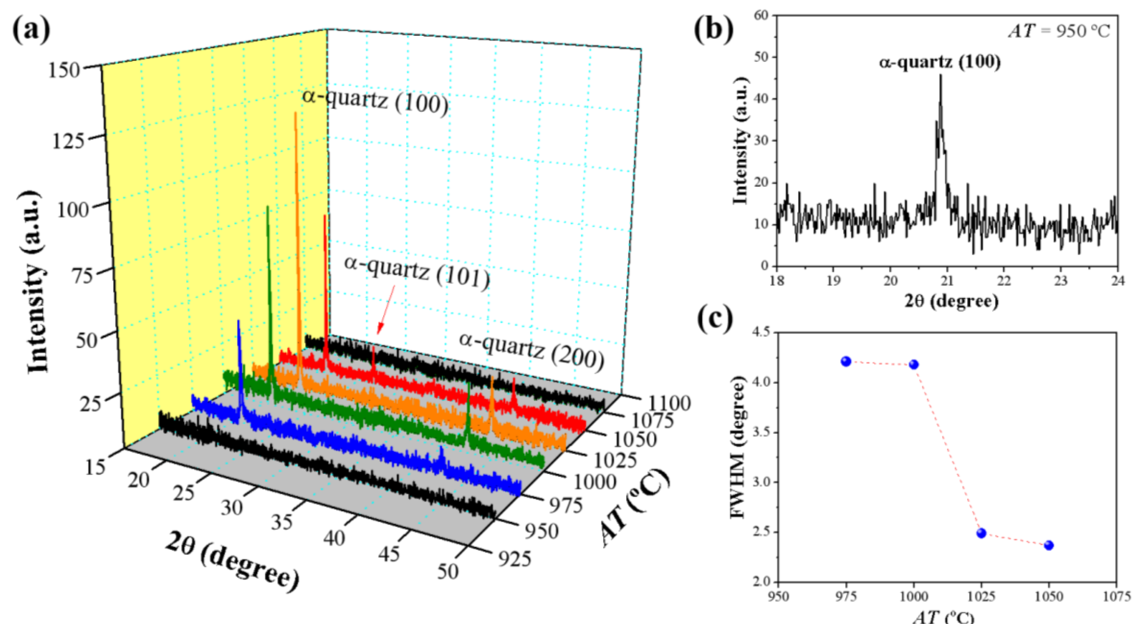

Figure 5.16. Crystallinity of films with $\boldsymbol{R}_{Sr}$ = 0.033 treated at different ***AT*** (from 950ºC to 1075ºC): **(a)** XRD θ-2θ patterns. **(b)** XRD θ-2θ pattern for ***AT*** = 950ºC increasing the acquisition time until the α-quartz(100) peak becomes visible. **(c)** FWHM of the rocking curves measurements at different ***AT***.

The crystallinity of films prepared with $\boldsymbol{R}_{Sr}$ = 0.033 after different ***AT*** is summarized in **Figure 5.16**. θ-2θ patterns (see **Figure 5.16a**) tell us that the effective crystallization only occurs in the range from 975ºC to 1050ºC as indicated by the obvious (h00) reflections of the α-quartz phase. Actually, the crystallization has already started for ***AT*** = 950ºC because the α-quartz(100) peak can be detected by increasing acquisition the step time from 0.15 s to 1 s (see **Figure 5.16b**). But this result confirms that the crystallization at ***AT*** = 950ºC is very slight and the annealed film can be considered as amorphous. According to the tendency presented of the intensities of the (h00) reflections in **Figure 5.16a**, the crystallinity increases steeply from 950ºC to 1025ºC with the crystallization running more and more complete and for ***AT*** = 1025ºC, the crystallization yields a dense microstructure which gives a much stronger response in diffraction. However, for ***AT*** = 1050ºC the intensities of the reflections decrease as a result of a distribution of dense crystals that is much sparser. What's more, the response of ***AT*** = 1050ºC film reveals a new peak corresponding to α-quartz(101) interplanar spacings, which is the most intense reflection of this phase

and which indicates that the film is partially polycrystalline. So, at this condition, the α-quartz phase is not only present in the form of epitaxial crystals grown from the substrate but also presents α-quartz which has not nucleated at the interface with the Si substrate but within the gel film.

The FWHM of the peaks obtained from rocking curve measurements (see **Figure 5.16c**) shows a switch-mode tendency because the film microstructure shifts from a microstructure dominated by pores to one characterized by dense quartz crystals between 1000 ºC and 1025 ºC. The ***AT*** = 950ºC condition has been excluded because its α-quartz(100) peak is too tiny to take a reliable Gauss fitting of the rocking curve. The two porous films (***AT*** = 975 ºC and 1000 ºC) present high values around 4.2º, which means the growth of α-quartz phase has a bigger misorientation. However, the values go down sharply to beneath 2.5º when ***AT*** reaches1025ºC and 1050ºC as the dense microstructure presents a highly mono-oriented growth.

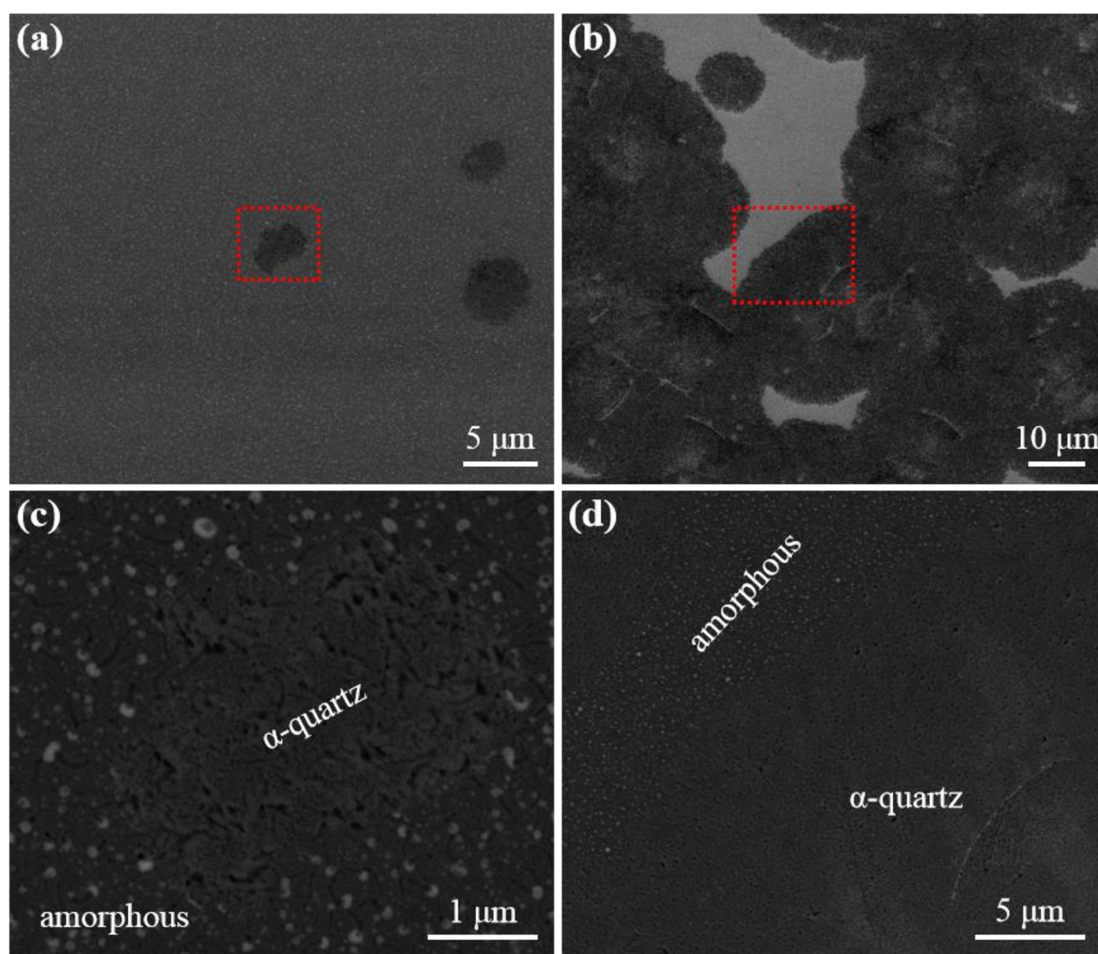

Figure 5.17. SEM images to show the microstructures of $\boldsymbol{R}_{Sr}$ = 0.033 films at ***AT*** = 950 ºC and 975 ºC conditions: **(a)** and **(b)** are the secondary electron images of ***AT*** = 950 ºC and 975 ºC films respectively. **(c)** and **(d)** are the BSE images of red dashed zones in **(a)** and **(b)** respectively.

Thinking of the differences in the crystallinity study due to the change of

microstructure, the microstructures of as-prepared samples were investigated by SEM. **Figure 5.17** presents the SEM results of $\boldsymbol{R}_{\mathrm{Sr}}$ = 0.033 films with porous microstructures. At ***AT*** = 950ºC condition, only several small (dimeter < 5 μm) spots (the dark contrast zones in **Figure 5.17a**) are crystallized into α-quartz phase and are very sparsely distributed. The rest of the surface outside these spots is amorphous and covered with Sr droplets which can be explained more in detail with the help of BSE image at high magnification (see **Figure 5.17c**). With ***AT*** increasing to 975ºC, the crystallization is much more significant. Under this condition, the crystalline spots grow and overlap mutually (shown as the dark zones in **Figure 5.17b**), but the crystallization is still incomplete. This is because there are some amorphous areas out of spots which can be distinguished more easily in the magnified BSE image (see **Figure 5.17d**).

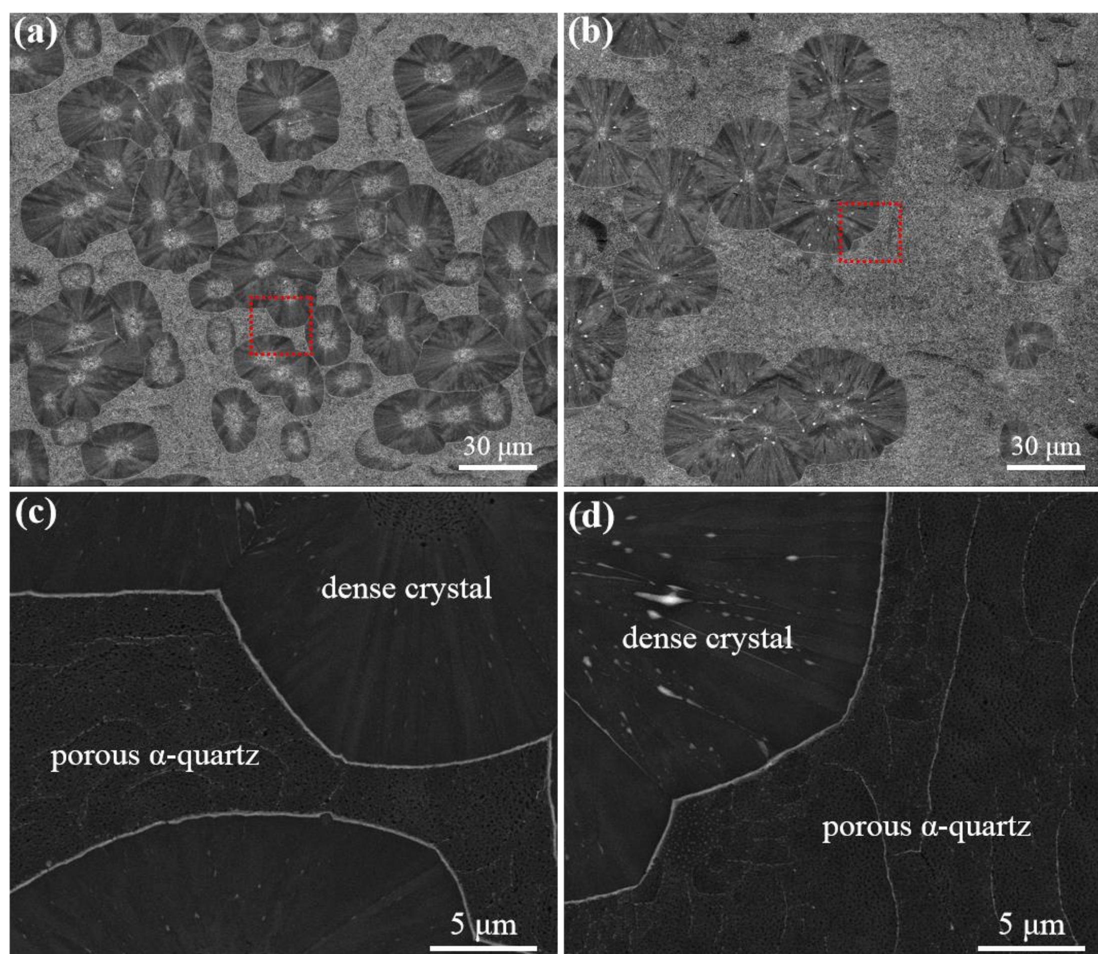

Figure 5.18. SEM images to show the microstructures of $\boldsymbol{R}_{\mathrm{Sr}}$ = 0.033 films at ***AT*** = 1025ºC and 1050 ºC conditions: **(a)** and **(b)** are the secondary electron images of ***AT*** = 1025ºC and 1050ºC films, respectively. **(c)** and **(d)** are the BSE images of red dashed zones in **(a)** and **(b)** respectively.

Then, **Figure 5.18** shows the SEM results of the dense crystal films made by low Sr content ($\boldsymbol{R}_{\mathrm{Sr}}$ = 0.033) but annealed at higher temperatures (***AT*** = 1025ºC and 1050ºC).

As discussed before, this kind of dense crystals (see **Figure 5.18a** and **b**) are different to the ones obtained by increasing $\boldsymbol{R}_{\mathrm{Sr}}$ (0.038 - 0.1) at ***AT*** = 1000ºC condition: these are larger in size but more sparsely distributed, especially for the ***AT*** = 1050ºC condition. Another difference is that, as can be seen in the BSE images (**Figure 5.18c** and **d**), at ***AT*** = 1050ºC condition the areas around the dense crystals consist of a porous α-quartz microstructure instead of being amorphous. A plausible explanation of this sort of dense crystal microstructure is that Sr can difuse more easily under higher temperatures. So, Sr accumulates in specific locations making possible the recrystallization which results in dense crystals, as in the usual recrystallization mechanism. Outside these areas there is a smaller quantity of Sr but which allows the growth a porous α-quartz microstructure under higher ***AT***.

5.2.2. The influence of ***AT*** on the crystallization of dense films $\boldsymbol{R}_{\mathrm{Sr}}$ region

After studying the influence of ***AT*** on films prepared with a low Sr to Si ratios ($\boldsymbol{R}_{\mathrm{Sr}}$ = 0.033), I have studied the influence of ***AT*** on the high $\boldsymbol{R}_{\mathrm{Sr}}$ region which typically yields a dense crystal microstructure upon crystallization. This was investigated by preparing 9 films with $\boldsymbol{R}_{\mathrm{Sr}}$ = 0.05 and using the different annealing temperatures from 900ºC to 1100ºC. Optical microscopy images of these films are presented in **Figure 5.19**.

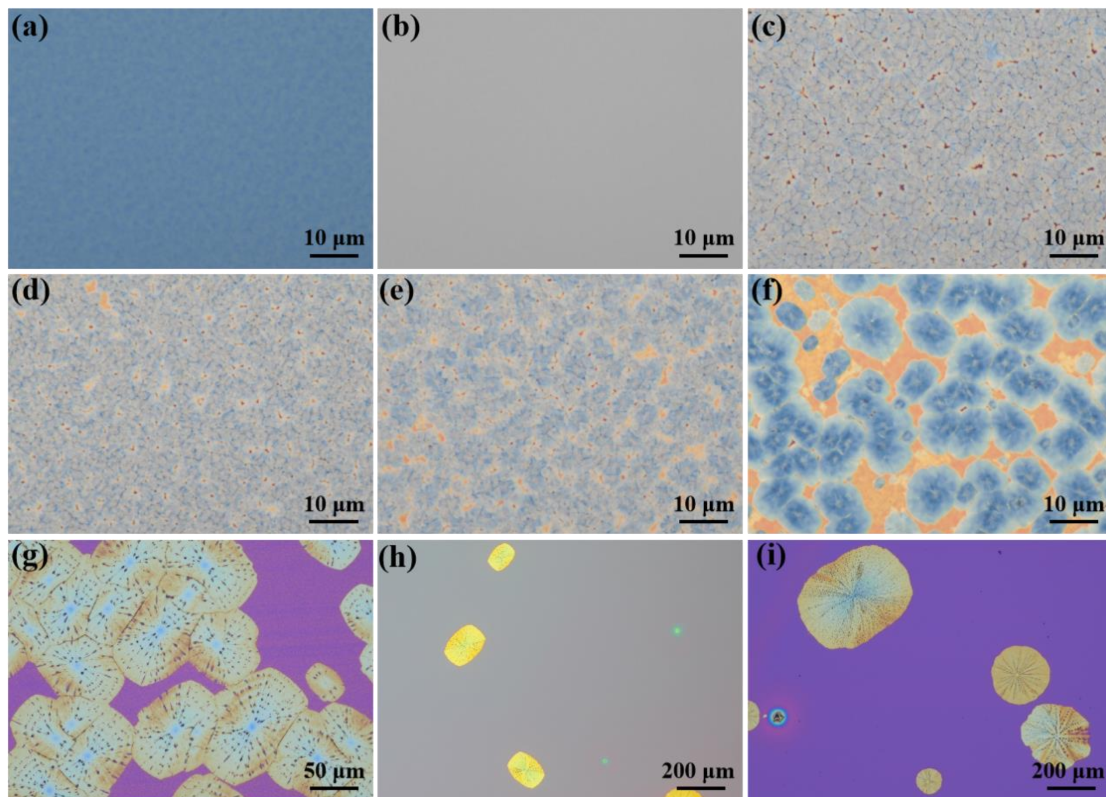

Figure 5.19. Optical microscopy images of films with $\boldsymbol{R}_{\mathrm{Sr}}$ = 0.05 after devitrification treatments at different ***AT***: **(a)** 900ºC, **(b)** 925ºC, **(c)** 950ºC, **(d)** 975ºC, **(e)** 1000ºC, **(f)** 1025ºC, **(g)** 1050ºC, **(h)**

1075ºC, **(i)** 1100ºC.

When ***AT*** is lower than 950ºC (see **Figure 5.19a** and **b**), crystals are not visible by optical microscopy, which indicates that the crystallization has not started or is very weak. However, when ***AT*** reaches 950ºC and 975ºC, the crystallizations are complete (see **Figure 5.19c** and **d**), and the images are quite similar to those of the typical dense crystals obtained ***AT*** = 1000ºC which are shown in **Figure 5.19e** for comparison. Then, with ***AT*** at 1025ºC (see **Figure 5.19f**), the dense crystals become larger and sparser similarly to what we have already discussed in earlier in this chapter for the films with R_{Sr} = 0.033 (see **Figure 5.15f** and **g**). Once ***AT*** reaches 1050ºC or higher, the dense crystals present a different shape and surface (the yellow rectangular zones in **Figure 5.19g-i**, which is similar to **Figure 5.15h** and **i** for the R_{Sr} = 0.033 condition, and they become huge and very sparse at higher ***AT***.

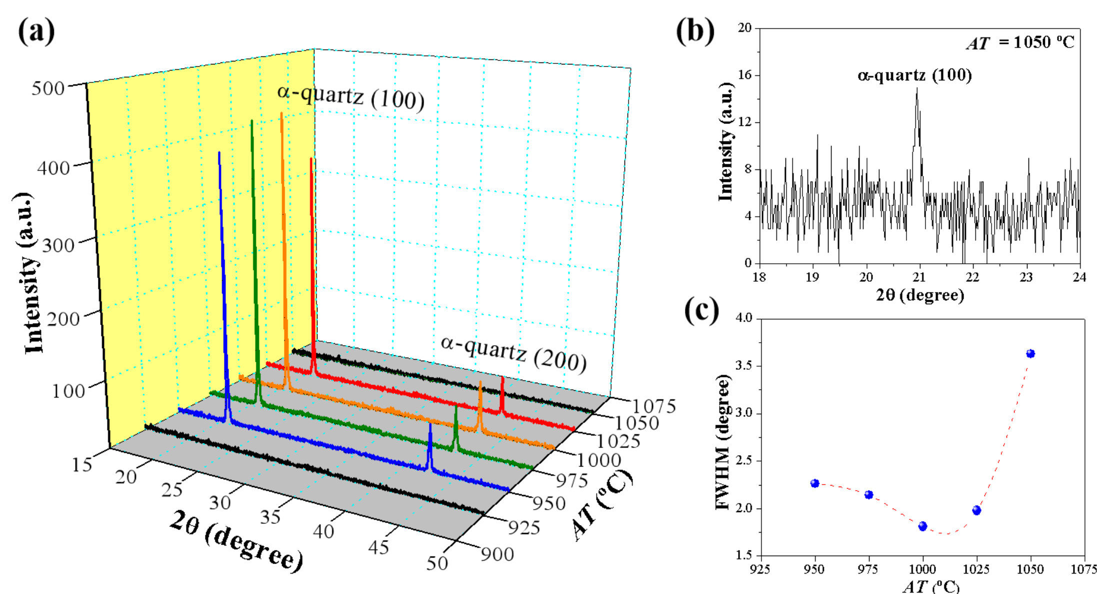

Figure 5.20. Crystallinity of as-prepared R_{Sr} = 0.05 films with different ***AT*** (925ºC to 1050ºC): **(a)** XRD θ-2θ patterns. **(b)** XRD θ-2θ pattern of ***AT*** = 1050ºC film showing the α-quartz(100) peak. **(c)** FWHM measurements of the α-quartz(100)rocking curves for as-prepared R_{Sr} = 0.05 films with different ***AT***.

The crystallinity study of R_{Sr} = 0.05 films annealed with different ***AT*** is summarized in **Figure 5.20**. The films only can be well crystallized between 950ºC and 1025ºC according to their strong signals in the θ-2θ diffractograms (see **Figure 5.20a**). The film annealed at ***AT*** = 1025ºC shows a smaller response because the dense crystals in the film is a bit sparser. The ***AT*** = 1050ºC film is also crystallized but very slightly (the tiny signal is shown specifically as **Figure 5.20b**). Besides, the FWHM results (see **Figure 5.20c**) tell us that the value is slowly declining (from 2.25º to 1.75º) when ***AT*** increases from 950ºC to 1000ºC, which means that the film is a bit more mono-orientated with ***AT*** increasing. But the value increases again to 2º when ***AT*** reaches

1025ºC. In general, all the conditions show a low FWHM value (around 2º) corresponding to films characterized by the presence of dense quartz crystals except for the film treated with ***AT*** = 1050ºC for which the FWHM is increased to above 3.5º.

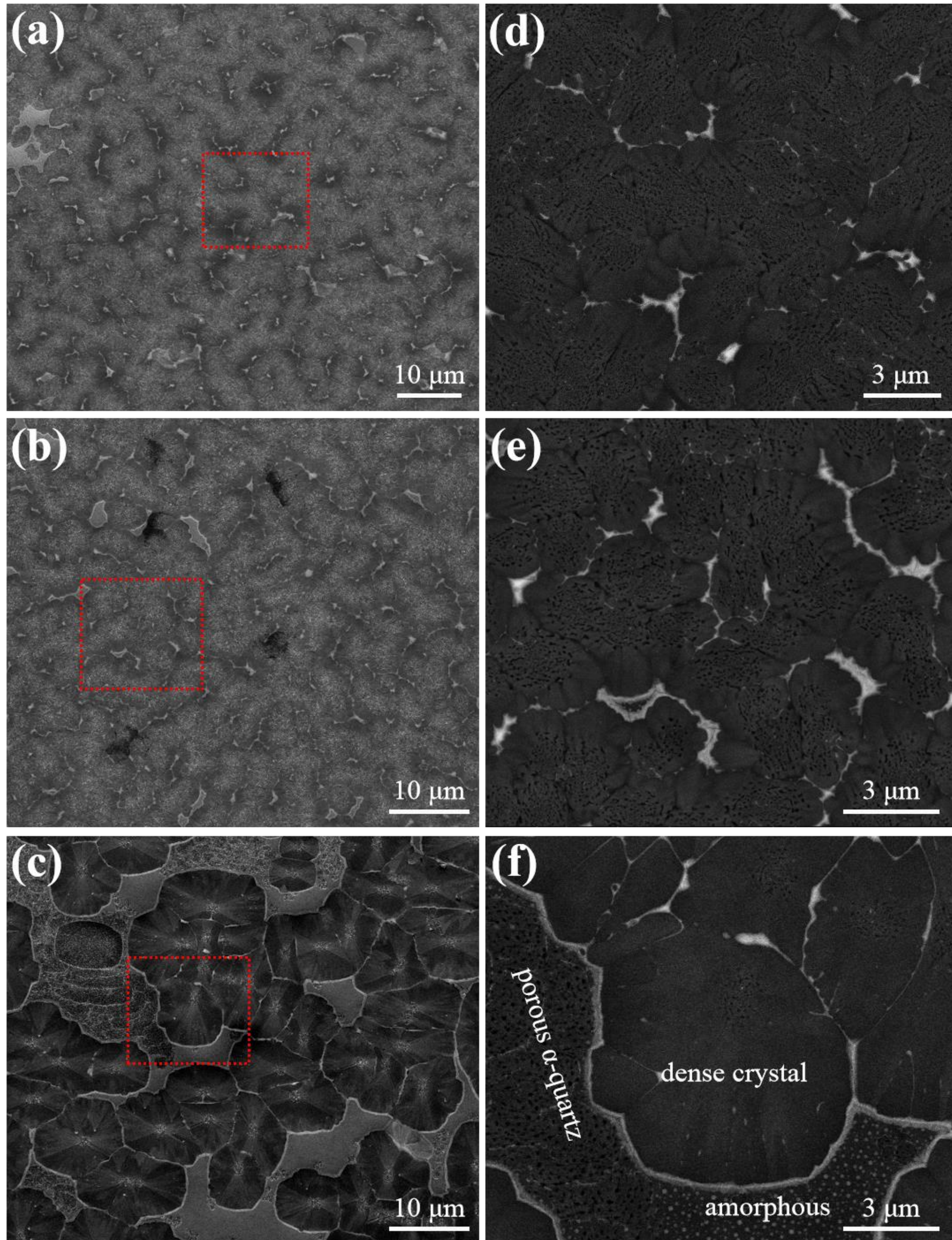

Figure 5.21. SEM images to show the microstructures of $\boldsymbol{R}_{\mathrm{Sr}}$ = 0.05 films at ***AT*** = 950ºC, 975ºC and 1025ºC conditions: **(a)** - **(c)** are the secondary electron images for ***AT*** = 950ºC, 975ºC and 1025ºC films, respectively. **(d)** - **(f)** are the BSE images of red dashed zones in **(a)** - **(c)**,

respectively.

The $\boldsymbol{R}_{Sr}$ = 0.05 films treated at ***AT*** = 950ºC, 975ºC and 1025ºC conditions are studied by SEM secondary electron images and BSE images in high magnification due to their strong diffraction response showing a better crystallinity, and the images are presented in **Figure 5.21**. For the films treated with ***AT*** lower than 1000ºC (950ºC and 975ºC), the secondary electron images (see **Figure 5.21a** and **b**) show that the microstructures are still predominantly porous. This is because there is no Sr-rich line network which can give rise to a wide densification. Instead, the distribution of Sr-rich zone is limited and disconnected (see BSE results shown in **Figure 5.21d** and **e**), which indicates that the mobility of Sr is not very important at these low temperatures.

For ***AT*** above 1000ºC, only in the case of ***AT*** = 1025ºC the film is well crystallized into a dense crystal microstructure. However, the dense crystals are less overlapped and the areas outside the dense crystals are larger than the ones prepared with ***AT*** = 1000ºC (see **Figure 5.21c**). According to the BSE image (see **Figure 5.21f**). The outside surface is separated into two different topographies. Some parts outside dense crystalized zones present a typical porous microstructure and are not covered by Sr droplets while the rest of the surface is covered by Sr droplets. All these different topographies can indicate that the Sr-assisted devitrification is not homogeneous and not synchronized at high ***AT*** condition.

5.2.3. Investigation of crystallization at extra ***AT*** conditions

To complete the studies on the effect of different annealing temperatures on the crystallization of both $\boldsymbol{R}_{Sr}$ = 0.033 and 0.05 films (see **Figure 5.16** and **Figure 5.20**), it is important to mention that not all ***AT*** can support an effective crystallization. It is easy to see that crystallization under low ***AT*** such as 900ºC and 925ºC does not occur. This could be due to the fact that the Sr-rich liquid has not been already formed or is with high viscosity. Another reason could be related to the reactivity of Sr ions which may not be sufficient to break the siloxane bonds and promote the SiO_2 devitrification. However, if ***AT*** is too high (i.e. in the region from 1050ºC to 1100ºC), the films present very sparse huge dense crystals which do not give any signal in is XRD.

Aiming to confirm this, the $\boldsymbol{R}_{Sr}$ = 0.05 films crystallized at ***AT*** = 1050ºC and 1100ºC were analyzed byElectron backscattered Diffraction (EBSD) point test. The results are summarized in **Figure 5.22**. Point A was chosen for the test of dense crystals of ***AT*** = 1050ºC film (see **Figure 5.22a**), and although the signal is too weak to be clearly seen (as the inset pictures of **Figure5.22**, the diffraction patterns only can be observed after increasing the contrast 10 times.), it can be assigned to α-quartz phase using the EBSD analysis software. However, the EBSD pattern does not correspond to the

orientation of α-quartz observed in the epitaxial films prepared in my PhD research. This, together with the fact that the EBSD signal is much weaker than the one observed in standard films (for instance see **Figure 4.2e** in **Chapter 4**), indicates that there is a very small amount of quartz and is not occupying the whole film thickness as in the case of the epitaxially grown crystals.

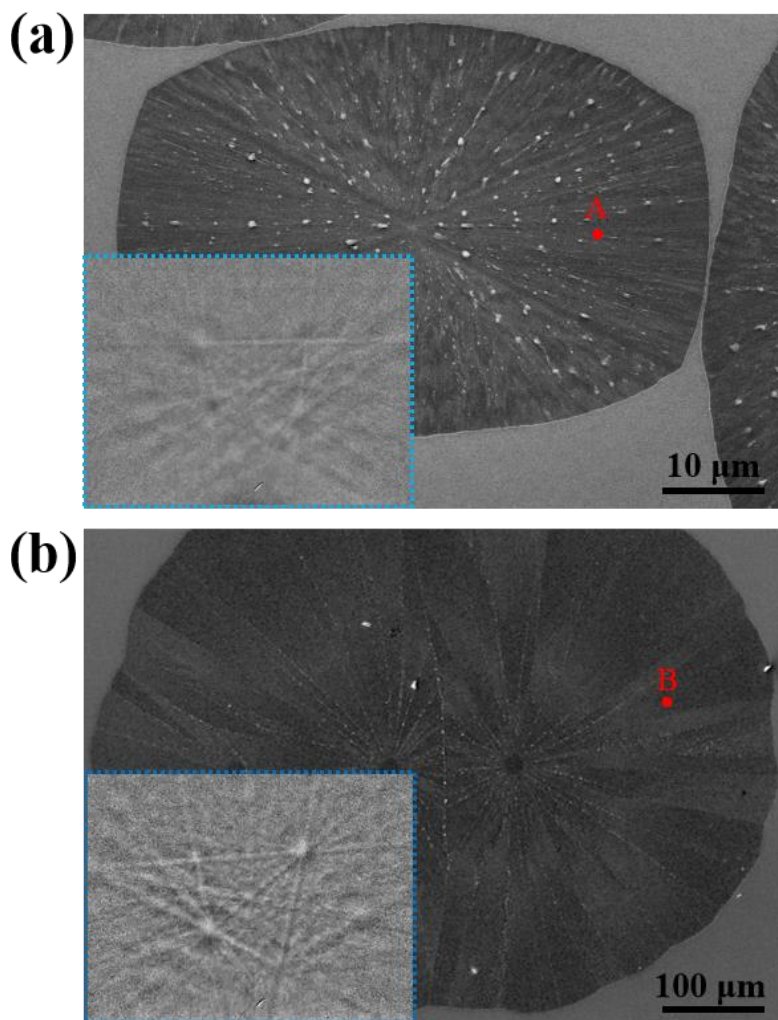

Figure 5.22. EBSD analysis of the films crystallized above 1025ºC for ($\boldsymbol{R}_{Sr}$ = 0.05): **(a)** The EBSD result for ***AT*** = 1050ºC. The red point A in the SEM image shows the test position, and the inset image surrounded by blue dotted line is the corresponding result of point A but after adding the contrast for 10 times. **(b)** The EBSD result for ***AT*** = 1100ºC. The red point B in the SEM image shows the test position, and the inset image surrounded by blue dotted line is the corresponding result of point B but after adding the contrast for 10 times.

The same characteristics are also found for the crystals grown at ***AT*** = 1100ºC condition. The result in **Figure 5.22b** shows that Point B, which is inside a dense crystal, is very thin for its tenuous response. From this EBSD tests, we can conclude that at these high temperatures (1050ºC and 1100ºC) the few crystals that are formed are huge in the lateral dimensions on the film surface, but presumably very thin along

the film normal.

5.3. Perforations caused by water-induced phase separation

Besides $\boldsymbol{R}_{\mathrm{Sr}}$, $\boldsymbol{T}_{\mathrm{gel}}$ and ***AT***, in my PhD work, other parameters such as relative humidity (RH) and type of surfactant cannot control the Sr inside film directly. However, these can play an important role to determine the formation of film and indirectly impact on the crystallization. One example of this are the perforations of the film which are provoked by the separation of water and organic phases on the wet gel layer of film during withdrawal, which both create micron size pores that change the appearance of film and impact the crystallinity by altering the distribution of Sr inside the films.

5.3.1. Water-induced phase separation

A previous work [5] shows that the films can be perforated into micron size pores in a process which is mainly controlled by relative humidity (RH) and the type of surfactant. This perforation is caused by the water-aggregation on the condensed sol layer as a result of a phase separation of water and organic phases, which is called as water-induced phase separation. According to the previous study on this phenomenon, the perforation made by water-induced phase separation can be explained as **Figure 5.23** illustrates.

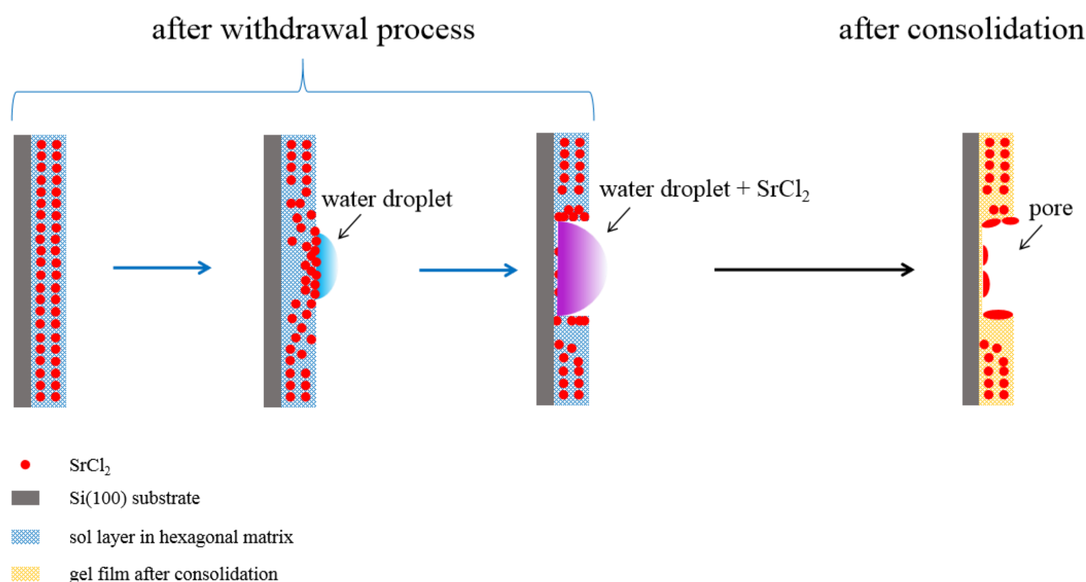

Figure 5.23. Schematics of mechanism of perforation driven by a water-induced phase separation.

To start a water-induced phase separation, the surfactant plays an essential role. In my work, the surfactant used by default has been Brij-58, which can form a hexagonal micelle microstructure to stabilize the homogeneous distribution of $SrCl_2$ once the wet gel film is fabricated after withdrawal process (as the first step in **Figure 5.23**). When the ambient RH is high enough, this hexagonal silica matrix absorbs the ambient

water in order to reduce the surface tension [6]. Thus, water droplets are formed on the surface of sol layer and induce the $SrCl_2$ aggregation at the droplet interface, as this salt is hydrophilic (second step in the schematic). Simultaneously, a sort of ionic surfactant/anion/metal cation assembly is formed to produce a $[(Brij\text{-}58)^{-}/Cl^{-}/Sr^{2+}]$ membrane while the absorption of water continues in order to minimize the surface tension. Hereby, the increase of water droplet can dissolve and break the sol layer and make a separation of salt-containing water phase and silica matrix phase (see the third step in **Figure 5.23**). Finally, after the drying of water phase via consolidation, the droplet area remains a large perforated pore with some agglomerates of Sr (see the last step in the schematic).

Based on the mechanism of water-induced phase separation, the perforation of film can be controlled by $\boldsymbol{R}_{Sr}$ and RH as always with the same surfactant (Brij-58). Considering that $\boldsymbol{R}_{Sr}$ is also the key parameter to determine the film microstructure, the study of perforation should be divided depending on the microstructure of film. Thus, in my study, the perforation caused by water-induced phase separation was investigated by using the typical porous film ($\boldsymbol{R}_{Sr}$ = 0.033, $\boldsymbol{U}_w$ = 5 mm/s and $\boldsymbol{AT}$ = 1000ºC) and dense film ($\boldsymbol{R}_{Sr}$ = 0.05, $\boldsymbol{U}_w$ = 5 mm/s and $\boldsymbol{AT}$ = 1000ºC) respectively. All other parameters are at their optimized conditions, which are described in more detail in **Section 3.2**.

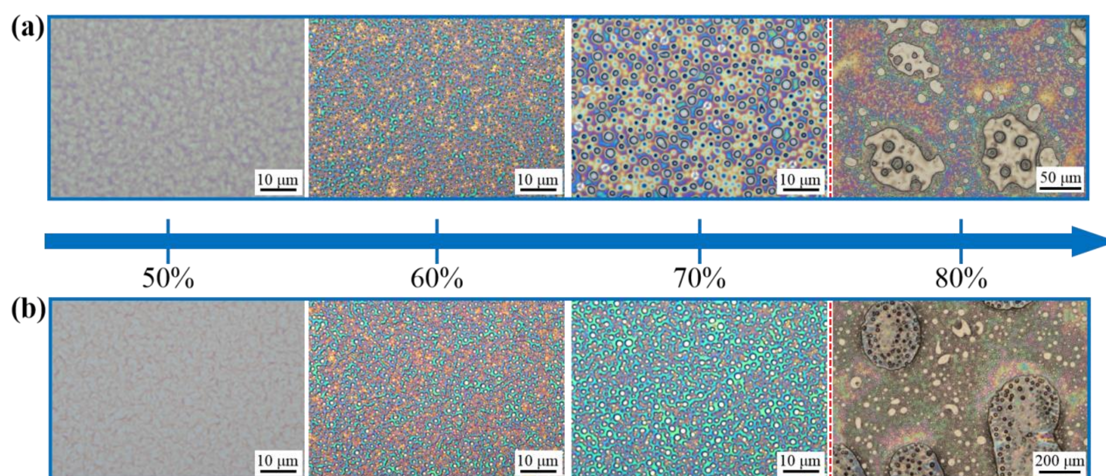

Figure 5.24. Optical microscopy of as-prepared gel films showing the perforation effects at different RH: **(a)** porous film series ($\boldsymbol{R}_{Sr}$ = 0.033), **(b)** dense film series ($\boldsymbol{R}_{Sr}$ = 0.05). The corresponding RHs are marked on the blue arrow.

Figure 5.24 displays the optical microscopy images of as-prepared gel films under different RHs. In general, both the porous and dense film conditions maintain the same evolution with increasing RH: The films do not present pores induced by phase separation at RH = 50% (the first pictures of **Figure 5.24a** and **b**), which indicates that the RH is too low to provide a wet surrounding to start the water absorption. The

perforation appears for all films from RH = 60% (second image of **Figure 5.24a** and **b**), and then goes more effective at RH = 70% for which the sizes of the perforations are increased (third image of **Figure 5.24a** and **b**). Unfortunately, the films are broken by the formation of huge spherical holes when RH is as high as 80% (last pictures of **Figure 5.24a** and **b**), which should be avoided, because the soft sol film is destroyed by dissolving under this extremely wet ambient.

Although the general tendencies of both porous and dense microstructures are the same, the perforation patterns for different film conditions are different. For instance, at RH = 70%, the dense film shows a more crowded and homogeneous distribution of perforations than the porous one. However, the optical microscopy images of gel films only can show some basic features of perforation. Therefore, the SEM analyses of crystallized films are needed to know the influence of perforation on the different microstructures of films.

5.3.2. Perforation of porous film

As mentioned, the perforation caused by water-induced phase separation not only makes a microporous pattern for the shape of film but can also impact the crystallinity by changing the distribution of Sr inside the films. Firstly, porous microstructure ($\boldsymbol{R}_{Sr}$ = 0.033) was studied to show this influence, and the SEM results are presented in **Figure 5.25**.

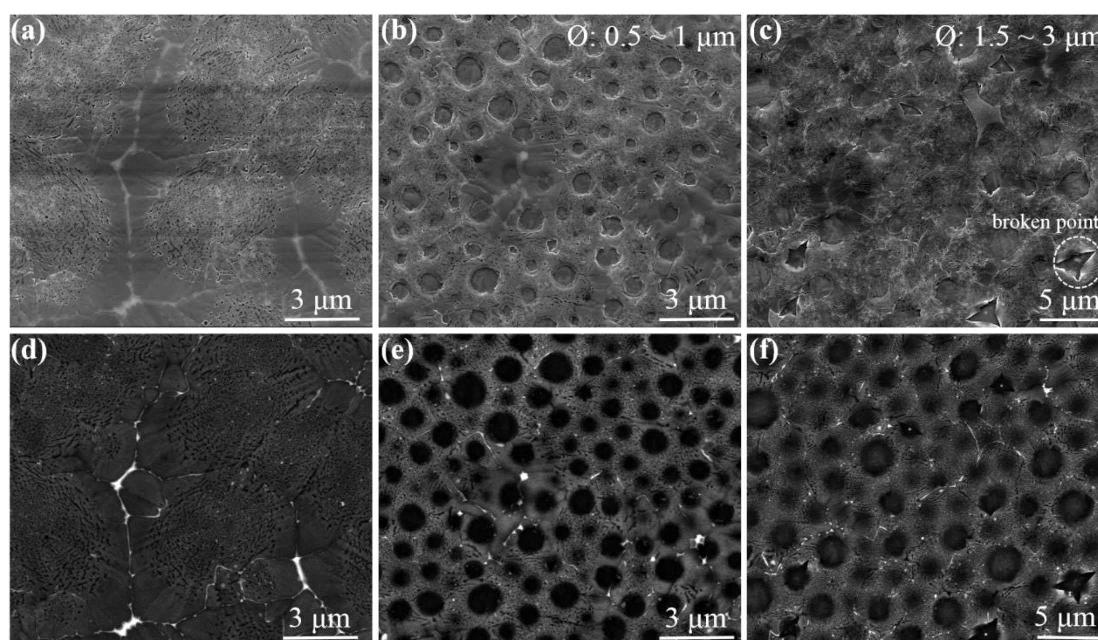

Figure 5.25. SEM analyses of the perforation effect for $\boldsymbol{R}_{Sr}$ = 0.033 films: **(a)** - **(c)** are the SE images of as-prepared α-quartz films with the RH of **(a)** 50%, **(b)** 60% and **(c)** 70%. **(d)** - **(f)** are the corresponding BSE images of **(a)** - **(c)** to show the distribution of perforations and Sr.

It is clearly seen that the dense α-quartz zone occupies a certain proportion (see

Figure 5.25a) with an area coverage reaching 33% (obtained via the measurement of a 50 µm × 50 µm AFM image with the software Image J). This indicates that the film is closer to dense crystal microstructure than to typical porous microstructure as the one displayed in **Figure 4.25a** in **Chapter 4**. The corresponding BSE image (see **Figure 5.25d**) also shows the effective densification which has occurred thanks to the concentrated Sr agglomerates that have been formed. However, perforation does not occur at this RH. Most likely this is because the size of water clusters is tiny and cannot dissolve the gel film. But since these clusters are effective in catching the Sr which accumulates at the water interface, then the aggregation of Sr is promoted, and this makes possible the α-quartz densification by recrystallization.

When RH increases to 60%, the images present a typical distribution of perforatingpores with a dimeter of about 0.5 - 1 µm (see **Figure 5.25b** and **e**). The microstructure of films is still porous because the Sr aggregation is not very important as can be observed in BES images (see **Figure 5.25e**). At RH = 70% condition, the size of micropores has tripled with the diameter of about 1.5 -3 µm and displays a larger polydispersity. The topography is very rugged (see **Figure 5.25c**) and the microstructure is kept as porous for the same reason as in the case of the film with RH = 60% (see **Figure 5.25f**). Besides, some of the perforations with a dimeter around 3µm are dehiscent after crystallization because of their strong surface tension.

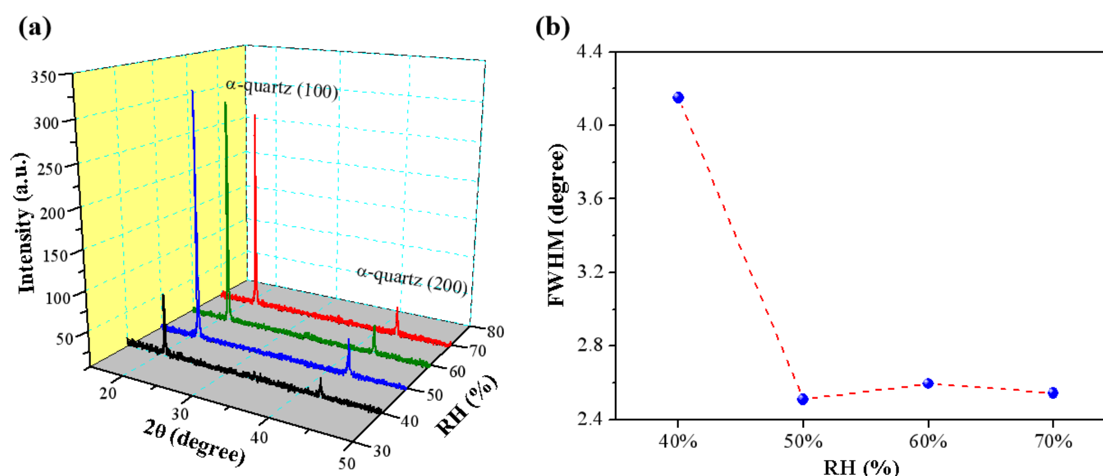

Figure 5.26 Crystallinity study of R_{Sr} = 0.033 films prepared under different RHs: **(a)** XRD θ - 2θ patterns **(b)** FWHM of rocking curve measurements.

The XRD θ - 2θ patterns (see **Figure 5.26a**) of R_{Sr} = 0.033 films with different RHs shows that the crystallinity of α-quartz phase has a qualitative leap when RH is above 40%. It makes sense since for RH = 50% the film shifts its microstructure into a dense-like one, which is responsible for the substantial increase of XRD response. However, for the perforated films (RH = 60% and 70%) the intensity of the reflections only shows a slight decrease which can be attributed to the lost area of epitaxial α-

quartz due to the presence of a certain area of perforations. So, in fact the films are actually also dominated by dense microstructures, but the perforation breaks the topography. The FWHM of the rocking curves also indicates the microstructural threshold at RH=50% with the characteristic low mosaicity of the dense structures appearing at this value and above it.

5.3.3. Perforation of dense films

For the dense crystal condition ($\boldsymbol{R}_{Sr}$ = 0.05), the microstructure of film has a similar evolution with increasing RH. The SEM analyses of as-prepared $\boldsymbol{R}_{Sr}$ = 0.05 films are displayed in **Figure 5.27**. At 50% RH, the film does not present perforations, but the dense crystals are less connected and occupy a smaller surface area of the film compared to the films prepared at RH=40% (see **Figure 5.27a**). This is equivalent to the shift of microstructure observed by increasing $\boldsymbol{R}_{Sr}$ directly (see the study of **Section 4.1.3**). The thick Sr-lines observed in BSE image (see **Figure 5.27d**) confirm an important presence of one-side densification which is only observed in the dense films prepared by high $\boldsymbol{R}_{Sr}$ conditions.

When RH reaches 60%, the perforations occur and present diameters ranging from 0.3 μm to 0.75 μm, which are smaller than in the case of $\boldsymbol{R}_{Sr}$ = 0.033 films. The dense crystal pattern is observed, but the porous and dense microstructures can still be distinguished (see **Figure 5.27b**) together with some zones of Sr aggregates visible in light contrast in the BSE image (see **Figure 5.27e**). RH = 70% contains same distribution of dense and porous microstructure according to the SE image (**Figure 5.27c**) and Sr accumulations are visible in the corresponding BSE image (**Figure 5.27f**). However, the sizes of the perforations are very polydisperse, displaying a range of dimeters between 0.35 μm and 2 μm, and are smaller than the ones of porous series and thus are not dehiscent.

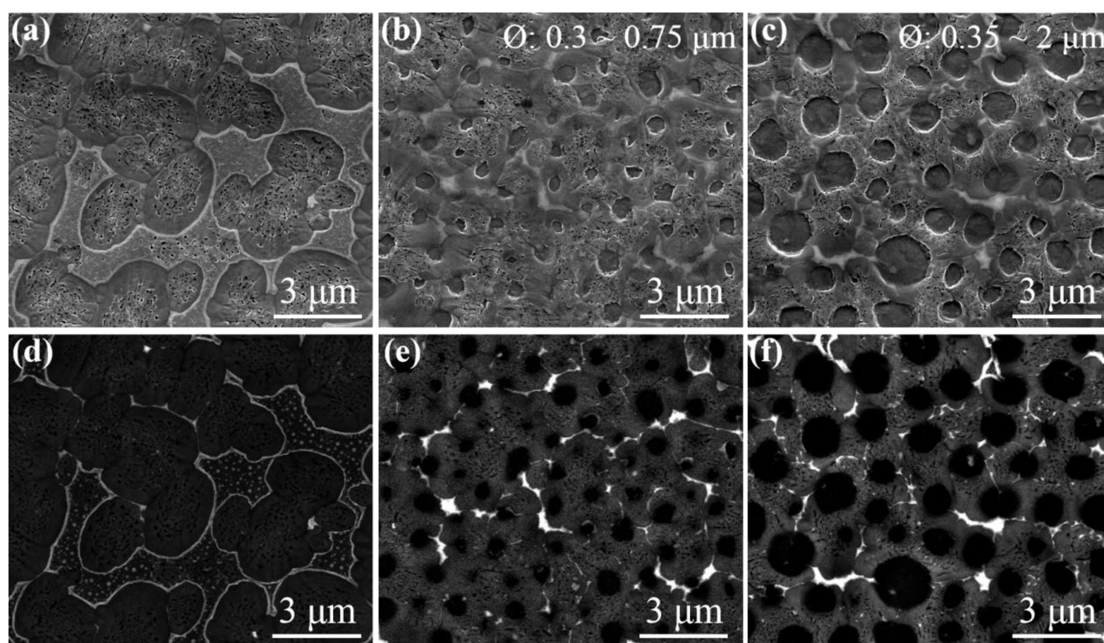

Figure 5.27. SEM analyses of the perforation effect in $\boldsymbol{R}_{\mathrm{Sr}}$ = 0.05 films: **(a)** - **(c)** are the SE images of as-prepared α-quartz films with the RH of **(a)** 50%, **(b)** 60% and **(c)** 70%. **(d)** - **(f)** are the corresponding BSE images of **(a)** - **(c)** to show the distribution of perforations and Sr.

The influence of perforation to the crystallinity for $\boldsymbol{R}_{\mathrm{Sr}}$ = 0.05 films was studied by XRD θ-2θ analysis and the FWHM of rocking curve measurements of α-quartz(100) peak. The results are summarized in **Figure 5.28**.

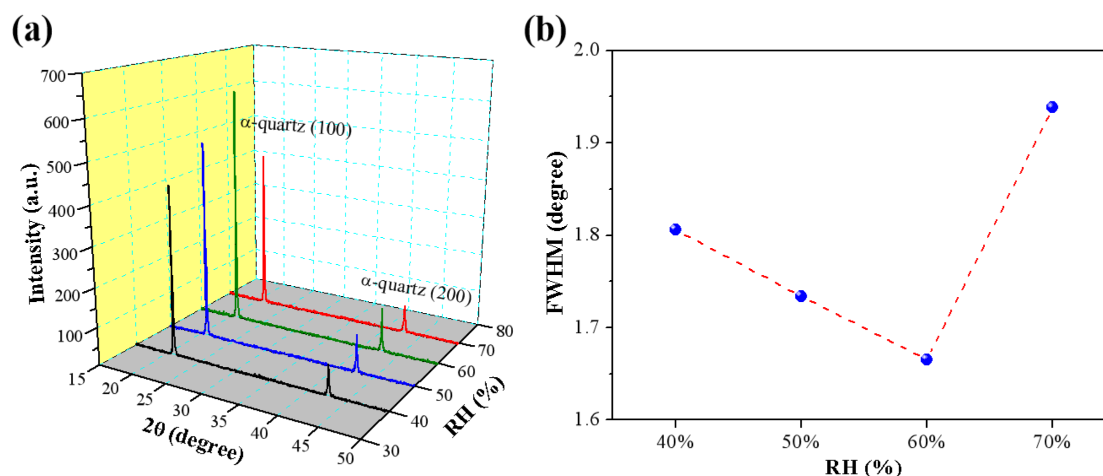

Figure 5.28 Crystallinity study of $\boldsymbol{R}_{\mathrm{Sr}}$ = 0.05 films prepared under different RHs: **(a)** XRD θ - 2θ patterns **(b)** FWHM of rocking curve measurements of α-quartz(100) peak.

The XRD θ - 2θ results (see **Figure 5.28a**) present a continuous increase of the reflection intensities with RH increasing from 40% to 60%. This means that the densification increases with the RH and indicates that the quantity loss of diffracting epitaxial α-quartz due to perforation is not obvious at RH = 60% and thus is

compensated by the increased crystallinity. However, for RH = 70%, the loss of epitaxial α-quartz phase due to the perforations is responsible for the decline of XRD signal. Correspondingly, the FWHM of rocking curves (see **Figure 5.28b**) shows that the mosaicity of α-quartz phase is improved a little with increasing of RH except for 70% condition. Even so, the differences in the FWHM values are very narrow and are in all cases below 2º, which shows that the α-quartz growth of dense dominated films can keep its low mosaicity regardless of RH.

5.3.4. The role of surfactant on the perforation of films

As discussed above, the perforation of films depends on the RH (which should be high enough to provide a water rich environment), the Sr salt (which is $SrCl_2$ in this Thesis) and surfactant (which is Brij-58). Among these three parameters, surfactant plays an essential role in two aspects. Firstly it is responsible for building a hexagonal silica matrix, which can pump water alike a sponge, to start the water-induced phase separation. Secondly, it makes a $[(\text{Brij-58})^-/Cl^-/Sr^{2+}]$ membrane at the interface between water and organic phases to prompt the absorption of water so that it can the final perforation can occur. To find further evidence of these two roles of Brij-58 in perforation of films, other two types of surfactant were tested for comparison.

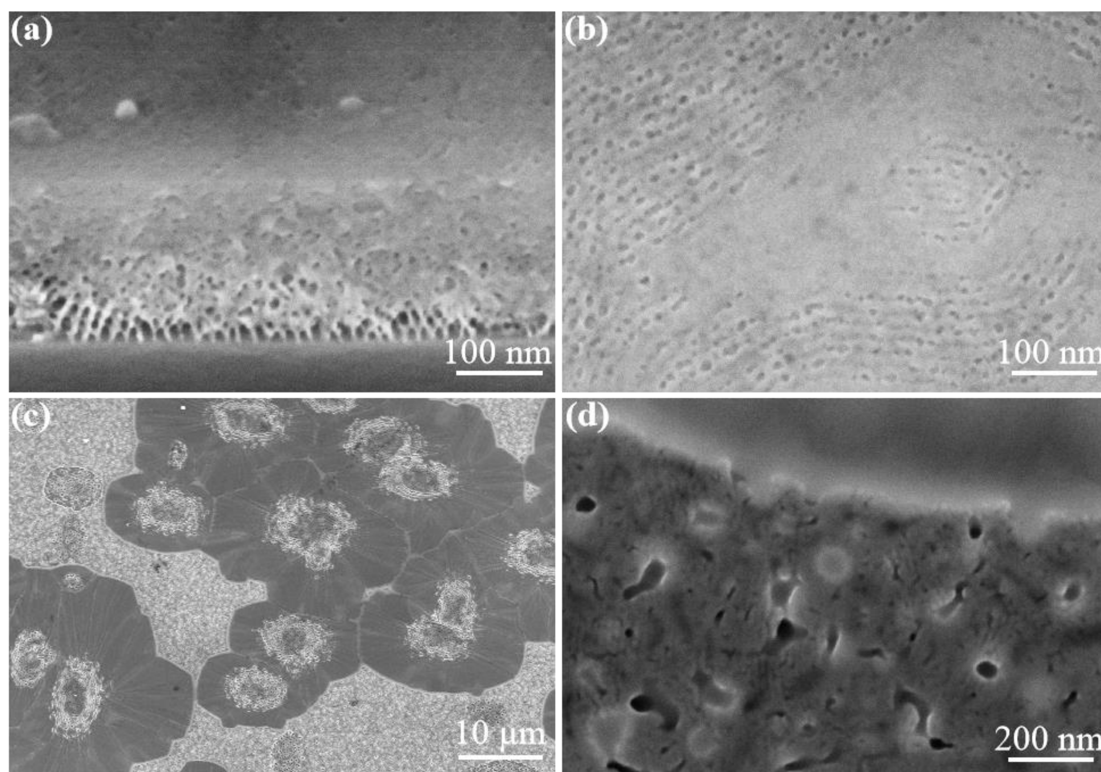

Figure 5.29. SEM images of the films prepared using F127 as surfactant at RH = 60% condition: **(a)** and **(b)** are the cross sections and surface of as-prepared gel film respectively to show the lamellar microstructure. **(c)** and **(d)** are the surface images of crystallized α-quartz film.

Firstly, F127 was used in the fabrication of $\boldsymbol{R}_{\mathrm{Sr}}$ = 0.05 films in replacement of of Brij-58 under RH = 60% condition to check if the perforation occurs. The SEM images of the as prepared films and after being annealed for 5 h at 1000ºC are shown in **Figure 5.29**. F127 is a classical surfactant for lamellar microstructure. So, the as-prepared gel film presents a typical lamellar pattern which is shown in **Figure 5.29a** and **b**. Unlike the hexagonal porosity of Brij-58 surfactant, the lamellar porosity is closed and does not present the capacity of absorbing water and thus can lock the Sr more effectively, as indicated by the sparse distribution of dense crystals on the surface of the crystalized film (see **Figure 5.29c**) due to the fact that Sr cannot easily move within the film during thermal annealing. Note that F127 is not a cationic surfactant and thus cannot form the [ionic surfactant/Cl^-/Sr^{2+}] assembly which allows maintaining the absorption of water for completing the perforation. As a result, the crystallized film does not present perforations and the lamellar array of silica is preserved (see **Figure 5.29d**).

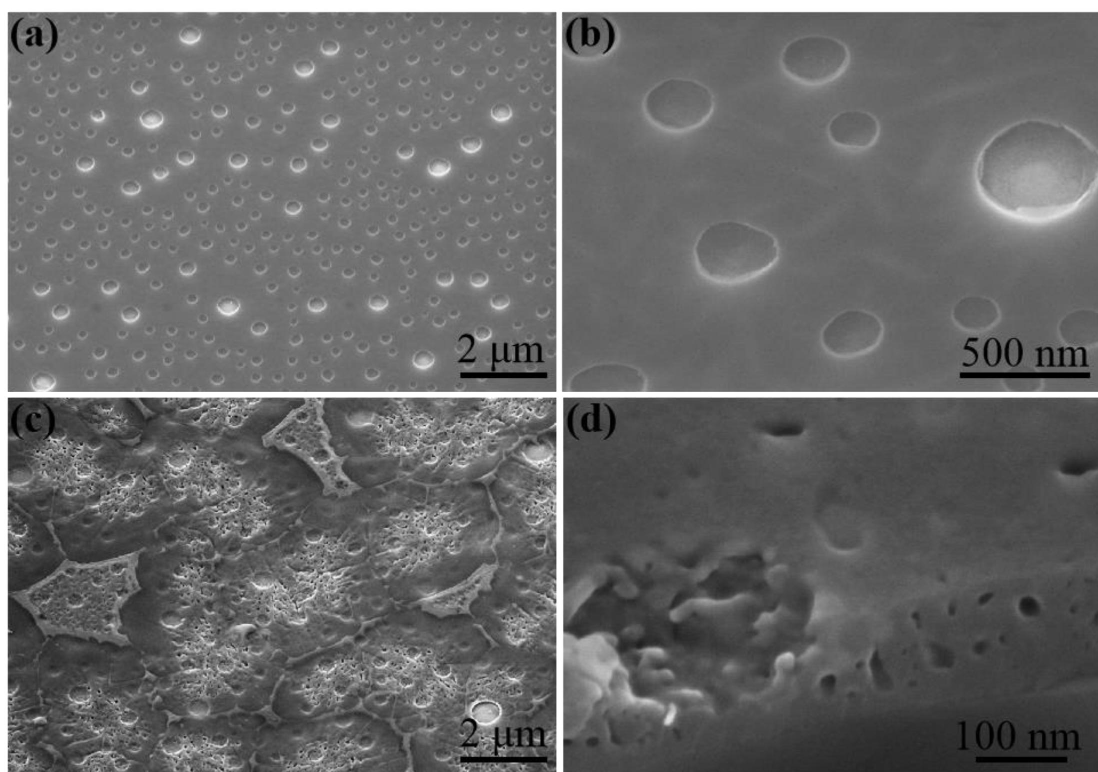

Figure 5.30 SEM images of films with CTAB at RH = 40% condition: **(a)** and **(b)** are the surface images of as-prepared gel film displaying the perforations. **(c)** is the surface image of crystallized α-quartz film. **(d)** is a high magnification image to show a single micropore remaining after crystallization.

Then, CTAB surfactant was also tested for its strong ionic character as well as its formation of hexagonal micelles in the films. Films with $\boldsymbol{R}_{\mathrm{Sr}}$ = 0.05 were prepared by using CTAB under RH = 40% condition and the SEM images of the as-prepared and crystallized films are presented in **Figure 5.30**. The images of as-prepared gel films

(see **Figure 5.30a** and **b**) show that the perforation is significant, which indicates that the further adsorption of water can be achieved even at low RH in comparison with the films prepared with Brij-58 for which the perforations did not occur at RH=40%. This is due to the fact that the [CTA^+/Cl^-/Sr^{2+}] assemblies are more easily and widely formed at the silica-water interfaces. Note that the perforated surface remains after the crystallization (see **Figure 5.30c** and **d**).

Hence, a suitable surfactant is a key ingredient for controlling the quartz film microstructure. Brij-58 has been chosen because it allows controlling the water phase separation, in contrast to CTAB, for which the phase separation cannot be avoided and F127 which does not allow obtaining phase separated films. The versatility displayed by Brij-58 in these regards is related to its capacity to form hexagonal micelles and being partly ionized in water [6] . This can help controlling the microstructure and altering the topography of the films to eventually include micron-size perforations with the cooperation of RH and $\boldsymbol{R}_{\mathrm{Sr}}$.

5.4. Chapter conclusion

In this chapter, we investigated the control of three important parameters for the film crystallization. In addition to the direct control through $\boldsymbol{R}_{\mathrm{Sr}}$, the thickness of gel film ($\boldsymbol{T}_{\mathrm{gel}}$), annealing temperature (***AT***), relative humidity (RH) and type of surfactant can also very important to control the microstructure of α-quartz films by affecting the Sr distribution inside the film.

$\boldsymbol{T}_{\mathrm{gel}}$ was firstly studied because it is the main route to adjust the total quantity of Sr inside the films by adding material once $\boldsymbol{R}_{\mathrm{Sr}}$ is fixed. $\boldsymbol{T}_{\mathrm{gel}}$ is controlled through the withdrawal rate ($\boldsymbol{U}_{\mathrm{w}}$) during dip-coating process, and their relationship fits the Landau-Levich Model. According to my research, the film is either partly crystallized for porous film condition ($\boldsymbol{R}_{\mathrm{Sr}}$ = 0.033) or inhomogeneous for dense crystal film condition ($\boldsymbol{R}_{\mathrm{Sr}}$ = 0.05) when $\boldsymbol{T}_{\mathrm{gel}}$ is in the mixed regime ($\boldsymbol{U}_{\mathrm{w}}$ = 1 to 3.5 mm/s). The main reason is that quantity and distribution of Sr is not good enough to enable a complete and homogenous crystallization when the gel film is thin and with ripples. For $\boldsymbol{U}_{\mathrm{w}} \geq 5$ mm/s, the crystallization goes quite well because the formation of gel film is perfect under the draining regime. The film microstructure can be altered by increasing $\boldsymbol{T}_{\mathrm{gel}}$, with a mechanism akin to the one at play when $\boldsymbol{R}_{\mathrm{Sr}}$ is increased and which in the end is related to the addition of Sr inside gel film. However, the maximum of $\boldsymbol{T}_{\mathrm{gel}}$ is 400 nm (for $\boldsymbol{U}_{\mathrm{w}}$ = 15 mm/s) because for larger $\boldsymbol{U}_{\mathrm{w}}$ the bottom part of the films are broken.

AT also should be considered because this parameter is the only route to provide the energy for crystallization. According to the results of this study, a higher ***AT*** can increase the mobility of Sr and its efficiency in breaking the siloxane bonds to promote devitrification and densification. In general, the Sr is not effective to start a

significant crystallization for low ***AT*** (900ºC - 950ºC). When ***AT*** is suitable for crystallization (950ºC - 1050ºC), there is always an evolution of microstructure from porous to dense no matter $\boldsymbol{R}_{\mathrm{Sr}}$ is 0.033 or 0.05. With ***AT*** one can achieve a microstructural control similar to that achieved by changing $\boldsymbol{R}_{\mathrm{Sr}}$ directly. However, the α-quartz phase cannot be obtained when ***AT*** is too high (> 1050ºC).

It is important to control the RH for creating perforations or avoiding its presence with the cooperation of surfactant and $SrCl_2$ inside film. When RH is high enough (≥ 60%), the perforation can be driven by the water-induced phase separation, and the surface of film presents large pores in the micron range. At the same time, the distribution of Sr is more aggregated, and the crystallinity of films is quite similar to that of a typical dense microstructure. Actually, the aggregation of Sr can be improved even when RH is not high enough to induce the perforation (RH = 50%), which can shift the film microstructure from porous to dense. However, the film will be broken by the formation of huge holes when RH is too high (RH = 80%). Moreover, an appropriate surfactant is an essential prerequisite to start the water-induced phase separation. A valuable surfactant, such as Brij-58, should make a hexagonal micelle microstructure and form the [ionic surfactant/Cl^-/Sr^{2+}] cluster to enable the continuous absorption of water.

After the studies presented in **chapters 4**, we know that the crystallization and microstructure of films can be controlled by $\boldsymbol{R}_{\mathrm{Sr}}$ without changing other parameters. Alternatively, in this chapter we have seen that the microstructure can also be controlled by other parameters during the synthesis. These results show that these parameters are also important giving more flexibility for microstructural control. For instance, we have seen that by only controlling $\boldsymbol{R}_{\mathrm{Sr}}$ one cannot get a porous microstructure with very small mosaicity, which is achieved when the film thickness is increased by using a high $\boldsymbol{U}_{\mathrm{w}}$.

5.5. Chapter references

1. Grosso, D., How to exploit the full potential of the dip-coating process to better control film formation. *Journal of Materials Chemistry* **2011,** *21* (43), 17033-17038.

2. Bindini, E., Naudin, G., Faustini, M., Grosso, D. Boissière, C., Critical role of the atmosphere in dip-coating process. *Journal of Physical Chemistry C* **2017,** *121*, 14572-14580.

3. Faustini, M.; Louis, B.; Albouy, P. A.; Kuemmel, M.; Grosso, D., Preparation of Sol-Gel Films by Dip-Coating in Extreme Conditions. *Journal of Physical Chemistry C* **2010,** *114* (17), 7637-7645.

4. Landau, L.; Levich, B., Dragging of a Liquid by a Moving Plate. *Acta Physicochimica U.R.S.S.* **1942,** *17* (1-2), 141-153.

5. Drisko, G. L.; Carretero-Genevrier, A.; Gich, M.; Gàzquez, J.; Ferrah, D.; Grosso, D.; Boissière, C.; Rodriguez-Carvajal, J.; Sanchez, C., Water-Induced Phase Separation Forming Macrostructured Epitaxial Quartz Films on Silicon. *Advanced Functional Materials* **2014,** *24* (35), 5494-5502.

6. Joos, P.; Van Hunsel, J., Adsorption Kinetics of Micellar Brij 58 Solutions. *Colloids and Surfaces* **1988,** *33* (1988), 99-108.

Chapter 6. Nanostructure Engineering of Piezoelectric α-Quartz Films

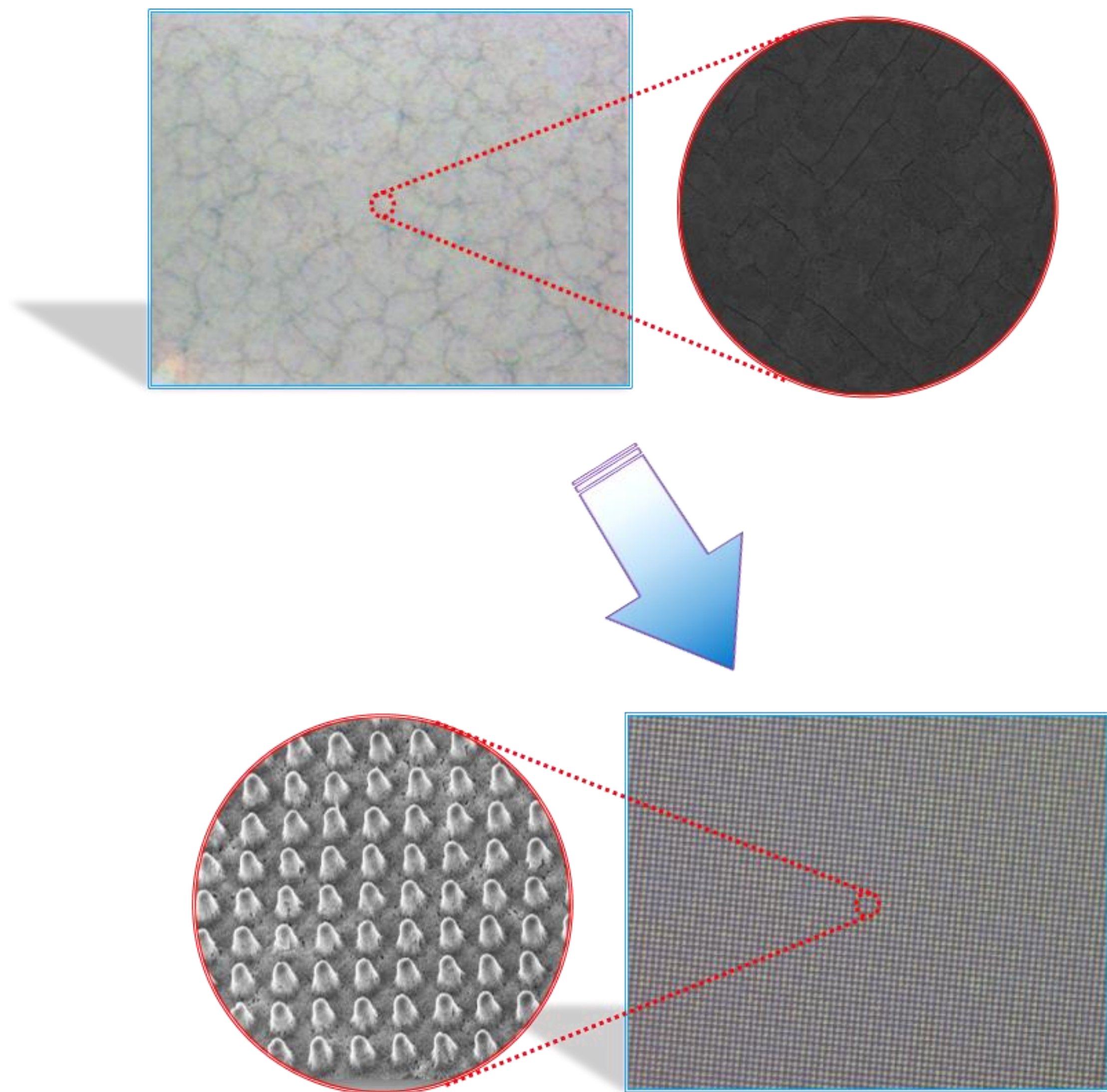

As we have seen in the two previous chapters, the microstructure of epitaxial α-quartz film on silicon can be tuned to finally improve its crystallinity. This feature can be reached by a simultaneous control of different parameters during synthesis. For instance, samples containing a Sr-doping level of $\boldsymbol{R}_{\mathrm{Sr}} = 0.05$ and thermally treated at $\boldsymbol{AT} = 1000$ºC have shown a microstructure based on dense high quality α-quartz crystals showing a lower value of mosaicity. Besides, it is possible to obtain ultra-flat dense 200 nm thick Sr-doped mesoporous silica gel films by selecting Brij-58 surfactant and using a constant withdrawal speed of $\boldsymbol{U}_{\mathrm{w}} = 5$ mm/s and a relative humidity condition of 40% to avoid the phase separation process described elsewhere [1].

My thesis work has consequently consisted in disentangling the epitaxial growth mechanism of α-quartz(100) films on silicon by a systematic study of the growth conditions above mentioned to fabricate an improved piezoelectric film required for the future dispositives. However, among the different optimized parameters, the thickness of the film remains the most important one since the piezoelectric frequency and signal will strongly depend on the final dimension of α-quartz. Up to now, I showed a chemical solution deposition process of α-quartz films limited to a maximum thickness value of 300 nm. For this reason, the development of an effective method able to control and increase the α-quartz film thickness until the micrometer scale is extremely important for applications.

This chapter aims at developing a multilayer deposition method to increase the final thickness of the films to micron range while maintaining the same crystal quality. Importantly, during this chapter it will show that the multilayer systems allow for the first time to the fabrication of ordered arrays of piezoelectric nanostructures by the combination of three cost effective lithographic techniques. This new development opens the opportunity to manufacture new high frequency resonators and high sensitivity sensors relevant in different fields of application [2, 3].

6.1. Integration of epitaxial α-quartz thick films via multilayer deposition

To exploit epitaxial α-quartz films in technological applications it is essential to increase the film thicknesses towards the micron range. In this section, I investigated the suitability of a multi-layer deposition approach: the sequential deposition and consolidation of several gel layers before a final annealing treatment to induce the epitaxial α-quartz growth. This novel method that was named as multilayer deposition, fixed the optimized lab conditions mentioned along the previous chapters. The experimental procedure is displayed in the **Section 3.2.2** of **Chapter 3**. This multilayer methodology is limited to 5-layer depositions, which offers 800 nm thick, before the appearance of cracks due to a strong surface tensile [4].

6.1.1. Multilayer deposition of films with dense microstructure

Taking advantage of the optimized growth conditions for a monolayer system, I developed the multilayer film synthesis that consists on the sequential deposition and consolidation of several gel layers before a final annealing treatment aiming to induce the epitaxial α-quartz growth. **Figure 6.1a** presents a series of SEM images corresponding to the cross sections of films consisting of 1 up to 5 layers after the crystallization treatment. One cannot distinguish the interfaces between successive layers and the thickness of the films increases linearly with the number of layers, reaching about 800 nm for the sample consisting of 5 layers.

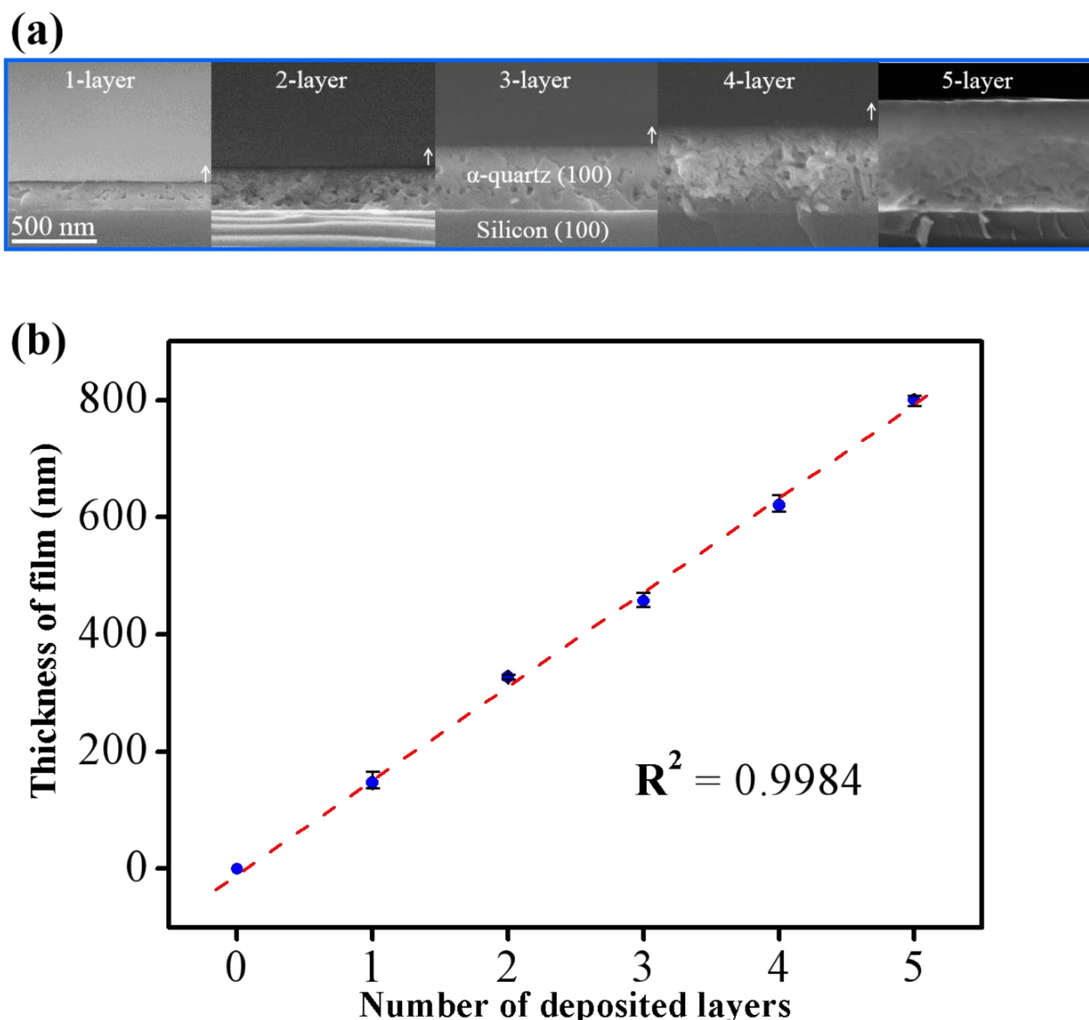

Figure 6.1. Thickness study of multilayer deposition: **(a)** SEM images of the cross-section of the as-prepared α-quartz films with different number of deposited layers. **(b)** The linear increasing of thickness with the adding the number of deposited layers.

Notice that the thicknesses of the different multilayer films correspond to the final α-quartz thicknesses plot in **Figure 6.1b**. The interval between each two nearby conditions is fixed around 170 nm, which is just the thickness of one monolayer..

The microstructure of multilayered films were observed by using SEM microscopy, as shown in **Figure 6.2**.

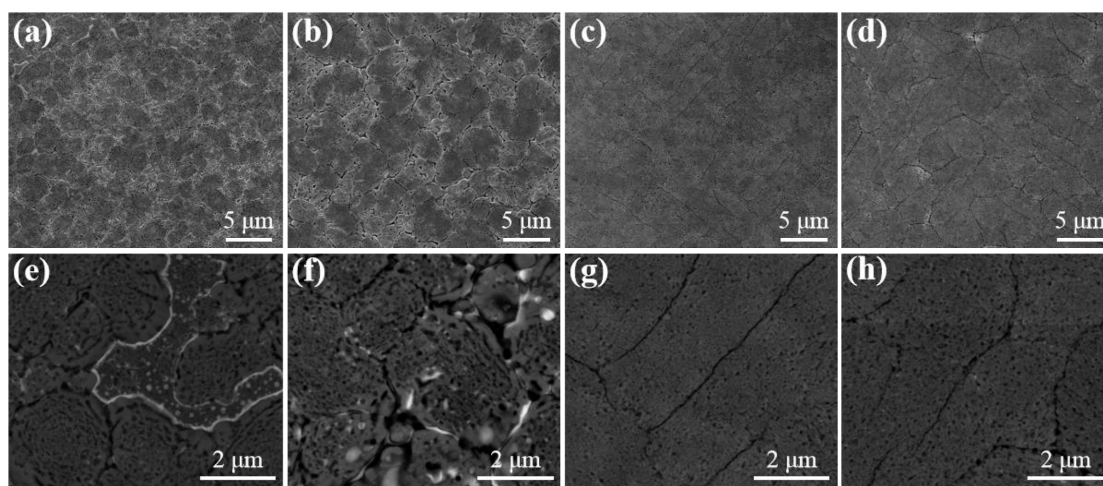

Figure 6.2. SEM images that shows the microstructures of $\boldsymbol{R}_{\mathrm{Sr}}$ = 0.05 multilayered α-quartz films: SEM images of the films with different deposited layers are shown in **(a)** 2-layer, **(b)** 3-layer, **(c)** 4-layer, **(d)** 5-layer respectively. The corresponding magnified BSE images of films are exhibited in **(e)**-**(h)** respectively to show the distribution of Sr.

According to the images in **Figure 6.2a-d**, the densification process of α-quartz disappears with the number of deposited layers. This feature is clearly demonstrated in **Figure 6.2e** where the dense recrystallized α-quartz crystals vanish after the second deposited layer. The main reason for this is that the grain boundaries are not interconnected along the different layers therefore the Sr cannot be accumulated like in the monolayer system (see **Figure 5.9d** and **Figure 5.10d** in **Chapter 5**). For these reasons, α-quartz films composed of 4 or 5 layers becomes porous with Sr-free grain boundaries (see **Figure 6.2c** and **d**). In that case, it was not possible to identify clustering of Sr on the surfaces (see **Figure 6.2g** and **h**). As a result, this new multilayer methodology allows to the fabrication of porous α-quartz films under dense crystal region (*i.e.* $\boldsymbol{R}_{\mathrm{Sr}}$ = 0.05).

From the XRD measurements of **Figure 6.3a** we can see that all the films present the usual α-quartz(100) out of plane texture and that the intensity of the proportional to the number of layers of the film. This indicates that the successive layers maintain the crystallinity and crystal orientation. The intensity of rocking curves of the α-quartz(100) reflection is also larger for the thicker films and the FWHM is close to 2° for all the films. This shows that the multilayer approach is not detrimental to the growth of α-quartz films. Further confirmation of this is given by the pole figure of the 5-layer film presented in **Figure 6.3b** which confirms that the multilayer synthesis preserves the epitaxial growth of the first layer.

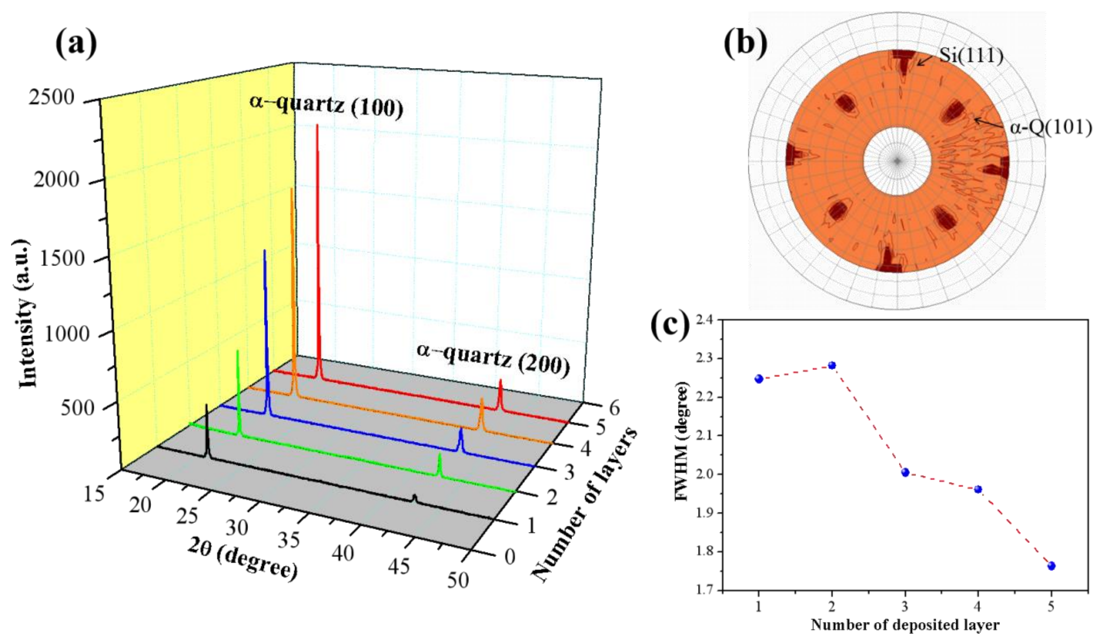

Figure 6.3. **(a)** XRD θ - 2θ scan showing the linear increase of α-quartz(100) reflections as the number of layers increases. **(b)** the pole figure for 5-layer film that shows that the epitaxial growth is maintained. **(c)** The FWHM measurement for different multilayer samples based on the rocking curve analyses.

6.1.2. Multilayer deposition of films with porous microstructure

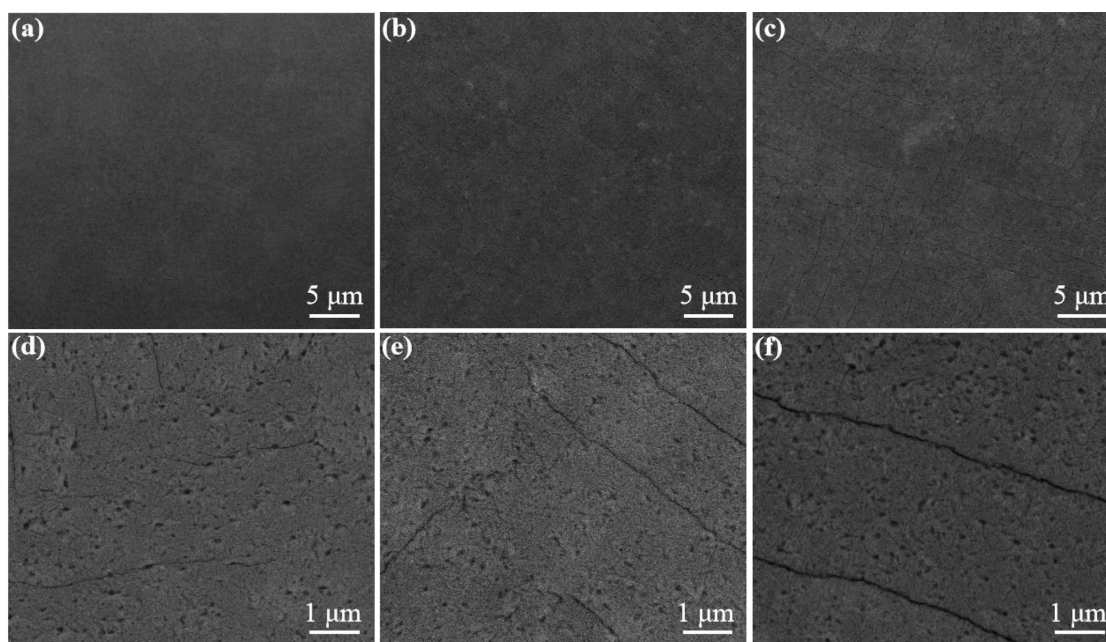

Figure 6.4. SEM images showing the microstructures of R_{Sr} = 0.033 multilayer α-quartz films: SE images of the films with different deposited layers are shown in **(a)** 2-layer, **(b)** 3-layer, **(c)** 4-layer, respectively. The corresponding magnified BSE images of films are exhibited in **(d)**-**(f)** respectively to show the distribution of Sr.

The multilayer deposition method of porous α-quartz films (*i.e.* $\boldsymbol{R}_{Sr}$ = 0.033) was also studied. Unlike the dense film microstructure previously described, the maximum of deposition layers before the film cracks is 4 layers, confirming that the low $\boldsymbol{R}_{Sr}$ cannot support a large surface tensile. The microstructure of as-prepared $\boldsymbol{R}_{Sr}$ = 0.033 multilayer films is presented in **Figure 6.4**. showing the typical porous microstructure already observed in the **Chapter 4**. Independently of the number of deposited layers, all samples show the same porous surface with several Sr-free grain boundaries (see **Figure 6.4a-c**). The BSE images (see **Figure 6.4d-f**) cannot distinguish Sr on the surface and within the grain boundaries. This feature is already reported in low densified porous α-quartz films.

Figure 6.5 shows the usual α-quartz (100) out of plane texture with the intensity of the peak proportional to the number of quartz layers. This indicates that the successive layers maintain the crystallinity and crystal orientation. The FWHM of rocking curves of the (100) reflection is also smaller for the thicker films and the is close to 2° for 4-layer system. This shows that the multilayer approach is not detrimental to the growth of porous α-quartz films (*i.e.* $\boldsymbol{R}_{Sr}$ = 0.033).

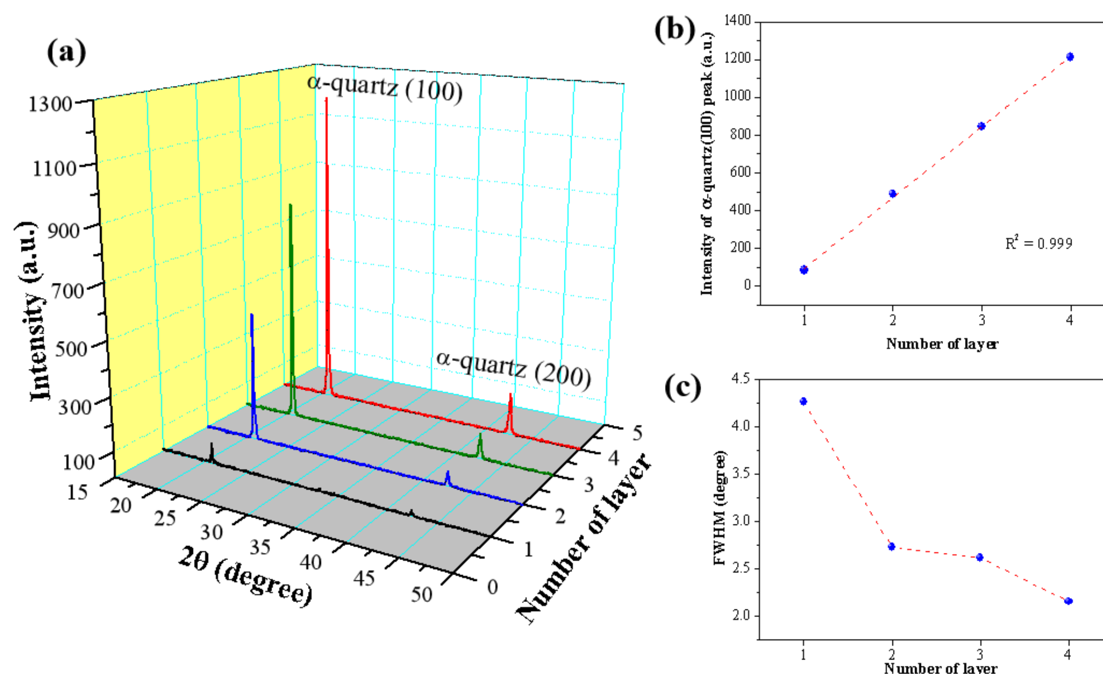

Figure 6.5. **(a)** XRD θ-2θ scan shows the linear increment of α-quartz (100) reflections as a function of the number of deposited layers. **(b)** The linear relationship between the intensity of α-quartz(100) peak and number of layer. **(c)** The FWHM measurements for different multi-layer samples show the better mosaicity value for the 4-layer system.

All these results confirm that the microstructure of this porous multilayered system does not change. However, the crystallinity and mosaicity of $\boldsymbol{R}_{Sr}$ = 0.033 multilayer films strongly varies with the thickness. This point is perfectly reflected by the XRD analysis (see **Figure 6.5a**). In that case, the response increases linearly with the

thickness. However, the intensity value for (100) reflection of porous film series ($\boldsymbol{R}_{Sr}$ = 0.033 multilayer films) is lower than dense film ones ($\boldsymbol{R}_{Sr}$ = 0.05 multilayer films, see **Figure 6.3a**), which fits with the results on the crystallinity study reported for single monolayer in **Chapter 4**. The FWHM values of multilayered quartz films $\boldsymbol{R}_{Sr}$ = 0.033 (see **Figure 6.5b**) shows a significant decrease of the FWHM value, which means that our multilayer deposition method can improve the orientation of α-quartz growth with porous microstructure. However, these FWHM values remains bigger than those for dense multilayered systems (see **Figure 6.3b**), meaning that porous microstructure has a bigger mosaicity probably caused by a lower content of Sr.

6.1.3. Disadvantages of multilayer deposition method

Although multilayer deposition method reveals an outstanding improvement of the thickness increment of α-quartz films, this new method still has some disadvantages caused by other synthesis parameters. For instance, α-quartz multilayered systems under $\boldsymbol{R}_{Sr}$ = 0.033 condition cannot obtain more than 4-layer film (containing the thickness of 740 nm) for the porous microstructure before the films cracks. **Table 6.1** show the maximum thicknesses of $\boldsymbol{R}_{Sr}$ = 0.05 films as a function of the withdrawal rate.

Table 6.1. The relationship among the withdraw rate used for each layer, the maximum of deposited layer and the total thickness of epitaxial quartz film under de deposition regime of $\boldsymbol{R}_{Sr}$ = 0.05 films.

Withdrawal Rate Used for Each Layer (mm/s)	The Maximum of Deposited Layer	Total Thickness of Crystalline Film (nm)
5	5	840
7.5	4	760
10	3	620
12.5	2	510
15	1	280

Table 6.1 summarizes that the multilayer deposition is mainly limited by the thickness of each layer. When the withdrawal rate reaches the maximum value of 15 mm/s for a complete film (see relative study in **Section 5.1.4**), the multilayer film methodology

does not work. We believe that the increase of surface tensile caused by the increment of thickness of each single layer can contribute to crack the multilayer system. The microstructure of α-quartz multilayered systems can be also influenced by the withdrawal rate, as shown in **Figure 6.6**.

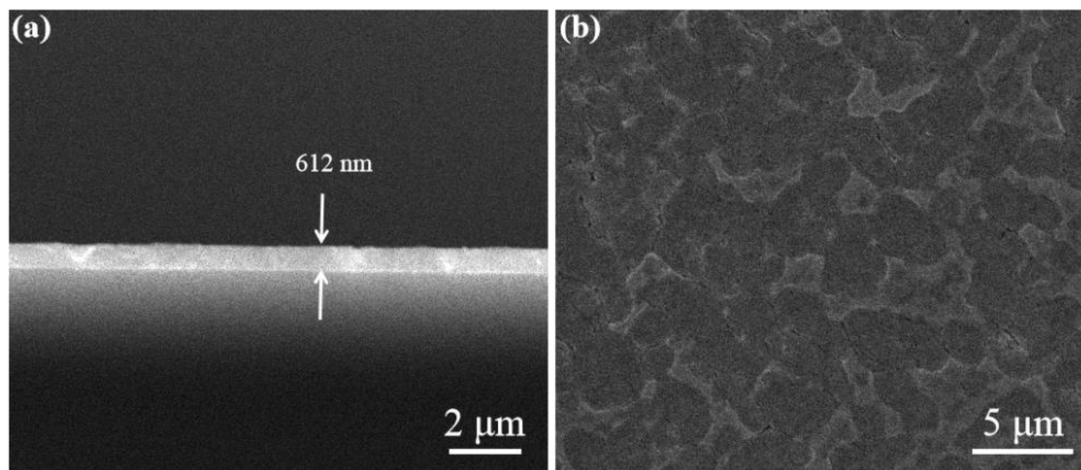

Figure 6.6. SEM images of as-prepared 3-layer dense film ($\boldsymbol{R}_{Sr}$ = 0.05) by using 10 mm/s withdraw rate. **(a)** cross-sectional image of quartz film showing ta thickness of 612 nm. **(b)** The surface of film shows a dense crystal microstructure.

The 3-layer system produced using withdrawal rate of 10 mm/s and a Sr concentration of 0.05 of $\boldsymbol{R}_{Sr}$ has a final thickness of 612 nm (as shown in **Figure 6.6a**). This thickness value is close to the 4-layer system produced after a withdrawal rate of 5 mm/s and exhibiting a flat and porous topography as shown in **Figure 6.4c** and **f**. However, the surface of this 3-layer film (see **Figure 6.6b**) is composed of densified quartz film which indicates that the microstructure of multilayer film is also controlled by other parameters and not just with the number of deposited layers.

We can conclude that a well and complete understanding of the multilayer deposition method depends on the control of many conditions. Nevertheless, this study points out that films produced with 5 mm/s of withdraw rate and 0.05 of $\boldsymbol{R}_{Sr}$ are ideal for the future applications since it is possible to reach the maximum thickness (over 800 nm) together with a most flexible control of thickness via depositing different number of layers (from 2-layer to 5-layer).

6.2. Nanostructure engineering of epitaxial α-quartz thick films on silicon

The enhanced control over the crystallization of epitaxial α-quartz and the multilayer deposition approach allowed an unprecedented integration of epitaxial α-quartz nanostructures on silicon [3]. In this section, I will explain how we have taken advantage of the multilayer deposition system combined with a set of cost-effective top-down lithographic techniques to fabricate large scale epitaxial nanopatterned α-

quartz thin films on silicon substrates with controllable nano and microstructures. This part of my thesis represents the first example that shows the possibility of engineering the integration on silicon of patterned quartz thin films, which precedes the production of nanostructured and microelectromechanical systems, as previously highlighted[4]. By engineering nanostructured α-quartz films on silicon, which are much thinner (200 nm ~ 1 μm) than those obtained by top-down technologies on bulk crystals, one can expect higher resonance frequencies. In addition, the control of the porosity, texture, shape, micro- and nano-patterning of α-quartz thin films opens the opportunity to produce more efficient devices. This is supported by the fact that nanostructured α-quartz thin films increase the specific area thus, enhancing the sensing properties of the future device.

6.2.1. The lithographic techniques used in my work

To produce controllable nano and microstructures such as 1D or arrays of pillars or lines from α-quartz multilayer films have been combined with three cost-effective lithographic techniques (see **Figure 6.7**) such as laser transfer lithography technique [5], Soft nanoimprint lithography [6] and a novel plasma-assisted self-assembled $SrCO_3$ nanoparticles reactive nanomask etching. Such procedures do not require any lithographic mask and allow obtaining a large scale and a precise control of epitaxial α-quartz nanostructures.

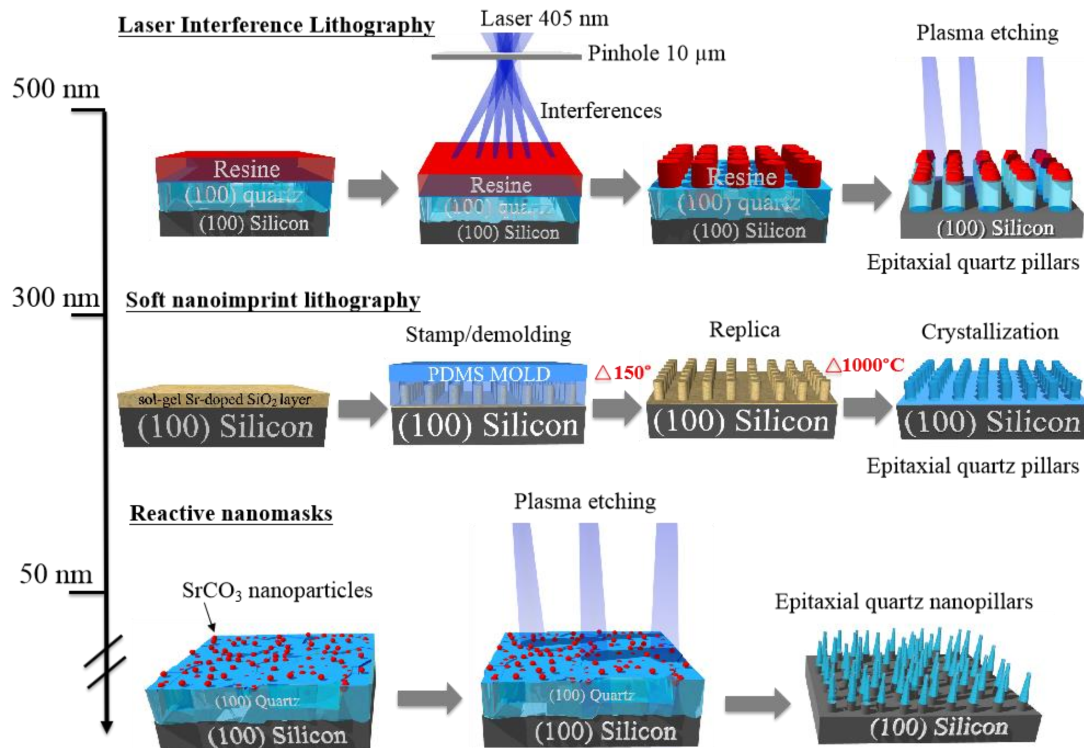

Figure.6.7. Schematics of three lithographic techniques used in my work by summarizing the key steps which were applied to produce lithographic patterns on as-prepared multilayer films dependent on the thickness of film.

The first technique that we used was the Laser Interference Lithography (LIL, also known as holographic lithography, shown as the top row of **Figure 6.7**). LIL is a top-down fabrication technique that is currently used to selectively pattern single crystals into dense vertical nanocolumn arrays [7]. This technique allows generating arrays of lines or dots in a photoresist film from an interference pattern generated by a UV laser over cm^2 surfaces and with pitches ranging between 400 nm up to 2400 nm. The mask-less exposure of the photoresist layer together with two or more coherent light beams offers a simple, low-cost, large-area nanolithography technique.

As an alternative route to LIL lithographic process, we applied soft nanoimprint lithography (NIL, show as the middle row of **Figure 6.7**), which combines top-down and bottom-up (sol-gel) approaches to produce epitaxial α-quartz nanopillar arrays with a precise control of pillar diameters and heights and inter-pillar distances on silicon. The experimental procedure consisted in the combination of dip-coating process to synthetize multilayer gel films of controlled thicknesses with NIL technique. In a first top-down fabrication step, large scale Si (100) masters made of nanopillars arrays were obtained by using LIL lithography and transferred by reactive ion etching at low pressure. Then, a second step involved the preparation of high quality Polydimethylsiloxane (PDMS) molds from Si(100) masters that produce perfectly imprinted array of nanopillars with controlled diameter and height.

Finally, we used the controlled outcropping of $SrCO_3$ nanoparticles on the surface as nanomasks to produce an array of α-quartz nanopillars from dense films. These particles are produced by a chemical reaction between SrO, CO_2 and H_2O (discussed in **Section 4.1.4**). The assembly of sintered $SrCO_3$ nanoparticles occurs during the annealing treatment at 1000°C of Sr-doped silica gel films as illustrated in bottom part of the **Figure 6.7**. In that case, the $SrCO_3$ nanoparticles are extremely stable under the reacting ion etching conditions. By this simple approach, one can produce arrays of α-quartz vertical nanopillars with a diameter down to 60 nm and a maximum height of 400 nm, depending on the original α-quartz film thickness. In our case, the $SrCO_3$ nanoparticles are formed during α-quartz crystallization and remained extremely stable during the reacting ion etching process (RIE etching), acting as an efficient nanomask that protects α-quartz from the plasma etching.

6.2.2. Direct patterning of multilayer films by laser interference lithography

Laser interference lithography produced the direct sub-micro patterning on 5-layer α-quartz film system (~ 800 nm). After the lithography process, the array of nanocolumns were checked and analysed by SEM, TEM, and electron diffraction (SAED). These results are summarized in **Figure 6.8**.

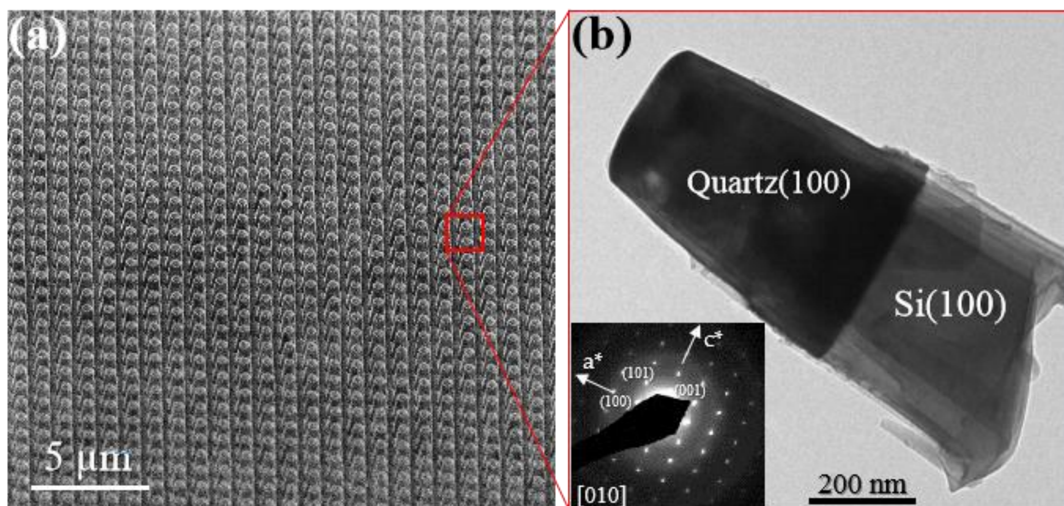

Figure 6.8. Analyses of the array of nanocolumns made by LIL: **(a)** SEM image of ultra-dense arrangement of nanocolumns. **(b)** TEM image and electron diffraction measurement (inset image) of the α-quartz/Si interface of a single nanocolumn view along the [010] zone axis of α-quartz crystallographic structure.

The SEM image of **Figure 6.8a** shows the lithographic pattern on 4-layer film by using LIL technique, which displays an ultra-dense arrangement of α-quartz nanocolumns with a precise control of the diameter, height and position. The TEM image (see **Figure 6.8b**) exhibits the shape of a single nanocolumn. The α-quartz/Si interface can be distinguished by different contrasts which means the microstructure of epitaxial growth is also remained perfectly after lithography. Besides, the corresponding electron diffraction pattern confirms that the epitaxial grow of α-quartz(100) on silicon and the crystallinity have been preserved.

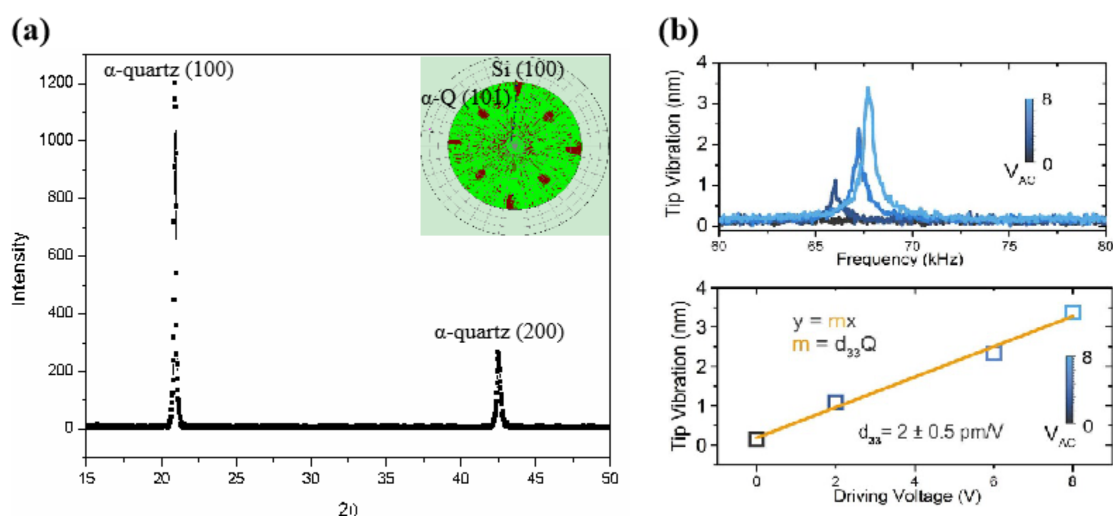

Figure 6.9. The crystallinity and piezoelectricity investigation of as-prepared nanocolumn array: **(a)** XRD θ-2θ pattern. The inset pole figure shows the α-quartz(100)//Si(100) epitaxial relationship. **(b)** PFM spectroscopic measurements on the nanopatterned film.

The crystallinity of 5-layer lithographed film (the array of nanocolumn) was also observed by using XRD and pole figure analysis, (see **Figure 6.9**). The XRD θ-2θ pattern (see **Figure 6.9a**) confirms that the α-quartz(100) crystallographic phase is remained after the lithographic process. Pole figure analysis shows the nanocolumns conserve the α-quartz(100)//Si(100) epitaxial relationship. Besides, no supplementary peaks from other reflections or polycrystallinity signal appears.

Piezoelectric coefficient d_{33} estimated by PFM on α-quartz nanocolumns were compared with those values obtained in dense α-quartz films before the lithographic process using an alternative method, direct piezoelectric force microscopy (DPFM) has reported in the previous chapter (see **Figure 4.30** in **Chapter 4**). We employed DPFM measurements to obtain the piezoelectric characterization of dense thick α-quartz film (5-layer film) and compared the results with the case of nanocolumns. The DPFM measurement is illustrated in **Figure 6.10**.

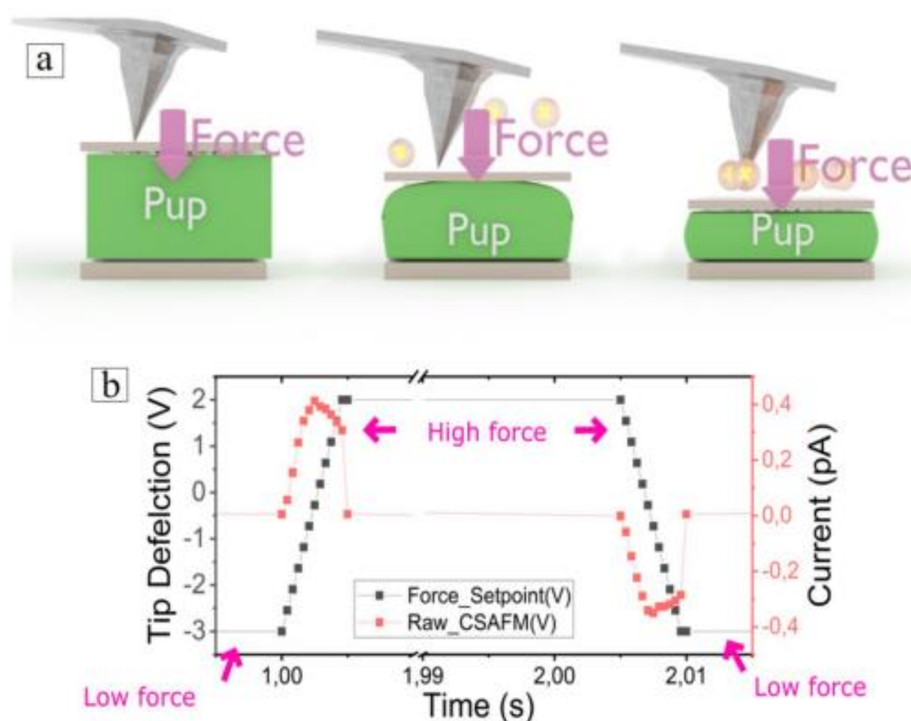

Figure 6.10. DPFM measurements on 5-layer film. **(a)** the schematic to show the mechanism of DPFM measurement. **(b)** the charge altering of film with the change of force responds to the measurement shown in **(a)**.

Figure 6.10a shows the schematic of Force and Piezoelectric current vs Time (s) for different applied forces on an 800 nm thick α-quartz film (made by 5-layer deposition) before lithographic process. Notice that the force profile starts with a constant value, while at 1 s the force is increased to a value of 380 μN in a 5 ms time

step. Following this step, a constant force is re-settled for an additional 1 s, while at 2 s, an unloading ramp is performed, reducing the applied force. While force is varied, the current channel is recorded simultaneously; current is depicted in red squares. Scheme of the spectroscopy experiments carried out in which the AFM tip applies a suitable force, within a given time, collecting the charges generated by the direct piezoelectric effect.

Figure 6.8b shows that a constant force builds up a constant charge, hence the recorded current remains zero. However, when the force is varied, through a loading or unloading event, there is an increase or decrease of the charge build up, whereas a constant current can be seen at a constant force rate applied. Curves performed in α-quartz dense film showing its piezoelectric response. The graphs were obtained by averaging 4x4 matrix volume spectroscopy experiments in an area of 10 microns, in order to depict the homogeneity of the sample. From these measurements we obtained a d_{33} of 4 ± 2 pC/N in agreement with the piezoelectric coefficient of α-quartz. Notice that DPFM methodology cannot be applied to nanostructured α-quartz films because the applied force breaks α-quartz nanocolumns, making impossible this kind of measurement. However, the combination of PFM and DPFM methodology was recently published confirming the quantification of the piezoelectric coefficient d_{33} at the nanoscale in $BiFeO_3$ ferroelectric epitaxial oxide thin films [8], therefore validating this approach in quartz films.

The piezoelectric properties of nanopatterned epitaxial α-quartz films were measured by using PFM technique in 800 nm thick nanocolumns (see **Figure 6.9b**). Both piezoelectric coefficient (d_{33}) are similar and comparable to that of the quartz bulk material [9] (*i.e.* $d_{33(PFM)} = 2\pm0.5$ pm/V and $d_{33(DPFM)} = 4\pm2$ pC/N) confirming that the piezoelectric functionality of nanocolumns is preserved. Notice that all DPFM measurements were compared with a reference based in a commercial ferroelectric Periodically Poled Lithium Niobate (PPLN) sample.

With the combination of multi-layer deposition approach with LIL lithography, we have produced high aspect ratio epitaxial α-quartz columns with micrometric heights from dip-coated films. This was feasible due to the multilayer deposition circumvents the maximum achievable thickness imposed by lateral tensile stresses that appeared during the densification of the layers [10]. A key step to overcome this obstacle has been to perform a temperature treatment to consolidate the gel layer (450ºC for 10 min in air atmosphere) after each deposition.

6.2.3. Soft nanoimprint lithography of multilayer films

Soft nanoimprint lithography (NIL) allowed to produce nanopatterned epitaxial thick α-quartz films by using a Poly Dimethyl Siloxane (PDMS) mold. The experimental

procedure consisted in the combination of dip-coating process to synthetize Sr-doped xerogel silica films of controlled thicknesses on silicon(100) substrates with LIL and Nano-Imprint (NIL) lithographic techniques. In a first top-down fabrication step, large scale Si (100) masters made of nanopillars arrays were obtained by using LIL lithography and transferred by reactive ion etching at low pressure. Then, a second step involved the preparation of high quality PDMS molds from Si(100) masters (see **Figure 6.11**) that produce perfectly imprinted Sr-doped silica nanopillars with controlled diameter and height on silicon. (See more details in **Section 3.3.2**).

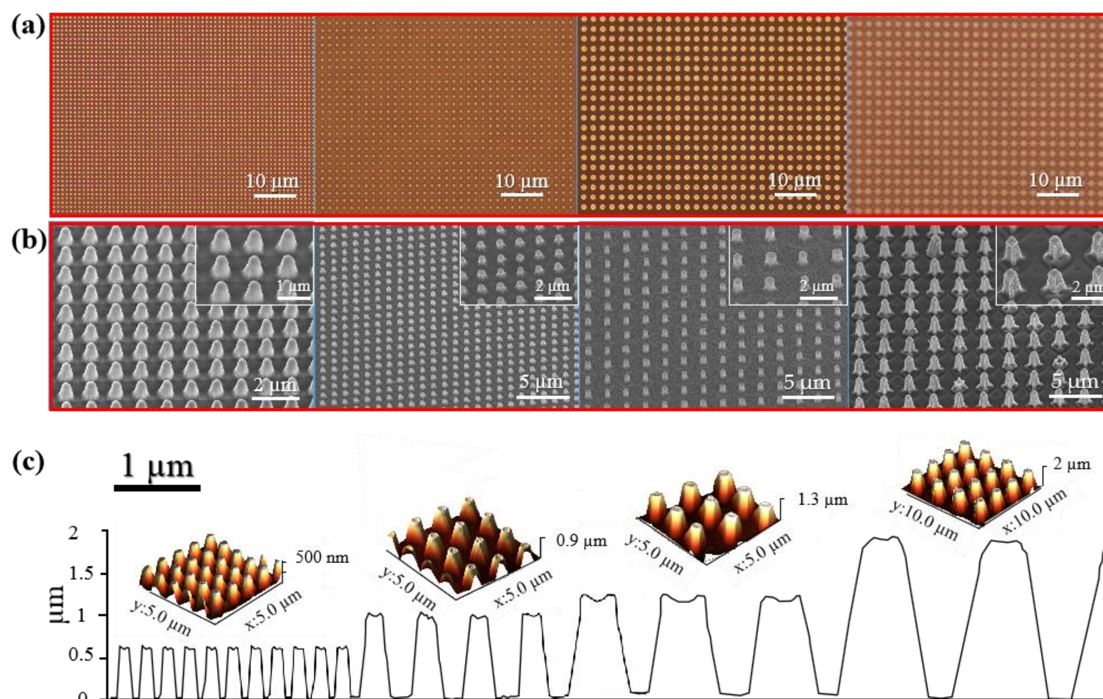

Figure 6.11. **(a)** Optical images of Si (100) masters used along this thesis work obtained by using LIL lithography. **(b)** FEG-SEM image of printed Sr-doped silica nanopillars with controlled diameter (down to 350 nm) and height (up to 2 µm) on silicon. The inset pictures show FEG-SEM images at higher magnification of pillars. **(c)** 3D AFM images showing silica nanostructured films prepared by NIL lithography in **b**. Below you can distinguish the profile analysis of the AFM image in **c**, revealing a perfect transfer of the different motives.

Finally, imprinted epitaxial α-quartz(100) nanopillars arrays on silicon were obtained applying a thermal treatment at 1000ºC for 5 hours (see **Figure. 6.12**). SEM images shows Sr-doped silica xerogel nanopattern composed of 600 nm height columns before crystallization process (see the left SEM image of **Figure. 6.12a**). The crystallized sample is shown in the right image of **Figure. 6.12a**, which exhibits the characteristic of a porous α-quartz samples previously reported in **Chapter 4** (See **Figure 4.5a** and **b**). Atomic resolution HAADF image of a single α-quartz nanocolumn/silicon interface reveals the epitaxial growth of α-quartz layer with an atomically sharp interface with the silicon substrate as shown in **Figure. 6.12b**.

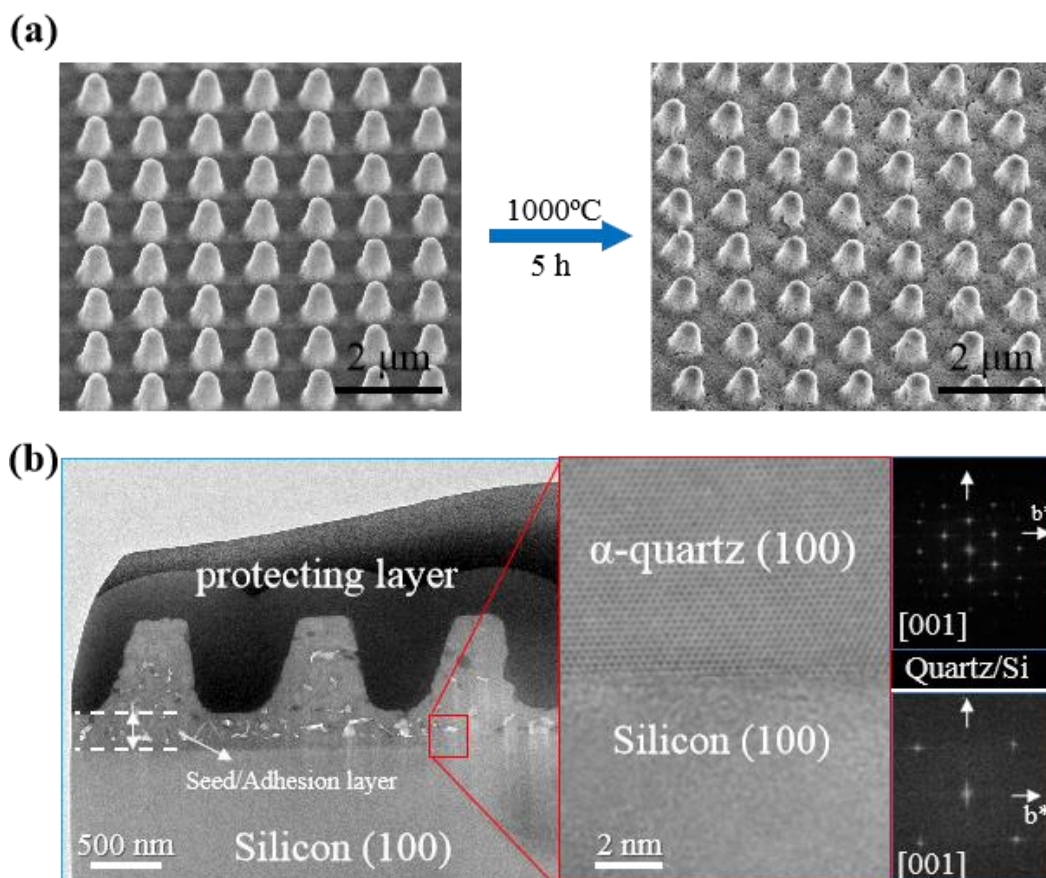

Figure 6.12. Microstructure investigation of lithographed film via soft nanoimprint lithography. **(a)** SEM images of the surfaces before calcination (the left image) and after calcination (the right image) to show the maintenance of as-prepared 500 nm height columns. **(b)** The high angle annular dark field (HAADF) Z-contrast analysis: the left low magnification image shows the α-quartz nanocolumns grown on the Si(100) substrate. The right atomic resolution Z-contrast image of the selected zone shows a single (100)-oriented quartz nanocolumn viewed along the [100]-crystallographic direction. Inset two figures at most-right side show the corresponding FFT of both the quartz film and the silicon substrate.

In order to attain both a continuous nanostructured crystalline α-quartz film and a perfect nanoimprinted pattern, the deposition conditions must be optimized. Likewise, a first mesoporous silica xerogel adhesion layer was needed to obtain an optimal print of PDMS moulds on the Si(100) substrate. This adhesion layer is consolidated at 450°C during 5 min, before the deposition of the final printable silica layer. Both layers have the same thickness (~ 200 nm) and are deposited under the same conditions (*i.e.* at 25°C, 45% of humidity after applying a withdrawal speed of 5 mm/s).

We demonstrate also that the multilayers system of silica xerogels on silicon (100) can facilitate the adhesion of the LIL nanostructured layer to replicate the columnar shapes when it is imprinted by the PDMS mold as shown in the **Figure 6.13**.

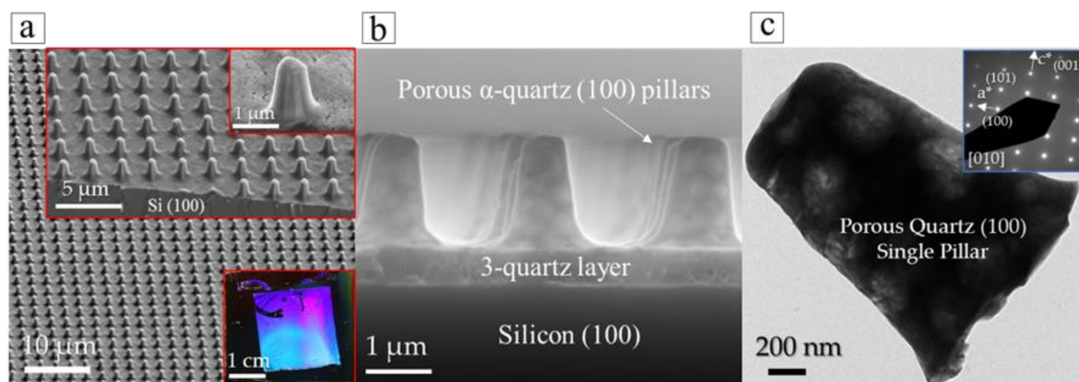

Figure 6.13. Patterning and crystallization of Sr-doped silica multilayers by soft imprint lithography. **(a)** FEG-SEM image of epitaxial quartz columnar pattern. The inset figures show higher magnifications FEG-SEM images illustrating the morphology of the quartz columns. The right-down inset corresponds to an optical image of the film which displays the characteristic wavelength reflectance selectivity of a 2-D photonic crystal. **(b)** Cross-sectional SEM image of a quartz column grown on the Si substrate assisted by the Sr^{2+} catalyst at 1000 °C for 5 hours. **(c)** Transmission Electron Microscopy image and electron diffraction measurement (inset image) of the α-quartz/Si interface of a single column.

The crystallinity and piezoelectricity of nanoimprinted 4-layer film with nanocolumn array is checked by XRD and PFM analyses. The results are summarized in **Figure 6.14**. The XRD pattern (see **Figure 6.14a**) displays that the intensities of α-quartz phase are higher than the 4-layer film (see **Figure 6.3a**) which means the nanocolumn array has a stronger response. Combining to the narrower FWHM of nanoimprinted film (see **Figure 6.14b**) with the comparation of 2-layer one (FWHM = 2.28º, see **Figure 6.3b**), NIL also can improve the crystallinity of films besides increasing the height. The most possible reason is that the Sr inside film is aggregated with the absorption effect of mould for building the tall nanocolumns.

To evaluate the piezoelectricity of the nanoimprinted α-quartz nanocolumns, we employed PFM technology. The amplitude image is represented in **Figure 6.14c** and the inset show the topographic AFM image of crystallized nanocolumns. Notice that the areas surrounding the nanocolumns show a slight change in the PFM amplitude, the signal remains constant both at the top of the columnar structures at the α-quartz film surrounding the base of these pillars. The change of the PFM amplitude signal in the perimeter of the nanocolumns is attributed to a topographic crosstalk artefact which is well known and reported by the community [8]. We were able to corroborate the electromechanical behaviour of our films by performing point-out spectroscopy measurements, see **Figure 6.14d**. The electromechanical behaviour of the microstructures was studied using frequency-sweeps to display the PFM contact resonant circuit. The electromechanical behaviour is studied outside and inside of the nanocolumns by placing the AFM tip in each respective position. The data shows an

increase of resonant amplitude with an increase of the applied AC bias, in a similar way as depicted in **Figure 6.9b**, confirming that the nanostructuration has not been detrimental to the electromechanical properties.

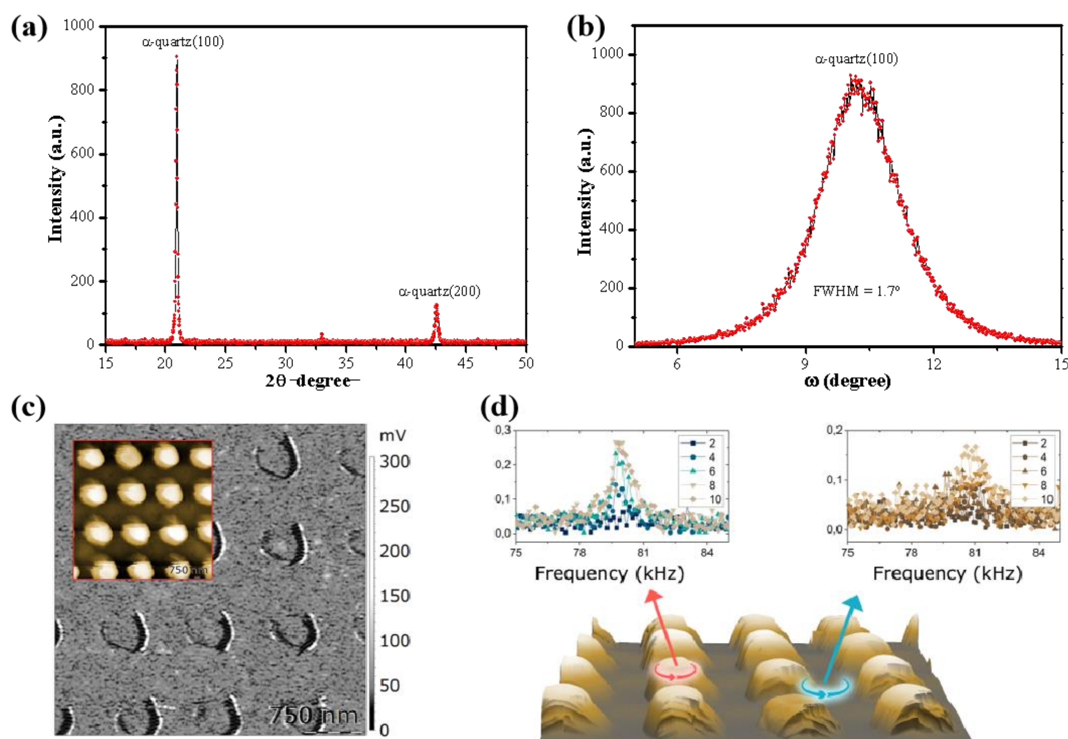

Figure 6.14. Crystallinity and piezoelectricity explores of lithographed film via soft nanoimprint lithography. **(a)** XRD θ-2θ pattern of lithographed film. **(b)** The corresponding rocking curve of lithographed film. **(c)** PFM amplitude and topography (inset) of as-prepared array of nanocolumns while applying a tip-substrate AC voltage of 10 V, showing area similar tip vibration level at the background film and top nanostructures. Point-out spectroscopy measurements recorded on top of the structures and bottom film, for different applied AC bias. **(d)** The data shows an increase of the PFM resonant frequency amplitude with an increase of the applied AC bias, confirming our expectation that piezoelectric functionality is preserved.

6.2.4. Self-assembled $SrCO_3$ nanomask lithography of dense films

$SrCO_3$ nanoparticles are formed during α-quartz crystallization and remained extremely stable during the RIE etching process, acting as an efficient nanomask that protects α-quartz from the plasma etching. This feature can be observed in **Figure 6.15** that shows $SrCO_3$ nanoparticles before and after RIE process. **Figure 6.15a** shows the typical morphology and size of the $SrCO_3$ nanoparticles on top of the epitaxial α-quartz thin film. The high matching between the $SrCO_3$ particles distributions (see **Figure 6.15a**) and the α-quartz nanopillars (see **Figure 6.15b**) verifies that the position of nanopillars is based on the Sr distribution of initial film.

The efficacy of the process was investigated by electron microscopy and electron diffraction characterization was used to assess the crystalline structure of the α-quartz

nanopillars. The etching has been applied in 100W RF and 200W LF of an inductively coupled plasma reactive ion etching (ICP-RIE) reactor using CHF_3/O2 gas mixture (see more details in **Section 3.3.3**). From the high magnified FEG-SEM image (see **Figure 6.15c**), we can confirm the conical-like shape of nanopillars with a diameter of 10 nm ~ 60 nm and height of 100 nm ~ 400 nm. Th morphology of the motifs is conical rather than needle-like because of an isotropic etching of CHF_3/O_2 flux. With the aim of producing networks of needle-like α-quartz nanostructures, we used ionized gases and gas mixtures such as Ar, CHF_3, SF_6 in order to control the anisotropy of the etching [11, 12].

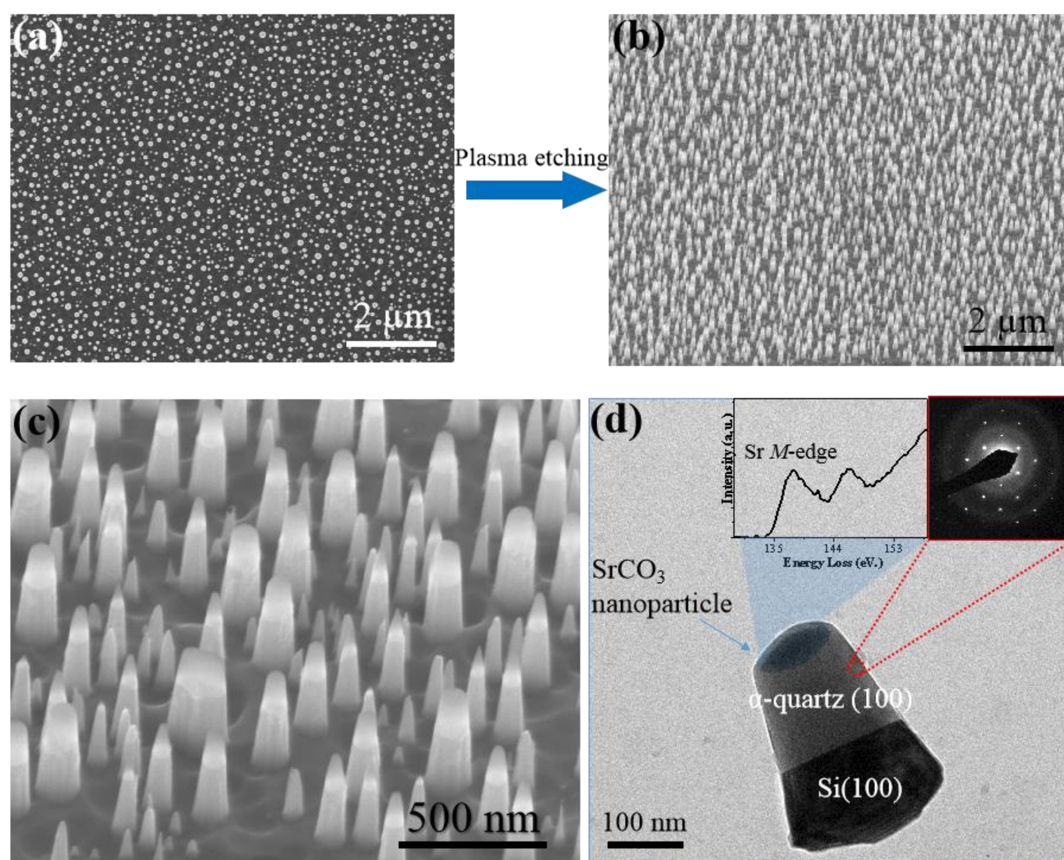

Figure 6.15. (a) SEM image illustrates the morphology of sintered $SrCO_3$ nanoparticles at 1000°C. **(b)** SEM image illustrates the as-prepared conical-like nanopillars after RIE etching of a dense film. **(c)** SEM image at high magnification to show the morphology of nanocolumns obtained by nanomask lithography. (**d**) TEM image illustrates the morphology of α-quartz single crystal conical-like nanopillars after RIE etching of a dense film. The inset images are the Sr M-edge EEL spectrum and electron diffraction pattern of a conical-like nanopillar.

The investigation of nanopillar formation is presented in **Figure 6.13**.The TEM image of a single as-prepared nanopillar (see **Figure 6.13d**) shows a consist of $SrCO_3$ top cover (confirmed by the Sr M-edge EEL spectrum)The electron diffraction pattern of a single α-quartz nanopillar presented in Fig. 6.13 reveals perfect α-quartz crystallinity similar to that of the initial dense α-quartz film., α-quartz(100) phase

body (checked by the typical pattern in SAED test), and Si(100) substrate bottom via the clear contrast. This kind of structure just accompanies to the mechanism of the lithography.

6.3. Chapter conclusion

In this chapter, a multilayer deposition method was successfully developed allowing the fabrication of thick (800 nm approximately)epitaxial α-quartz(100) films with preserving the microstructures and properties of quartz. This technology can avoid the limitation of dip-coating condition for the monolayer film, therefore preparing extremlly homogeneous and flat films with required

This multilayer approach allowed to engineer the nanostructuration of epitaxial quartz films on silicon using three scalable lithographic methodologies that do not require masks. The laser interference lithography allows to prepare α-quartz nanocolumns with diameters between 400 nm and 800 nm and heights in the range of 200 nm to 1000 nm. The lithographed microstructures maintain the crystallinity and epitaxial orientation of α-quartz(100)//Si(100). On the other hand, we have established the conditions to shown that NIL lithography combined with sol-gel process is a versatile method to replicate several dimensions of Sr doped silica pillars depending on the characteristics of PDMS mould. Specifically, a withdrawal speed of 5 mm/s at 25°C and 45% of relative humidity and the deposition of adhesion layer are required to obtain a perfect nano-imprinted crystalline continuous α-quartz pattern. Thus, the interplay between temperature, humidity, dip-coating conditions, and epitaxial growth plays a key role for the fabrication epitaxial quartz nanopillars on silicon substrates by NIL lithography. Besides, the controlled outcropping of $SrCO_3$ nanoparticles on top of epitaxial α-quartz thin films allows producing α-quartz vertical nanopillars having diameters down to 60 nm and a maximum height of 400 nm under the reacting ion etching conditions.

In all cases, the nanostructuration of α-quartz films preservesthe piezoelectric properties of quartz,. We used two techniques, DPFM and PFM, to quantify the piezoelectric coefficient d_{33} of nanostructured and dense α-quartz films using in all cases a reference based in a commercial ferroelectric Periodically Poled Lithium Niobate (PPLN) sample.

All these works demonstrate the integration on silicon of lithographic patterning of epitaxial quartz films at micron size, which precedes the production of micro-electromechanical systems. The control at the nanoscale over the shape, micro-/nano-patterning of α-quartz films opens the opportunity to fabricate new high frequency resonators and highly sensitive sensors relevant in different fields of application.

6.4. Chapter references

Chapter 6

1. Drisko, G. L.; Carretero-Genevrier, A.; Gich, M.; Gàzquez, J.; Ferrah, D.; Grosso, D.; Boissière, C.; Rodriguez-Carvajal, J.; Sanchez, C., Water-Induced Phase Separation Forming Macrostructured Epitaxial Quartz Films on Silicon. *Advanced Functional Materials* **2014,** *24* (35), 5494-5502.

2. Brinker, C. J.; Clem, P. G., Quartz on Silicon. *Science* **2013,** *340* (6134), 818-819

3. Seo, J.-H.; Park, J.; Kim, S.-I.; Ju Park, B.; Ma, Z.; Choi, J.; Ju, B.-K., Nanopatterning by Laser Interference Lithography: Applications to Optical Devices. 2015.

4. Hamouda, F.; Bryche, J.-F.; Aassime, A.; Maillart, E.; Gâté, V.; Zanettini, S.; Ruscica, J.; Turover, D.; Bartenlian, B., Soft nanoimprint lithography on SiO2 sol-gel to elaborate sensitive substrates for SERS detection. *AIP Advances* **2017,** *7* (12), 125125.

5. Santybayeva, Z.; Meghit, A.; Desgarceaux, R.; Teissier, R.; Pichot, F.; Marin, C. d.; Charlot, B.; Pedaci, F. In *Fabrication of quartz microcylinders by laser interference lithography for angular optical tweezers*, SPIE: 2016; p 5.

6. Vila-Fungueiriño, J.M.; Gómez, A.; Antoja-Lleonart, J.; Gázquez, J.; Magén, C.; Noheda, B.; Carretero-Genevrier, A., Direct and converse piezoelectric responses at the nanoscale from epitaxial $BiFeO_3$ thin films grown by polymer assisted deposition. *Nanoscale*, **2018**, *10*, 20155-20161.

7. Newnham, R. E., *in Properties of materials: Anisotropy, Symmetry, Structure (Oxford University Press*. 2005.

8. Landau, L.; Levich, B., Dragging of a Liquid by a Moving Plate. In *Dynamics of Curved Fronts*, Pelcé, P., Ed. Academic Press: San Diego, 1988; pp 141-153.

9. Seol, D.; Kim, B.; Kim, Y., Non-piezoelectric effects in piezoresponse force microscopy. *Current Applied Physics* **2017,** *17* (5), 661-674.

10. Li, L.; Abe, T.; Esashi, M., Smooth surface glass etching by deep reactive ion etching with SF6 and Xe gases. *Journal of Vacuum Science & Technology B* **2003,** *21* (6), 2545-2549.

Chapter 7. General Conclusion & Future Expectations

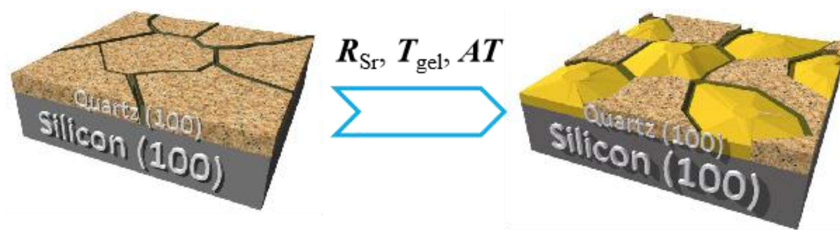

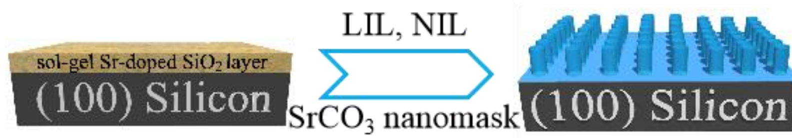

Chapter 7

7.1. General conclusions

The studies performed in this work concerning the understanding of epitaxial quartz thin films growth mechanism on silicon substrate have led to a synergy of results where the main goal has been the optimization of the synthesis parameters in order to prepare highly flat α-quartz films which are sufficiently thick to be patterned by different techniques.

The results here presented will open the door to future developments in the field of electromechanical systems (MEMS), taking advantage of the excellent piezoelectric properties of α-quartz and of the fact that this material is directly nanostructured on Silicon. These achievements involve the validity and generality of chemical solution deposition assisted by dip coating process for the microstructural control of α-quartz thin films and the generation of different nanostructured systems.

Studies conducted regarding the microstructural and mosaicity control of epitaxial α-quartz thin films and the nanostructuration of this material assisted by cost-effective lithographic techniques yielded several conclusions that can be resume into three main aspects: (i) the catalytic role of Sr network modifier agent of the amorphous silica to finally crystallized into α-quartz, (ii) the versatile control of the final thickness of the α-quartz films and the (iii) nanostructure engineering of α-quartz multilayer films.

7.1.1. Investigation on the Sr-assisted devitrification mechanism of α-quartz films

The mechanism and behavior of the devitrifying agent (Sr) were investigated as the central role of α-quartz crystallization. To this aim, the content of Sr in the gel was perfectly controlled by adjusting the ratio of $SrCl_2$ to SiO_2 in the final solution ($\boldsymbol{R}_{Sr}$). We identified the range of $\boldsymbol{R}_{Sr}$ (0.033 ~ 0.1) for a complete crystallization and how Sr content modify the microstructure, crystallinity and mosaicity of these α-quartz films (see **Figure 7.1**).

We have identified two types of microstructure in quartz thin films, which includes porous flat microstructure and dense crystals microstructure. This crystallization mechanism can be described as follow: first a crystallization of amorphous silica into α-quartz results in a porous microstructure because α-quartz phase is denser than amorphous silica. Then a second recrystallization process consisting of a densification of the primary porous α-quartz results in a microstructure characterized by micrometric dense crystals. This recrystallisation and densification process only occurs in films with high $\boldsymbol{R}_{Sr}$ because the the Sr element can be accumulated in high concentrations within the grain boundaries of α-quartz.

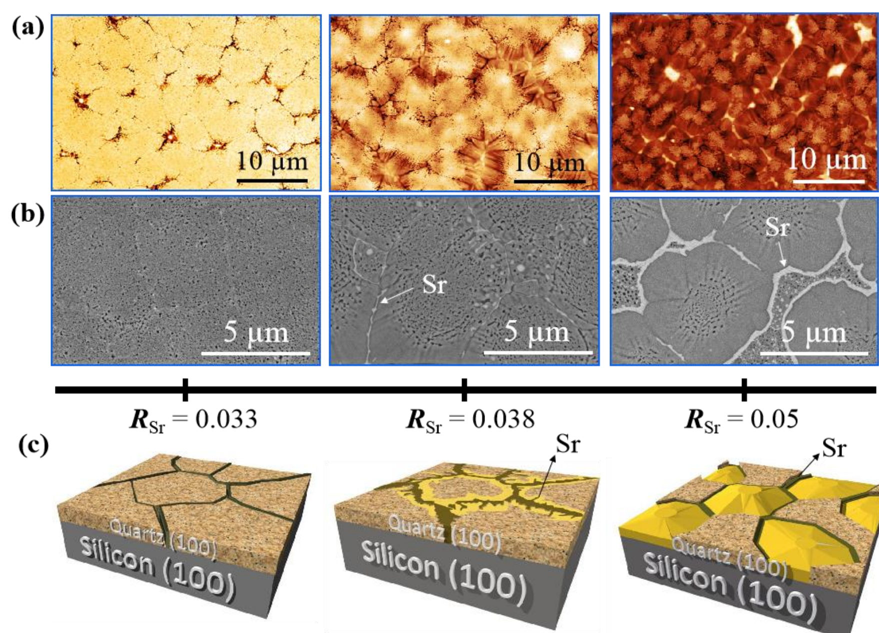

Figure 7.1. The microstructures of α-quartz films containing different amounts of Sr ($0 < R_{Sr} < 0.05$ indicated in a scale below the images) are revealed by AFM **(a)** and SEM in backscattered electrons mode **(b)**. The salient features of these microstructures are illustrated in 3D model **(c)**. Those films were prepared with a withdrawal speed of 5 mm/s in a relative humidity of 40% at 25ºC using Brij-58 as surfactant. The annealing treatment was at 1000ºC for 300 minutes in air atmosphere.

7.1.2. Versatile control of α-quartz films

Others important parameters for the film crystallization that modify the distribution and activity of Sr catalyst such us the thickness of gel film (T_{gel}), annealing temperature (***AT***), relative humidity (RH) and type of surfactant were investigated during this thesis.

T_{gel}, was controlled by the withdrawal rate during dip-coating process (U_w, 1 ~ 12 mm/s), showing a similar effect to the R_{Sr} (*i.e.* an increment of the Sr content within the silica film when U_w increases). This feature, however, is limited to a draining regime (which needs $U_w \geq 1$ mm/s) because the quantity and distribution of Sr is not enough to enable a complete and homogenous crystallization when the gel film is thinner than 200 nm. Moreover, the T_{gel} also has a maximum thickness value around 400 nm (U_w = 15 mm/s) producing cracks of film's surface. Another important parameter that has been studied along this thesis was ***AT***. We have observed that a higher ***AT*** the mobility of Sr increases, promoting devitrification and densification. We have identified the optimal temperature to reach a perfect crystallization of α-quartz thin films on silicon witch is 950ºC ~ 1050ºC. Conversely, when ***AT*** is too high (> 1050ºC) the α-quartz phase cannot be obtained.

Relative humidity (RH) has been identified as the parameter that interacts with the chemical nature of the surfactant producing a phase separation during the deposition of the precursor solution. In order to avoid this phase separation we have studied different surfactants at different RH values. We identified that RH values under 50 % combined with a non-ionic surfactant (Brij-58) improved that the crystallinity of film avoiding the phase separation therefore producing a dense film. The optimization of all these synthesis parameters allowed to the fabrication of thicker film (~µm range) by a novel multilayer deposition methodology while preserving the microstructures, epitaxial and piezoelectric properties of α-quartz. This is an important result that avoid the limitation of dip-coating condition for the monolayer system.

7.1.3. Nanostructural engineering of α-quartz multilayer films

Epitaxial thick films of 800 nm allowed to engineer the nanostructuration of epitaxial quartz films on silicon. During this thesis, three scalable lithographic techniques, which do not require mask, were tested to achieve the first nanopattern of quartz thin films. Importantly, α-quartz nanocolumns with diameters between 400 nm and 800 nm and heights in the range of 200 nm to 1000 nm were obtained by using laser interference lithography; Another process that showed a successful patterning of α-quartz films was he nanoimprint lithography combined with sol-gel process, producing α-quartz vertical nanopillars having diameters down to 250 nm nm and a maximum height of 2000 nm.

Finally, nanopillars down to 50 nm were obtained via direct reacting ion etching by using the controlled outcropping of $SrCO_3$ nanoparticles on top of epitaxial α-quartz thin films. All these α-quartz nanostructures maintain the epitaxial crystallinity and piezoelectric property, whitch can open the golden door to the microfabrication of new high frequency resonators and highly sensitive sensors relevant in different fields of application.

7.2. Future work

As a result of the experience achieved along this thesis, new possibilities have appeared. Importantly new MEMS sensors based on these results are now under developing within the frame on the ERC Starting Grant project SENSiSOFT coordinated by Dr. Carretero-Genevrier.

7.2.1. Integration and device prototype

The knowledge gathered concerning the growth of low cost large scale α-quartz vertical nanorods when using proper synthesis conditions assisted by dip-coating, could be easily implemented on MEMS devices. This opens a window through new strategies for advanced nanostrucutred α-quartz crystal microbalance (QCM) devices

to create a new horizon of interfacial mass sensing technology (see **Figure 7.2**). In this regard, the elucidation of the reaction path and growth mechanism leading to the α-quartz thin films on top of silicon oxide insulating (SOI) substrate is an issue that would require a deeper study. The complete structural and chemical characterization of α-quartz on SOI substrates at the atomic level should be further investigated, in order to provide the necessary knowledge for a controlled production of epitaxial α-quartz on these substrate needs for MEMS engineering.

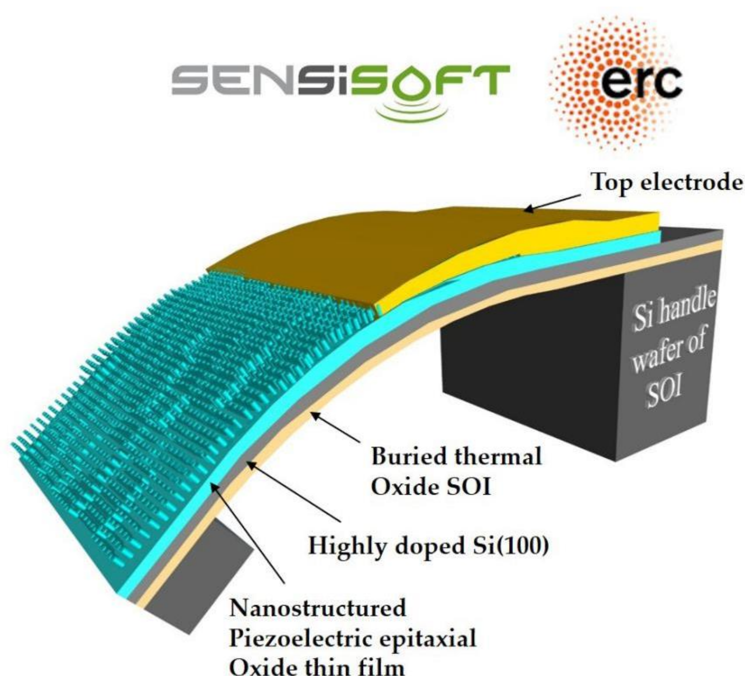

Figure 7.2. Schematic representation of one of the demonstrators to be developed in the SENSiSOFT project

7.2.2. Preparation of epitaxial α-quartz thin films on silicon with high-performance piezoelectric response

The stage at which the quartz form nucleates in epitaxial single crystal remains unknown. The understanding of the structural changes associated with such structural evolution shall provide the necessary clues to fully understand the transformation mechanism of silica into quartz and enhance the piezoelectric response. To achieve this objective It would be very appealing to perform a study of crystallization mechanism at the Si-quartz interface via in-situ synchrotron X-ray diffraction. The main idea is to observe, the crystalline phase changes, the tensile mechanism and the nucleation stages that take place during the epitaxial growth of α-quartz in real time. Also, the experiment will eventually evidence whether α-quartz formation is driven by the presence of intermediate silicate phases that will vanish after and assist the

epitaxial α-quartz crystallization at the interface during the oxidation process. To complement synchrotron X-ray and neutron diffraction experiments, it would be also very appealing to study the catalytic role of strontium during the crystallization process via X-ray photoemission. This study could show how strontium acts as a catalyst in the transformation of amorphous silica thin films into epitaxial α-quartz during annealing by "*in-situ*" and "*ex-situ*" X-ray photoemission experiments (XPS).

7.2.3. Design of new quartz based materials in thin films with novel structural and physical properties

Finally, the other field in which an extensive work could be done is concerns the modification of the chemical composition of the initial sol-gel precursor solution, making possible the design of new and desired single crystal piezoelectric oxide thin films and nanostructures on silicon substrate such us GeO_2 or langasite with new physical and structural properties. To reach this objective, silicon element could be replaced with similar cations but with small ionic radius and low limit in the stability field of the quartz structure (*i.e.* Ge, Al, Ga, etc.), which could able to promote quartz related structures with helicoidal cell type (see **Figure 1.2** and **Figure 1.3** in **Chapter 1**).

Scientific Activities during My PhD Period

List of publications

1) Zhang, Qianzhe; Sánchez-Fuentes, David; Gómez, Andrés; Desgarceaux, Rudy; Charlot, Benoit; Gàzquez, Jaume; Adrian Carretero-Genevrier Gich, Martí. Tailoring the crystal growth of quartz on silicon for patterning epitaxial piezoelectric films. *Nanoscale Advances*. **2019**. doi: 10.1039/C9NA00388F

2) Q. Zhang; D. Sánchez-garcia; R. Desgarceaux; A. Gomez; P. Escofet-Majora; J. Oró-soler; J. Gazquez; G. Larrieu; B. Charlot; M. Gich; A. Carretero-Genevrier. Nanostructure engineering of epitaxial piezoelectric α-quartz thin films on silicon. arXiv:1908.07016. (under consideration in Advanced Functional Materials)

3) Zhang, Qianzhe; Romain, Bachelet; Geneviève, Grenet; Gich, Martí; Adrian Carretero-Genevrier and Juan Rodriguez-Carvajal. Neutron powder thermo-diffraction study of silica gel: The catalytic role of Sr catalyst toward the epitaxial growth of α-quartz films on silicon. (under preparation)

Invited presentations

J. M. Vila-Fungueiriño, A. Gómez, Q. Zhang, D. Sanchez, G. Saint-Girons, N. Mestres, C. Magén, J. Gázquez, R. Bachelet, M. Gich, A. Carretero-Genevrier. Soft chemistry assisted nanostructured functional oxides on Si integrated systems. *EMRS Nice* **2019**.

Poster presentations

1) Qianzhe Zhang, Juan Rodríguez-Carvajal, Romain Bachelet, Geneviève Grenet, Adrian Carretero-Genevrier, Martí Gich. **"Stabilization of epitaxial quartz on Si from amorphous silica films"**. *Ipolymorphs: Novel Routs to Inorganic Polymorphs*, University of the Basque Country, San Sebastian, Spain. 22nd - 24th June, 2016.

2) J. Antoja-Lieonart, S. Zhou, V. Ocelík, A. Carretero-Genevrier, Martí Gich, Q. Zhang and B. Noheda. **"Chemical routes to Si-based piezoelectrics"**. $F^2c\pi^2$ *Joint Conference*, Laussane, Switzerland. 14th - 19th July, 2019.

Joint research

October 2017 to July 2018, Research grant (Erasmus +) at the NanochemLab of Institut d'Electronique et des Systèmes (IES) in the University of Montpellier.